



THE UNIVERSITY  
*of* ADELAIDE

# High Resolution Distributed Sensing Using Exposed-Core Fibres

*by*

**Lu Peng**

*A thesis submitted for the degree of Doctor of Philosophy*

**School of Physical Sciences  
(Faculty of Sciences)**

September 2021

We are all in the gutter, but some of us are looking at the stars.

- *Oscar Wilde*

The only limits for tomorrow are the doubts we have today.

- *Pittacus Lore*

Brave does not mean you are not scared. It means you go on even though you are scared.

- *Angie Thomas*

# Contents

<b>Abstract</b> . . . . .	iv
<b>Declaration</b> . . . . .	vi
<b>Acknowledgements</b> . . . . .	vii
<b>Publications</b> . . . . .	ix
<b>List of Figures</b> . . . . .	xii
<b>List of Tables</b> . . . . .	xiv
<b>Acronyms</b> . . . . .	xv
<b>1 Introduction</b>	<b>1</b>
1.1 Motivation . . . . .	2
1.2 Project aims . . . . .	3
1.3 Thesis structure . . . . .	4
<b>2 Literature review</b>	<b>6</b>
2.1 Introduction . . . . .	7
2.2 Optical fibres . . . . .	8
2.2.1 Conventional optical fibres . . . . .	8
2.2.2 Microstructured optical fibres . . . . .	10
2.3 Non-distributed fibre sensing . . . . .	13
2.3.1 Extrinsic fibre-tip . . . . .	14
2.3.2 Surface plasmon resonance . . . . .	15
2.3.3 Whispering gallery modes . . . . .	16
2.3.4 Fibre gratings . . . . .	18
2.3.5 Two-beam interferometer . . . . .	20
2.4 Distributed fibre sensing . . . . .	22
2.4.1 Conventional distributed fibre sensor . . . . .	22

2.4.2	Evanescent field sensing . . . . .	26
2.5	Imaging with optical fibres . . . . .	29
2.5.1	Fibre endoscopes . . . . .	29
2.5.2	Optical coherence tomography . . . . .	30
2.5.3	Multimode fibres for endoscopy . . . . .	32
2.6	Small particle detection . . . . .	33
2.6.1	Flow cytometry . . . . .	34
2.6.2	Fibre-based particle sensing . . . . .	35
2.7	Discussion and relevance to this thesis . . . . .	36
<b>3</b>	<b>Theory and experimental details</b>	<b>39</b>
3.1	Motivation and theory overview . . . . .	40
3.2	Mode launching . . . . .	48
3.3	Particle/scatterer positioning . . . . .	54
3.4	Particle size detection . . . . .	58
3.5	ECF as a WGM coupler . . . . .	61
3.6	Further investigations . . . . .	62
<b>4</b>	<b>ECFs for distributed sensing</b>	<b>68</b>
4.1	Distributed sensing of micron-scale particles . . . . .	69
4.1.1	Publication overview . . . . .	69
4.1.2	Statement of contribution . . . . .	69
4.2	Two-dimensional mapping of surface scatterers . . . . .	78
4.2.1	Publication overview . . . . .	78
4.2.2	Statement of contribution . . . . .	79
<b>5</b>	<b>Particle detection and whispering gallery modes</b>	<b>93</b>
5.1	Particle size characterisation . . . . .	94
5.1.1	Manuscript overview . . . . .	94
5.1.2	Statement of contribution . . . . .	94
5.2	Whispering gallery mode excitation using ECFs . . . . .	104
5.2.1	Publication overview . . . . .	104
5.2.2	Statement of contribution . . . . .	104

<b>6</b>	<b>Conclusions and future work</b>	<b>116</b>
	<b>Appendices</b>	<b>120</b>
A	In vivo pH fibre probe using ECFs . . . . .	120
A.1	PMMA ECF fabrication . . . . .	131
B	Nanoscale particle detection using ECFs . . . . .	134
B.1	Small core ECFs spliced to small core SMFs . . . . .	148
C	Particle flow measurements . . . . .	149
D	Mode launching using a spatial light modulator . . . . .	152
	<b>Bibliography</b>	<b>156</b>

## Abstract

Distributed fibre sensors were proposed more than 40 years ago, with their primary applications in physical sensing for civil infrastructure monitoring. Based on optical frequency domain reflectometry (OFDR), this thesis extends distributed sensing to biomedical applications, with a focus on the detection of small particles. A high-resolution distributed sensing method has been proposed, in which an exposed-core fibre (ECF) is used to detect micro-scaled sized particles. While the ECF has been reported for chemical detection in the past with high sensitivity due to the axial evanescent field along the entire fibre length, this thesis further reveals spatial distributed information of the micro-scaled particles by using the OFDR technique. The proposed scheme offers a compact and all-in-fibre approach, which avoids bulky instruments and external collection optics. Based on both theoretical analysis and experimental results, spatial distributions of micro-scaled particles in one dimension to two dimensions are detected using the few-mode property of the ECF. The size characterisation of micro-scaled particles has also been demonstrated using machine learning algorithms based on the multimode property of the ECF.

The ECF OFDR platform is also demonstrated as a useful tool for whispering gallery mode (WGM) excitation of spherical particles, where both Fano resonance and multi-particle (integrated in a single ECF) WGM excitation are demonstrated. The multi-particle WGM excitation opens opportunity to build multi-point sensors or lasers, and to study coupling effects resulting from multiple closely spaced resonators.

Overall, this thesis reports the novel applications of using ECFs for distributed detection of small particles with a detectable size down to 10  $\mu\text{m}$  and two-dimensional spatial resolution of several microns. The particle detection with both spatial distributions and size characterisation using fibre optics bridges the gap between fibre sensing and imaging, which brings insights towards *in vivo* cellular studies in the future.

**Keywords:** *high spatial resolution, distributed sensing, micro-scaled particles, optical*

*fibre, optical fibre sensing, microstructured optical fibres, label free.*

## Declaration

I certify that this work contains no material which has been accepted for the award of any other degree or diploma in my name, in any university or other tertiary institution and, to the best of my knowledge and belief, contains no material previously published or written by another person, except where due reference has been made in the text. In addition, I certify that no part of this work will, in the future, be used in a submission in my name, for any other degree or diploma in any university or other tertiary institution without the prior approval of the University of Adelaide and where applicable, any partner institution responsible for the joint-award of this degree.

I acknowledge that copyright of published works contained within this thesis resides with the copyright holder(s) of those works.

I also give permission for the digital version of my thesis to be made available on the web, via the University's digital research repository, the Library Search and also through web search engines, unless permission has been granted by the University to restrict access for a period of time.

Signed:

Date:

03/09/2021



## Acknowledgements

This four-year PhD studying experience is a true treasure of my life, which has rooted deeply into the bottom of my heart. I cannot tell how much this experience has shaped myself, which I would appreciate in the rest of life. The thing I am 100% sure for now and forever is this life-changing experience would be a solid foundation of my future no matter in life or in research. I would like to give my sincere acknowledgements to those who have helped me though, and also my apologies to those not listed below but all your helping hands are memorised.

Firstly, I would like to acknowledgement the great support and guidance from my supervisors: Dr. Stephen C. Warren-Smith, Dr. Jiawen Li, and Prof. Heike Ebendorff-Heidepriem. I could not imagine how this PhD would end up like this if without their support, encouragement and patience during the whole period. They are being role models in many aspects, and their attitudes in research and life would always remind me to be a better me. I still feel there are so much to learn from them, and I will do so in future.

Specifically, Dr. Stephen C. Warren-Smith has provided me with all the theoretical and experimental support during my research, and he is always patient and humble to help me strengthen my own confidence in research. His strict requirements for culturing me to have good habit in the lab in the earlier stage is also very important for a future researcher. His willingness to help me in every aspect is being a strong support for both my research and psychological well-being. I will remember the time he has spent on revising and polishing my paperwork; I will remember the moment when we discuss the next experimental scheme in front of a whiteboard or in my regular meetings.

Prof. Heike Ebendorff-Heidepriem is an expert in glass science and optical fibre fabrication, and she has given lots of critical suggestions during the regular discussion. She is always smiling and open-minded to welcome students and being a great mentor for all of us. Dr. Jiawen Li is an expert in optical coherence microscopy and fibre endoscopic probe fabrication, and she is giving quite suggestive feedback and detailed help during my experiments and paper writing all the time.

I would like to acknowledge the senior researchers and colleagues within the Fibres

and Photonics Materials group at the Institute for Photonics and Advanced Sensing for their helping hand, discussions and suggestions with respect to my research, as well as the team within The Australian National Fabrication Facility OptoFab node for their help with fabrication of various research tools.

I have to acknowledge the caring and help from my previous group: Prof. Guiyao Zhou and lab friend Dr. Boyao Li during my PhD. Also, I would like to thank Dr. Tony Evelyn Pain who helped me to pass the IELTS test especially in writing and speaking before applying for my PhD scholarship, while Prof. Yinlan Ruan helped me go through some documents during the PhD application. I would like to acknowledge the assistance from the lab friends and colleagues including Dr. Anna Radionova, Dr. Erik Schartner, Dr. Xuegang Li, Liushun Xie, Mengke Han, Xuanzhao Pan, Dr. Yunle Wei, Weikun Huang.

I acknowledge all financial support throughout my PhD period from the China Scholarship Council (201706750012), Adelaide University China Fee Scholarships and top-up scholarship/travel funds from the Australia Research Council Centre for Nanoscale BioPhotonics. I acknowledge the Hans-Jurgen and Marianna Ohff Research Grant from the University of Adelaide to support the research-related Germany trip in 2019.

I would like to acknowledge the great emotional support from my friends, family and relatives. On the one hand, my long-term good friends: Huini Liu, Maofang Yang, Jiaoli Wang, Senglin Xu, Jian Zheng and Heng Gu, are the sunshine of my life to support me get through the darkness and encourage me to look forward. On the other hand, I am being so grateful that my mom and dad are being supportive and caring all the time to encourage me to chase what I want. I am so lucky to have my old brother and sister-in-law to be around, and their son-my little nephew Shunuo-brings me lots of joy and happiness. I have to thank my aunt Shenghui Gong who is being a role model in my life to show me how strong and resilient a person can be. I have to thank my mom's dad-my another grandfather-who is wise, diligent and intelligent to build such an extended lovely family to let me feel being caring and loving all the time.

Last but not the least, I would never forget how my passed grandparents had shaped and nourished my personality and values. Every journey is not easy, but I am ready to embrace tomorrow carried with all the strength and love from these people.

# Publications

## Journal publications

[P1]. **Lu Peng**, Jiawen Li, Robert A. McLaughlin, Heike Ebendorff-Heidepriem, and Stephen C. Warren-Smith. “*Distributed optical fiber sensing of micron-scale particles*”. *Sensors and Actuators A: Physical*, 303: 111762 (2019).

[P2]. **Lu Peng**, Linh V. Nguyen, Jiawen Li, Nicolas Riesen, Dale Otten, David G. Lancaster, Heike Ebendorff-Heidepriem, and Stephen C. Warren-Smith. “*Two-dimensional mapping of surface scatterers on an optical fiber core using selective mode launching*”. *APL Photonics*, 6(2), 026105 (2021).

[P3]. **Lu Peng**, Nicolas Riesen, Jiawen Li, Mengke Han, Linh V. Nguyen, Heike Ebendorff-Heidepriem, and Stephen C. Warren-Smith. “*Whispering gallery mode excitation using exposed-core fiber*”. *Optics Express*, 29, 23549 (2021).

[P4]. Asma Khalid, **Lu Peng**, Azim Arman, Stephen C. Warren-Smith, Erik P. Schartner, Georgina M. Sylvia, Mark R. Hutchinson, Heike Ebendorff-Heidepriem, Robert A. McLaughlin, Brant C. Gibson, and Jiawen Li. “*Silk: A bio-derived coating for optical fiber sensing applications*”. *Sensors and Actuators B: Chemical*, 311: 127864 (2020).

[P5]. Nicolas P. Mauranyapin, Lars S. Madsen, Larnii Booth, **Lu Peng**, Stephen C. Warren-Smith, Erik P. Schartner, Heike Ebendorff-Heidepriem, and Warwick P. Bowen. “*Quantum noise limited nanoparticle detection with exposed-core fiber*”. *Optics Express*, 27(13), 18601-18611 (2019).

The following manuscript is included in this thesis but has not yet been submitted:

[M1]. **Lu Peng**, Linh V. Nguyen, Jiawen Li, Nicolas Riesen, Mengke Han, Heike Ebendorff-Heidepriem, and Stephen C. Warren-Smith. “*Particle size characterization using a multimoded exposed-core fiber*”. To be submitted to *Photonics Research*.

These above listed papers are included in this thesis. When referred to in the text the reference number is prefixed by a ‘P’ or ‘M’. For example, the first publication in this list is referred to as [P1].

Co-authored journal publications during candidature but not contained in this thesis:

[P6]. Jonas H. Osório, William M. Guimarães, **Lu Peng**, Marcos A. R. Franco, Stephen C. Warren-Smith, Heike Ebendorff-Heidepriem, and Cristiano M. B. Cordeiro. “*Exposed-core fiber multimode interference sensor*”. Results in Optics, 5, 100125 (2021).

[P7]. Pengqi Gong, Yiming Wang, Xue Zhou, Shankun Wang, Yanan Zhang, Yong Zhao, Linh V. Nguyen, Heike Ebendorff-Heidepriem, **Lu Peng**, Stephen C. Warren-Smith, and Xuegang Li. “*In situ temperature-compensated DNA hybridization detection using a dual-channel optical fiber sensor*”. Analytical Chemistry, 93, 10561-10567 (2021).

## Conference presentations and publications during candidature

[C1]. **Lu Peng**, Jiawen Li, Heike Ebendorff-Heidepriem, and Stephen C. Warren-Smith. “*Micron-scaled resolution distributed sensing using exposed core fibre*”. Australian Conference on Optical Fibre Technology (ACOFT), poster presentation in Perth, Australia, Dec.09-13, 2018.

[C2]. **Lu Peng**, Asma Khalid, Azim Arman, Stephen C. Warren-Smith, Erik P. Schartner, Georgina M. Sylvia, Mark R. Hutchinson, Heike Ebendorff-Heidepriem, Robert A. McLaughlin, Brant C. Gibson, and Jiawen Li. “*Chemical sensing based on silk coated exposed-core fibers*”. International Society for Optics and Photonics, Biophotonics Australasia, 11202,112020G, Dec. 05-08, 2019.

[C3]. **Lu Peng**, Linh V. Nguyen, Nicolas Riesen, Jiawen Li, Dale Otten, David G. Lancaster, Robert A. McLaughlin, Heike Ebendorff-Heidepriem, and Stephen C. Warren-Smith. “*Towards distributed particle sensing using a few-mode exposed-core optical fibre with a spatially referenced evanescent field*”. Conference on Lasers and Electro-Optics Pacific Rim (CLEO-PR), Aug. 02-06, 2020.

[C4]. **Lu Peng**, Linh V. Nguyen, Jiawen Li, Nicolas Riesen, Mengke Han, Heike Ebendorff-Heidepriem, and Stephen C. Warren-Smith. “*Particle size characterisation using a multimode fibre*”, submitted to the upcoming Australian and New Zealand Conference on Optics and Photonics (ANZCOP), will be held on Nov. 18-19, 2021.

## List of Figures

2.1	Traditional optical fibres . . . . .	9
2.2	Microstructured optical fibres . . . . .	10
2.3	Fundamental mode distributions of SCFs . . . . .	12
2.4	Exposed-core fibres . . . . .	13
2.5	Non-distributed and distributed sensors . . . . .	14
2.6	Fibre tip sensor . . . . .	15
2.7	Surface plasmon resonance . . . . .	16
2.8	Fibre taper couples to a resonator . . . . .	17
2.9	Fibre grating sensors . . . . .	19
2.10	Two-beam interferometric fibre sensors . . . . .	20
2.11	OTDR detection . . . . .	24
2.12	OFDR detection . . . . .	25
2.13	Accessible evanescent fields . . . . .	26
2.14	Fractional power inside the nanowire region vs. nanowire diameters . . . . .	27
2.15	In-house made MOFs . . . . .	28
2.16	Fibre bundle . . . . .	30
2.17	OCT configuration . . . . .	31
2.18	ANN model . . . . .	32
2.19	Flow cytometry . . . . .	34
2.20	Individual particle detection . . . . .	35
3.1	Flow chart of the main body of this thesis . . . . .	40
3.2	Red blood cells . . . . .	41
3.3	Concept of this thesis . . . . .	42
3.4	Polystyrene beads imaged under optical microscope . . . . .	42
3.5	Cross-section images of ECFs . . . . .	43
3.6	Simulated fibre modes . . . . .	45

3.7	Experimental set-up . . . . .	46
3.8	Multimodes' reflection . . . . .	49
3.9	Fibre splicing results . . . . .	50
3.10	Distributed sensing of particles . . . . .	51
3.11	Intermodel interference . . . . .	52
3.12	Illustration of an OFDR signal . . . . .	53
3.13	Particles distributed on the ECF . . . . .	54
3.14	fs-laser ablations . . . . .	55
3.15	Particle positioning . . . . .	56
3.16	SEM images of particles on the ECF . . . . .	56
3.17	Stability of particle's signals . . . . .	57
3.18	Particle measurements . . . . .	59
3.19	Particle excited with WGMs . . . . .	60
3.20	Modulated ECF modes . . . . .	62
3.21	Fixing particles on the ECF . . . . .	63
3.22	Set-up for particle/dust detection via free space launching . . . . .	64
3.23	Detection of dusted particles . . . . .	65
3.24	Optimised WGM excitation . . . . .	67
4.1	Illustration of 2D imaging . . . . .	78
A.1	The first PMMA ECF preform . . . . .	131
A.2	PMMA dehydration process . . . . .	132
A.3	PMMA non-structured fibres . . . . .	132
A.4	PMMA ECF preform with a short slot . . . . .	133
A.5	Fabricated PMMA ECFs . . . . .	133
B.1	Fibre sensor using small core ECF . . . . .	148
C.1	Flow cell configuration . . . . .	149
C.2	Tracking polystyrene particles . . . . .	150
C.3	Biological cell measurements . . . . .	151
D.1	Holographic masks . . . . .	152
D.2	Calibration for SLM . . . . .	153
D.3	ECF output modulated by SLM . . . . .	154
D.4	Signal drop-off . . . . .	154

## **List of Tables**

3.1	Comparison of several fibres . . . . .	49
3.2	Expected MMI within the ECF . . . . .	53
B.1	Fibre splicing results . . . . .	148



## Acronyms

ANN	Artificial Neural Network
CROW	Coupled-Resonator Optical Waveguide
EBL	Electron-Beam Lithography
ECF	Exposed-Core Fibre
EM	Electromagnetic
FBG	Fibre Bragg Grating
FEM	Finite Element Method
FFT	Fast Fourier Transform
FM	Fundamental Mode
FP	Fabry-Perot
FWHM	Full Width at Half Maximum
GIF	Graded Index Fibre
HCF	Hollow Core Fibre
HOM	Higher-Order Mode
ID	Inner Diameter
LPG	Long Period Grating
LSPR	Localised Surface Plasmon Resonance
MMF	Multi Mode Fibre
MOF	Microstructured Optical Fibre
MZI	Mach-Zehnder Interferometer
NA	Numerical Aperture
OCT	Optical Coherence Tomography
OFDR	Optical Frequency Domain Reflectometry
OTDR	Optical Time Domain Reflectometry
PMMA	Poly (methyl methacrylate)
RI	Refractive Index

SEM	Scanning Electron Microscope
SLM	Spatial Light Modulator
SMF	Single Mode Fibre
SPP	Surface Plasmon Polaritons
SPR	Surface Plasmon Resonance
WGM	Whispering Gallery Mode

# **CHAPTER 1**

## **Introduction**

## 1.1 Motivation

Development of optical fibre sensors started in the 1970s, almost as soon as the first low loss silica fibre had been demonstrated [1]. Fibre sensors are widely reported for applications in fields such as optical telecommunication, defence, and infrastructure for temperature, pressure, strain and gas leakage measurements [2–5]. These widespread applications benefit from the key advantages of optical fibres such as distributed or multipoint sensing, immunity to electromagnetic interference, corrosion resistance, and their light weight. Also, the miniaturised size and remote operation allows their deployment not only in traditional industries but also in biomedical fields for *in vivo* sensing and endoscopic imaging. This thesis aims to expand optical fibre sensing towards biomedical applications, particularly particle detection and characterisation.

One of the big interest of studying individual small particles is to ultimately understand their dynamics including physical force and biomedical interactions, and the thorough understanding of biomedical reaction would help disease diagnostics and drug research eventually [6, 7]. Driven by this purpose, many fibre sensing schemes for single particle detection have been reported. For example, an optical tracking method was proposed for tracing single nanoparticles using an optical fibre, which was achieved by fabricating a nanofluidic channel inside conventional single mode fibre, proposed by S. Faez *et al.* in 2015 [8]. Similar particle detection configurations have been introduced using fibre with an eccentric nano-channel or using a hollow core fibre [9, 10]. Tapered fibres have been used for the quantification of particles, by measuring the drop-off in the transmitted signal due to the scattering loss induced by individual particles attached on the tapered region [7]. These approaches rely on either external optics to collect the particle's scattering information or highly fragile fibre tapers, preventing out-of-lab usage. Neither of these approaches have the capability to integrate both spatial information and characteristics of particles (e.g., size and shape). Is it possible to develop practical, minimally-invasive, label-free and multiplexed fibre sensing schemes for particle detection, tracking and characterisation?

Evanescent field fibre sensing has the potential to meet this demand. The challenge is to have sufficient evanescent field available for interacting with the environment.

At the University of Adelaide, suspended core fibres (SCFs) and exposed-core fibres (ECFs) with small optical cores have been developed for this purpose. These fibres have been demonstrated for long-distance fluorescence measurements with improved response time [11], biosensing measurements [12], and distributed fluorescence sensing with 0.5 m spatial resolution through time-resolved measurements [13].

The unique feature of ECFs is an open channel that directly exposes the fibre core to the surrounding environment. The accessible longitudinal evanescent-field of ECFs can be used for distributed sensing. Their outer jacket does not only provides standard fibre dimensions (e.g., 160  $\mu\text{m}$ ) to splice with conventional step index fibres to build fully fibre-integrated sensors, but also acts as a partial shield for deposited or attached particles/objects from the disturbance of outside environments. Therefore, ECFs could be a good candidate to detect small particles including their presence, spatial distribution and size characterisation.

## 1.2 Project aims

This thesis aims to bridge the gap between fibre sensing and imaging, that is, to realise multi-dimensional high resolution distributed sensing of small particles using a single ECF. The specific aims related with distributed sensing are listed as follows:

- Aim 1: high spatial resolution distributed fibre sensing of microscale particles using the OFDR technique.
- Aim 2: two-dimensional mapping of surface scatterers using selective individual mode launching.
- Aim 3: size characterisation of micro-scaled particles.

In addition to distributed sensing, this thesis aims to demonstrate the ECF as a versatile photonic platform for sensing, including:

- Aim 4: WGM excitation of spherical particles.

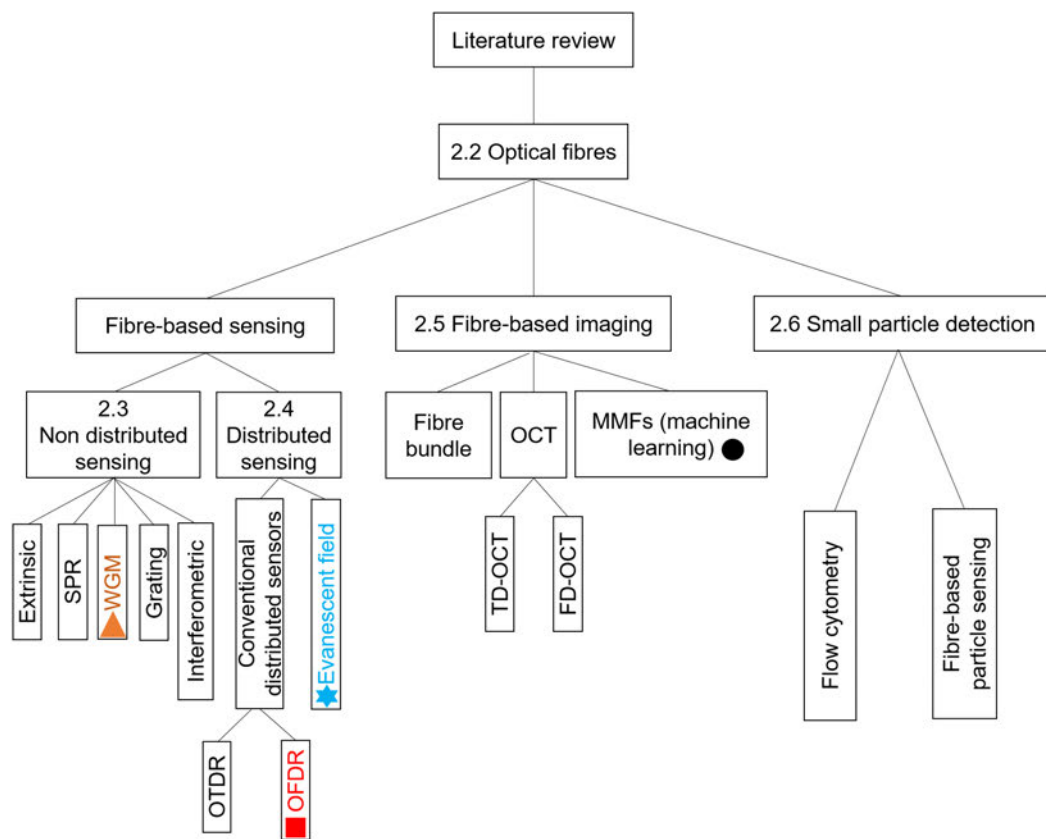
The proposed sensing method has the potential to be implemented in biomedical and biochemical applications such as particle tracking, cell counting and sizing, disease diagnostics and concentration analysis of biological aqueous suspensions.

### 1.3 Thesis structure

This thesis covers several topics that contribute to high-resolution distributed fibre particle sensing, with a view towards high-sensitivity *in vivo* application. The structure of this thesis is depicted in the flow chart below.

The literature review in Chapter 2 will provide a broad background of current optical fibre sensing, and also fibre endoscopic imaging techniques. At the end of the literature review, current research for the measurement of individual particles is introduced, which is the foundation for the discoveries in this thesis.

Chapter 3 includes the principle theory and experimental approaches to give an overview of the projects reported in this thesis. Other chapters mainly consist of publications. One-dimensional sensing of micro-scaled particles and two-dimensional mapping of micro-scaled scatterers are demonstrated in Chapter 4.1 and Chapter 4.2, respectively. Particle size characterisation using machine learning algorithms is discussed in Chapter 5.1. The use of the ECF for WGM excitation is demonstrated in Chapter 5.2. In the appendices, there are two studies that progress other important aspect of optical fibre sensing using ECFs. This includes using silk to create a functional and compatible coating for *in vivo* sensing, and a demonstration of detecting particulates (suspended in liquid) using a heterodyne detection method. While not explicitly aligned to the main aims of this thesis, they demonstrate progress towards highly sensitive *in vivo* sensing, which is the future target of this project.



**Chapter 3**  
Theory and experimental methods

**Chapter 4**  
P1  
P2

**Chapter 5**  
P3  
M1

- ( ★ ■ ▲ ● )
- OTDR
  - OFDR
  - OCT
  - SPR
  - WGM
  - MMFs
  - Evanescent field
  - P Publications
  - M Manuscript

## **CHAPTER 2**

### **Literature review**



## 2.1 Introduction

Optical fibre sensors can be designed to measure any parameter from the environment that could be transduced on the optical properties of the fibre. This can be an effect on properties such as the light intensity, wavelength, phase and polarisation [2, 3]. The key effort in optical fibre sensing is to sensitively correlate a physical, chemical or biological variation to one of these optical parameters, while considering practical factors such as multiplexing, cross-sensitivity, robustness, and cost. A number of fibre sensors to measure physical parameters have become commercially available over the last few decades, with the most prominent types being fibre grating sensors, fibre interferometric sensors and fibre distributed sensors [14–18]. The advantages of optical fibres for sensing applications are concluded as following:

- The intrinsic advantage of optical fibres is their immunity to electromagnetic (EM) interference due to its electrical insulation, which is favourable for applications that exist in strong EM fields such as magnetic resonance imaging.
- Their extrinsic advantages are being light weight, miniaturised, flexible and remote-controllable, enabling them to get into hard-to-access regions including *in vivo* biological tissues.
- Distributed or multipoint sensing.

In parallel, imaging techniques are great tools for visualisation of the micro-scaled biological world [19]. Recently, the breakthrough of super-resolution microscopy has brought a revolution in visualisation of the microscopic world.

This thesis is to detect small particles including their size and spatial distributions based on fibre technique, which in a sense builds a connection between fibre sensing and imaging. The literature review presents an overview of the applications of optical fibres in sensing and imaging. The detection of micro-scaled particles using fibre optics is presented at the end, which forms the foundation of this thesis. That is, to develop a distributed technique for mapping micro-scaled particles in a fibre sensing manner towards *in vivo* detection in the future.

Optical fibres are introduced in Sec. 2.2. Fibre-based sensing applications are then classified according to their detection regions, being non-distributed fibre sensing in

Sec. 2.3 and distributed fibre sensing in Sec. 2.4. Fibre-based imaging techniques are reviewed in Sec. 2.5. Flow cytometry and fibre-based research for individual small particle detection are reviewed in Sec. 2.6. A final discussion in Sec. 2.7 summarises the relevance of this literature to the work in this thesis, and the focus of this thesis is to detect micro-scaled particles including both spatial distributions and morphology (i.e., size and shape) based on a fibre sensing technique.

## 2.2 Optical fibres

In 1979, optical fibres were first reported to achieve an attenuation less than 0.2 dB/km at 1.55  $\mu\text{m}$ , which has directly driven the revolution of modern optical telecommunication [20]. Conventional silica optical fibres, those used for optical telecommunications, are drawn from a preform fabricated via vapor deposition (i.e., modified chemical vapor deposition and plasma chemical vapor deposition). The realisation that optical fibres can also play a role in applications such as nonlinear light generation and sensing, has sprouted new classes of fibre and new fabrication techniques. For example, microstructured optical fibres (MOFs), which are primarily fabricated using the stack-and-draw approach with other methods including drilling or extrusion (i.e., for non-silica glass) depending on the specific structure and material properties [21–23].

### 2.2.1 Conventional optical fibres

Conventional optical fibres can be further classified as: step index fibres and graded index fibres (GIFs) based on the index distributions of the fibre core as shown in Fig. 2.1. Step index fibres are composed of two materials: a higher index core and a lower index cladding. The propagating principle is based on total internal reflection [24, 25]. By total internal reflection, the light can be confined in the higher index core, while the loss is majorly caused by material absorption and Rayleigh scattering. GIFs have graded index distributions (e.g., quadratic decrease from the core centre to the core-cladding interface) inside of the fibre core as shown in Fig. 2.1(b), so they could be designed to adjust the group velocity of the output modes to allow different modes to arrive at the end-face simultaneously. This is the key advantage of using GIFs due to reduced intermodal dispersion caused by various group velocities. On the other hand,

GIFs are generally having higher loss (e.g., 20 dB/km) because of the graded index profile causing larger scattering loss and geometrical confinement loss, so they are generally suitable for short distance (e.g., 1 km) data transportation (e.g., 1 Gb/s) in the commercial telecommunication system [26]. The GIFs can also be deployed as an imaging lens due to their ability to focus light [27–29].

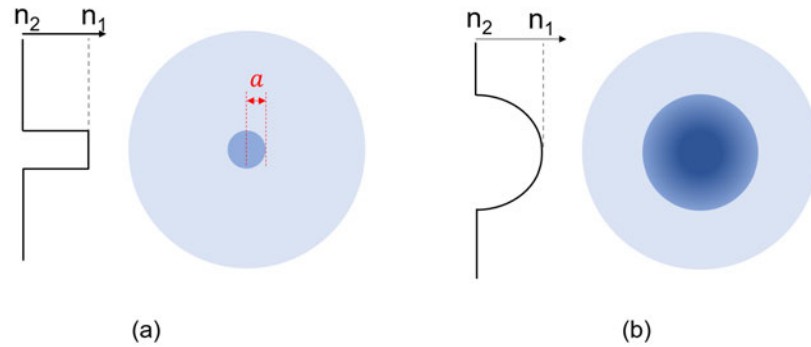


**Fig. 2.1** (a) Illustration of a step index fibre. (b) Illustration of a graded index multimode fibre.

Considering the quantity of propagating modes, optical fibres can be categorised as single mode fibres (SMFs) and multi-mode fibres (MMFs). SMFs are widely used in long distance telecommunications due to the single mode transmission without intermodal dispersion. Determining whether a step index fibre is single mode or multimode can be done by analysing the fibre's V-number [25]:

$$V = NA \cdot a \cdot \frac{2\pi}{\lambda} \quad (2.1)$$

where  $a$  is the radius of fibre core and  $\lambda$  is the free space wavelength. The numerical aperture (NA) is expressed by [25]:

$$NA \approx \sqrt{n_1^2 - n_2^2} \quad (2.2)$$

where  $n_1$  and  $n_2$  are core and cladding index, respectively. The single-mode condition is held when  $V \leq 2.405$ , and the cut-off wavelength for SMFs is thus determined by this value. In optical telecommunications, SMFs typically have core diameters less than 10  $\mu\text{m}$ , while MMFs have much larger core diameters (e.g., 62.5  $\mu\text{m}$  and 125

$\mu\text{m}$ ). Although SMFs have driven the digital revolution of the current global society, exploiting fibres for space division multiplexing is an area of active research.

The approximate number of total modes ( $M$ ) supported by a step index fibre can be estimated by:

$$M \approx \frac{V^2}{2} \quad (2.3)$$

The main issue of MMFs is the intermodal dispersion, as it leads to data errors during signal transmission since different modes suffer different time delays. However, the large capacity to quickly access multiple information is one of the key demands currently in optical telecommunications, and many achievements could be found including few-mode fibres and multiple core fibres with improved capacity from 45 Mb/s to tens of Tb/s over the past 40 years allowing both space division and wavelength division multiplexing techniques [30, 31]. In addition, the application of MMFs is not limited to telecommunications, and other applications such as imaging will be introduced in Sec. 2.5.3.

## 2.2.2 Microstructured optical fibres

Microstructured optical fibres (MOFs) are made by introducing air holes longitudinally in a single material as shown in Fig. 2.2. The successful fabrication of the first MOFs in the middle of the 1990s [32, 33] has boosted research in applications such as ultra-fast pulses, optical amplifiers and super-continuum fibre lasers. The flexibility in the MOF geometry allows for unique optical properties such as tunable dispersion/non-linearity/birefringence and endless single mode optical operation [21, 22, 34].

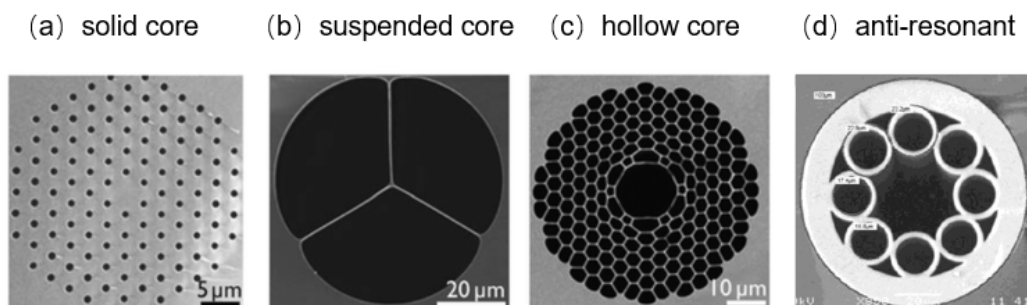


**Fig. 2.2** Different types of MOFs while (a-c) are from Ref. [35], and (d) is from Ref. [36].

In theory, these various interior structures induce difficulty to define the boundary condition, which cannot be solved using a general analytical solution as is possible for step-index fibres [25]. Numerical simulations based on the finite element method (FEM) are normally used to study these complicated structures, by discretising the waveguide domain into small elements. Therefore, FEM is a common solution to solve the electromagnetic field and propagation constants of the fibre.

The guidance mechanism of the MOFs is based on two different principles: modified total internal reflection and the photonic bandgap effect. In terms of total internal reflection, it was demonstrated in 1996 by stacking silica capillaries in a hexagonal structure [32] with a similar one shown in Fig. 2.2(a). Based on total internal reflection, it was then realised that there is no need to have regular geometric alignment of the inner air holes to support the light propagation, with an example displayed in Fig. 2.2(b). In fact, photonic bandgap fibres were firstly proposed as MOFs by P. Russell in 1992 with an example shown in Fig. 2.2(c), which was inspired by the Bloch phenomenon shown in two dimensional planar photonic crystals [37]. In 1998, the photonic bandgap fibre was experimentally demonstrated by introducing six sub-micron air holes in the core centre running along the entire fibre length [33]. Since periodic photonic crystals confine the light via optical interference, some frequencies are forbidden in the periodic cladding to only allow transmission in a defect in the crystal. The large hole in the centre is such a defect (as shown in Fig. 2.2(c)) which forms the fibre core. Anti-resonant fibres as displayed in Fig. 2.2(d), were further proposed to have no requirement for the periodic cladding structure [36, 38, 39].

### **Hollow core fibres**

Hollow core fibres (HCFs) are particularly practical for the following applications. Firstly, the long light-matter interaction [40] along the hollow core, has been demonstrated to greatly increase the Raman and Brillouin scattering of gas molecules—filled into the core to contribute to nonlinear optics such as lasing, frequency combs and interactions with atoms [41–45]. Secondly, HCFs are favourable for high power laser transportation due to the ultra-low overlap between the mode profile and the solid material, having much higher damage threshold compared with solid core fibres [46]. Thirdly, ultra-fast transmission speed could be achieved in the

hollow core without suffering non-linear effects and material dispersion [47]. Fourthly, thermo-optic instability would be greatly avoided in HCFs, making them advantageous for the next generation of fibre gyroscopes, which has been majorly restrained due to non-linear effects and the thermo-polarisation effect [48]. In addition, hollow core MOFs are expected to have lower loss theoretically [49], with a documented achievement less than 1 dB/km in the L band (1565-1625 nm) in 2020 [50].

### Suspended core fibres

The suspended core fibre (SCF) was proposed to be an ideal candidate for evanescent field sensing due to the small suspended core surrounded by air channels [51–53], leading to a significant fraction of the guided optical field propagating as an evanescent field in the fibre air holes shown in Fig. 2.3 [54]. Large air holes enable quick filling for liquid and gases for evanescent field interaction with the guided core modes. Many SCFs chemical sensors have been reported such as detection of acetylene,  $NaCl_2$ , and fluorescent solutions [12, 53, 55].

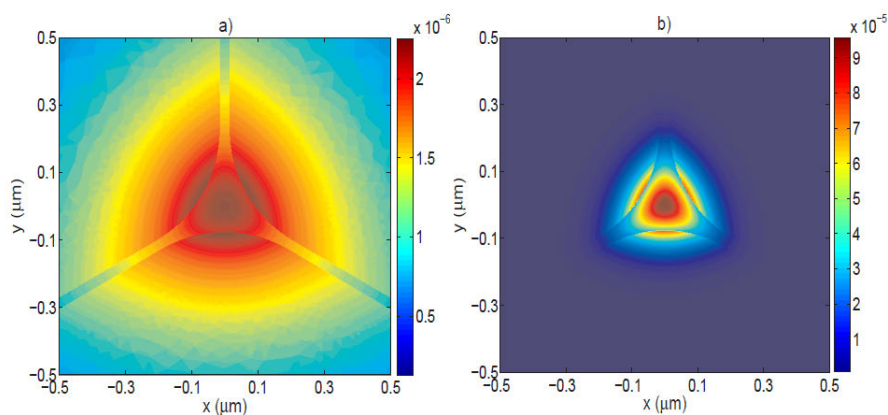


**Fig. 2.3** SCFs with a core diameter of  $0.2 \mu\text{m}$ . (a) Simulated fundamental mode of a silica fibre. (b) Simulated fundamental mode of a bismuth fibre. Both mode intensity distributions were simulated at a wavelength of 590 nm from Ref. [54].

### Exposed core fibres

Exposed core fibres (ECFs) were developed from SCFs, which exposed the fibre core to allow easy access to the evanescent field along the length of the fibre. Many research papers demonstrated attempts to achieve such a purpose based on etching/polishing

methods in the past [56–58]. In 2007, ECFs were first reported to have the exposed-side directly drawn into fibre as shown in Fig. 2.4(a) based on a drilling method using polymethylmethacrylate (PMMA) [59], while the exposed-side channel was made from discrete small drilling sections on the preform. Glass-based ECFs preforms were then fabricated based on extrusion [11, 60] or direct drilling [61] as shown in Fig. 2.4(b) with the corresponding drawn fibre in 2.4(c). They could be drawn with a continuous exposed-side up to kilometres at once. Various core diameter ECFs could be made with the reported smallest core diameter of  $1.65 \mu\text{m}$ , which was used to investigate non-linear effects [62]. Silica-based ECFs have been used for evanescent field sensing of microscale particles in this project, with more detailed descriptions in Sec. 2.4.2.

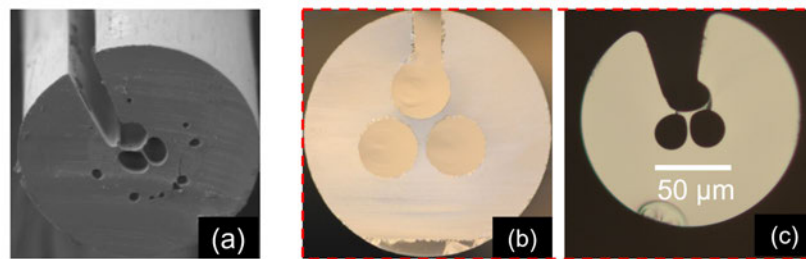


**Fig. 2.4** (a) PMMA exposed-core fibre from [59]. (b) ECF preform made by a drilling method. (c) The ECF drawn from the preform in (b).

### 2.3 Non-distributed fibre sensing

Many photonic devices have been invented in the last two decades for lasing, sensing, and optical filters/couplers, but the main focus in this thesis is fibre-based sensing. An optical sensor is made by transducing the measurand to a variation of the optical signal (e.g., wavelength, amplitude, phase and polarisation) [2, 3], and the mechanisms behind include fluorescence/indicators, evanescent field interactions (e.g., surface plasmon resonance and whispering gallery modes resonance), and optical interference. Therefore, these types of sensors are introduced in the following as two major sections according to their detection regions: non-distributed fibre sensing as illustrated in Fig. 2.5(a1, a2, a3), and distributed fibre sensing illustrated in Fig. 2.5(b1). This classification is to highlight the relevance with the work implemented in this thesis.

Here, non-distributed fibre sensing includes any sensor that does not provide

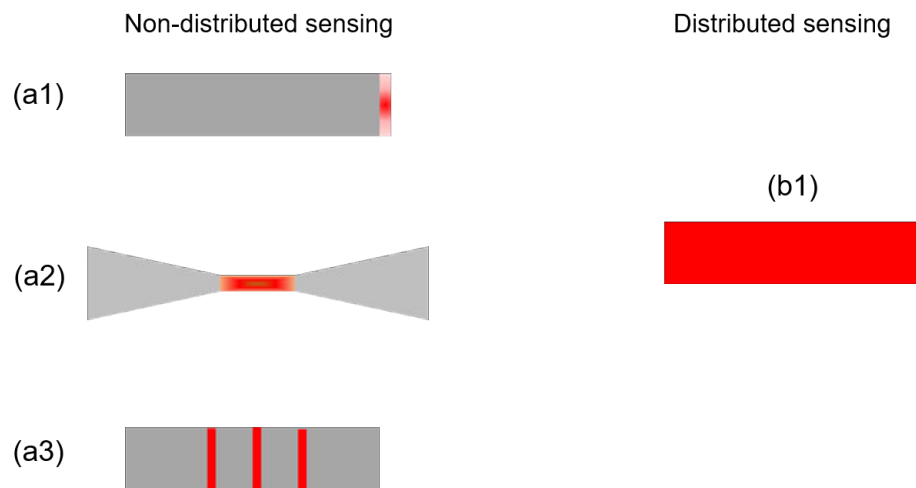


**Fig. 2.5** (a1) Fibre-tip sensor where the signal is collected back to the fibre through back-scattering. (a2) Sensing a single point along the fibre such as a fibre taper. (a3) Multipoint sensing such as using grating fibre sensors. (b1) Distributed sensors where the detection range is along the entire fibre length with longitudinal spatial resolution depending on the detection method and experimental instruments.

continuous spatially resolved measurement along the fibre. This includes both extrinsic fibre-tip sensors and intrinsic fibre sensors. Intrinsic fibre sensors consist of evanescent field interactions, gratings, intrinsic scattering and interferometry. They typically either have energy exchange/transfer (e.g., surface plasmonic resonance, whispering gallery mode resonance and fluorescence) or have a phase change in the optical signal (interferometric-based sensors) due to the presence of an analyte.

### 2.3.1 Extrinsic fibre-tip

Extrinsic fibre sensors are where the fibre acts only to carry the light. That is, an optical fibre is applied as a light link to interface external instrumentation to a targeting element [63]. An illustration of the extrinsic fibre-tip sensor is shown in Fig. 2.6, in which the backscattered signal from the measurand is carried back via the fibre's guided modes [64]. The feature of fibre-tip sensors is portability due to the miniaturised size while maintaining a robust handling, making them well suitable for biochemical or biomedical fields. The key working mechanism is that the surrounding measurand has to be interactive with the coated/doped material at the tip, leading to detectable changes in the optical signals such as the intensity of fluorescence [65]. Many fluorophores, quantum/carbon dots, and rare-earth ion doped particles are



commercially available for fabricating fluorescence-based fibre sensors, such as for sensing pH, gases (e.g., nitric oxide, oxygen, carbon monoxide, and hydrogen), and ions (e.g., calcium and mercury) [65, 66]. Porous but transparent materials (e.g., polymers and sol-gel) have been used to encapsulate fluorophores. MMFs are widely used for signal collection as their large core and high numerical aperture allows for good signal collection.



**Fig. 2.6** Illustration of a fibre-tip sensor for detecting the surrounding environment, which are generally gases or liquids.

### 2.3.2 Surface plasmon resonance

A surface plasmon wave (SPW) is formed when surface plasmon polaritons (SPPs) propagate along an interface between a metal layer (e.g., gold and silver) and a dielectric material under evanescent field excitation as shown in Fig. 2.7 [67]. The occurrence of the surface plasmon resonance (SPR) leads to a sharp feature observed in the transmission spectrum in the visible to near-infrared waveband [68]. This results from a phase-matching process between the guided wave and the SPW, enabling the energy to transfer from the waveguide to the metallic material at resonant frequencies. The propagation constant of the SPW is determined by [67]:

$$\beta_{spp} = \frac{\omega}{c} \sqrt{\frac{\varepsilon_m \varepsilon_s}{\varepsilon_m + \varepsilon_s}} \quad (2.4)$$

where  $\varepsilon_m$  and  $\varepsilon_s$  are permittivities of the metal and the surrounding medium, respectively,  $c$  is the speed of light in vacuum, and  $\omega$  is the angular frequency of the light. Therefore, the resonant condition is affected by the refractive index change of the surrounding material. The change of the real part of the refractive index contributes to a wavelength shift, and the change of the imaginary part modulates the resonant amplitude [69].

Localised SPPs exist in metallic nanostructures when the dimension of the

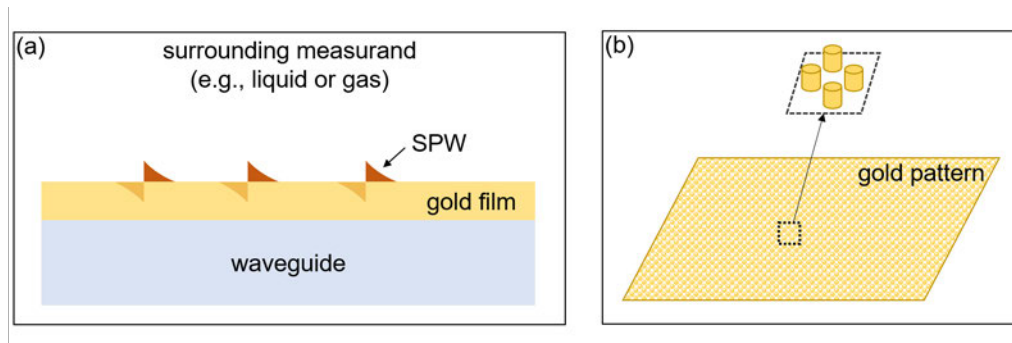


**Fig. 2.7** (a) An illustration of SPW formed on a continuum surface. (b) LSPR formed on a discontinuous metallic structure.

nano-cells is smaller than the wavelength of the incident light, resulting in a strong confinement of the local electromagnetic field around the nano-cells. This is so-called localised SPR (LSPR), and widespread applications have been reported such as highly-sensitive fibre sensors and surface enhancement Raman spectroscopy [70, 71]. Specifically, LSPR is generated when the frequency of incident photons matches with the collective oscillation frequency of the electrons from metallic nano-cells, which leads to strong attenuation of incident light at the resonant frequency. The resonant frequency and strength could be adjusted by changing the alignment, size and shape of the metal nanostructures [72, 73].

Optical fibres have been shown as promising platforms for SPR sensing [74]. This includes ECFs, where the accessible evanescent field allows ECFs to be amenable for SPR based sensing platforms. Reported demonstrations include deposition of both metal films and gold nanoparticles on the ECFs [75, 76].

### 2.3.3 Whispering gallery modes

Whispering gallery modes (WGMs) occur when light propagates around a concave surface such as a sphere due to total internal reflection. They were inspired by the soundwave whispering around the roof of the St. Paul cathedral in London back in 1878. The concept has had lasting impact in many fields such as lasing, frequency combs, quantum opto-mechanics and biosensing, due to its high achievable Q-factor in a microscale size with less cost and less-complicated alignment compared with Fabry-Perot (FP) cavities [77–82]. Although many cavities are reported to support WGMs including spherical, cylindrical, toroidal, hexagonal, and rectangular objects

[83]; spheres, rings, and toroids are still the most widely used WGM resonator geometries for achieving high Q-factors. The huge interest of WGMs in biosensing is because of its extreme sensitivity for label-free detection at a single molecule level [84] and even single atomic ions [82], while a Q-factor of up to  $10^8$  was demonstrated in 2007 [85]. The coupling platforms to generate WGMs include prisms, fibre tapers [86, 87], and microstructured optical fibres (MOFs) [88–91]. Among them, fibre tapers are still widely used due to the ultra-high coupling efficiency of up to 99% [92], but the complicated positioning between the supporting platform and the fragile ultra-thin fibre taper remains a big challenge for out-of-lab usage as shown in Fig. 2.8.

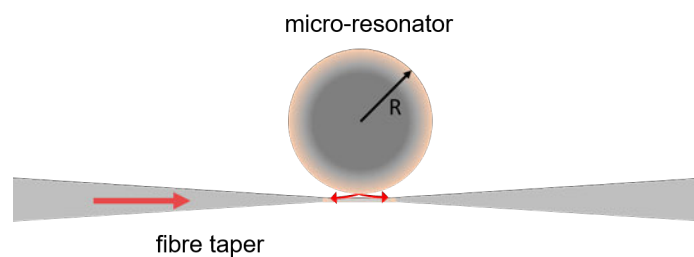


**Fig. 2.8** Guided light from a fibre taper couples to a micro-resonator where WGMs are excited.

Integrated fibre couplers have been proposed for bringing the possibility of lab-in-fibre, such as etching/melting the optical fibre to expose the core to allow a light-matter interaction for generating WGM resonance while retaining the outer structure to support resonators [91, 93, 94]. An alternative approach is to use MOFs, which have the ability to hold the resonators directly by one of the air channels without etching/tapering/melting post-processing [88–90]. ECFs show good potential due to the longitudinal exposed channel that can position multiple resonators with a high degree of flexibility [54, 95]. The excitation of WGMs using ECFs is one of the major topics in this thesis (Chapter 5). In addition to biosensing applications, WGM resonance can be used in applications such as Fano resonance, for building photonic devices. This topic is introduced in Chapter 5, where ECFs are demonstrated as a potential platform for achieving such an application.

### WGM sensing

The traditional WGM biosensing mechanism is based on the shift of the resonant wavelength. The wavelength spacing between adjacent fringes can be expressed by the

free spectral range (FSR) [6]:

$$FSR = \frac{c}{2\pi n_{eff}R} \quad (2.5)$$

where  $c$  is the speed of light in vacuum,  $n_{eff}$  is the effective index of the resonator's mode and  $R$  is the radius of the resonator. In a simplified explanation, any attached molecules or chemicals increasingly form a layer on the resonator's outer surface, leading to a geometric path change ( $R$ ) of the resonator, and this shifts the resonant wavelength [6].

To improve this approach, a splitting mechanism was proposed resulting from the disturbance of outer scatterers, leading to a degeneracy lift between the counter-clockwise and clockwise propagating modes based on a heterodyne detection [96]. The split modes are referenced with each other to enable the subtraction of external noise (e.g., instruments and the surrounding environment) for better sensing performance. A WGM lasing scheme based on the splitting mechanism was designed for virus detection, as lasing peaks resulting from a non-linear resonance could improve the resonant strength significantly, accompanied by an enhanced sensitivity due to an achievable ultra-narrow linewidth [97].

Note that WGM-based fibre sensors can work not only as single point sensors through functionalisation for selective detection of biological samples (e.g., proteins, DNA, and virus) around the resonator, but also can act as multi-point/distributed sensors depending on the quantity of the microspheres and designed sensing configurations. A more recent interest is to introduce micro-resonators into biological cells [98], where lasing the resonator would enable monitoring the kinetics of intracellular interactions [99]. This would potentially contribute to understanding the fundamental dynamics in the biological world and bring insights for biomedical research.

### 2.3.4 Fibre gratings

Grating-based fibre sensors are often applied to structural health monitoring (e.g., buildings, dams, bridges, aircraft, and electric power industries), by measuring physical parameters such as temperature and strain [100]. They are mainly divided

into two categories: fibre Bragg gratings (FBGs) and long-period fibre gratings (LPGs) [100–102]. Fibre gratings consist of a periodic modulation in the refractive index (RI) along the longitudinal axis of the optical fibres, typically several millimetres long. In an FBG scheme, the resonant wavelength (Bragg wavelength) is reflected back, while the light outside of the Bragg wavelength would transmit as shown in Fig. 2.9(a). The Bragg wavelength is given by [25]:

$$m\lambda_B = 2n_{eff}\Lambda \quad (2.6)$$

where  $m$  is the order of the Bragg wavelength. This reflected wavelength is dictated by Bragg's law, which depends on both the RI ( $n_{eff}$ , the effective index of the propagating mode in the fibre core) and the pitch ( $\Lambda$ ) of the grating.

An FBG has a period of hundreds of nanometres. FBG temperature sensors primarily detect the change from RI of the fibre core due to the thermo-optic effect, while the strain sensors are based on changes in the pitch when the fibre is physically under strain [100]. Multiple gratings can be interrogated using wavelength division multiplexing along a single fibre for quasi-distributed sensing [103, 104]. Due to the narrow resonant peak resulting from the Bragg grating, it allows FBG sensors to be multiplexed with other types of fibre sensing (such as SPR) [105, 106],

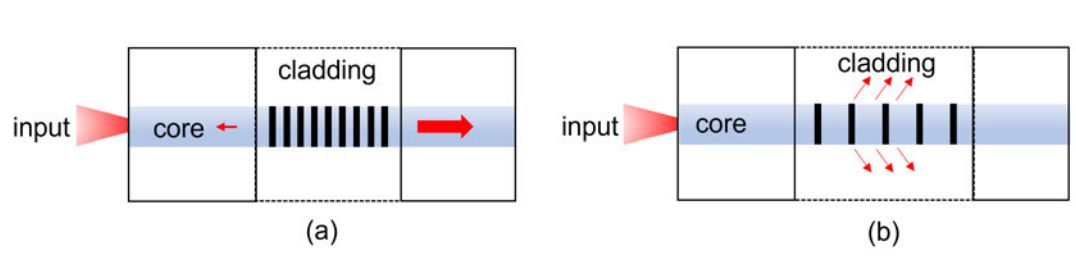


**Fig. 2.9** (a) FBG inscribed inside the fibre core. (b) LPG inscribed inside the fibre core.

The LPG has a period of hundreds of micrometres and is typically used to couple the fundamental mode to forward propagating cladding modes in optical fibres [100], as shown in Fig. 2.9(b). Variations in the external environment surrounding the fibre changes the coupling resonance between the fundamental mode and cladding modes. The resonance occurs when the phase matching condition is satisfied [107]:

$$\lambda_{re} = (n_{core} - n_{clad})\Lambda \quad (2.7)$$

These external changes (e.g., RI of the surrounding liquid/gas) can thus be detected by monitoring the shift of the resonant wavelength. Chemical sensors based on both LPGs and SPR have been reported [68, 108] such as the monitoring of chemical battery performance, where the strength of the resonant wavelength was monitored during the charging and discharging process [109]. The ions' chemical reaction changes the imaginary part of the refractive index, leading to a change in resonant amplitude/strength [69].

### 2.3.5 Two-beam interferometer

Two-beam interferometric fibre sensors can be classified as four classic types: Michelson, Mach-Zehnder, Fabry-Perot, and Sagnac. Their working principle can be simplified as two beams interfering, as expressed by [2]:

$$I = I_1 + I_2 + 2\sqrt{I_1 I_2} \cos\left(\frac{2\pi n_m L}{\lambda}\right) \quad (2.8)$$

where  $I_1$  and  $I_2$  are intensities from two beams, respectively. The key sensing mechanism is that any change in the optical path difference ( $n_m L$ ,  $L$  is the physical length of the interferometer) induced by the surrounding medium is transduced into a change of the optical interference signal.

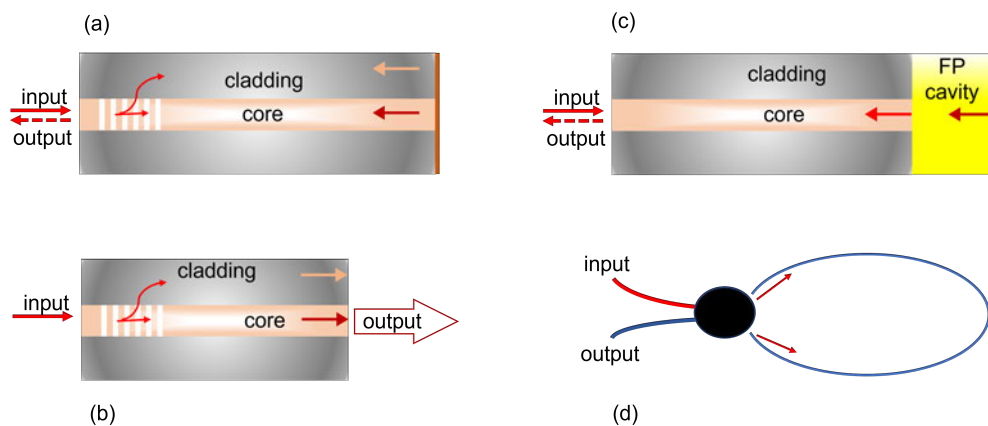


**Fig. 2.10** (a) Michelson interference occurs in a single mode fibre based on an LPG scheme. (b) MZI in a single mode fibre based on an LPG scheme. (c) FP interference based on a single mode fibre. (d) Sagnac interference based on a single mode fibre with counter propagating beams.

The Michelson interferometer was made famous by the Michelson-Morley

experiment, where a light beam was separated into two arms after a beam splitter to detect the supposed luminiferous aether. One arm acts as the reference arm, while another arm is undertaking measurements. Two beams are then reflected back to yield detectable interference. Many successful applications, such as optical coherence tomography for biomedical imaging [110], the Twyman-Green interferometer used to test optical components [111] and even gravitational wave detection [112], are based on the principle of Michelson interference. A Michelson interferometer in fibre optics can be implemented such as multimoded interference within the core, or using LPGs to excite the cladding modes, then reflect back from the fibre far-end. A coating layer on the fibre distal end-face could act as a mirror to increase the reflection efficiency as shown in Fig. 2.10(a).

The advantage of the Michelson interferometer configuration is the compact size with both input and output at the same fibre end, to allow for distal end measurements with greater operating flexibility. The Mach-Zehnder interferometer (MZI) configuration is quite similar to the Michelson interferometer, but it operates in transmission rather than a reflection mode, so the optical interference is collected from the far fibre end, as illustrated in Fig. 2.10(b). MZI integrated in an optical fibre could be realised such as multimode interference within the core [113], or core mode interfering with cladding modes through either LPGs, or core mismatch between fibres through splicing schemes [114].

Fibre Fabry-Perot (FP) sensors are generally formed by a short cavity with micro-scaled length as illustrated in Fig. 2.10(c), where the FP cavity is made either sealed or with an open side. Sealed FP cavities are used to measure physical parameters such as temperature [115] and pressure [116, 117]. Open side cavities [118, 119] are favourable for biochemical sensors, as it allows direct filling of analytes which could be either fluids or gases. The light is reflected by the two surfaces of the cavity, where a change of an analyte inside the cavity causes a change in the optical path difference between the two beams, leading to a detectable change (e.g., wavelength shift or phase change) in the optical interference spectrum.

In the late 1960s, researchers demonstrated that the ring laser could generate a Sagnac effect creating a gyroscope, which then was applied to commercial aircraft for the navigation system to map real-time rotation speed/direction. The first SMF based

ring interferometer was reported in 1976 [120], which has led to successful commercialised optical fibre-based gyroscopes for detection of lower angular velocities particularly. The Sagnac effect results from relativistic effects, when two light signals transmit through a loop with opposite directions from the same light source and output in the same direction under rotation as illustrated in Fig. 2.10(d). The rotation rate from the external environment can be measured via the optical interference between two beams. There are many other sensing applications proposed by using the Sagnac effect, such as for measurements of magnetic field [121, 122], temperature [123], and bulk refractive index [124].

## **2.4 Distributed fibre sensing**

### **2.4.1 Conventional distributed fibre sensor**

The fibre sensors described in Sec. 2.3 are all non-distributed sensors where measurement occurs at either a single point or multiple discrete points. In this section, the focus is on distributed sensing where the detection occurs along the entire fibre length. Distributed sensors were first proposed in 1976 [125], and they are now commercially available [18]. These conventional distributed fibre sensors introduced here operate by detecting the backscattered light, which varies by interacting with the ambient environment such as temperature, strain and vibration [126, 127]. The significant advantage of distributed sensors is their capability for long-range detection in applications such as structural health monitoring with real-time detection along distances up to tens of kilometres. Distributed sensing can be performed using three types of scattering phenomena within the fibre, being Rayleigh scattering, Raman scattering and Brillouin scattering.

#### **Rayleigh scattering**

Rayleigh scattering results from the material itself—inherent random fluctuations, and this leads to unavoidable attenuation losses of the transmitted light in solid-core fibres. Rayleigh scattering, as an elastic scattering, has no energy exchange but only a changed direction of the scattered light during the light propagation, and the scattering intensity is proportional to the incident intensity. The returned signal suffers a sudden change



when large loss is encountered from external analytes or other imperfections of the fibre; otherwise, the back-scattered signal decreases exponentially with an increasing propagation distance [128].

### **Raman scattering**

Raman scattering is an inelastic scattering, involving energy exchanging between the incident light and the propagating medium, leading to a frequency shift [129]. If the frequency of the emitted photons is lower than that of the incident photons, then this phenomenon is named as Stokes, while the frequency of emitted photons higher than that of incident photons is named as anti-Stokes. Raman scattering responds actively to the temperature of the optical fibre, and the temperature can be determined by measuring the ratio of the two shifted frequencies [128]. Many distributed temperature fibre sensors based on Raman scattering have been reported [130, 131].

### **Brillouin scattering**

Brillouin scattering is caused by acoustic oscillations of the material at the intermolecular level. Acoustic phonons experience a frequency-shift that is affected by the surrounding strain and temperature [132]. Although the Brillouin signal is weaker compared with the Rayleigh scattering signal, much focus have been placed to amplify the signals in recent years based on this type of distributed sensors due to their advantages of being able to measure both temperature and strain [5].

### **Detection methods**

There are two common types of distributed detection approaches, which are optical time domain reflectometry (OTDR) and optical frequency domain reflectometry (OFDR). OTDR achieves longitudinal resolution by resolving the time delay of pulsed light launched into the fibre, which is detected by a photo-diode with a temporal resolution as shown in Fig. 2.11.

OFDR is based on optical interference, where a swept/tunable laser source with a scanning bandwidth of tens of nanometres is implemented [133]. A reference fibre is used to act as a reference arm, and optical interference is then generated with light scattered from the measurement fibre. This signal is then demultiplexed via Fourier

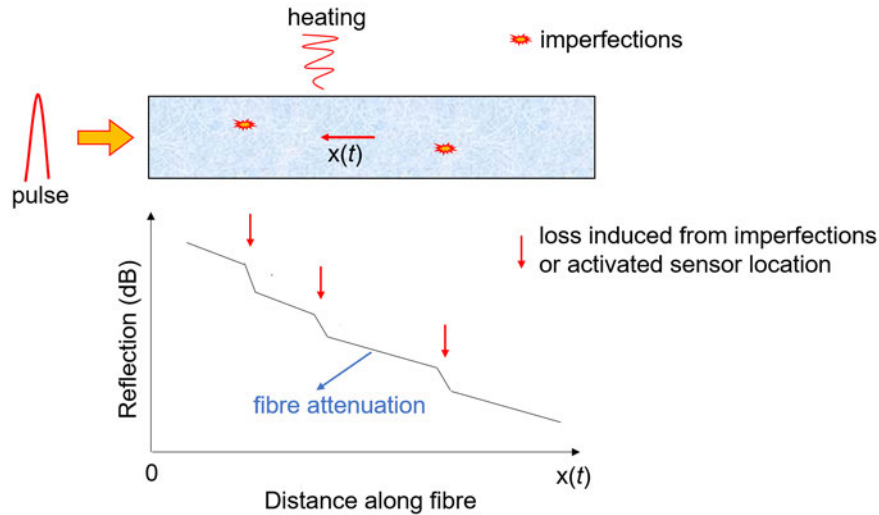


**Fig. 2.11** Schematic diagram based on OTDR detection.

transform, as shown in Fig. 2.12. The detection distance is determined by the coherence length of the laser source, while the coherence length depends upon the linewidth of the swept frequency spacing/resolution. OTDR based distributed sensors are deployed for long distance detection with spatial resolution in the order of one metre, while OFDR based distributed sensors have spatial resolutions of microns to millimetres for localised detailed information.

The traditional distributed fibre sensor was based on OTDR where the arrived scattered signal excited by pulsed light returns back to the detection system through reflection as a function of time ( $x = ct/2n$ ,  $c$  is the speed of light,  $n$  is the effective index of the waveguide and  $t$  is the traveling time). Changes in the local environment ( $x$ ) can be traced due to the distinct difference compared with the remaining part of the fibre. The spatial resolution  $\Delta z$  is calculated by [127]:

$$\Delta z = \frac{c\tau}{2n} \quad (2.9)$$

which is proportional to pulse width ( $\tau$ ). However, it is not easy to achieve high spatial resolution based on OTDR, as a millimetre resolution would require a bandwidth of 10 GHz detection system and a very high sampling rate, leading to large costs [127, 134, 135]. Many distributed Brillouin fibre sensors are reported based on OTDR with spatial resolution around 1 m for temperature or strain measurements in civil infrastructure,

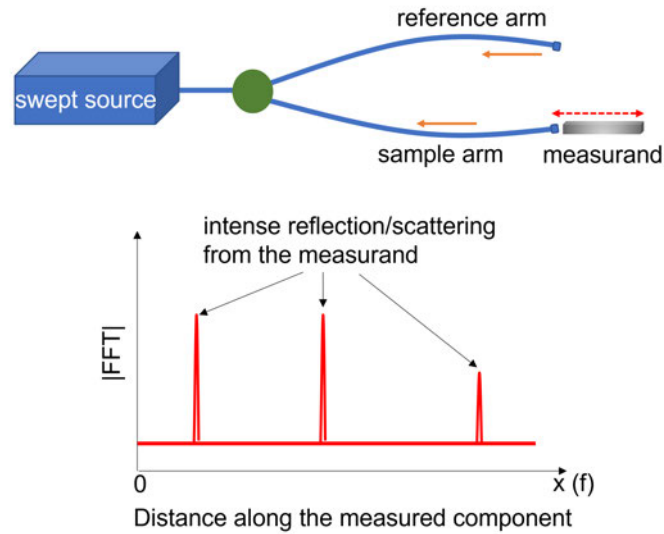


**Fig. 2.12** Schematic diagram based on OFDR detection for monitoring fine details with high spatial resolution (micrometre to millimetre scale) after fast Fourier transform (FFT).

such as pipelines and bridges [5, 136].

The OFDR detection offers opportunity to realise high spatial resolution. The resolution has an inverse relationship with the scanning frequency range ( $\Delta f$ ) of the swept laser, according to [133]:

$$\Delta z = \frac{c}{2n \times \Delta f} \quad (2.10)$$

The swept frequency ( $f$ ) has a linear function with time and the backscattered signal has a group velocity ( $v_g$ ):

$$v_g = \frac{c}{n_g} \quad (2.11)$$

where  $n_g$  is the group index of the propagating medium. Thus, during a transit time ( $2x/v_g$ ), there is a frequency change of:

$$\Delta f = \frac{2x}{v_g} \cdot \frac{df}{dt} \quad (2.12)$$

so the changed frequency is associated with the local position ( $x$ ). This is how the local longitudinal position could be simultaneously mapped out based on this interferometric technique by converting the frequency information into the

length-related signal based on Fourier transform [137]. While many OFDR-based distributed sensors are reported having several millimetre resolution [138], Luna OFDR instruments offer spatial resolution with  $10\ \mu\text{m}$  for optical component testing. Nonetheless, the trade-off between long distance detection and high spatial resolution is a common issue in distributed fibre sensing. Similarly, optical coherence tomography (OCT) is also developed based on optical interference to show the depth/layer information for mapping tissues/organs in biomedical field. Frequency domain OCT (introduced in Sec. 2.5.2) is quite similar to the OFDR mechanism described here.

### 2.4.2 Evanescent field sensing

An evanescent field exists at the boundary between two different dielectric materials when light propagates based on total internal reflection. The evanescent field decays exponentially in the normal direction towards the lower index material. This is one of the commonly used mechanisms for fibre-based biosensing [139], where surface bound biology or chemistry can interact with the evanescent field.

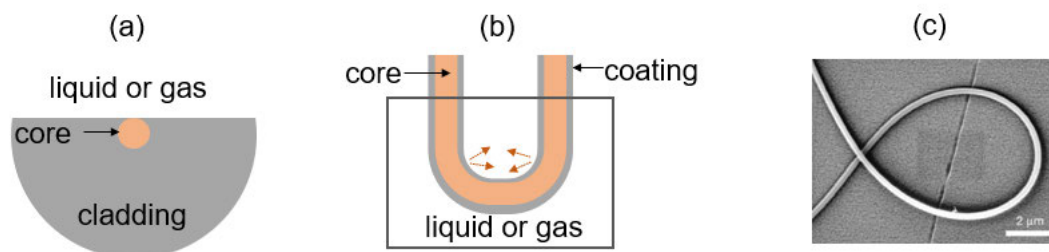


**Fig. 2.13** (a) D-shaped optical fibre evanescent field sensor. (b) U-shaped fibre sensor. (c) A silica nanowire is shown with 280 nm diameter from Ref. [140].

Here, several conventional approaches for making evanescent field fibre sensors are briefly reviewed, where the overarching approach is to expose the fibre core for creating access to the surrounding environment. Tapering, etching or polishing (e.g., the D-shape fibre in Fig. 2.13(a)) are general approaches to achieve such a purpose in the past [141, 142]. For example, a tapered fibre sensor was reported to detect bacteria with a detection limit of  $25\ \mu\text{g/L}$  by coating a polymer layer encapsulated with a luminescent material in 2001 [143]. U-shaped fibres have been proposed for measurements such as

humidity and pH, by coating measurand-sensitive materials onto a piece of bare MMF [4, 144]. An enhanced evanescent field results from a large bending angle to allow the signals (e.g., fluorescence and output intensity) to be easily observable [145, 146]. The sensing length is made at least several millimetres long to enhance the light-matter interaction, as shown in Fig. 2.13(b). However, these mechanical procedures such as tapering/etching/bending produce fragile structures that are time-consuming and lack high repeatability.

Nanowires made by crystal, polymer or glass are optically ideal for evanescent field sensing [140, 147]. These nanowires have significant evanescent fields due to the ultra-small core as shown in Fig. 2.13(c). This was well explained in earlier work calculated based on the silica-air step index model [148], where the power inside the silica region of a fundamental mode as a function of the diameter of the silica nanowire is shown in Fig. 2.14. An evanescent field of 90% is achieved in a 513 nm silica wire at a wavelength of 1500 nm.

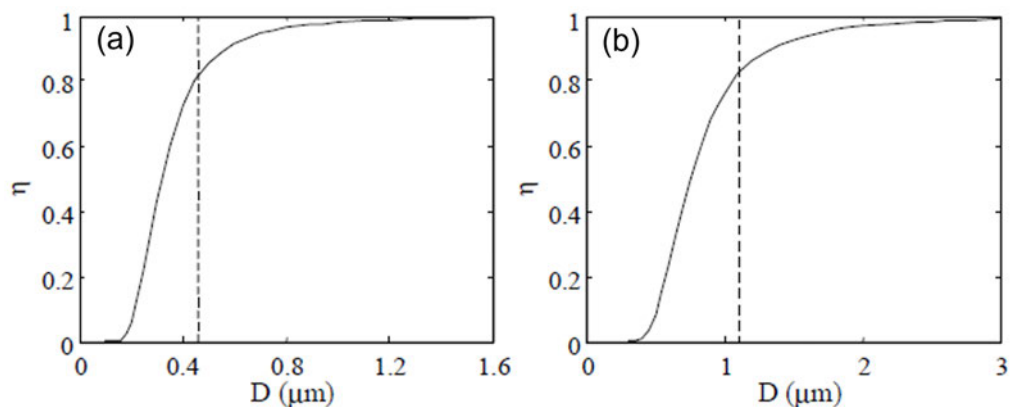


**Fig. 2.14** Calculations of fractional power ( $\eta$ ) inside the silica region of the fundamental mode as a function of the diameter ( $D$ ) of the silica (cladding is composed by air) fibres at an operating wavelength of 633 nm in (a) and 1500 nm in (b) from Ref. [148]. The dashed lines are indicative of 80% power inside the silica region of a fundamental mode under different wavelengths.

However, the handling of nanowires is quite challenging, preventing practical use for sensing. With the increasing maturity of fibre fabrication techniques, the desire for robust fibre handling and high repeatability have motivated the designs of novel fibres.

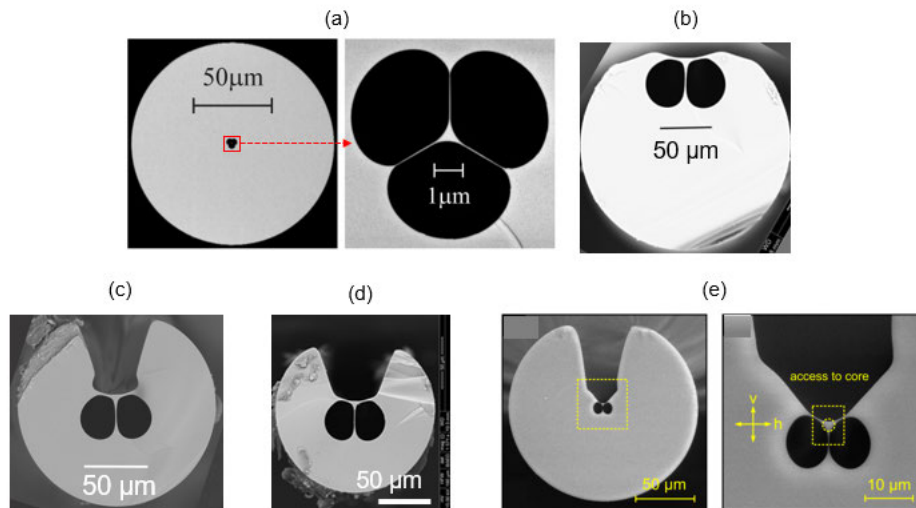


**Fig. 2.15** Different types of optical fibres fabricated in-house (The University of Adelaide) for evanescent field sensing. (a) Silica-based SCF with a core diameter of  $1 \mu\text{m}$ , supporting single mode operation in the telecommunications window from Ref. [12]. (b) Silica-based offset ECF with a core diameter of  $9.3 \mu\text{m}$  from Ref. [61]. (c) Silica-based ECF with a core diameter of  $7.5 \mu\text{m}$ . (d) Silica-based ECF with a core diameter of  $5.4 \mu\text{m}$ . (e) Silica-based ECF with a small core diameter of  $2.5 \mu\text{m}$  from Ref. [149].

To this end, suspended core microstructured optical fibres (SCFs, as shown in Fig. 2.15(a)) have been proposed for sensing due to the large evanescent field while being able to be filled with liquid along the entire fibre length [11, 12, 54, 95]. A silica ECF made in-house at the University of Adelaide has an outer-jacket as shown in Fig. 2.15(b-e), and they were particularly fabricated with a standard fibre dimension (outer diameter:  $150 - 200 \mu\text{m}$ ) to allow for splicing with commercial optical fibres. Meanwhile, the ECF exposed channel provides direct contact with the ambient environment. The evanescent field along the whole fibre length of the ECF allows for distributed sensing, and the highlight of work demonstrated in this thesis is to apply this property to detect small particles including sizes and spatial distributions. Different core sizes are illustrated in Fig. 2.15(c-e), allowing for tuning of the evanescent field.

## 2.5 Imaging with optical fibres

Microscope techniques for *in vitro* biomedical research have developed over the centuries, but optical diffraction is the principle limitation where the imaging resolution is limited to half of the optical wavelength [19]. Recent breakthrough in super-resolution microscopy has brought a revolution in visualising the microscopic world. Many of these techniques have been reported such as metallic based sub-microscopy probes [150, 151], confocal fluorescence microscopy and stimulated emission depletion super resolution microscopy, while the last two methods primarily rely on luminescent nanoparticles to target desired biomarkers after selective functionalisation. Significant complementary efforts have been spent in synthesising luminescent particles including quantum dots and up-conversion nanoparticles, due to their intense luminescence and high stability for applications in super-resolution microscopy [152, 153]. While microscope-based techniques are mainly used for *in vitro* study, the following will introduce optical imaging techniques for *in vivo* applications based on fibre optics.

### 2.5.1 Fibre endoscopes

Fibre bundles normally consisting of hundreds of optical fibres were the first generation of endoscopic imaging tool for clinic usage. The first glass fibre for medical usage was produced in the middle of the last century [154]. An illustration of a fibre bundle is shown in Fig. 2.16, where the illumination and imaging part are separate in this case. The spatial resolution is dependent upon the diameter of each fibre, and they have been widely used in the clinic such as imaging the stomach and lungs. However, as an endoscopic tool, their millimetre outer diameter usually brings uncomfortable experience to patients.

While a fibre bundle consists of multiple single fibres, a coherent fibre bundle (also called imaging fibres) has been proposed with a resolution of several microns three decades ago [155]. By stacking thousands of individual fibres in the preform, they are drawn together to fuse as a single imaging fibre. That is, multiple guided cores are built in a single fibre (outer diameter less than 1 mm), and the cross-coupling between the cores is the main limitation for achieving higher resolution [156]. Each intrinsic fibre

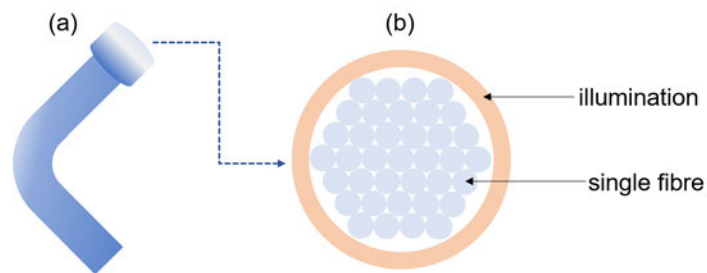


**Fig. 2.16** Illustration of a fibre bundle consisting of multiple single fibres.

in the imaging fibre acts as a pixel, and the object could be imaged and carried from one end to another, with commercially available products for decades. Some specialty fibres were reported for imaging purposes in the last decade based on a stack-and-draw approach [157–159]. The imaging resolution is determined by both the quantity of cores and the refractive index contrast, while more cores and higher index contrast would contribute to a higher resolution in a same fibre dimension. For example, an air-cladding fibre (diameter of  $600\ \mu\text{m}$ ) with 1,000 doped silica cores and a pixel size of only  $2.19\ \mu\text{m}$  was achieved in 2018 [158].

## 2.5.2 Optical coherence tomography

Optical coherence tomography (OCT) was first reported in the 1990s [160, 161] inspired by the ultrasound imaging technique. While ultrasound examination is based on acoustic waves reflected by internal structures of the human body, OCT is based on the optical scattering signal from tissue layers. OCT is one of the most successful clinical techniques for achieving real-time and high resolution imaging in human retinas and other near-surface tissues/organs [162–166].

The core principle of OCT is based on Michelson interference, where a reference beam interferes with a sample beam to form interference fringes [110]. The amplitude of the interference represents sample information due to different scattering properties from different layers/depth. The OCT detection technique can be classified into two categories: time-domain OCT and frequency-domain OCT, as illustrated in Fig. 2.17, while the frequency-domain OCT could be further classed as spectral-domain OCT and swept-source OCT.



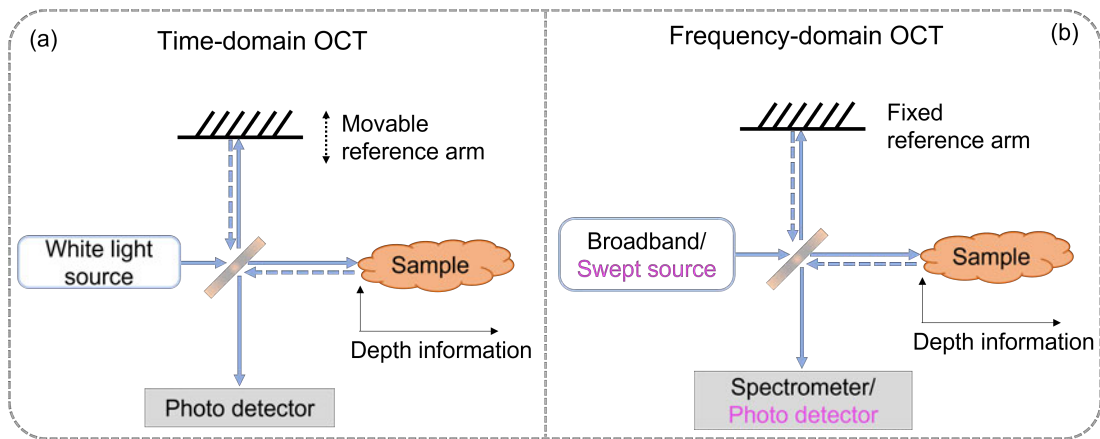


**Fig. 2.17** (a) An illustration of time-domain OCT, where the light source is a low coherence lamp. (b) An illustration of frequency-domain OCT, where the purple colour is to match the light source with the detector based on swept-source OCT, compared with the spectral-domain OCT in black colour.

The time-domain OCT requires a movable reference arm that is scanned to match with the depth from different tissue layers to generate optical interference, and the layer information is then resolved by recording the movement of the reference arm. The main limitation of time-domain OCT is the image acquisition speed, as the scanning vibrational mirror can only reach 1 kHz [167]. Frequency-domain OCT uses either a broadband source or swept source, and the layer information could be resolved after Fourier transform to a series of frequencies without moving the reference arm, with tens to hundreds of times improvement of the imaging acquisition speed compared with time-domain OCT. While the speed of spectral-domain OCT is still limited by the imaging components (i.e., COMS/CCD array), swept-source OCT has the potential to be widely used due to the simplified detection (photo-diode).

Fibre-based OCT has gained increasing interest due to the demand in miniaturised and less-invasive devices to reach into the internal lumen of organs. Many efforts have been reported in the last decade, such as to solve astigmatism/nonchromatic aberration while retaining a reasonable focus depth and cellular resolution in an integrated fibre probe [168, 169].

Different kinds of imaging techniques based on optical fibres are introduced above. Although they have developed for years, they are still limited by some issues such as flexibility, spatial resolution, and depth of focus. There is a desire to discover some interesting and potential possibilities for imaging field with greater feasibility and

performance.

### 2.5.3 Multimode fibres for endoscopy

MMFs are widely deployed in telecommunication and biomedical research for fluorescence collection. Despite their seemingly chaotic and random propagation characteristics, MMFs are gaining attention as an alternative platform for imaging. The interest in using MMFs for fibre endoscopy rises from the hundreds of propagating modes, which can act as multiple pixels for capturing and delivering images [170–172]. However, the fundamental challenge is the complex multimoded interference along the propagation, leading to a speckle pattern at the fibre output. Some wavefront shaping approaches have been attempted to solve this issue, such as digital phase conjugation [173, 174] and transmission matrix [175–178]. In addition to the multimode interference along the fibre length, any noise from the outside environment would also lead to variations at the output interferometric pattern, such as vibration and temperature. One approach is to optimise the transmission matrix to account for perturbations [179], while recent efforts include the use of artificial neural networks (ANNs) to learn speckle patterns for MMF imaging [180–182].

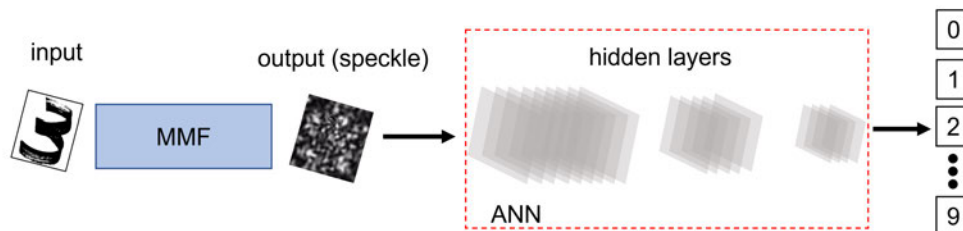


**Fig. 2.18** A schematic diagram of using an ANN model to learn image propagation in an MMF.

An ANN model can be trained with thousands of labelled input images. As shown in Fig. 2.18, an ANN consists of many hidden layers that allow a concept model to be trained, which would not be possible by conventional mathematical or physical analysis. An unseen image could be well recognised by using this trained ANN model. However, the prediction accuracy depends upon the complexity of both the training database and the targets. So far, the recent development of using MMFs for the

purpose of image delivery is still limited to the transport of simple images (e.g., handwritten digits). In 2018, N. Borhani *et al.* proposed a deep learning assisted method to reconstruct input images through an MMF after training a database of 16,000 handwritten digits by recording the intensity of each speckle output [181].

### **Other applications using MMFs**

In 2020, W. Xiong *et al.* reported ultra-fast pulse characterisation using an MMF, where deep learning was used for phase recovery [183]. The above mentioned literature focus on the transportation of light from the input end to the output end, while what happens during the propagation is less investigated. Recently, sensing applications using MMFs based on machine learning have been proposed for detecting physical parameters such as bending and temperature [184–186]. The machine learning algorithm enables fibre sensors with the capability to demultiplex complex perturbations such as temperature, pressure and vibration, simultaneously.

Taking the advantage of machine learning for solving complex problems, the work introduced in Chapter 5.1 uses the multimode property of the ECFs to correlate scattering (under evanescent field excitation) with particle size with a combination of machine learning algorithms. The idea to acquire particle information in multiple dimensions including size characteristics and spatial distributions using a fibre technique would bring new insights to sensing and imaging communities towards *in vivo* applications with greater flexibility.

## **2.6 Small particle detection**

The detection of individual small particles (e.g., biological cells) is critical for biomedical research applications such as disease diagnostics or drug research [187–191]. Cellular size quantisation would help to recognise cell types for some disease diagnoses (e.g., breast cancer, prenatal screening and epithelial cancer [192, 193]); cell population analysis would help to diagnoses such as anemia and blood cancer [194, 195]; and cell's abnormal shape is also a sign of other disordered disease [196].

### 2.6.1 Flow cytometry

Flow cytometry is a well-established commercially available technique for cell measurements (physical and chemical characteristics) [192, 197–199]. Flow cytometers can integrate both cell counting and sorting techniques to analyse cells according to their optical properties by incorporating fluorescence-based detection, and hydrodynamic focusing is a widely used approach to align cells in single file as illustrated in Fig. 2.19.

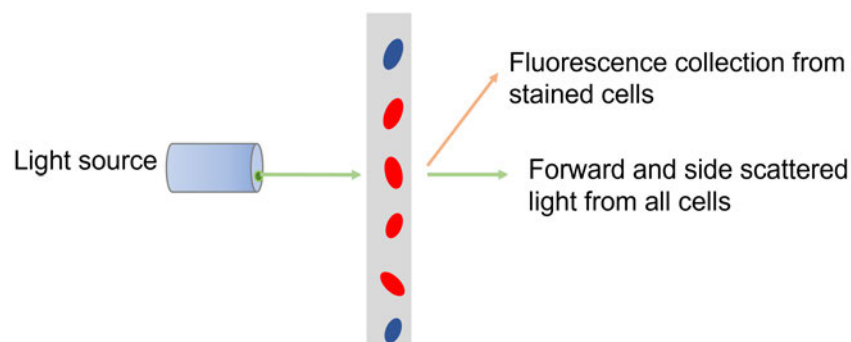


**Fig. 2.19** An illustration of flow cytometry for individual cell detection including both stained and unstained cells.

This type of equipment greatly contributes to clinical diagnostics, and they have the ability to test thousands of cells in a second [200]. However, such an equipment is bulky and requires sample staining for precise characterisation of different phenotype, making it suitable for laboratory use only [201]. Therefore, many portable devices with real-time measurements such as chip-based and fibre-based optical devices are reported, as introduced below. Microfluidic chips integrated with optics as simplified single-cell platforms have been demonstrated in the last decade including cell manipulation, detection, and treatment [196, 201]. Passive and active techniques are used to do particle separation and sorting. While passive techniques utilise the physical properties of the microfluidic structure and the flow field, the active approach requires external fields (e.g., optical, magnetic, and acoustic) to interact with the particles. Among them, optical fibres are often used to probe and collect the signals to

make integrated devices [200, 202, 203].

### 2.6.2 Fibre-based particle sensing

Fibre-based techniques have shown the possibility towards *in vivo*, minimally invasive and label-free measurements by detecting the light scattered from particles (e.g., cells) [197]. Fibre-tip probes used for sensing particles have been proposed. For example, a scheme for particle size detection was proposed by monitoring the phase shift induced by optical scattering when a particle passed through a fibre tip based on the mechanism of optical interference [192]. A fibre probe with integrated multiple micro-lenses on the fibre end-face to trap and kill targeted cells was reported in 2016 [204].

The following examples are highlighted to demonstrate how optical fibre-based devices can be used for tracking particles while showing spatial information. In 2015, a nanoscale individual particle detection scheme was proposed using a built-in nano capillary (250 nm) inside the core centre, which acted as a fluidic channel for particles flowing through which simultaneously interacted with the guided light via the evanescent field [8]. Elastic scattering signals were collected by a microscope objective placed perpendicular to the fibre axis, which provided partial spatial information within the field of view, as shown in Fig. 2.20.

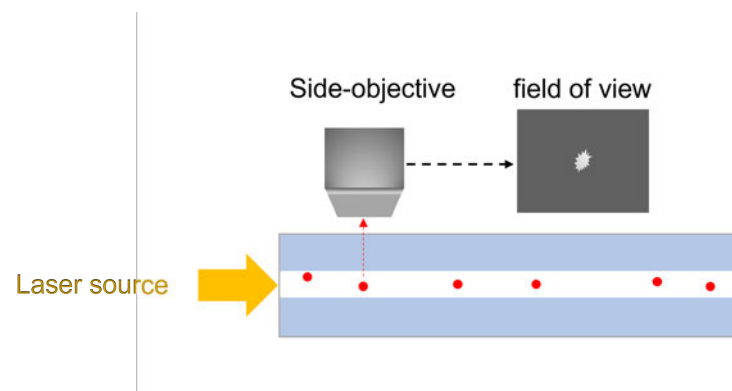


**Fig. 2.20** Particles inside of a nano channel are detected by a side-objective based on optical scattering.

In 2020, a similar dynamic tracking scenario showed the ability to retrieve three-dimensional information of nano-scaled particles diffused inside a channel (running parallel to the fibre core within the evanescent field) [9]. The same group proposed another scheme for Brownian motion detection using an HCF, where the hollow core

directly acted as the fluidic channel for a strong light-matter interaction [10]. A large diffusion space was realised by using such an HCF in contrast to the previous nanoscale channel. The natural weak optical scattering signal due to the lower index contrast between biological cells/objects and the surrounding fluid (water) remains challenging, so it still requires numerous efforts to make these sensor devices towards out-of-lab usage.

In parallel, some interesting discoveries have been undertaken by manipulating small particles based on optical trapping technology [205], including recent developments for holographically manipulating small particles in three dimensions using an MMF [206]. The related terminology is named as opto-mechanics, which focuses on small forces (e.g., scattering and mechanic force) from particles induced by light and their mutual interactions to reveal their optomechanical dynamics. In 2015, a physical sensing scheme was proposed using flying particles inside an HCF for precise distributed measurements of temperature and electric field [207]. In 2018, a scheme was proposed using optical scattering and trapping techniques to manipulate a particle-array inside an HCF, for studying fundamental forces in the microscale world [208].

Therefore, the detection of small particles including biological particles, synthesised particles or atoms is indeed an active field, which would bring value to multiple disciplines. Fibre-based sensing and imaging applications are introduced in previous sections. In fibre sensing, distributed sensing has shown one dimensional mapping of spatial information. In fibre imaging, two-dimensional spatial information is directly depicted. This Sec. 2.6.2 is to highlight the individual particle detection based on fibre-based configurations, while the detection includes the particles' characterisation (size, shape and population) and their spatial information. A fibre-based technique to show particle information (e.g., size and/or shape) with spatial information included, would bridge the gap between fibre sensing and imaging.

## **2.7 Discussion and relevance to this thesis**

Many optical fibre sensors are covered in this chapter from non-distributed fibre sensors to distributed fibre sensors. In parallel, imaging techniques are introduced including a brief introduction to microscopy techniques and OCT. While the

microscopy-based approach is too bulky to support flexible *in vivo* imaging, OCT is limited by the penetration depth to a few millimetres. Other fibre endoscopic techniques are introduced to emphasise the recent interest in using MMFs, and the incorporation of machine-learning algorithms to take advantage of the inherent complexity of such fibres.

Fibre-based particle sensing configurations have been reported by multiple groups, but an external objective is always required for the collection of light scattered from the particles. They are thus limited to showing the particles' movements within the field-of-view of the microscope objective. There is a curiosity-driven research for label-free and portable detection of micro-scaled objects, but this is the bottleneck of both current fibre endoscopic techniques and small particle tracking scenarios. Although the difference between the sensing and imaging techniques exists, there are possibilities to bridge the gap as shown by the main work in this thesis.

Traditional distributed fibre sensors are used for temperature, vibration and strain measurements along the entire fibre length with spatial resolution ranging from millimetres to metres. Their major applications, however, remain in physical sensing for structural health monitoring. The capability to show distributed detection is also attractive for biomedical applications, where individual particles could be detected with a high-resolution. An ECF-based distributed sensing scheme is proposed in this thesis based on the OFDR mechanism (Chapter 3), which offers high-resolution sensing of micro-scaled particles (Chapter 4.1). To further advance the detection capability, the few-mode property of the proposed ECF has extended the detection dimension in the transverse direction for two-dimensional mapping of microscale scatterers (Chapter 4.2). The platform capabilities are extended through the application of machine learning algorithms, which are used to determine the particles' size characterisation based on the same distributed sensing scenario (Chapter 5.1). Meanwhile, spherical particles themselves can act as sensing tools, and WGM resonance is observed when the light propagating in the ECF couples to microspheres (Chapter 5.2). To prove the feasibility of the proposed ECFs sensors towards real-world biological environments, two ECF-integrated fibre probes are used for sensing measurements based on the evanescent field interaction. A fibre pH sensor is demonstrated by monitoring the *in vivo* pH in a hypoxic mouse (Appendix A); the

---

detection of nanoscale particles using an ECF probe is presented (Appendix B).



## **CHAPTER 3**

### **Theory and experimental details**

### 3.1 Motivation and theory overview

This chapter will give an overview of the main work done in this thesis including all theories and experimental procedures. The link between this Chapter 3 with other Chapters (4, 5) in the thesis body is illustrated as a flow chart in Fig. 3.1.

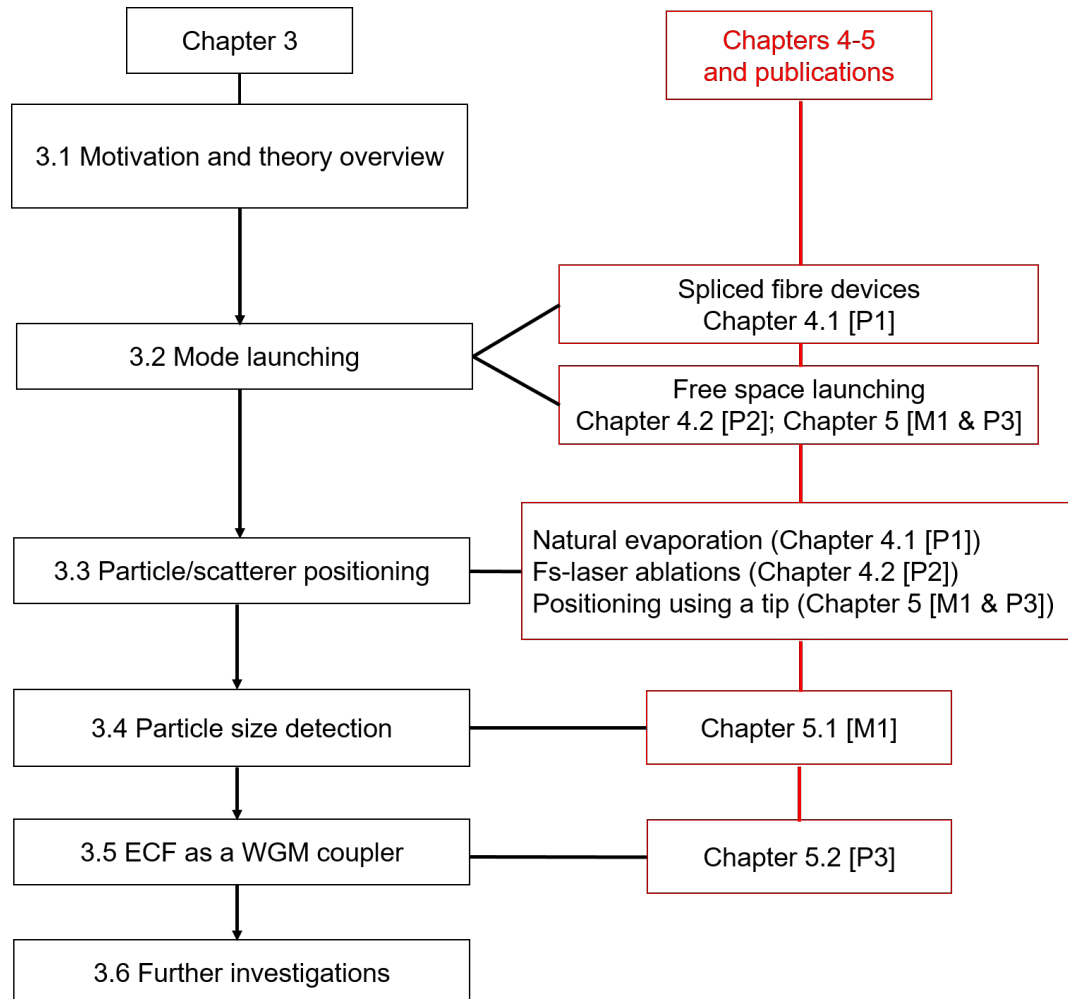


**Fig. 3.1** Flow chart of the main body of this thesis to show the link between Chapters 3-5.

The primary aim of this thesis is the detection of individual micro-scaled particles, which in future could be used for measuring small biological objects. Although many approaches have been reported in the past for such a purpose, such as using microscopy and flow cytometry, they have limited field of view, use bulky instruments, and are incompatible with *in vivo* applications.

### Concept

In this thesis, polystyrene spheres have been used as models to mimic biological cells due to their similar size, as shown in Fig. 3.2. Exposed-core fibres (ECFs) are useful due to its longitudinally exposed channel, which enables interactions between the optical field and the surrounding environment as shown in Fig. 3.2(c).

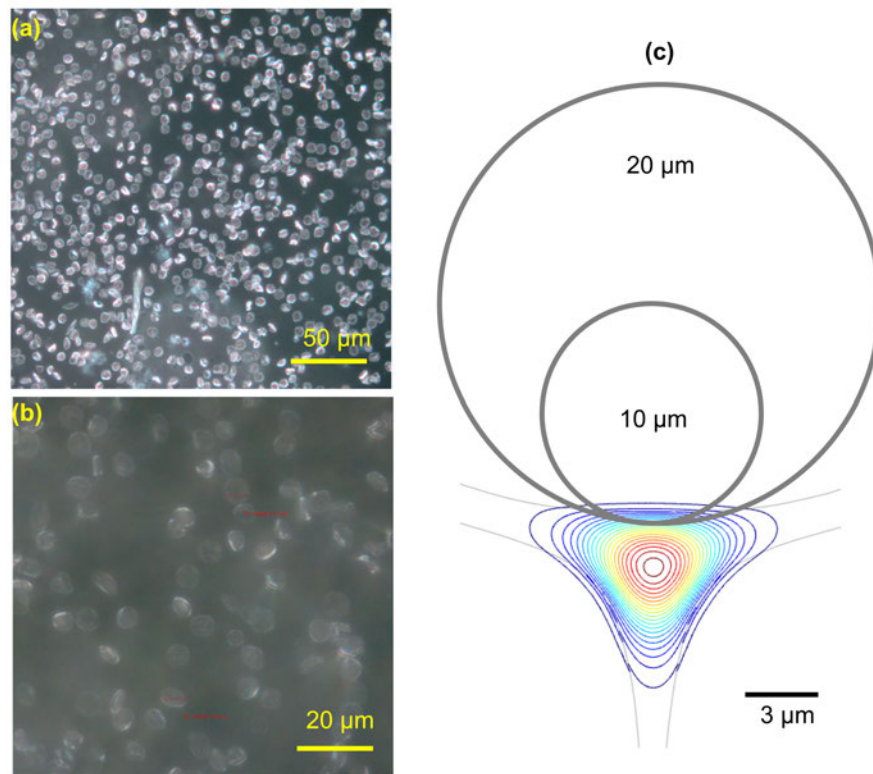


**Fig. 3.2** (a) Fresh red blood cells from a mouse with an average diameter of 6-8  $\mu\text{m}$  and a magnified figure is in (b). (c) An illustration of how different sized spheres would interact with the evanescent field of the ECF.

Optical frequency domain reflectometry (OFDR) is used as the main mechanism for micro-scaled particle detection. As illustrated by the following configuration in Fig. 3.3, reflection at the ECF splice due to silica-air interface (between the solid fibre and the ECF input) acts as a reference arm; the scattering from micro-scaled particles via evanescent field interaction is able to optically interfere with the reference light. Therefore, micro-scaled particles can be mapped longitudinally along the fibre based on the OFDR technique after a fast Fourier transform (FFT). Note that the splice is not a compulsory condition, the key is the silica-air interface to generate the Fresnel

reflection (e.g., free space launching).

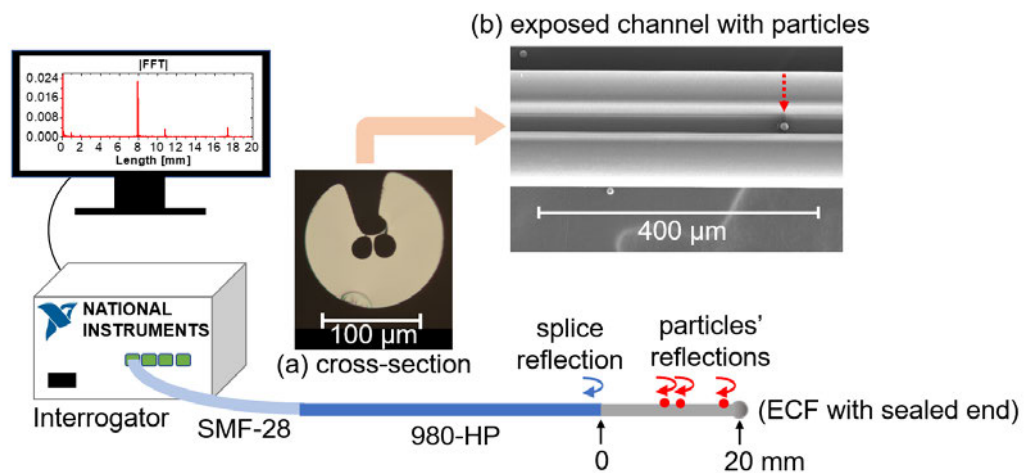


**Fig. 3.3** A schematic diagram of the experimental set-up used for micro-scaled particle sensing. Here particles are located on the exposed channel. Optical interference signals were real-time transformed to length-related information after FFT as displayed on the computer screen.

Polystyrene spheres (diameters: 5, 10, and 20 μm) suspended in ethanol or milli-Q water were used as sensing targets as shown in Fig. 3.4. The suspension could be dropped onto the ECF, leaving behind physically absorbed particles after solvent evaporation.

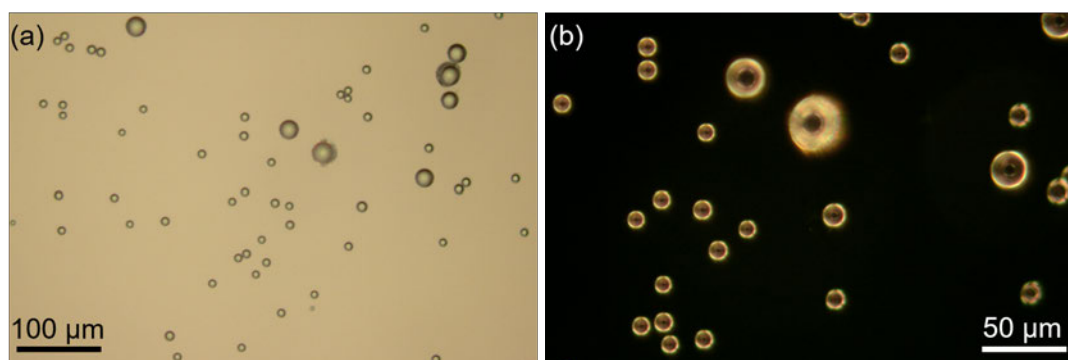


**Fig. 3.4** (a) Bright field image of three different sizes (with average 5, 10 and 20 μm) of polystyrene spheres distributed inside a water droplet on a glass slide. (b) Dark field image from the polystyrene spheres.

### ECF fabrication

Cross-sectional images of the silica ECFs used in this thesis are displayed in Fig. 3.5. Preforms used to draw the ECF were prepared by a drilling method. Firstly, three air holes (diameter: 2.8 mm) based on an equilateral triangle geometry (3.2 mm centre-to-centre between holes) were drilled along a silica rod (diameter: 12 mm) longitudinally and then a slot (from 2.0 to 2.8 mm) was made by opening one of the holes directly. The preform was then drawn to fibre with positive pressure used to slightly inflate the air holes, with the drawn fibres shown in Fig. 3.5(a, b, c). For the smaller core silica ECF displayed in Fig. 3.5(d), two drawing steps were required by stacking the first drawn cane into the preform to thus achieve a smaller core after the second draw [209].

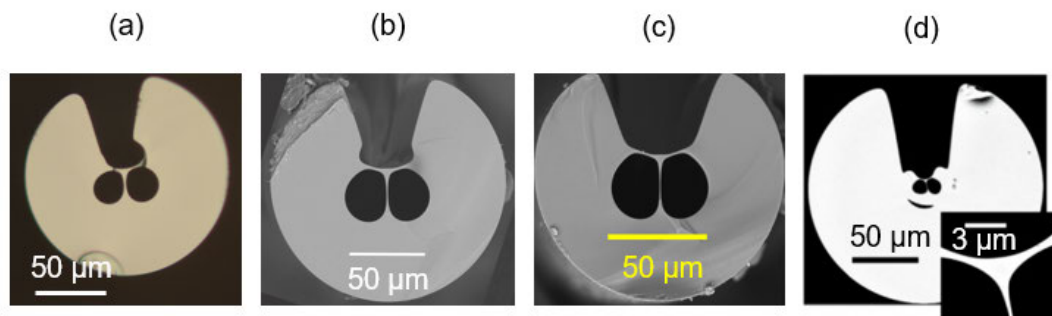


**Fig. 3.5** Cross-section images of different ECFs used in this thesis. (a) Optical microscopic image of an asymmetric ECF, which came from the artifacts during the preform drilling procedure, used in [P1]. Scanning electron microscopy (SEM) images in (b-d). (b) This fibre has a nearly perfect symmetry and was used in [P2] and [P4]. (c) The SEM of another ECF (used in [P3, M1]), and this was specifically drawn for this project to avoid the concave edges inside of the exposed channel shown in (b). (d) Small core ECF used in [P5].

Several types of ECFs were used in this project, and they are presented sequentially in Chapters 4-5. A slight deviation in the structure is shown in Fig. 3.5(a, b, c), but it does not affect the performance of distributed detection via the evanescent field, due to their similar core and struts sizes and the same base material: silica. The main reason for using several types of ECF was to optimise the particle positioning process. The ECF shown in Fig. 3.5(c) was particularly fabricated for this project to avoid the concave edges for better particle positioning during the natural liquid evaporation process. It is important to mention that a controllable approach of particle positioning was developed

afterwards, which is described in the Sec. 3.3. This allowed polystyrene spheres to be positioned manually. Experimental results are shown in Chapters 5.1 [M1] and 5.2 [P3]. The ECF in Fig. 3.5(d) was used in Appendix B [P5], due to the small core size around 1.8  $\mu\text{m}$  resulting in greater evanescent field for nanoscale particle detection.

### Simulation

Particles/dust located on the exposed channel can be detected by interacting with the evanescent field of the ECF's guided modes. The optical scattering from the particles can then be captured back into the fibre's guided modes, depending on its scattering properties such as material and geometrical shape. The captured scattering signal from particles  $I_p$  could be approximated by [25]:

$$I_p = a_s \iint_C \vec{P}(x, y) dx dy \quad (3.1)$$

where  $\vec{P}(x, y)$  is the Poynting vector, C is the integration region given by the particle's cross-section, and  $a_s$  is a coefficient of the scattering back into the fibre's guided modes. Given that the complexity of the evanescent field excitation of particles that are located at different transverse positions, a rigorous theoretical exploration of the particle's scattering captured back into fibre guided modes is not the focus in this thesis.

The Poynting vector distributions of the ECF's guided modes were simulated for the symmetric ECF shown in Fig. 3.5(b) based on the finite element method (FEM) (COMSOL 5.3) for a wavelength of 1550 nm. There is negligible difference in the evanescent field compared to the asymmetric ECF due to their similar core diameters. The SEM image of the ECF's cross-section was imported into COMSOL to build a two dimensional model, where the mesh size is displayed in Fig. 3.6(a). The 'FM' represents the fundamental mode while other high-order modes are labelled as 'HOM' with sequential integers from '1-3'. Phase effective indices ( $n_p$ ) are calculated from the simulation as shown in Fig. 3.6(b). This is different from a group index ( $n_g$ ) which can be expressed by:

$$n_g = n_p - \lambda \frac{dn_p}{d\lambda} \quad (3.2)$$

where  $\lambda$  is the free space wavelength. The group index is used in the following calculations associated with optical path difference. Higher order modes extend the

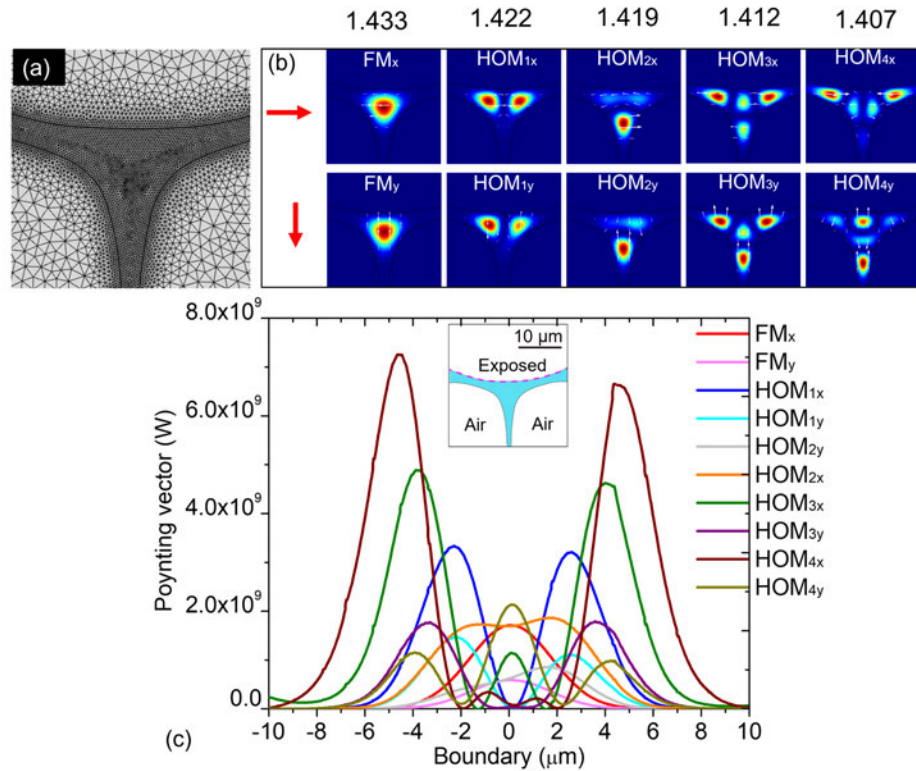


**Fig. 3.6** (a) Simulation model with mesh for FEM. (b) Several guided ECF modes with the corresponding phase index is displayed on the top for each pair of mode (ignoring the minor birefringence from two orthogonal polarised modes). The horizontal red arrow indicates the dominant electric field direction of modes on the top images, while the vertical red arrow is to indicate the dominant electric field direction of modes on the bottom images. (c) The evanescent field distribution of each mode along the dashed magenta curve of the inset.

energy distributions towards the boundaries (along the dashed magenta curve in the inset) as seen in Fig. 3.6(c). In Chapter 4.1 [P1] and Appendices [P4, P5], the FM is used as a primary mode in the integrated fibre devices, while the FM and the HOMs are all used via free space launching in Chapter 4.2 and Chapter 5 for expanding the transverse detection and gaining transverse information such as particle size.

### Experimental set-up and principles

Two experimental schemes have been used in this thesis for the demonstration of distributed sensing of small particles and feasibility towards practical biological applications. An integrated fibre sensor was initially made for a first demonstration of one-dimensional mapping of microscale particles based on OFDR as shown in Fig. 3.7(a), which is described in Chapter 4.1 [P1]. An *in vivo* pH sensing probe is

presented in Appendix A [P4] and a nanoscale particle detection based on a heterodyne approach is demonstrated in Appendix B [P5]. A free space scheme as shown in Fig. 3.7(b) was then allowed for two-dimensional mapping of microscale surface ablations (written by femto-second ablations), which is demonstrated in Chapter 4.2 [P2] based on both OFDR and the few-mode property of the ECF. Particle size characterisation via free space launching based on the multimode property of ECFs is investigated in Chapter 5.1 [M1]. The microspheres positioned on the ECF show whispering gallery mode excitation, which is reported in Chapter 5.2 [P3].

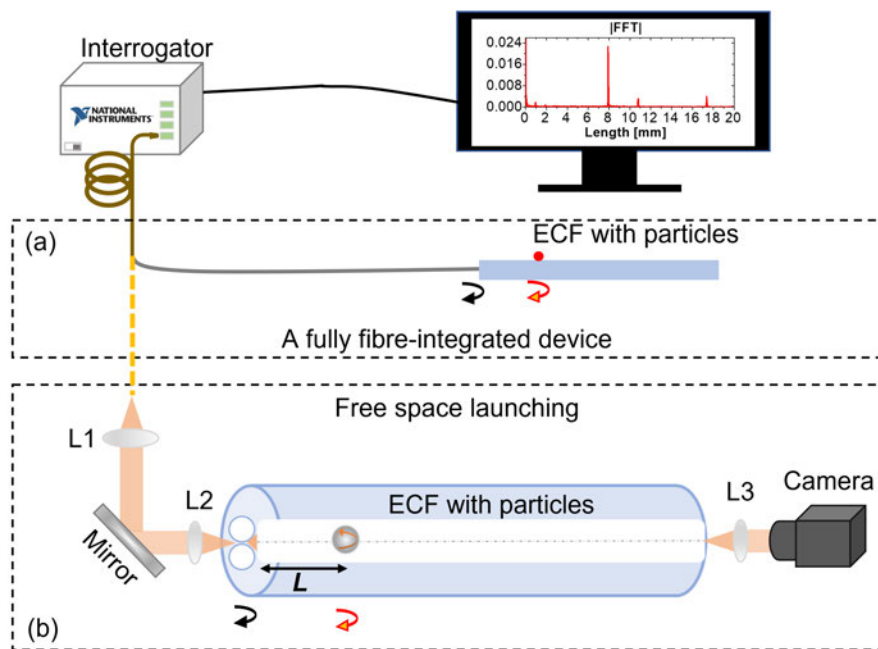


**Fig. 3.7** Two different schemes used for distributed sensing of microscale particles. (a) The experimental set-up used for an integrated fibre device. (b) The set-up based on free space launching.

An interrogator (National Instruments, PXIe-4844, 1510-1590 nm, sampling rate 10 Hz, scanning wavelength spacing of 4 pm) integrated with both swept source and photodetector was used for optical measurements in a reflection mode as shown in Fig. 3.7. OFDR was utilised in this thesis as the main mechanism for high resolution detection of micro-scaled particles. Specifically, the reflection light formed from the ECF input due to silica-air interface was used as the reference light (black arrow), and micro-scaled particles located on the ECF are point scatterers (red arrow) to interfere with the reference light as shown in Fig. 3.7. The particles' longitudinal positions



were mapped out using FFT to resolve the optical interferences.

The mathematical relationship between the frequency domain and time domain in a swept source system is described below [133]. The swept frequency ( $f$ ) is a linear function of time, and the backscattered signal with a group velocity ( $v_g$ ):

$$v_g = c/n_g \quad (3.3)$$

where  $n_g$  is the group index of the propagating medium,  $c$  is the speed of the light in vacuum, during a transit time ( $2L/v_g$ ) experiences a frequency change:

$$\Delta f = (2L/v_g) \cdot df/dt \quad (3.4)$$

The distance traveled in a single path ( $L$ ) could be solved after an inverse FFT as follows:

$$L = c/(2n_g \times \Delta f) \quad (3.5)$$

In general, the interference between an ECF input-end and a single particle could be considered as a Fabry-Perot interference in this configuration (illustrated by two coloured arrows in Fig. 3.7), so the optical interference could be expressed by a two-beam interferometer:

$$I = I_r + I_p + 2\sqrt{I_r I_p} \cos(k \cdot OPD) \quad (3.6)$$

where  $I_r$  is the intensity of the reference light (ECF input),  $k$  is the wave number and  $I_p$  is the intensity of the sample light from the particle (associated with Eq. 3.1). Their optical path difference (OPD) is  $2n_g L$ , so the total phase term is expressed by:

$$k \cdot OPD = \frac{4\pi n_g L}{\lambda} \quad (3.7)$$

An arbitrary period of an interference fringe satisfies:

$$\frac{4\pi n_g L}{\lambda_1} - \frac{4\pi n_g L}{\lambda_2} = 2\pi \quad (3.8)$$

where  $\lambda_1$  and  $\lambda_2$  are adjacent wavelengths such as adjacent crests or troughs, and a

single path  $L$  (cavity length: ECF input-particle) could be solved:

$$L = \frac{\lambda_1 \lambda_2}{2n_g(\lambda_1 - \lambda_2)} \quad (3.9)$$

Multiple interferences are generated due to multiple particles involved, which can then be differentiated in the frequency domain. Each interference would be resolved as an individual frequency associated with each cavity length (ECF input–individual particle) after an FFT shown by the peaks (red curves) in the screen of Fig. 3.7. The FFT peak height is determined by both the particle size and transverse locations, ignoring the coherence length of the light source (discussed in Chapter 4.1 [P1]). The theoretical spatial resolution of the interrogator (in a single path) is calculated by [127]:

$$L_{re} = \frac{c}{n_g \times \Delta f} = \frac{\lambda^2}{n_g \times \Delta \lambda} \approx 10 \mu m \quad (3.10)$$

where  $\Delta \lambda$  is the scanning wavelength range of the swept source (80 nm, as the interrogator scans from 1510 to 1590 nm),  $f$  is the frequency, and  $n_g$  is the group index of the propagating mode within the fibre.

The number of interference fringes ( $N$ ) is known according to the interference spectrum, so a single path  $L_N$  from an interference cavity (between an ECF input and a particle) can be calculated according to Eq. 3.9:

$$L_N = N \times \frac{1510 \times 1590}{2n_g(1590 - 1510)} \quad (3.11)$$

## 3.2 Mode launching

The ECF is a few-moded fibre due to the large index contrast between the silica core and the air cladding. This section shows how different mode launching schemes were used in this thesis for different applications.

### An integrated fibre probe

A fully fibre-integrated scheme incorporating ECF spliced to SMF allows the fibre sensor to have deployment flexibility for out-of-lab usage. To maximise the coupling efficiency, several types of SMFs (Table 3.1) were considered here to splice with the



**Fig. 3.8** An illustration of a single mode fibre (SMF) spliced to an ECF, where a few modes from the ECF are excited and reflected back to interfere with the reference light reflected from the splice between the SMF and the ECF.

ECF. In this case, the aim was to suppress HOMs to allow strong FM excitation and a clean OFDR signal. This requires the effective mode area to be well matched between the two fibre types. The efficiency of FM versus HOM excitation was monitored during splicing by measuring the OFDR signal resulting from interference between the ECF far end and the reflection from the splice (silica-air interface due to large air holes and exposed channel) as illustrated in Fig. 3.8.

Fibre details			
Name	NA	Core diameter ( $\mu\text{m}$ )	Mode field diameter ( $\mu\text{m}$ )
ECF (Fig. 3.5(a))	1.02	6.8	7.5
SMF-28	0.14	8.2	10.4
980HP	0.20	3.6	6.8
UHNA1	0.28	2.5	4.8
UHNA4	0.35	2.2	4.0

**Table 3.1** Core diameter and mode field diameter comparison of several optical fibres, to maximise the coupling efficiency between ECF and SMFs. The spliced results was shown in Fig. 3.9.

The FM contributes to the first peak due to a smaller group index to form a shorter optical path length ( $n_g L$ ). Other HOMs follow sequentially depending on the group index. The angle inside of each plot in Fig. 3.9, is the cleaved angle of the ECF far-end displayed from the splicer (Fujikura: FSM-100P). As the standard SMF-28 has larger core compared with that of the ECF, as shown in the Table 3.1, only the results from other smaller core SMFs are shown. 980HP shows the clearest single-peak in Fig. 3.9 with HOMs suppressed. This means the primary mode excited in the ECF is the FM when spliced with 980HP. Therefore, 980HP was determined to be the ideal SMF for splicing to the ECF, which was applied in Chapter 4.1 [P1] for making an integrated

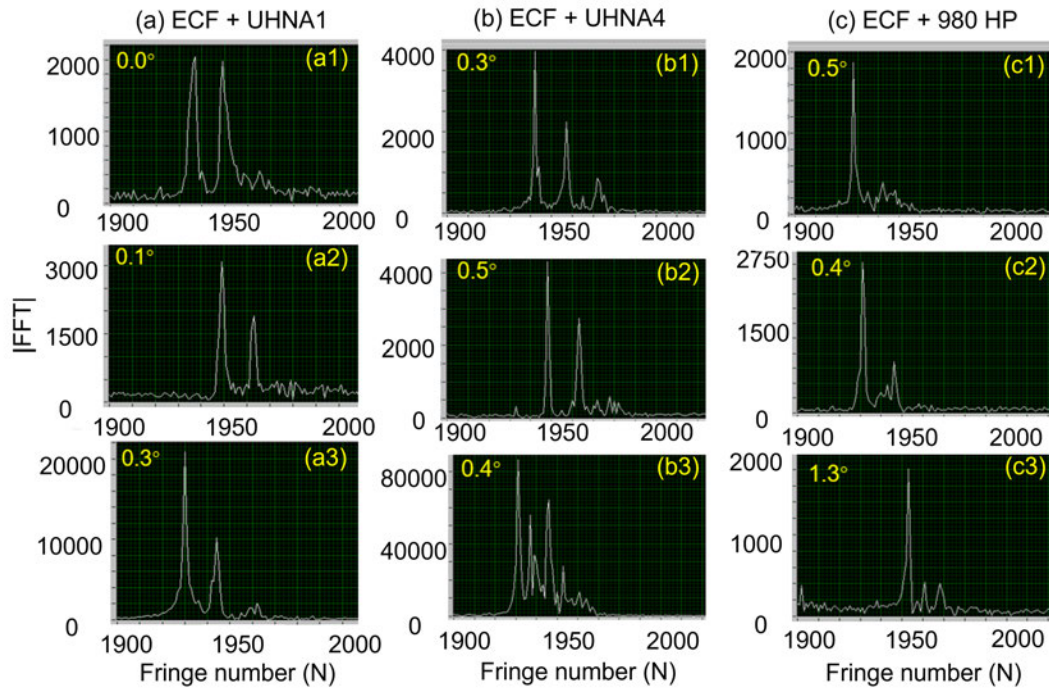


**Fig. 3.9** Results of mode excitation using different SMFs spliced to the ECF (Fig. 3.5(a)). (a) Three pieces of ECF spliced to a piece of UHNA1, with three different OFDR results in (a1, a2, a3). (b) Three pieces of ECF spliced to a piece of UHNA4, with three different OFDR results in (b1, b2, b3). (c) Three pieces of ECF spliced to a piece of 980HP, with three different OFDR results in (c1, c2, c3). The x-axis in these images represents the number of interfered fringes (N), e.g., number 2000 indicates a single path length of  $L_N \approx 20$  mm according to Eq. 3.11. The angle (yellow font) inside of each small figure represents the cleaved angle from the far-end of the ECF (measured fibre length approximately 20 mm).

fibre sensor for microscale particle detection. The UHNA4 was spliced with the small core ECF to make integrated fibre sensors for nanoscale particle detection in Appendix B [P5], with the splicing details in Appendix B.1.

### Particle sensing using an integrated fibre sensor

The detection of particles using an integrated ECF sensor based on the OFDR technique is shown in Fig. 3.10. A red light source (632 nm) was connected to the fibre input patch cable to indicate both the fibre splicing location and the particles/dust positions, imaged under an optical microscope. Red laser scattering from the splice, dust, polystyrene spheres and sealed far-end could be found. Dust and particles' positions away from the splice spot measured under the microscope match with the OFDR detection as shown by two major FFT peaks at 3.4 mm (dust) and 4.9 mm (polystyrene spheres). However, two

closely spaced  $10\ \mu\text{m}$  sized particles could not be distinguished due to a limited spatial resolution of used interrogator. The practical resolution is  $20\ \mu\text{m}$  after considering the full width at half maximum of a single FFT peak, and this is explained in Chapter 4.1 [P1].

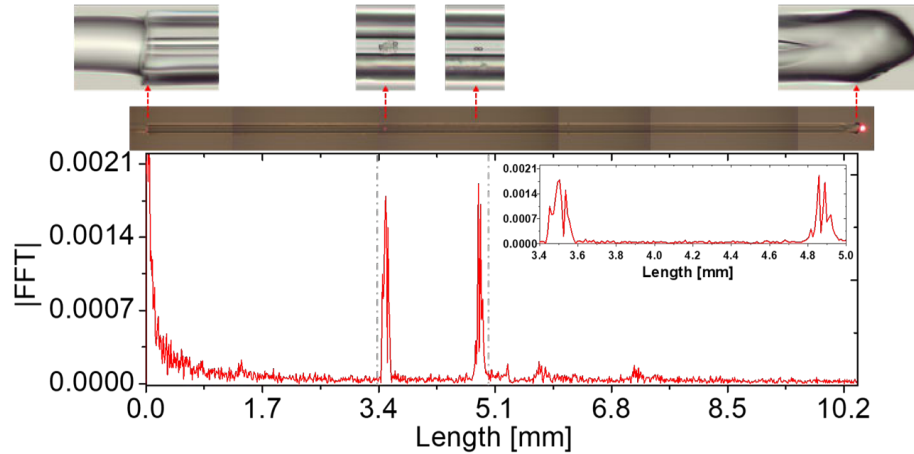


**Fig. 3.10** A fibre sample with both dust and polystyrene spheres was tested using the OFDR technique and the corresponding distributed measurement of these particles was shown in the red curve where the longitudinal positions shown in the x-axis are positions of these particles after FFT.

Nonetheless, this was a first demonstration of distributed sensing of micro-scaled particles/dust using an integrated fibre device. The signal drops off with increasing distance away from the splice due to the coherence length of the light source [133]. The input power ( $66\ \mu\text{W}$ ) and signal-to-noise ratio from the interrogator further limits the practical detectable length. The practical detection length was 20 mm during experimental trials, although the theoretical coherence length is up to 260 mm as expressed in the Eq. 3.10 (the  $\Delta\lambda$  is the scanning wavelength linewidth: 4 pm, in this case). In this integrated fibre sensing scheme, the fibre far-end was sealed as shown in the Fig. 3.10 by melting a ball shape using a splicer, to prevent liquid contamination into the ECFs internal holes and strong reflection from this end. A more detailed description about the integrated fibre device is in Chapter 4.1 [P1].

### Free space launching

Free space launching allows control of launched modes, which brings possibility to expand the transverse detection. Multimode interference (MMI) generated resulting from the free space launching is also considered here.

Due to the few-mode property of the ECF, the effective indices from different order modes are quite different especially in lower-order modes, enabling individual mode launching. Here, it is shown how the free space launching would affect the intermodal interference of the ECF by measuring the OFDR signals. A bare ECF sample (with total fibre length around 210 mm) with both ends cleaved was used for testing, and the relevant OFDR results are shown in Fig. 3.11. Different modes were launched into the ECF separately, where the label of each coloured curve matches with the label of the corresponding output near-field mode image. The calculated optical path difference from several groups of lower-order modes is shown in Table 3.2. These calculations are in good agreement with the experimental measurements in Fig. 3.11, where three major FFT peak groups (indicated by dashed grey lines) result from MMI of lower-order modes. For example, the dominant peak at 0.5 - 1.0 mm corresponds to HOM interference.

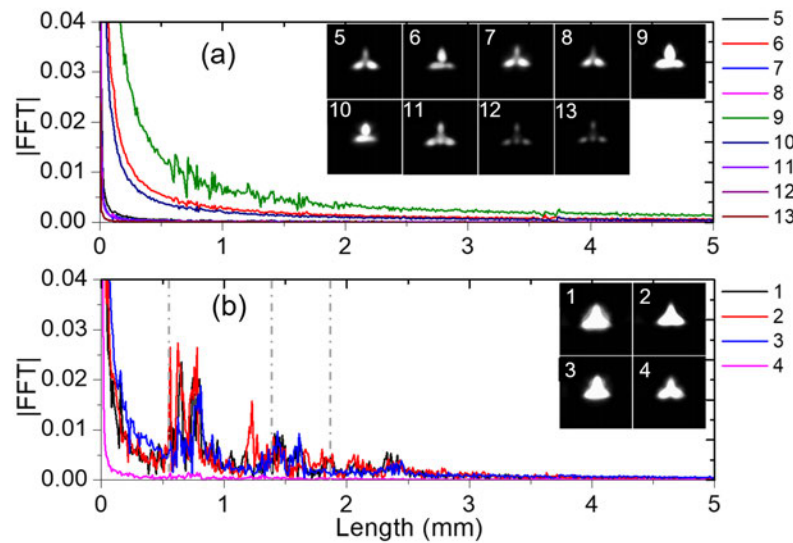


**Fig. 3.11** Intermodal interference signals measured from a bare ECF sample with length of 210 mm. Different curves are under different launching conditions with the output near-field mode profiles shown in the inset. (a) The single mode launching leads to weaker intermodal interference, while superposition mode launching leads to strong intermodal interference in (b). The labelled numbers between the mode image and the corresponding FFT are matched.

The intermodal interference is much weaker (no obvious FFT peaks) under individual single mode launching as shown in Fig. 3.11(a), while the intermodal interference is much stronger (large FFT peaks) under superposition mode excitation

as shown in Fig. 3.11(b). It means that individual mode launching would maintain the mode propagation, without attributing to obvious intermodal interference. The results in Fig. 3.11 also show that the scattering signal within the fibre is majorly carried back by the same mode. That is, peaks would be observed if the light couples back into other modes due to the MMI. More details on the robustness of the individual mode launching are given in the supplementary information in Chapter 4.2 [P2].

ECF intermodal interference		
Mode	Horizontal polarisation group index	Physical cavity length (mm)
FM	1.472	$(\text{FM} - \text{HOM}_1)L / n = 1.37$
HOM <sub>1</sub>	1.482	$(\text{HOM}_4 - \text{HOM}_1)L / n = 1.88$
HOM <sub>3</sub>	1.491	$(\text{HOM}_3 - \text{HOM}_1)L / n = 1.33$
HOM <sub>4</sub>	1.495	$(\text{HOM}_4 - \text{HOM}_3)L / n = 0.59$

**Table 3.2** Calculation of MMI within the ECF (Fig. 3.5(c)). The corresponding Poynting vector distributions with labels are displayed in Fig. 3.6.

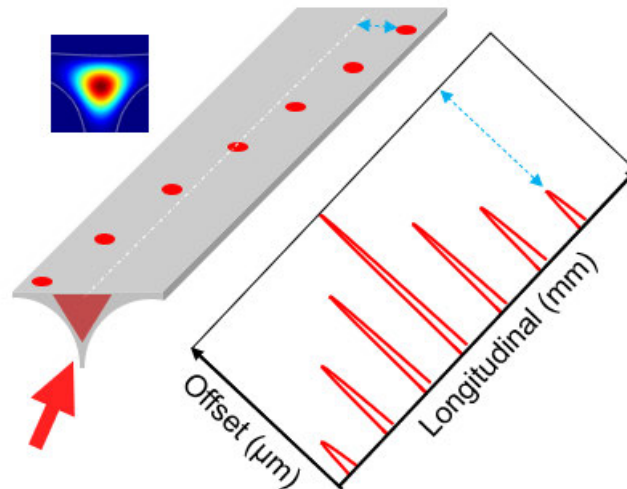


**Fig. 3.12** Concept diagram showing how scatterers with transverse distributions on the ECF surface would respond to the launched mode. Fundamental mode launching would show a Gaussian distribution along the exposed transverse boundary and detected signals from particles would fall into this curve depending upon their transverse locations.

By launching multiple modes, one at a time, two-dimensional (2D) sensing is possible, based on both the few-mode property of the ECF and the OFDR mechanism.

It overcomes the limitation by only a major single mode scheme described in the above integrated fibre device. By using more than one mode, the evanescent field could transversely cover a larger range of the ECF exposed boundary. Individual mode launching is important in this scenario to avoid MMI.

In theory, the returned signal carried from the scattering of the particle is expected to be proportional to the evanescent field when the particles are distributed as shown in Fig. 3.12. That is, the strongest signal would be from the particle in the core centre under an FM launching. This is the central idea of the paper presented in Chapter 4.2 [P2], whereby HOM launching allowed for 2D mapping of scatterers on the ECF surface.

### 3.3 Particle/scatterer positioning

#### Natural evaporation

In initial experiments, polystyrene spheres were randomly deposited on the exposed channel of the ECF after liquid evaporation, as shown in Fig. 3.13. However, many of the particles stuck to the walls of the exposed channel as displayed in Fig. 3.13(b), due to the capillary effect and surface tension.

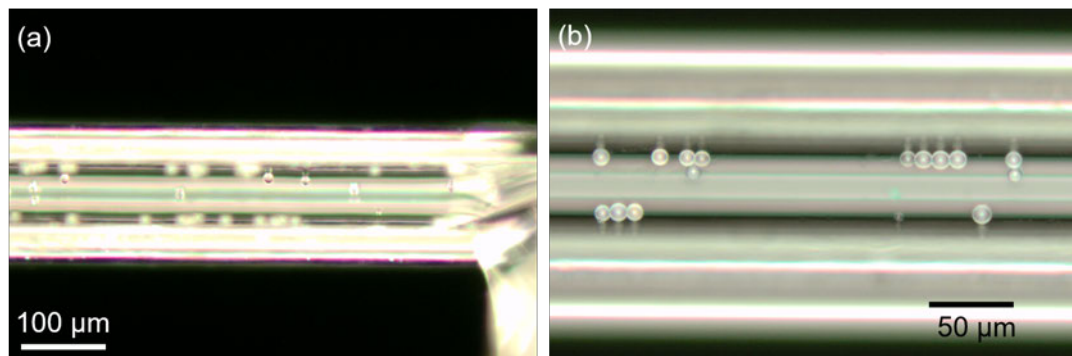


**Fig. 3.13** Dark field microscope images. (a) Polystyrene spheres positioned randomly on the exposed channel from a droplet of the particle suspension. (b) Particles remaining on the exposed channel after water evaporation, which stuck to the walls of the exposed channel. Various particles sizes can be seen.

The ECF in Fig. 3.5(a) is an asymmetric fibre which results from the artifact during the drilling procedure and this was used in Chapter 4.1 [P1]. Using this asymmetric fibre can alleviate both the capillary effect and surface tension during the liquid evaporation



process. This was further improved using the ECF in Fig. 3.5(c), which has no concave surfaces near the core.

### Surface scatterer fabricated by fs-laser ablation

An alternative, more controllable method of placing scattering sites on the ECF core was the use of fs-laser ablations. The fibre shown in Fig. 3.5(b) produced the results presented in Chapter 4.2 [P2], where silica-air ablations written by fs-laser were used in this paper to act as surface scatterers due to controllable laser-written points and their relative spacing as shown in Fig. 3.14. This allowed the demonstration of two-dimensional mapping using this fibre sensing technique. In this case, the micro-scatterers were inscribed permanently on the ECF, and the relative spacing between each point was known. During the fs-laser inscribing process, the second harmonic wave of a 1064 nm fs-laser with pulse energy of 150 nJ was implemented for inscribing each ablation, which was similar to that described for making fibre Bragg gratings (FBG) previously (Fig. 3.14(a)) [210].

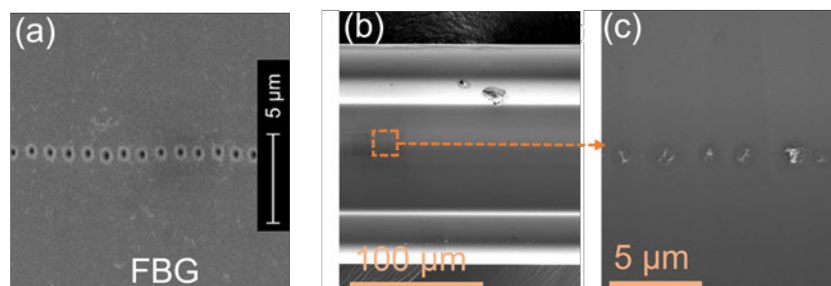


**Fig. 3.14** SEM images of fs-laser ablations on the exposed surface of the ECF. (a) An example FBG made by fs-laser ablation on the exposed surface from Ref. [210]. (b) Example of fs-laser ablations with  $3\ \mu\text{m}$  spacing with the magnified image in (c).

In Fig. 3.14(b), the fibre was imaged from the top of the exposed channel and the orange rectangle indicates the fs-laser writing area with the magnified image shown in Fig. 3.14(c). They were aligned in a straight line along the axial direction with the spacing between each adjacent point of  $3\ \mu\text{m}$ . Note that the fibre sample described here was specifically prepared for checking the quality of ablations under SEM, to ensure the fs-laser inscribing set-up was functioning properly. Fs-laser ablation patterns with large axial separation were then created for optical testing, as described in Chapter 4.2 [P2].

### Particle positioning using a glass tip

Particles in Chapter 4.1 [P1] were deposited naturally after liquid evaporation without manual control. Now a controllable approach to position particles is presented. Polystyrene spheres were suspended in milli-Q water and 1  $\mu\text{L}$  solution was placed on the top of the exposed channel of the ECF as shown in Fig. 3.15(b). The water was allowed to evaporate, leaving some particles remaining inside of the exposed channel.

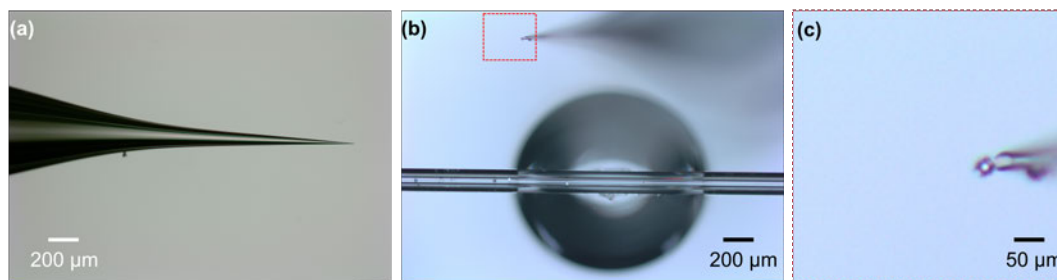


**Fig. 3.15** Positioning particles using a tapered glass capillary. (a) A tapered glass capillary with the tip size of 200 nm. (b) A drop of suspension (particles in water) is placed on the ECF, where the red dashed box is magnified in (c) with the particle attached on the tapered glass capillary tip.

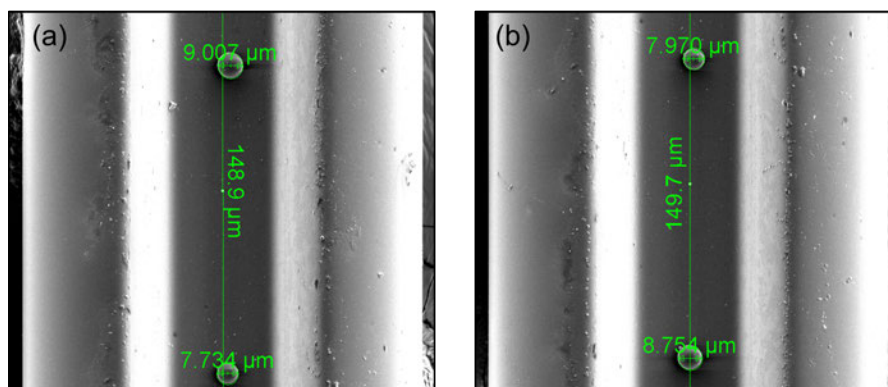


**Fig. 3.16** Particles on the ECF imaged under an SEM to show the positioning accuracy. (a) and (b) were imaged from the same ECF sample but at different locations. The slight variation from both the transverse locations and sizes could be seen from the particles.

By controlling both a three-axis translation stage and the microscope's built-in translation stage, a micro-scaled glass capillary (made in-house [211]) could be used to physically move the particles as shown in Fig. 3.15(a). Undesired particles or dust could be removed during this process, and positioned particles were attached to the silica surface through physisorption. There is no specific requirements for the tip size

as long as it is small enough to get into the exposed channel and be able to move the particles. As seen in Fig. 3.15(c), the tip size is comparable to the particle size ( $20\ \mu\text{m}$ ). While more precise control of displacement needs more advanced equipment, the positioning approach here is sufficient to support current experiments with positional accuracy within  $\pm 3\ \mu\text{m}$  as shown in Fig. 3.16.

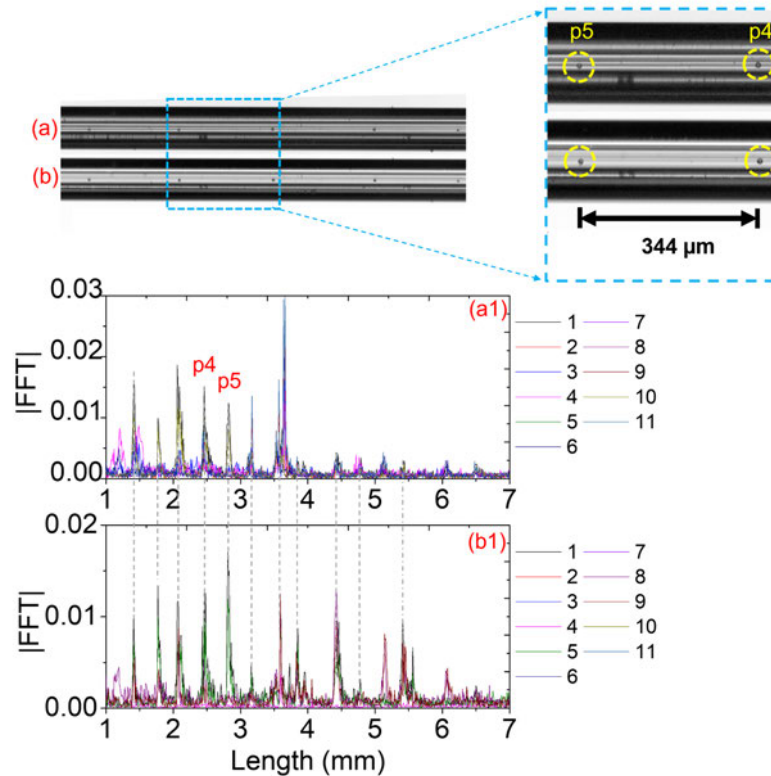


**Fig. 3.17** (a) The fibre sample with mechanically positioned polystyrene spheres captured by an optical microscope before the first measurement with the measured FFTs in (a1). A few days later, the same fibre sample was imaged in (b) with the second measured FFT results in (b1). Where spheres ‘p4’ and ‘p5’ are magnified in the right-hand side, they are also marked in the measured OFDR results. The dashed lines are indicative of the stability of polystyrene spheres sitting on the fibre. Labelled numbers (or different coloured curves) represent different launching conditions in (a1) and (b1) by slightly adjusting the three-axis optical stage when the ECF was fixed on the stage.

To demonstrate the stability of particles sitting on the ECF exposed surface, Fig. 3.17 shows the results where the same sample in Fig. 3.17(a) and (b) was captured under an optical microscope at different times with several days interval. The first measurement with the image in Fig. 3.17(a) shows the corresponding OFDR results in Fig. 3.17(a1). This fibre sample was then moved out of the optical stage and stored in

a closed plastic container. After a few days, the same fibre sample was moved back to the optical stage and measured again with both microscope images in Fig. 3.17(b) and OFDR results in Fig. 3.17(b1). The dashed lines inside the figure are used to indicate the highly repeatable peak positions from the two measured results, where each major peak is from a polystyrene sphere with a longitudinal position (away from the ECF input-end) shown in the bottom of axis. Particles 'p4' and 'p5' are marked in both fibre images and FFT results.

These results show the stability of polystyrene spheres on the ECF. Here, only one comparison is shown, but tens of fibre samples were checked to show similar stability during experiments. Note that the variation of the intensity from two measurements in the downstream polystyrene spheres are mainly due to the different launching conditions. However, located particles were observed to have large movement and even disappear when the fibre was cleaved by a ceramic blade near the place where particles were located. This is well explained by the destructive mechanic force induced by manually operating the ceramic blade.

### 3.4 Particle size detection

The previous sections have introduced the detection of spatial location of microscale particles on the ECF based on OFDR. Furthermore, the ability to use a portable and flexible sensing scheme for detection of microscale particle size is important. To optically mimic biological cells, the size of polystyrene spheres should be smaller than real biological cells to contribute similar scattering strength, owing to the refractive index contrast. However, in this thesis, the size equivalence (cells and model spheres) matters, because the scattering cross-section is vital in the proposed configuration (Fig. 3.2). That is to say, the size of model spheres equivalent to cells would be able to mimic the geometric scattering cross-sections, because the scattered signals are carried back via the fibre's backwards propagating modes. Large particles would potentially interact with more modes and vice versa. The preliminary experiments in a flow cell configuration to track individual polystyrene spheres ( $5 \mu\text{m}$ ) is also considered (see Appendix C). However, the real shape of cells are diverse rather than only spherical, so the possibility of detecting particle' size is discussed here based on OFDR technique.

Experiments were carried out where polystyrene micro-spheres with different sizes

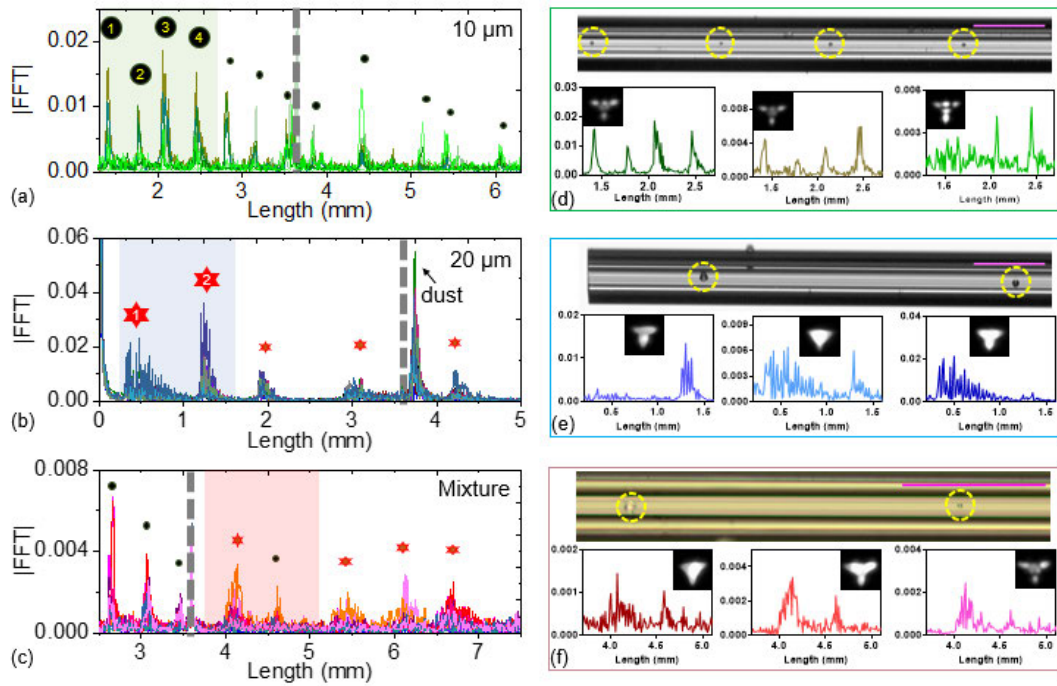


**Fig. 3.18** Experimental measurements of three fibre samples with (a)  $10\ \mu\text{m}$  spheres, (b)  $20\ \mu\text{m}$  spheres, and (c) a mixture of  $10$  and  $20\ \mu\text{m}$  spheres. Each panel (a), (b) and (c) is composed of multiple FFT signals, while the shaded area is magnified at right with individual FFT signals to see clearly with correlated output mode profiles shown in the insets. The grey dashed lines in the left column are from system noise (around  $3.65\ \text{mm}$ ). The yellow dashed circles indicate the polystyrene spheres which are either  $10\ \mu\text{m}$  or  $20\ \mu\text{m}$  positioned on the exposed channel of the ECFs, and the magenta scale bar is  $200\ \mu\text{m}$ . Note that there is a grey dashed line at the same longitudinal position ( $3.65\ \text{mm}$ ) in each left column panel which is an artefact arising from the noise in the experimental set-up.

were distributed along ECFs, and example FFT results are shown in Fig. 3.18(a, b, c), with particles of average size  $10\ \mu\text{m}$  (marked as black dots),  $20\ \mu\text{m}$  (marked as red stars) and both  $10$  and  $20\ \mu\text{m}$ , respectively. Their relevant OFDR signals overlap in each figure under several different launching conditions. The shaded areas are magnified in Fig. 3.18(d, e, f), respectively, with corresponding colour. Individual FFT signals are presented separately in each inset with a real-time near-field image to display the output modal super-position. The positioned polystyrene beads that contribute to the OFDR signal in the shaded area are shown at right parallel with the yellow dashed circles, as captured under an optical microscope. Only several particles are included in each fibre sample to enable them to be easily seen in the microscopic images in Fig. 3.18(d, e, f). The longitudinal position of particles located on the ECF could be directly detected based on the OFDR technique under certain launching conditions that is in

good agreement with the microscope images. The strength of FFT peaks from different particles differ depending on their sizes, transverse locations and launching conditions. As the scale of the x-axis is consistent for each figure, it is clear to see the difference in OFDR signals from different particles. It can be seen that OFDR signals from the 10  $\mu\text{m}$  particles are much narrower and single-peaked compared with broad and messy peaks from the 20  $\mu\text{m}$  particles.

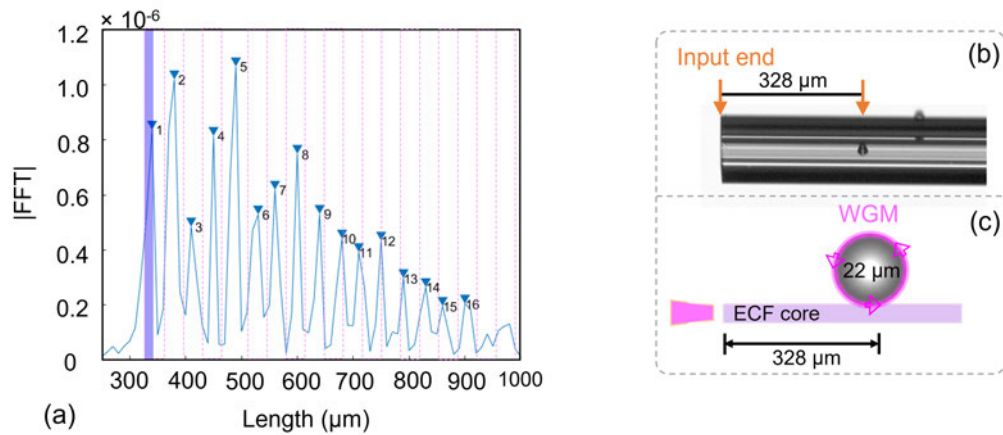


**Fig. 3.19** (a) FFT peaks (1-16) generated from a polystyrene sphere. The dashed light purple lines indicate consecutive interference from WGM circling with the ECF input. The dark purple stripe highlights the possible contribution from the multimodes disturbances by interfering with the ECF input-end with details in Chapter 5.1 [M1]. (b) The diameter of 22  $\mu\text{m}$  polystyrene sphere deposited on the ECF, with the FFT results shown in (a). (c) The illustration of WGMs circling around the sphere interfering with the ECF input-end to thus form the FFT peaks.

The multiple peaks from larger spheres in the right hand side image of Fig. 3.18(e) is magnified in Fig. 3.19(a) with the sampled particle shown in Fig. 3.19(b). This is due to the excitation of whispering gallery modes (WGMs) that interfere with the ECF input as illustrated in Fig. 3.19(c). In principle, the oscillating peaks would reflect the size difference based on both WGMs and OFDR, as the spacing of adjacent peaks is related to the optical path length of the sphere. However, the specific phase-matching requirements for exciting WGMs between waveguides and morphology-dependent micro-resonators (sphericity at the excitation plane) is challenging, and thus limits the ability to use WGMs in complex situations. In other words, these evenly spaced FFT peaks are not observed in all the large spheres ( $\geq 20 \mu\text{m}$ ) but only from a few particles during the experiments. Moreover, only near-perfect spherical particles will exhibit

WGMs, whereas real biological particles may have sphericity but will not typically support WGMs. Therefore, there is a necessity to seek other methods (e.g., machine learning algorithms) to analyse the complex reflection spectrum, with more details for distinguishing the particle sizes discussed in Chapter 5.1 [M1].

### 3.5 ECF as a WGM coupler

WGMs were observed when the light is coupled from ECFs to polystyrene microspheres under phase-matching conditions in the previous section. Here, microspheres can be used as sensing tools while the ECF acts as a novel WGM coupler. The general interest of studying WGMs is due to their achievable ultra-high Q-factor, bringing developments of single-molecule detection and low threshold lasing resulting from strong light-matter interaction [6, 77, 78].

Compared with Fabry-Perot resonators, WGM resonators are relatively easy to fabricate, and spheres, rings and toroids are used widely as miniaturised resonators. Except from the morphology-dependent property for exciting WGMs, another imperative point is to couple the light into resonators. Many coupling schemes have been reported in the past, such as prisms, fibre tapers, planar waveguides, photonic crystals and microstructured optical fibres (MOFs). Among them, fibre tapers are frequently used due to the achievable ultra-high coupling efficiency up to 99% [92].

However, the fragility of using fibre tapers remains a challenge for practical implementations. External platforms are often required to support both the fibre taper and the micro-resonator. Other coupling schemes such as using D-type fibres or microstructured optical fibres have been reported in the past, and they have the ability to embed, encapsulate or support particles directly on the fibre [91, 141, 142]. However, either complicated post processing such as melting/etching/polishing is required, or the ability to position particles is limited [89].

The interest of lasing using WGMs in biological cells is an active topic as a potential capability to track or sense small biological objects of interest (e.g., DNA and proteins). Some configurations for exciting WGMs in cells have been reported, and most of them are achieved through embedding micro-resonators inside the cells [99]. Their coupling methods are performed through a direct illumination from the bottom of the petri dish, a capillary or in free space. Therefore, a new WGM coupler using ECFs is proposed in

Chapter 5.2 [P3], which overcomes the challenge of using fragile fibre tapers and brings new possibilities towards integrating multiple resonators in a single fibre for possible applications such as multi-point sensing and lasing [212].

The main advantages of using ECFs for a WGM coupler is summarised as follows:

- There is no need of post processing since the evanescent field is directly accessible in an exposed-core fibre.
- The exposed side provides accessibility for positioning microspheres and there is ability to integrate multiple resonators on a single fibre.
- The ECF has an outer diameter of  $160\ \mu\text{m}$ , which is suitable for practical handling.
- The outer jacket of the ECF provides a partial physical protection for deposited microspheres from disturbance of the surrounding environment.

### 3.6 Further investigations

In this section several investigations that were not included within publications, but show directions for future work, are described.

#### Spatial light modulator

A spatial light modulator (SLM) was used to modulate the light wavefront to obtain desired light patterns (i.e., fibre mode profiles). This enables ECF HOMs to be launched with flexibility and accuracy in the future, and several launched single HOMs are shown in Fig. 3.20. More specific details are described in Appendix D.

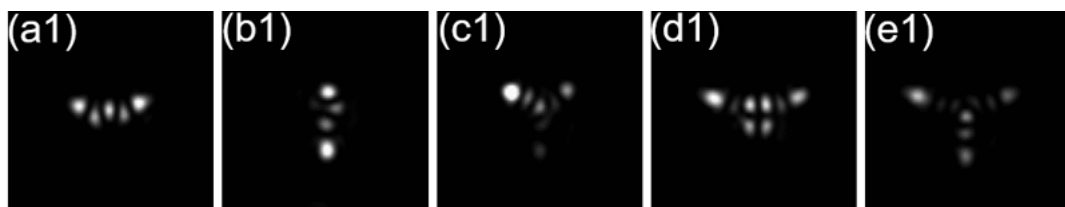


**Fig. 3.20** (a1-e1) Experimentally observed ECF high-order modes after using the holographic masks operated through a liquid crystal SLM.

#### Fixing particles on the fibre



Although the stability of the deposited particles using ECFs as a WGM platform is presented in Sec. 3.3, the ability to work in a liquid environment would be favourable for practical biological applications. If the particles were only attached to the surface through physisorption, water and a capillary effect from the exposed channel would move the particles. Therefore, a method to fix polystyrene spheres on the ECF has been proposed. By heating the polystyrene material until its softening temperature, it allows the polymer spheres to stick to the silica surface without significantly affecting its sphericity.

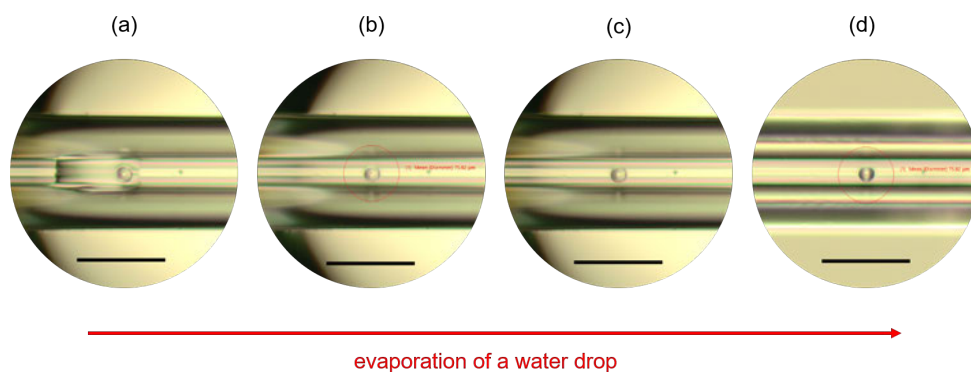


**Fig. 3.21** A polystyrene sphere was fixed on the ECF through a thermal fusing method. A droplet of water was then placed on the top of this sphere to test the particle's stability.

A series of tests were performed to find a suitable temperature from 125 to 168°C by using the thermal fusing method. Below 145°C, polystyrene spheres have not shown a good stability under water immersion, while the suitable temperature range was found to be from 145 to 168°C. For example, an ECF sample with deposited particles was heated at 168°C with 30 minutes inside the oven. This fibre sample was then tested under an optical microscope as shown in Fig. 3.21(a-d), under the water evaporation process. The particle did not move during this process, demonstrating good fixation by the thermal fusing method.

Note that for a more detailed and serious conclusion about the softening procedure for the good performance of morphology-dependent WGMs, more experiments would be required in the future to compare the Q-factor of the WGMs. Nonetheless, this is a preliminary demonstration showing the potential of the proposed WGMs platform for working in biological environments, and more details about WGM coupling using the ECF is introduced in Chapter 5.2 [P3].

### Particle morphology detection

The capability for distinguishing different sizes of polystyrene spheres was considered in Sec. 3.4. It would be advantageous if the sensor can be extended to investigate the particle morphology. While spheres are generally considered as having point-contact with the ECF surface, non-spherical particles would have more physical contact and are therefore expected to show differences in the signal due to their strong interaction with the evanescent field as shown in Fig. 3.22.

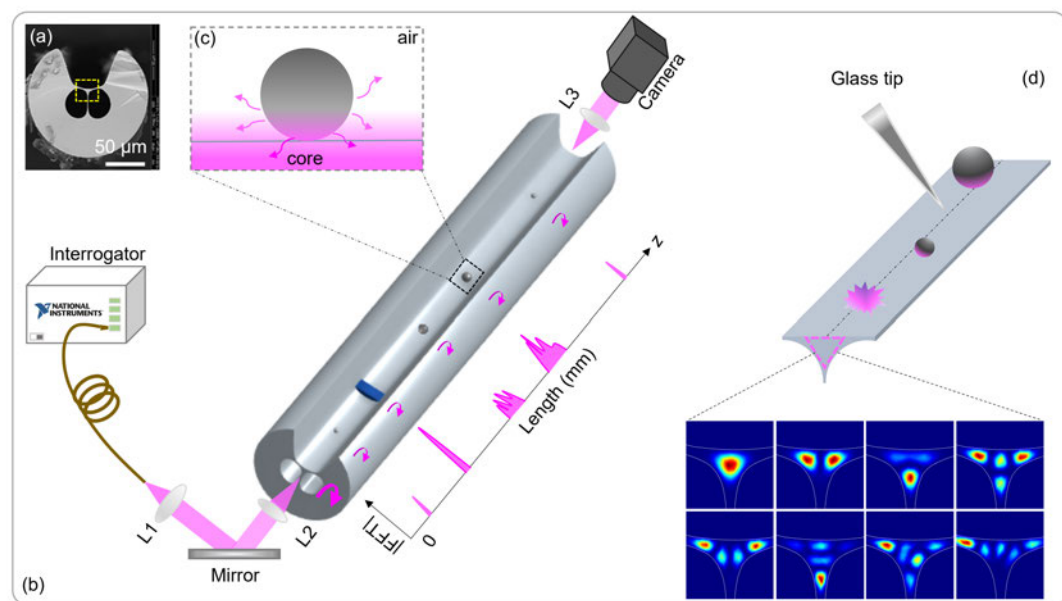


**Fig. 3.22** (a) An SEM image of the cross-section of the ECF (Fig. 3.5(c)). (b) Experimental set-up with a correlated signal map of micron-scale particles (including a non-spherical particle (blue) and microspheres with different sizes) based on the OFDR detection. The output near-field mode profile is monitored by an InGaAs camera. (c) Complex scattering from the particle excited by the evanescent field. (d) A micron-scale glass tip is used to position particles. Several guided modes supported by the ECF are shown, which interact differently with the various particles through the evanescent field. A black dashed line in the middle of waveguide indicates the centre of the ECF core.

Here some irregular particles were prepared including polyethylene ‘p1’, ‘p2’ and ‘p7’, a salt crystal ‘p3’ (crystallisation from sodium solution on the ECF) and a random dust particle ‘p5’ from the residue of the particle solution to compare with the results from polystyrene spheres ‘p4’ and ‘p6’ as shown in Fig. 3.23(a). Note that polyethylene bulks (‘p1’, ‘p2’ and ‘p7’) were formed by fully melting irregular micro-scaled polyethylene pieces (came from mechanically damaged 90  $\mu\text{m}$

blue-coloured polyethylene spheres, with refractive index  $\approx 1.50$ ) onto the ECF after heating for 30 minutes inside an oven around  $125^{\circ}\text{C}$ ) to obtain fully fixed and irregular particles sticking on the ECF. This is different from the previous proposal for fixing polystyrene spheres on the ECF which have to maintain the sphericity to enable WGM excitation.

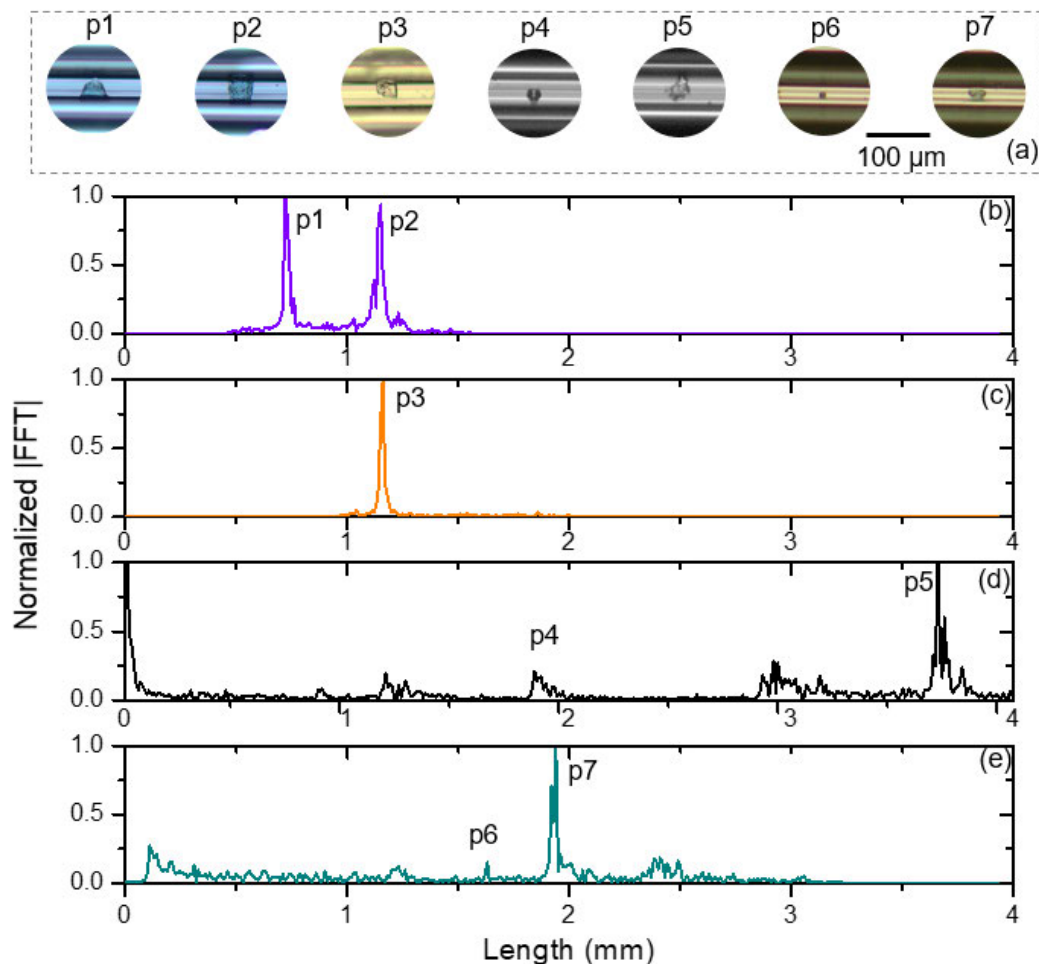


**Fig. 3.23** (a) Particles including polystyrene spheres and non-spheres located on ECFs. (b) FFT signals from irregular polyethylene particles ‘p1’ and ‘p2’ and they were located on different locations of the same ECF. (c) The FFT signal from a salt crystal ‘p3’, on the ECF. (d) FFT signals from a  $20\ \mu\text{m}$  polystyrene sphere ‘p4’ and dust ‘p5’ from the solution residue. Note that, this fibre sample is the same as shown in Fig. 3.18(b), which mainly consists of  $20\ \mu\text{m}$  polystyrene spheres leading to weak and broad FFT peaks compared with the dust signal (‘p5’). (e) FFT signals focused on a  $10\ \mu\text{m}$  polystyrene sphere ‘p6’ and an irregular polyethylene particle ‘p7’.

FFT signals from particles ‘p1’, ‘p2’, and ‘p3’ in Fig. 3.23(b) and (c), show significant single-narrowed peaks. One of the reasons is that these irregular particles

have more than one point-contact with the fibre surface, contributing to stronger signals. In comparison, a random dust particle 'p5' and 20  $\mu\text{m}$  polystyrene spheres were located on the same ECF, and an intense signal strength was observed from this dust particle in Fig. 3.23(d) compared with a polystyrene sphere 'p4'. In Fig. 3.23(d), other small broad peaks were also from the 20  $\mu\text{m}$  spheres, and this was the same fibre sample used in Fig. 3.18(b) where the marked "dust" was 'p5' here. Meanwhile, Fig. 3.23(e) shows a fibre sample consisting of irregular particles, 10  $\mu\text{m}$  and 20  $\mu\text{m}$  polystyrene spheres. Although the peak widths from 10  $\mu\text{m}$  polystyrene spheres and dust particles seem to be similar according to these results when referring to Fig. 3.18(a) and (d), the irregular polyethylene particle 'p7' displays a significant signal compared with the rest of signals from polystyrene spheres (i.e., signal from a 10  $\mu\text{m}$  polystyrene sphere 'p6').

These preliminary results have shown the potential to distinguish particle morphology by characterising their signal strength based on the OFDR technique. Both composition (refractive index) and shape of particles would affect the scattering signals, leading to differences in measured OFDR signals. In Chapter 5.1 [M1] it will be shown that this technique can be used for detecting the size of spherical particles. To understand the complex scattering data from these particles, particularly when the ECF is multimoded, machine learning algorithms are applied. The results here show the potential for expanding this method towards non-spherical particles, which would have greater applicability for real biological sensing.

### **Optimised coupling**

Now a proposal for an optimised coupling using ECFs as coupling platforms is presented. Due to the geometric structure of this ECF, both the particle's located position and the launched modes would affect the performance of the WGM resonances. For excitation of WGMs from a single particle, it requires careful control of the launched mode(s) to satisfy the phase-matching condition between the fibre waveguide and the microsphere and thus generate the WGMs. To avoid off-resonance, for example, a gap with 1.8  $\mu\text{m}$  was reported to be the optimised distance between the tapered fibre (diameter: 3  $\mu\text{m}$ ) and the resonator (silica sphere diameter: 150  $\mu\text{m}$ ), for achieving a coupling efficiency up to 99% [92].

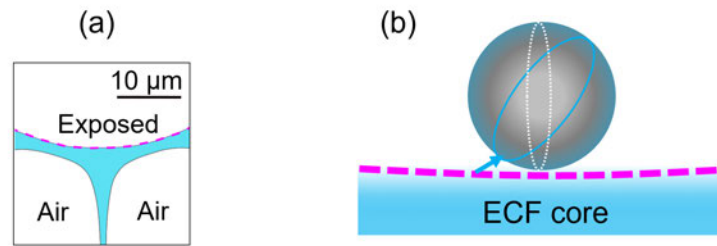


**Fig. 3.24** (a) The cross-section of the ECF. (b) A configuration of WGM excitation using ECF where the dashed magenta curve is the exposed boundary, which is consistent with (a). The white circle represents the equatorial plane contacting with the ECF surface while the blue circle represents the offset excitation with a slight gap.

Here, the possibility to achieve an optimised coupling even though the particles are physically attached to the exposed surface of the ECF is proposed. Launched HOMs have energy extended transversely along the exposed surface. This enables the evanescent field of a certain mode to excite the microsphere with a slight gap (marked as a blue circle) rather than a direct excitation in the equatorial plane contacting the fibre surface (marked as a white circle) as illustrated in Fig. 3.24.

## **CHAPTER 4**

### **ECFs for distributed sensing**

## **4.1 Distributed sensing of micron-scale particles**

This section focus on one-dimensional distributed sensing of micron-scale particles using an ECF integrated fibre sensor, based on the OFDR technique.

### **4.1.1 Publication overview**

This work [P1] has demonstrated distributed sensing of micron-scale particles with high spatial resolution using an integrated fibre sensor device. Based on the OFDR, a fraction of scattered light from the particles is coupled back via backwards ECF modes to interfere with the reference light, so particles' axial distributions along the ECF are thus mapped out. Both theoretical analysis and experimental implementation are presented in this publication. This is the foundation for the whole project, which is distributed sensing of micron-scale particles towards biomedical applications.

### **4.1.2 Statement of contribution**

## Statement of Authorship

Title of Paper	High-resolution distributed sensing of micro-scaled particles
Publication Status	<input checked="" type="checkbox"/> Published <input type="checkbox"/> Accepted for Publication <input type="checkbox"/> Submitted for Publication <input type="checkbox"/> Unpublished and Unsubmitted work written in manuscript style
Publication Details	Lu Peng, Jiawen Li, Robert A. McLaughlin, Heike Ebendorff-Heidepriem and Stephen C. Warren-Smith. "Distributed optical fiber sensing of micron-scale particles". Sensors and Actuators A: Physical, 2019, 303: 111762.

### Principal Author

Name of Principal Author (Candidate)	Lu Peng
Contribution to the Paper	All the experiments, analysis and paper writing were majorly done by Lu Peng.
Overall percentage (%)	70%
Certification:	This paper reports on original research Lu Peng conducted during the period of her Higher Degree by Research candidature and is not subject to any obligations or contractual agreements with a third party that would constrain its inclusion in this thesis. Lu Peng is the primary author of this paper.
Signature	<div style="border-bottom: 1px solid black; width: 100%;"></div> <div style="display: flex; justify-content: space-between; align-items: center;"> <span>Date</span> <span>10-08-2021</span> </div>

### Co-Author Contributions

By signing the Statement of Authorship, each author certifies that:

- i. the candidate's stated contribution to the publication is accurate (as detailed above);
- ii. permission is granted for the candidate to include the publication in the thesis; and
- iii. the sum of all co-author contributions is equal to 100% less the candidate's stated contribution.

Name of Co-Author	Jiawen Li
Contribution to the Paper	Jiawen Li helped conceptualise the research. She provided some suggestions especially for the loss measurements in Fig. 3 of the paper. She contributed to many discussions for the paperwork and helped revise the manuscript.
Signature	<div style="border-bottom: 1px solid black; width: 100%;"></div> <div style="display: flex; justify-content: space-between; align-items: center;"> <span>Date</span> <span>09-08-2021</span> </div>

Name of Co-Author	Robert A. McLaughlin
Contribution to the Paper	Robert A. McLaughlin helped conceptualise the research. He provided general suggestions for paper writing and helped revise the manuscript especially in the introduction.
Signature	<div style="border-bottom: 1px solid black; width: 100%;"></div> <div style="display: flex; justify-content: space-between; align-items: center;"> <span>Date</span> <span>10/08/2021</span> </div>



Name of Co-Author	Heike Ebendorff-Heidepriem		
Contribution to the Paper	Heike Ebendorff-Heidepriem helped conceptualise the research. She contributed to general discussions for how to present the work in the paper and helped polish the paper.		
Signature		Date	9 Aug 2021

Name of Co-Author	Stephen C. Warren-Smith		
Contribution to the Paper	This work was mainly conceptualised by Stephen C. Warren-Smith, who provided specific theoretical and experimental guidance during the process and helped to structure/revise the paper.		
Signature		Date	10-08-2021



## Distributed optical fiber sensing of micron-scale particles

Lu Peng<sup>a,b,c,\*</sup>, Jiawen Li<sup>b,c,d</sup>, Robert A. McLaughlin<sup>b,c,d</sup>, Heike Ebendorff-Heidepriem<sup>a,b,c</sup>, Stephen C. Warren-Smith<sup>a,b,c</sup>

<sup>a</sup> School of Physical Sciences, The University of Adelaide, Adelaide, SA 5005, Australia

<sup>b</sup> Institute for Photonics and Advanced Sensing, The University of Adelaide, Adelaide, SA 5005, Australia

<sup>c</sup> Australian Research Council Centre of Excellence for Nanoscale Biophotonics, The University of Adelaide, Adelaide, SA 5005, Australia

<sup>d</sup> Adelaide Medical School, The University of Adelaide, Adelaide, SA 5005, Australia



### ARTICLE INFO

#### Article history:

Received 8 September 2019

Received in revised form 4 November 2019

Accepted 19 November 2019

Available online 20 November 2019

#### Keywords:

Distributed sensing  
Microstructured optical fiber  
Optical fiber sensing  
Interference

### ABSTRACT

Distributed sensing of micron-scale particles is achieved with an exposed-core microstructured optical fiber using optical frequency domain reflectometry. The reference and sample signals of the interferometer are generated in the same fiber path, which gives this fully fiber-integrated sensor the potential to be used as a portable probe for *in-vivo* sensing. This sensing concept has great advantages over reported single-point fiber sensors due to its distributed sensing property. We demonstrate the technique using 10  $\mu\text{m}$  polystyrene beads, by detecting their locations along the fiber through backscatter of the exposed-core fiber's evanescent field. A simplified theoretical model is proposed to estimate the relationship between the particle's size and detection distance after considering the system's inherent losses. The proposed sensing platform offers opportunities for distributed sensing of biological targets.

© 2019 Elsevier B.V. All rights reserved.

### 1. Introduction

Distributed optical fiber sensors were first demonstrated by measuring backward Rayleigh scattering to determine loss along the optical fiber length [1]. Subsequently, distributed sensors for physical parameters, such as temperature and strain, have been developed for many applications in structural health monitoring [2–6]. Detection distances up to several kilometers can be realized, while their detection resolutions are in the order of several millimeters to meters [3,7,8]. Distributed fiber sensors with high resolution (micrometers) have also been achieved using interference-based techniques for applications such as optical components diagnostics [9–11]. However, the use of distributed fiber sensing for biological applications has thus far been very limited.

Many single-point optical fiber-based sensors have been demonstrated for bio-related sensing applications, with the promise of portable, low-cost, real-time and minimally invasive measurements [12–14]. The optical fiber is typically used as a method of flexibly delivering light to a distal location, which then either directly or indirectly collects spectroscopic information on the biological sample. For example, Schartner et al. reported a

single-point fiber pH probe that could be utilized for assessing breast cancer margins during surgery, using a fluorescent dye embedded within a polymer and coated onto the fiber end-face [15]. Single-point fiber-based *in-vivo* temperature measurements have also been demonstrated by coating rare-earth doped glass onto the fiber end-face, where fluorescence of the coating varied with temperature [16].

Microstructured optical fibers (MOFs), which are fabricated with longitudinal air holes that facilitate the light guidance, show great promise for chemical and biological sensing due to the ability to have a significant portion of the guided optical mode propagate external to the host glass [17,18]. The internal holes can also be readily filled with liquid analytes via capillary action or applied pressure to perform sensitive length integrated chemical [19,20] and biological [21,22] measurements. However, they can still only be considered as point sensors because the analyte is drawn from the distal end of the fiber.

A limitation of all single-point sensors is that the optical fiber must be moved to acquire multiple measurements over a region. Probe movement or physical scanning is not feasible in many *in-vivo* measurement applications, and risks causing trauma to highly delicate tissue in living organisms. The ability to obtain information along the whole length of the fiber would enable new capabilities for *in-vivo* sensing. The particular interest in our work is the distributed detection of single particles, which in a biological set-

\* Corresponding author at: School of Physical Sciences, The University of Adelaide, Adelaide, SA 5005, Australia.

E-mail address: [lu.peng@adelaide.edu.au](mailto:lu.peng@adelaide.edu.au) (L. Peng).

<https://doi.org/10.1016/j.sna.2019.111762>

0924-4247/© 2019 Elsevier B.V. All rights reserved.

2

L. Peng, J. Li, R.A. McLaughlin et al. / Sensors and Actuators A 303 (2020) 111762

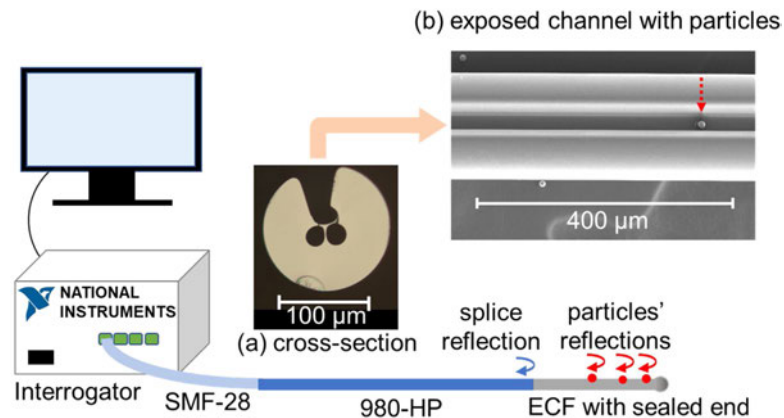


**Fig. 1.** Schematic of the experimental setup, where the particle sensing occurs along a 20 mm length of ECF and the reflection at the splice forms the reference arm. (a) Cross-sectional microscope image of the ECF. (b) The exposed channel of the ECF with deposited round polystyrene bead (marked with a red dashed arrow). (For interpretation of the references to colour in this figure legend, the reader is referred to the web version of this article).

ting could be targeted towards cancer cells, bacteria, viruses, or nanoparticles [23].

Single particle detection and tracking within a structured fiber was demonstrated Faez et al. in 2015 [24]. Here the Rayleigh scattering from nanoparticles loaded inside the nanofluidic channel of a nanobore optical fiber was tracked. While this was an effective technique to track motion along the fiber, it relied on an external microscope objective to image the side of the fiber to acquire the scattered signals from the particles. In order to be used as a portable and *in-vivo* probe, the excitation and scattering signals would need to be guided by the same fiber. Alternatively, a high spatial resolution (tens of micrometers) sensor was reported by Bykov et al. for physical sensing, through launching a flying silica particle inside the hollow core of a microstructured optical fiber and detecting various optical properties [25]. In this case the particle was used as a sensor element, rather than the optical fiber being used to detect external particles.

In 2009 Warren-Smith et al. demonstrated distributed sensing of an external parameter, in this case a fluorescent chemical species, using a time domain approach with an exposed-core microstructured optical fiber (ECF) [26]. This class of MOF has a portion of the cladding removed such that the core is directly exposed to the external environment along the entire length [27–29]. The exposed-core is highly sensitive due to the small diameter (several microns), whilst being supported by an outer jacket with a standard fiber diameter. This configuration has significantly improved robustness over other reported fiber sensors made through tapering or etching [30], while having higher sensitivity (evanescent field fraction) compared to D-shaped fiber [31,32]. However, time-domain distributed sensing has a spatial resolution on the order of one meter, limiting its potential use to large scale structural health monitoring applications rather than biological applications.

In this paper, we propose high-resolution distributed particle sensing along an ECF using the principle of optical frequency domain reflectometry. We demonstrate the technique by measuring the locations of 10  $\mu\text{m}$  sized particles over several centimeters detection range.

## 2. Experimental configuration and principle

Fig. 1 shows the experimental setup, which consists of an optical sensors interrogator, a computer, and a fiber sensor. Fig. 1(a) shows

the cross-section of the ECF used in this experiment, which was fabricated as described previously [28,33]. Briefly, a 20 mm diameter silica rod was drilled with three air holes (diameter =2.8 mm) and a 1 mm slot, which was then drawn to 160  $\mu\text{m}$  fibers. Two air holes (22–26  $\mu\text{m}$ ) and an open channel (width 35–45  $\mu\text{m}$  and depth 57–69  $\mu\text{m}$ ) surround the silica glass core, such that the open channel allows analytes to directly access the fiber core. The fiber sensor was fabricated by first splicing a section of 980-HP fiber to a standard single mode fiber (SMF-28) using an arc splicer (Fujikura FSM-100 P). The opposite end of the 980-HP fiber was then spliced to a 20 mm length of ECF. The distal end of the ECF was sealed by melting it into a ball shape using the splicer, both to minimize back-reflections from the fiber end and to prevent solvent from entering the two air holes. We chose to splice 980-HP fiber with the ECF due to their similar mode field diameters (MFDs), being 6.19  $\mu\text{m}$  (980-HP) and 5.18  $\mu\text{m}$  (ECF fundamental mode) [28], which allows the fundamental mode of the ECF to be predominantly launched and thus give a single clear interference signal from each particle.

Polystyrene beads were selected as a model system to show the proof-of-concept of our sensing technique because of their similarity to biological cells both in refractive index and size. To demonstrate distributed sensing, polystyrene beads with size  $9.7 \pm 0.4 \mu\text{m}$  (Thermo Fisher) were deposited along the open channel of the ECF by dropping 1  $\mu\text{L}$  solution (polystyrene beads in ethanol) on a small portion of the ECF. The solution traveled along the open channel of the ECF via capillary action, subsequently evaporating and leaving particles randomly located inside the channel as shown by the microscope image in Fig. 1(b).

The sensing principle is based on optical interference between the sample reflections (from the polystyrene beads) and a reference reflection. Here, a small portion of the light that propagates along the 980-HP fiber is reflected at the 980-HP to ECF splice (blue curved arrow in Fig. 1) due to a small overlap with the ECF holes (glass-air interface), providing a reference reflection. Scattered light from particles near the center of the ECF core is collected via the evanescent field and returns back along the ECF (red curved arrows in Fig. 1), forming a sample reflection from each particle.

The optical sensor interrogator (National Instruments PXIe-4844) consists of a swept wavelength laser source with a wavelength range from 1510 to 1590 nm and a wavelength resolution of 4 pm (separated into 20,000 points). The achievable axial

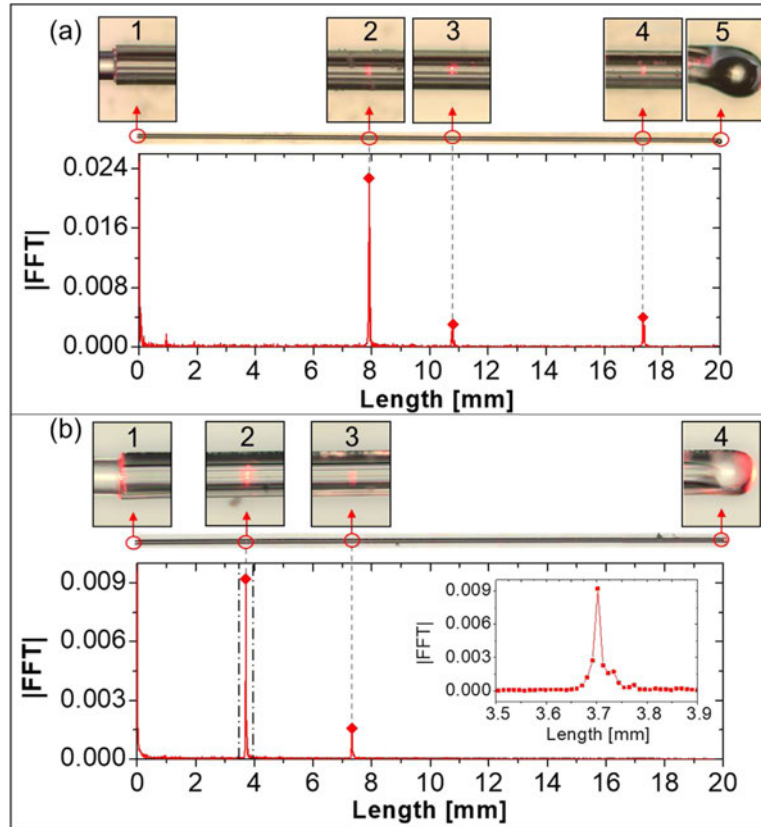


**Fig. 2.** (a) and (b) show the FFT of the optical interference signals for two different ECFs with different distributions of particles. Red diamonds indicate detection events with a signal to noise (SNR) greater than 3.0. The small insets above are microscope images of the ECF showing the splicing points, particles (red spots), and sealed ends of the ECFs, while the entire ECF sensors (20 mm) are shown under the insets. Visible red spots in the images were formed by replacing the interrogator with a red laser source in order to view the scattering during microscope imaging and thus confirm the locations of the particles. The inset in (b) shows a magnified plot of the peak at 3.7 mm. (For interpretation of the references to colour in this figure legend, the reader is referred to the web version of this article).

resolution of this distributed ECF sensor can be calculated using Eq. (1) [2]:

$$\Delta z = \frac{c}{2n_{eff}\Delta F} \quad (1)$$

where  $c$  is the speed of light,  $n_{eff}$  is the effective refractive index of the ECF, and  $\Delta F$  is the scanning frequency range of the laser source. An axial resolution of  $10.4 \mu\text{m}$  can theoretically be achieved. Higher resolution could be realized by using a swept wavelength light source with a broader wavelength scanning range. The signal processing of this experiment is comparable to that used in swept-source optical coherence tomography, extracting the locations of the polystyrene beads along the optical path from the interference spectrum via fast Fourier transform (FFT) [34].

### 3. Results and discussion

Fig. 2(a) and (b) show two nominally identical spliced ECF sensors with different random distributions of particles, and their corresponding interference signals. Numbered insets are microscope images at locations where polymer beads were deposited (red circles and arrows) along the length of the ECF sensors

(20 mm). The magnified inset 1 shows the 980-HP + ECF splice and inset 5 shows the sealed ECF tip in Fig. 2(a). To confirm the positions of the particles along the ECF under a microscope, the interrogator was replaced with a red laser source. Red light scattering from the particles is shown in insets 2–4 and matches longitudinally with the related peaks in the FFT of the interference signal. Each peak in the interference signal demonstrates the interference between a particle and the reference signal. The horizontal axis shows the positions of the particles located along the ECF relative to the 980-HP + ECF splice. For reference, the diameter of the 980-HP is  $125 \mu\text{m}$  and the diameter of the ECF is  $160 \mu\text{m}$ . Fig. 2(b) shows the results for a second ECF, nominally identical, sensor with a different particle distribution to demonstrate the repeatability of this method and the inset shows a magnified view of the peak at 4 mm. Here we see that adjacent data points are separated by  $10.4 \mu\text{m}$  along the ECF length, as was calculated in Sec. 2, yielding a minimum resolvable spatial resolution of approximately  $20 \mu\text{m}$ . The strong correlation between the polymer bead locations and the FFT peaks demonstrates that the axial distribution of micron-scale particles located on the exposed-core can indeed be mapped using frequency domain reflectometry.

4

L. Peng, J. Li, R.A. McLaughlin et al. / Sensors and Actuators A 303 (2020) 111762

It can be seen in Fig. 2 that there are variations in the intensities of the peaks, despite the particles having nominally the same size. There are several potential causes for this. First, the channel of the ECF is larger than the particles, which leads to the distribution of beads transversely across the core of the fiber. The ECF is more sensitive to particles at the center of the core where the evanescent field of the fundamental mode is the strongest. In general, the shape of the fundamental mode of the ECF is approximately Gaussian, thus the highest scattered signal occurs when particles are centered at the base of the channel and therefore centered on the core. In future, this issue could be solved by either nanofabrication or chemical binding techniques to fix the location of particles to the center of the core or through the use of higher order modes to determine the distance of particles from the core. The later technique also has the potential to discriminate the particles' size as well as position, giving a full picture of any particles within the evanescent field of the fiber.

Secondly, scattering due to polystyrene beads and contaminants such as dust or residue from particles' solution (if they are near the center of the open channel) can lead to reflected signals and loss. Thus, intensities of peaks can decrease with greater distance from the 980-HP + ECF splice.

Thirdly, the swept source has a limited coherence length, leading to a decrease in the interference signal as the path length between the reference arm (splice) and the sample arm (particles) increases [35,36]. We have characterized this effect by measuring the interference signal from a spliced ECF with a cleaved end at varying ECF lengths, with the results shown in Fig. 3. Each color represents a different ECF length. Specifically, we cleaved the distal end-face of the ECF five times, i.e. cut-back measurement, numbered 1–5 in Fig. 3. The initial ECF length was 42 mm, decreasing by several millimeters with each subsequent cleave of the fiber sensor. The result shown in Fig. 3 characterizes a signal drop-off of 0.73 dB/mm with

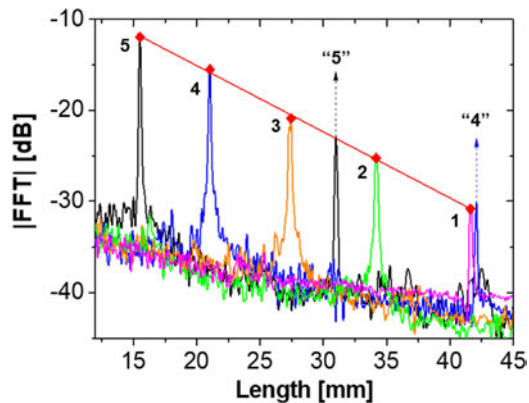


**Fig. 3.** Cut-back measurement of the interference signals for different ECF lengths. Numbers 1–5 represent the cleave sequence from the same fiber sensor. The signals are presented after minimizing the noise through signal processing (with 8pts FFT smooth) in OriginPro8.5. Red solid diamonds show peaks while the red line shows a linear fit (Slope =  $-0.73$  dB/mm, Adj. R-Square = 0.99823). Redundant peaks named “4” and “5” (with quotation marks) can be ignored as they are due to double-pass reflections. (For interpretation of the references to colour in this figure legend, the reader is referred to the web version of this article).

increasing detection length. This loss value can be used to correct the heights in Fig. 2. Redundant peaks named “4” and “5” (with quotation marks) are due to multiple-pass reflection paths of light between the spliced point and the end-face of fiber after cleaving 4 and 5 respectively, and may be ignored for calculation of the loss of signal with path length. This was evident as their axial positions are equal to twice the single-pass optical path length.

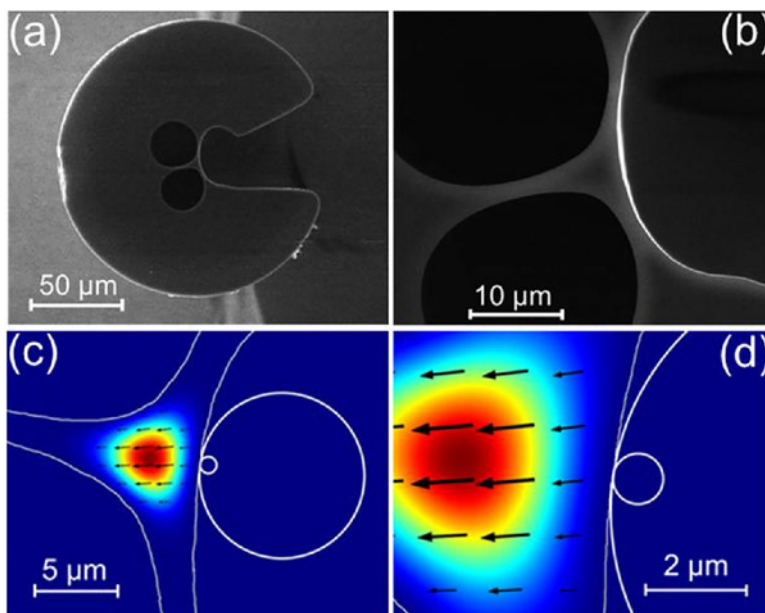


**Fig. 4.** (a) SEM image of the ECF. (b) Magnified image of (a), showing the fiber core region, which was imported into the numerical model. (c) Geometry of the 2D model (white lines), the Poynting vector distribution of fundamental mode (color plot) and the electric field polarization (black arrows). The two white circles represent particles of 1  $\mu\text{m}$  and 10  $\mu\text{m}$  diameter. (d) Magnified image of (c).

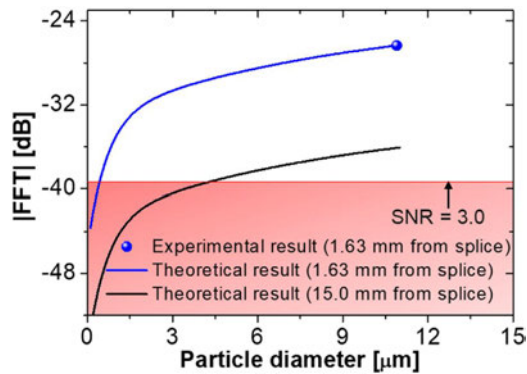


**Fig. 5.** The blue data point shows the optical interference signal of a polystyrene bead at a location of 1.63 mm along the ECF. The blue line shows the extrapolated relative scattering of smaller particles as given by the numerical model. The black line represents the relative particle scattering based on this fiber sensor at the position of 15 mm along the ECF, down-shifted by 9.8 dB relative to the blue line using Fig. 3. For reference, the red line shows the reflection intensity when the SNR = 3.0. (For interpretation of the references to colour in this figure legend, the reader is referred to the web version of this article).

To estimate the minimum detectable particle size using the current experimental setup, we have performed a simple theoretical simulation integrated with experimental data. A two-dimensional (2D) model was built (COMSOL v5.2, Comsol Inc. MA, USA) with the finite element method based on an imported scanning electron microscope (SEM) image as shown in Fig. 4(b) (magnified image of Fig. 4(a)). A polymer bead was approximated as a circle located at the center of the exposed-core channel. Circles with diameter 1  $\mu\text{m}$  and 10  $\mu\text{m}$  are shown as examples in Figs. 4(c) and (d). In this model we assume that the amount of scattering from the particle,  $\alpha_p$ , is proportional to the overlap of the fundamental mode Poynting vector with the cross section of the circle (i.e. polymer bead) as shown in Eq. (2), where  $\vec{e}$  and  $\vec{h}$  are the electric and magnetic fields of the fundamental mode, respectively.

$$\alpha_p \propto \frac{\int_{\text{circle}} (\vec{e} \times \vec{h}) \cdot d\vec{A}}{\int_{A_\infty} (\vec{e} \times \vec{h}) \cdot d\vec{A}} \quad (2)$$

Note that this model makes the approximation that the polymer bead has no effect on the guided mode and assumes that the scattering from different sized particles are equally coupled back into the guided mode of the fiber.

The overlap integral was calculated for various particle diameters. The simulated results are shown in Fig. 5, where detectable signals for two fixed lengths of the same ECF sensor are shown (blue line for 1.63 mm and black line for 15 mm). The blue line was adjusted by adding a y-axis constant to match with the experimental data (solid blue sphere). This data point was from one of the experimental results, which depicts the interference intensity where a polystyrene bead was in the center of the open channel at a location of 1.63 mm from the 980-HP + ECF splice. The black line corresponds to the particle being located 15 mm away from the 980-HP + ECF splice after correcting the signal (blue line) by using the signal drop-off relationship illustrated in Fig. 3. The level at which the SNR equals three (allowing clear detection of a particle), based on the background noise from the experimental data point, is shown as filled light red in Fig. 5. Note that this noise level is not equivalent to the noise observed in Fig. 3 as the signals in Fig. 3 are from cleaved fiber end-faces, which have a different

background noise compared to the particle sensing experiments. The results show that the smallest particle that this sensor could detect at up to 15 mm detection length is 4  $\mu\text{m}$  or down to approximately 500 nm for a detection length of 1.63 mm. The detection size and range have potential for improvement by reducing the detection noise, increasing the laser coherence length, and increasing the laser power.

#### 4. Conclusion

In summary, we have demonstrated a distributed fiber sensor that can detect the axial positions of micron-scale particles with high repeatability and stability. In this work we detected 10  $\mu\text{m}$  polystyrene particles, which have a similar refractive index and size to biological cells, suggesting that the system has potential for biomedical applications such as sensing the location of cancer cells, bacteria, viruses, or nanoparticles. Furthermore, the experimental setup is compatible with being deployed as a flexible fiber probe and uses commercial optical fiber sensor interrogation equipment, making it portable and simple to implement.

#### Declaration of Competing Interest

The authors declare that they have no known competing financial interests or personal relationships that could have appeared to influence the work reported in this paper.

#### Acknowledgements

The authors acknowledge Peter Henry and Alastair Dowler for their contribution to the fiber fabrication. This work was performed in part at the Optofab node of the Australian National Fabrication Facility utilizing Commonwealth and South Australian State Government Funding.

#### Declaration of Competing Interest

The authors declare that they have no known competing financial interests or personal relationships that could have appeared to influence the work reported in this paper.

#### Funding

Australian Research Council (CE140100003). Stephen C. Warren-Smith is funded by a Ramsay Fellowship provided by the University of Adelaide. Lu Peng acknowledges financial support from the China Scholarship Council. Jiawen Li is funded by the Australian Heart Foundation (Postdoctoral Fellowship102093). Robert A. McLaughlin is funded by a Premier's Research and Industry Fund grant provided by the South Australian Government Department for Industry and Skills.

#### References

- [1] M.K. Barnoski, S.M. Jensen, Fiber waveguides: a novel technique for investigating attenuation characteristics, *Appl. Opt.* 15 (9) (1976) 2112–2115.
- [2] X. Bao, L. Chen, Recent progress in distributed fiber optic sensors, *Sensors*. 12 (7) (2012) 8601–8639.
- [3] X. Bao, D.J. Webb, D.A. Jackson, 32-km distributed temperature sensor based on Brillouin loss in an optical fiber, *Opt. Lett.* 18 (18) (1993) 1561–1563.
- [4] M. Froggatt, J. Moore, High-spatial-resolution distributed strain measurement in optical fiber with Rayleigh scatter, *Appl. Opt.* 37 (10) (1998) 1735–1740.
- [5] T. Kurashima, T. Horiguchi, M. Tateda, Distributed-temperature sensing using stimulated Brillouin-scattering in optical silica fibers, *Opt. Lett.* 15 (18) (1990) 1038–1040.
- [6] C. Ma, T. Liu, K. Liu, J. Jiang, Z. Ding, L. Pan, M. Tian, Long-range distributed fiber vibration sensor using an asymmetric dual Mach-Zehnder interferometers, *J. Lightwave Technol.* 34 (9) (2016) 2235–2239.

6

L. Peng, J. Li, R.A. McLaughlin et al. / Sensors and Actuators A 303 (2020) 111762

- [7] A. Barrias, J.R. Casas, S. Villalba, A review of distributed optical fiber sensors for civil engineering applications, *Sensors* 16 (5) (2016) 748.
- [8] A. Denisov, M.A. Soto, L. Thevenaz, Going beyond 1000000 resolved points in a Brillouin distributed fiber sensor: theoretical analysis and experimental demonstration, *Light Sci. Appl.* 5 (5) (2016), e16074.
- [9] B.L. Danielson, C.D. Whittenberg, Guided-wave reflectometry with micrometer resolution, *Appl. Opt.* 26 (14) (1987) 2836–2842.
- [10] T.G. Giallorenzi, J.A. Bucaro, A. Dandridge, G.H. Sigel, J.H. Cole, S.C. Rashleigh, R.G. Priest, Optical fiber sensor technology, *IEEE J. Quantum Electron.* 18 (4) (1982) 626–665.
- [11] B.J. Soller, D.K. Gifford, M.S. Wolfe, M.E. Froggatt, High resolution optical frequency domain reflectometry for characterization of components and assemblies, *Opt. Express* 13 (2) (2005) 666–674.
- [12] C. Caucheteur, T. Guo, J. Albert, Review of plasmonic fiber optic biochemical sensors: improving the limit of detection, *Anal. Bioanal. Chem.* 407 (14) (2015) 3883–3897.
- [13] A. Leung, P.M. Shankar, R. Mutharasan, A review of fiber-optic biosensors, *Sens. Actuator B-Chem.* 125 (2) (2007) 688–703.
- [14] X.-D. Wang, O.S. Wolfbeis, Fiber-optic chemical sensors and biosensors (2013–2015), *Anal. Chem.* 88 (1) (2015) 203–227.
- [15] E.P. Schartner, M.R. Henderson, M. Purdey, D. Dhattrak, T.M. Monro, P.G. Gill, D.F. Callen, Cancer detection in human tissue samples using a fiber-tip pH probe, *Cancer Res.* 76 (23) (2016) 6795–6801.
- [16] J. Li, E. Schartner, S. Musolino, B.C. Quirk, R.W. Kirk, H. Ebendorff-Heidepriem, R.A. McLaughlin, Miniaturized single-fiber-based needle probe for combined imaging and sensing in deep tissue, *Opt. Lett.* 43 (8) (2018) 1682–1685.
- [17] O. Frazao, J.L. Santos, F.M. Araujo, L.A. Ferreira, Optical sensing with photonic crystal fibers, *Laser & Photonics Rev.* 2 (6) (2008) 449–459.
- [18] E.P. Schartner, G. Tsiminis, A. François, R. Kostecki, S.C. Warren-Smith, L.V. Nguyen, S. Heng, T. Reynolds, E. Klantsataya, K.J. Rowland, Taming the light in microstructured optical fibers for sensing, *Int. J. Appl. Glass Sci.* 6 (3) (2015) 229–239.
- [19] S.C. Warren-Smith, S. Heng, H. Ebendorff-Heidepriem, A.D. Abell, T.M. Monro, Fluorescence-based aluminum ion sensing using a surface-functionalized microstructured optical fiber, *Langmuir* 27 (9) (2011) 5680–5685.
- [20] S. Heng, M.-C. Nguyen, R. Kostecki, T.M. Monro, A.D. Abell, Nanoliter-scale, regenerable ion sensor: sensing with a surface functionalized microstructured optical fiber, *RSC Adv.* 3 (22) (2013) 8308–8317.
- [21] Y. Ruan, T.C. Foo, S. Warren-Smith, P. Hoffmann, R.C. Moore, H. Ebendorff-Heidepriem, T.M. Monro, Antibody immobilization within glass microstructured fibers: a route to sensitive and selective biosensors, *Opt. Express* 16 (22) (2008) 18514–18523.
- [22] J.B. Jensen, P.E. Hoiby, G. Emilianov, O. Bang, L.H. Pedersen, A. Bjarklev, Selective detection of antibodies in microstructured polymer optical fibers, *Opt. Express* 13 (15) (2005) 5883–5889.
- [23] H. Shen, L.J. Tauzin, R. Baiyasi, W. Wang, N. Moringo, B. Shuang, C.F. Landes, Single particle tracking: from theory to biophysical applications, *Chem. Rev.* 117 (11) (2017) 7331–7376.
- [24] S. Faez, Y. Lahini, S. Weidlich, R.F. Garmann, K. Wondraczek, M. Zeisberger, M.A. Schmidt, M. Orrit, V.N. Manoharan, Fast, label-free tracking of single viruses and weakly scattering nanoparticles in a nanofluidic optical fiber, *ACS Nano* 9 (12) (2015) 12349–12357.
- [25] D.S. Bykov, O.A. Schmidt, T.G. Euser, P.S.J. Russell, Flying particle sensors in hollow-core photonic crystal fibre, *Nat. Photonics* 9 (7) (2015) 461–465.
- [26] S.C. Warren-Smith, E. Sinchenko, P.R. Stoddart, T.M. Monro, Distributed fluorescence sensing using exposed core microstructured optical fiber, *IEEE Photonics Technol. Lett.* 22 (18) (2010) 1385–1387.
- [27] S.C. Warren-Smith, S. Afshar, T.M. Monro, Theoretical study of liquid-immersed exposed-core microstructured optical fibers for sensing, *Opt. Express* 16 (12) (2008) 9034–9045.
- [28] S.C. Warren-Smith, R. Kostecki, L.V. Nguyen, T.M. Monro, Fabrication, splicing, Bragg grating writing, and polyelectrolyte functionalization of exposed-core microstructured optical fibers, *Opt. Express* 22 (24) (2014) 29493–29504.
- [29] R. Kostecki, H. Ebendorff-Heidepriem, C. Davis, G. McAdam, S.C. Warren-Smith, T.M. Monro, Silica exposed-core microstructured optical fibers, *Opt. Mater. Express* 2 (11) (2012) 1538–1547.
- [30] M. Pospišilová, G. Kuncová, J. Trögl, Fiber-optic chemical sensors and fiber-optic bio-sensors sensors, *Sensors (Basel)* 15 (10) (2015) 25208–25259.
- [31] K. Zhou, X. Chen, L. Zhang, I. Bennion, High-sensitivity optical chemsensor based on etched d-fibre Bragg gratings, *Electron. Lett.* 40 (4) (2004) 232–234.
- [32] G. Stewart, W. Jin, B. Culshaw, Prospects for fibre-optic evanescent-field gas sensors using absorption in the near-infrared, *Sens. Actuator B-Chem.* 38 (1–3) (1997) 42–47.
- [33] X.G. Li, L.V. Nguyen, Y. Zhao, H. Ebendorff-Heidepriem, S.C. Warren-Smith, High-sensitivity Sagnac-interferometer biosensor based on exposed core microstructured optical fiber, *Sens. Actuator B-Chem.* 269 (2018) 103–109.
- [34] J.M. Schmitt, Optical coherence tomography (OCT): a review, *IEEE J. Sel. Top. Quantum Electron.* 5 (4) (1999) 1205–1215.
- [35] M. Wojtkowski, R. Leitgeb, A. Kowalczyk, T. Bajraszewski, A.F. Fercher, In vivo human retinal imaging by Fourier domain optical coherence tomography, *J. Biomed. Opt.* 7 (3) (2002) 457–464.
- [36] M. Choma, M. Sarunic, C. Yang, J. Izatt, Sensitivity advantage of swept source and Fourier domain optical coherence tomography, *Opt. Express* 11 (18) (2003) 2183–2189.

### Biographies

**Lu Peng** achieved her M.S. from South China Normal University, China, in 2017. She is awarded an Adelaide University China Fee Scholarships (AUCFS) and is studying as a PhD student in the University of Adelaide since 2017. Her research interests are fiber interferometry sensors, plasmonic sensors for biochemical applications, and design of nanoscale photonic devices.

**Jiawen Li** received her PhD degree in Biomedical Engineering from University of California Irvine in 2015 on developing multimodal optical-ultrasonic probes. She joined the University of Adelaide in 2016. She is currently supported by Australian National Heart Foundation to develop miniaturized multimodal fiber probes by two-photon polymerization 3D printing technology. Her research interests include optical coherence tomography, intravascular imaging, multimodality imaging, and ultra-thin endoscopes.

**Robert A. McLaughlin** received his PhD in Electronic Engineering from The University of Western Australia in 2000. After three years as a postdoctoral researcher at The University of Oxford, UK, he spent several years in commercial positions in the medical device industry. He is currently a professor at the University of Adelaide and Chair of Biophotonics. His research focuses on the development of miniaturized optical imaging devices for medical applications, and novel image processing algorithms.

**Heike Ebendorff-Heidepriem** obtained her PhD in chemistry from the University of Jena, Germany in 1994 and subsequently held two prestigious fellowships. From 2001–2004 she was with the Optoelectronics Research Centre at the University of Southampton, UK. Heike came to the University of Adelaide in 2005. She was awarded the Woldemar A. Weyl International Glass Science Award in 2001, the International Zwick Science Award in 2009 and the University of Adelaide Women's Research Excellence Mid-Career Award in 2014. Heike has published over 230 refereed journal papers and conference proceedings, including 5 review papers and 9 post-deadline papers, and raised approximately \$12 M for research. Heike's research focuses on the development of novel optical glasses, fibers, surface functionalization and sensing approaches.

**Stephen C. Warren-Smith** completed his PhD in 2011 at the University of Adelaide, Australia, on the topic of microstructured optical fiber chemical sensing. He was then employed from 2011 to 2014 as an Australian Research Council (ARC) Super Science Fellow at the Institute for Photonics and Advanced Sensing and the School of Chemistry and Physics at the University of Adelaide, working on optical fiber biosensing for women's health applications. In 2015 and 2016 he worked as a European Union Marie Curie International Incoming Fellow at the Leibniz Institute of Photonic Technology, Jena, Germany, on a project investigating the micro/nanostructuring of optical fibers for sensing. Since October 2016 he is with the University of Adelaide as a Ramsay Fellow.

## 4.2 Two-dimensional mapping of surface scatterers

The one-dimensional (1D) distributed sensing concept based on the OFDR mechanism was demonstrated in Sec. 4.1. However, the 1D sensing in the integrated sensing configuration is limited to only detect particles nearby the core centre, while particles away from the core centre are difficult to be detected. This is due to the fundamental mode launching, where the evanescent field from the core towards the edge is a Gaussian distribution and limits the transverse detection range.

This section expands the sensing ability to another dimension: transverse direction. The micro-scaled particles' information is mapped in 2D based on mode-multiplexed OFDR signal analysis as illustrated in the Fig. 4.1.

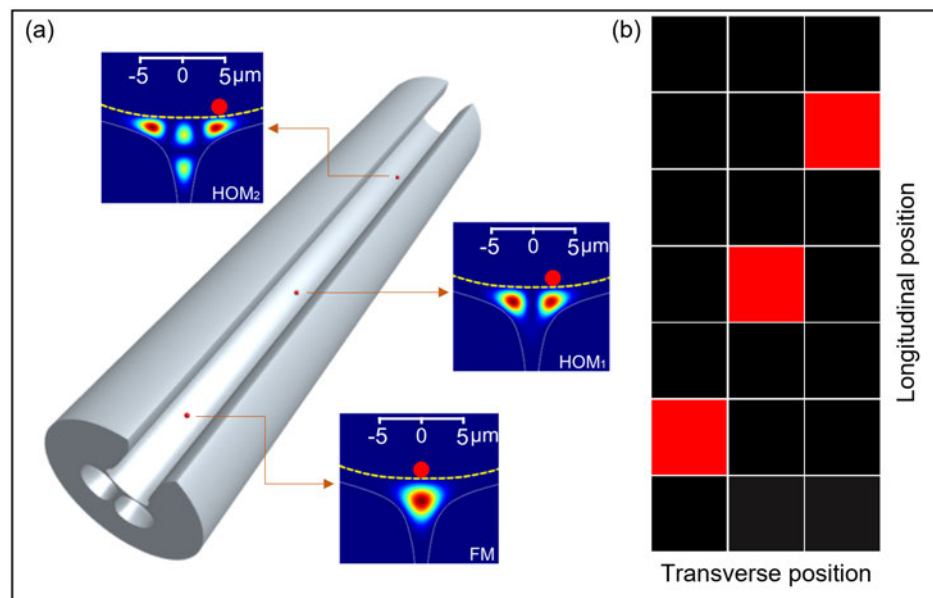


**Fig. 4.1** (a). A schematic diagram of the proposed 2D imaging, where red dots with same size located on the fibre are detected based on the OFDR technique. The signals combined with a matrix approach reveal the particle's 2D distributions as illustrated in the red pixels of (b).

### 4.2.1 Publication overview

This work [P2] aims to advance the sensing capability into two dimensions, while Sec. 4.1[P1] has only demonstrated 1D detection of micro-scaled particles. The fibre sample was fabricated using a femto-second (fs) laser inscribing technique. By using the few-mode property of the ECF, the second dimension could be obtained by



---

inscribing surface scatterers made by the fs-laser based on the proposed OFDR technique. The experimental measurements are in good agreement with the theoretical hypothesis. This publication is a proof-of-concept demonstration of 2D mapping of surface scatterers by using a single ECF, avoiding the deployment of bulky and complicated configurations.

#### **4.2.2 Statement of contribution**

## Statement of Authorship

Title of Paper	Two-dimensional mapping of surface scatterers on an optical fiber core using selective mode launching
Publication Status	<input checked="" type="checkbox"/> Published <input type="checkbox"/> Accepted for Publication <input type="checkbox"/> Submitted for Publication <input type="checkbox"/> Unpublished and Unsubmitted work written in manuscript style
Publication Details	Lu Peng, Linh Viet Nguyen, Jiawen Li, Nicolas Riesen, Dale Otten, David G. Lancaster, Heike Ebendorff-Heidepriem and Stephen C. Warren-Smith, (2021), Two-dimensional mapping of surface scatterers on an optical fiber core using selective mode launching. APL Photonics, 6(2), 026105.

### Principal Author

Name of Principal Author (Candidate)	Lu Peng
Contribution to the Paper	The idea was mainly conceptualised by Lu Peng. All the experiments, analysis, and paper writing were majorly done by Lu Peng.
Overall percentage (%)	70%
Certification:	This paper reports on original research Lu Peng conducted during the period of her Higher Degree by Research candidature and is not subject to any obligations or contractual agreements with a third party that would constrain its inclusion in this thesis. Lu Peng is the primary author of this paper.
Signature	<div style="display: flex; justify-content: space-between; align-items: center;"> <div style="border-bottom: 1px solid black; width: 80%;"></div> <div style="border: 1px solid black; padding: 2px;">Date</div> <div style="border: 1px solid black; padding: 2px;">09-08-2021</div> </div>

### Co-Author Contributions

By signing the Statement of Authorship, each author certifies that:

- i. the candidate's stated contribution to the publication is accurate (as detailed above);
- ii. permission is granted for the candidate to include the publication in the thesis; and
- iii. the sum of all co-author contributions is equal to 100% less the candidate's stated contribution.

Name of Co-Author	Linh Viet Nguyen
Contribution to the Paper	Linh Viet Nguyen fabricated the fibre samples by inscribing the femto-second ablations on the fibre. He contributed to general discussions and revised the manuscript.
Signature	<div style="display: flex; justify-content: space-between; align-items: center;"> <div style="border-bottom: 1px solid black; width: 80%;"></div> <div style="border: 1px solid black; padding: 2px;">Date</div> <div style="border: 1px solid black; padding: 2px;">09-08-2021</div> </div>

Name of Co-Author	Jiawen Li
Contribution to the Paper	Jiawen Li contributed to general discussions for drafting the manuscript and revising the manuscript.
Signature	<div style="display: flex; justify-content: space-between; align-items: center;"> <div style="border-bottom: 1px solid black; width: 80%;"></div> <div style="border: 1px solid black; padding: 2px;">Date</div> <div style="border: 1px solid black; padding: 2px;">09-08-2021</div> </div>

Name of Co-Author	Nicolas Riesen
Contribution to the Paper	Nicolas Riesen assisted with the fabrication of the fibre samples and revised the manuscript.
Signature	<hr/>
Date	09-08-2021

Name of Co-Author	Dale Otten
Contribution to the Paper	Dale Otten assisted with the fabrication of the fibre samples and revised the manuscript.
Signature	<hr/>
Date	09 Aug 2021

Name of Co-Author	David G. Lancaster
Contribution to the Paper	David G. Lancaster provided the lab facilities and helped revise the manuscript.
Signature	<hr/>
Date	17 Aug 2021

Name of Co-Author	Heike Ebendorff-Heidepriem
Contribution to the Paper	Heike Ebendorff-Heidepriem contributed to general discussions and helped revise the manuscript.
Signature	<hr/>
Date	9 Aug 2021

Name of Co-Author	Stephen C. Warren-Smith
Contribution to the Paper	Stephen C. Warren-Smith organised the sample fabrication and contributed to building the theoretical work. He helped structure and edit the manuscript.
Signature	<hr/>
Date	09-08-2021

## Two-dimensional mapping of surface scatterers on an optical fiber core using selective mode launching

Cite as: APL Photonics 6, 026105 (2021); <https://doi.org/10.1063/5.0036300>

Submitted: 03 November 2020 . Accepted: 27 January 2021 . Published Online: 12 February 2021

 Lu Peng,  Linh Viet Nguyen,  Jiawen Li,  Nicolas Riesen,  Dale Otten,  David G. Lancaster,  Heike Ebendorff-Heidepriem, and  Stephen C. Warren-Smith



View Online



Export Citation



CrossMark

APL Photonics

SPECIAL TOPIC: Coronavirus and Photonics


Submit Today!

AIP  
Publishing

# Two-dimensional mapping of surface scatterers on an optical fiber core using selective mode launching

Cite as: APL Photon. 6, 026105 (2021); doi: 10.1063/5.0036300  
Submitted: 3 November 2020 • Accepted: 27 January 2021 •  
Published Online: 12 February 2021



Lu Peng,<sup>1,2,3,a)</sup>  Linh Viet Nguyen,<sup>1,2,4</sup>  Jiawen Li,<sup>2,3,5</sup>  Nicolas Riesen,<sup>1,2,4</sup>  Dale Otten,<sup>4</sup>   
David G. Lancaster,<sup>4</sup>  Heike Ebendorff-Heidepriem,<sup>1,2,3</sup>  and Stephen C. Warren-Smith<sup>1,2,3,4</sup> 

## AFFILIATIONS

<sup>1</sup>School of Physical Sciences, The University of Adelaide, Adelaide SA 5005, Australia

<sup>2</sup>Institute for Photonics and Advanced Sensing, The University of Adelaide, Adelaide SA 5005, Australia

<sup>3</sup>Australian Research Council Centre of Excellence for Nanoscale Biophotonics, Adelaide SA 5005, Australia

<sup>4</sup>Future Industries Institute, University of South Australia, Mawson Lakes SA 5095, Australia

<sup>5</sup>Adelaide Medical School, The University of Adelaide, Adelaide SA 5005, Australia

<sup>a)</sup>Author to whom correspondence should be addressed: [lu.peng@adelaide.edu.au](mailto:lu.peng@adelaide.edu.au)

## ABSTRACT

The tracking of small particles is an important but challenging task for biological applications such as disease diagnostics and medical research. Current methods are limited to the use of bulky instruments such as flow cytometers and microscopes. Here, a novel technique for the detection and measurement of micron-scale optical scatterers using a few-mode exposed-core microstructured optical fiber is proposed. Through selective mode launching combined with optical frequency domain reflectometry, scatterers located on the fiber core surface can be simultaneously mapped with both longitudinal and transverse information. This technique is demonstrated by detecting the two-dimensional positions of several femtosecond-laser-inscribed micron-scale ablations written at different locations on the fiber core surface. Due to the compact nature of the optical fiber and its local sensitivity to scatterers that are in close proximity to it, this technique has the potential for the measurement and detection of micron-scale particles in difficult to reach biological environments for *in vivo* applications.

© 2021 Author(s). All article content, except where otherwise noted, is licensed under a Creative Commons Attribution (CC BY) license (<http://creativecommons.org/licenses/by/4.0/>). <https://doi.org/10.1063/5.0036300>

## I. INTRODUCTION

Significant effort has been invested in manipulating and measuring small particles with light in order to enrich our knowledge of the dynamics and interactions of the microscale world.<sup>1-5</sup> The use of optical fibers for this purpose is gaining interest due to their small size and flexibility, allowing them to reach into difficult-to-access regions, such as deep inside the body. For example, advanced techniques for particle tracking include the use of optical fiber probes with microlenses to trap and manipulate targeted cells<sup>6</sup> and holographic manipulation of particles via a multimode fiber.<sup>7</sup> The manipulation of particles can also allow them to be exploited for sensing, exemplified by the demonstration of controlled propagation

of micron-scale particles inside hollow core fibers for high spatial resolution temperature and electric field sensing.<sup>8,9</sup>

Sensing and tracking small targets is motivated by a desire to understand their presence, size, dynamics, and interactions within microscale and even nanoscale biological environments, with an aim toward disease diagnostics, medical research, and drug delivery.<sup>4,5,10</sup> Optical fiber based approaches include the detection of nanoparticles using a tapered nanofiber pair,<sup>11</sup> the use of an exposed-core microstructured optical fiber (ECF) coupled with a dark-field heterodyne measurement technique,<sup>12</sup> and evanescent field based fluorescence detection of upconversion nanocrystals in microstructured optical fibers.<sup>13</sup> Fiber-based schemes with the ability to detect spatial information of micro-/nano-objects have also been reported, such as

the use of a nanofluidic fiber for single virus detection,<sup>14</sup> a similar nanofluidic fiber sensor for three-dimensional detection of nano-objects,<sup>15</sup> and a hollow core fiber to study the Brownian motion of nano-objects.<sup>16</sup> Although these methods are able to image nanoscale particles, they rely on bulky external optics that increase the system complexity and prevent their implementation as an *in vivo* device.

Parallel efforts for fiber-based *in vivo* sensing probes have been reported including the integration of simultaneous temperature sensing and optical coherence tomography<sup>17</sup> and pH measurements for surgical assistance.<sup>18</sup> However, these fiber tip-based probes are single-point sensors that must move over a region to collect spatial information, potentially leading to additional mechanical damage of delicate biological tissues. We recently reported a silk-coated *in vivo* ECF-based sensor, which collects information along the entire fiber length but was still limited as an averaged fluorescence measurement without the capability of providing spatial information.<sup>19</sup> There is a need for advancing these techniques to obtain spatial information within confined and challenging biological systems.

To achieve a portable fiber-based device with a long detection range and micron-scale resolution, we seek to apply a technique known as optical frequency domain reflectometry (OFDR),<sup>20</sup> which allows for distributed sensing along an optical fiber with high spatial resolution. Our ECF has an exposed channel enabling direct evanescent field contact with the ambient environment without the need for post-processing procedures, enabling repeatable and robust sensing measurements. We recently demonstrated that micron-scale particles could be detected along an ECF using OFDR.<sup>21</sup> This method could detect the presence and longitudinal position of scattering particles, but not their size or transverse position. In this paper, we propose and experimentally demonstrate a novel approach that adds transverse information to this

method through the selective launching of several modes in a few-mode ECF. Using the numerically simulated evanescent field profiles of the optical modes, we add the ability to detect a scatterer's transverse position using a matrix approach, thus demonstrating two-dimensional (2D) sensing. We anticipate this technique could be deployed for micron-scale particle detection based on a single fiber path for disease diagnostics and drug delivery in clinical applications.

## II. CONCEPT

We demonstrate our technique using an in-house fabricated ECF as shown in Fig. 1(a), with the yellow dashed core region magnified in Fig. 1(b). Our ECF has a core diameter of  $7.5\ \mu\text{m}$  and a mode field diameter of  $5.18\ \mu\text{m}$  for the horizontally polarized fundamental mode (FM) (i.e., polarized parallel to the exposed surface) at a wavelength of  $1550\ \text{nm}$ . The fabrication of this ECF has been described previously.<sup>22</sup> To achieve 2D distributed sensing, the few-mode nature of the ECF plays a key role. As illustrated in Fig. 1(c), scatterers (shown as red dots) located at different transverse positions across the ECF core surface interact with different modes, such as those displayed in Figs. 1(d)–1(f), with different strengths due to their varying spatial distribution of energy across the core surface. For example, Fig. 1(d) shows the Poynting vector distribution of the fundamental mode (FM), which can interact most strongly with a scatterer located at the core center. Compare this to the higher-order modes in Figs. 1(e) and 1(f) labeled  $\text{HOM}_1$  and  $\text{HOM}_2$ , which can interact relatively more strongly with scatterers at different offset positions away from the center. Figure 1(g) shows the time averaged z-component (propagating component) of the Poynting vector for the three modes considered along the exposed boundary of the ECF [dashed yellow line in Figs. 1(d)–1(f)] and the

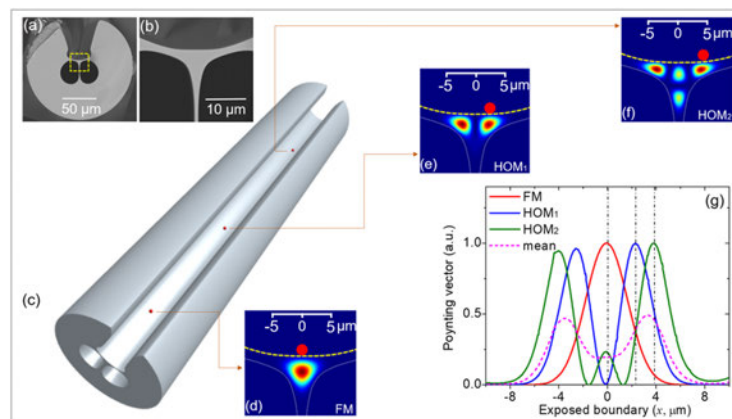


**FIG. 1.** (a) Scanning electron microscope (SEM) image of the ECF. (b) Core region of the ECF corresponding to the yellow dashed box in (a). (c) Illustration of the ECF with scatterers (red points) located at different longitudinal and transverse positions along the exposed channel. These scatterers can interact with different propagating transverse optical modes as shown in (d)–(f), depending on their transverse offset from the center. (g) Calculated Poynting vector distributions (normalized to 1) of several selected modes on the exposed boundary [yellow dashed line in (d)–(f)], while the magenta dashed curve shows the mean of three modes. Dashed dark lines correspond to scatterers (d)–(f) at different transverse positions. All simulations (d)–(g) are based on the finite element method (COMSOL) using a free space wavelength of  $1550\ \text{nm}$ .

mean of the three modes (dashed magenta curve) using the following expression:<sup>23</sup>

$$P_m(x) = \frac{1}{2} |a_m|^2 \operatorname{Re} \left\{ \hat{\mathbf{e}}_m(x) \times \hat{\mathbf{h}}_m(x) \cdot \hat{\mathbf{z}} \right\}, \quad (1)$$

where  $a_m$  is the modal coefficient for the  $m$ th mode (FM, HOM<sub>1</sub>, and HOM<sub>2</sub>),  $\hat{\mathbf{e}}_m$  and  $\hat{\mathbf{h}}_m$  are the orthonormal electric and magnetic fields for each mode, respectively, and  $x$  represents the distance along the ECF exposed boundary (as opposed to a Cartesian coordinate), with  $x = 0$  at the center of the core. In Fig. 1(g), the modal amplitudes have been adjusted such that the plot is normalized to unity to clearly see the variation in energy distribution at the exposed-core surface for the three modes considered. Note that in this work, including the above simulated modes and the following experiments, we consider only the horizontally polarized modes as they generally have greater field intensity at the surface compared to vertically polarized modes. The black dashed lines in Fig. 1(g) indicate scatterers at different transverse positions crossing the ECF boundary corresponding to Figs. 1(d)–1(f), respectively, showing how the different modes interact with scatterers at different transverse positions.

We now describe how multiple launched optical modes can be used to determine quantitative transverse spatial information about the size and position of scatterers. We assume that the returned scattered signal is first longitudinally resolved using OFDR and our task is now to resolve the transverse position using the scatterer from multiple modes. We assume that the returned signal intensity from each scatterer is proportional to the evanescent field of the particular excited optical mode and its overlap with the scatterer at the surface. This neglects the evanescently coupled distribution of backscatter into the counter-propagating modes of the fiber but allows us to consider the system using a linear matrix approach. We then spatially divide the transverse location across the core into discrete regions that equal the number of modes. For example, if we launch three optical modes, then the transverse region can be resolved into three separate regions. In the general case of  $N$  modes, we can resolve into  $N$  regions and write the total scattered light for each mode using the following expression:

$$I_m = u_1 \int_{R_1} P_m(x) dx + u_2 \int_{R_2} P_m(x) dx + \dots + u_N \int_{R_N} P_m(x) dx, \quad (2)$$

where  $I_m$  is the returned signal from the OFDR measurement for a given longitudinal position for the  $m$ th launched optical mode and  $u_i$  is a scattering factor that represents the degree of returned scatter signal from the  $i$ th transverse region  $R_i$ . This can be expressed as the following matrix equation:

$$\bar{I} = M\bar{u}, \quad (3)$$

where  $\mathbf{I} = (I_1, I_2, \dots, I_N)$ ,  $\mathbf{u} = (u_1, u_2, \dots, u_N)$ , and  $M$  is an  $N \times N$  matrix given by

$$M = \begin{bmatrix} \int_{R_1} P_1 & \int_{R_2} P_1 & \dots & \int_{R_N} P_1 \\ \int_{R_1} P_2 & \dots & \dots & \vdots \\ \vdots & & & \\ \int_{R_1} P_N & \dots & \dots & \int_{R_N} P_N \end{bmatrix}. \quad (4)$$

We can then solve for the unknown scatter vector  $\mathbf{u}$  through a matrix inversion,

$$\bar{\mathbf{u}} = M^{-1}\bar{I}. \quad (5)$$

In order to implement this approach in practice, the matrix  $M$  is calculated using the numerically simulated Poynting vector distributions as shown in Fig. 1(g) where the regions can be arbitrarily defined but should approximately match the spatial extent of the launched modes. The vector  $\mathbf{I}$  is the experimentally measured values from the OFDR signal. In the following experimental results, we demonstrate the application of this method for the three modes shown in Fig. 1 to yield both longitudinal and transverse spatial locations of surface scatterers. We note, however, that the same technique could be applied to any number of supported optical modes, provided they can be discretely launched, and for any location of scatterers including inside the waveguide and not only on the surface.

### III. RESULTS AND DISCUSSION

#### A. Inscription of surface scatterers and experimental setup

Scatterers were introduced to the ECF surface using a femtosecond (fs) laser writing technique, which produces permanent silica-air ablation points. A wavelength doubled (524 nm), ultra-fast laser (IMRA DE0210) was used with pulse duration  $<250$  fs and pulse energy of 150 nJ. The ECF was imaged using the same lens as used for the fs laser writing to locate the optical fiber core, similar to a method previously used for fiber Bragg grating inscription.<sup>24</sup> Seven points were written in total, as indicated by the red spots with numbers from 1 to 7 in Fig. 2(a), which have a longitudinal spacing of 500  $\mu\text{m}$  between each point and a transverse spacing of 1  $\mu\text{m}$ . The ablation point number 4 was written with a transverse position as close to the center of the optical fiber core as possible, within experimental error. The ECF sample viewed under a camera with visible (red) laser light coupled into the core to show the scatterer locations is shown in Fig. 2(b). The left-hand side red dot in Fig. 2(b) corresponds to the input end of the ECF, while the furthest right-hand side red dot in the dashed yellow box is the seventh ablation point.

The OFDR signal was generated by a swept wavelength (1510 nm–1590 nm) optical sensor interrogator (National Instruments PXIe-4844), which integrates a source (60  $\mu\text{W}$ ) and photodetector with a dynamic range of 40 dB and the sampling rate of 10 Hz. The OFDR signal was then generated by optical interference between the reflection from the cleaved end-face of the ECF due to the air-silica interface [black arrow in Fig. 2(a)] and the reflected light from each introduced fs-laser ablation scattering point (red arrows). The interference from each point can then be demultiplexed by applying a fast Fourier transform (FFT) to convert the interference spectrum into longitudinal spatial information with a resolution of  $\sim 10$   $\mu\text{m}$  as described previously.<sup>21</sup>

The mode launching was controlled by manually adjusting a three-axis optical stage to adjust the axial and transverse positions. The launched mode(s) was monitored using an infrared camera, and the stage was adjusted until one of the three desired modes supported by the ECF was predominantly launched.

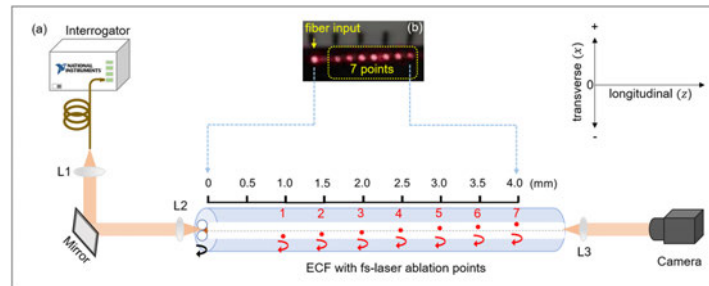


**FIG. 2.** (a) Schematic of the experimental setup. The black arrow represents reflection at a cleaved surface where  $\sim 3.3\%$  of the incident light is reflected back due to the air-silica interface, which is used as the reference to generate the interferometric signal. L1, L2, and L3 are optical lenses. The red points represent fs laser ablation points (numbered from 1 to 7) on the surface of the ECF, and the red arrows depict their scattered signals captured back into the ECF's guided modes to generate interference with the reference signal. The black scale bar above the ECF shows the axial distributions of the introduced points, with each point separated by  $500\ \mu\text{m}$  in the axial direction. The coordinate system is illustrated, where the transverse direction,  $x$ , is shown with positive and negative signs from the center of the ECF. The mode launching was monitored at the far end of the ECF using an InGaAs camera. The fiber sample was  $\sim 200\ \text{mm}$  in length, and both ends were fixed on three-axis optical stages during the experiments. (b) Image of the fs-laser inscribed fiber sample showing the scattering of red laser light coupled to the ECF core. The ruler image has a  $1\ \text{mm}$  scale.

## B. OFDR results

Figures 3(a1)–3(c1) show the near field images of the three separately launched modes, which correspond well with the three simulated modes shown in Figs. 3(a2)–3(c2). OFDR traces were then acquired separately for each launched mode, by applying an FFT to the reflected interference spectra. The signal from the seven ablation points can clearly be seen as seven peaks in Figs. 3(a3)–3(c3). Each

peak represents the interference generated between reflection from an ablation point and the cleaved end-face of the ECF, and their longitudinal positions distributed along the ECF are shown on the lower  $x$ -axis. As expected from Fig. 2, there is  $0.5\ \text{mm}$  spacing between each ablation point, and the points lie within  $1\ \text{mm}$ – $4\ \text{mm}$  of the input cleaved end-face of the ECF. We note that there is a small peak at the lower  $x$ -axis position of  $0.5\ \text{mm}$  in all measured FFT

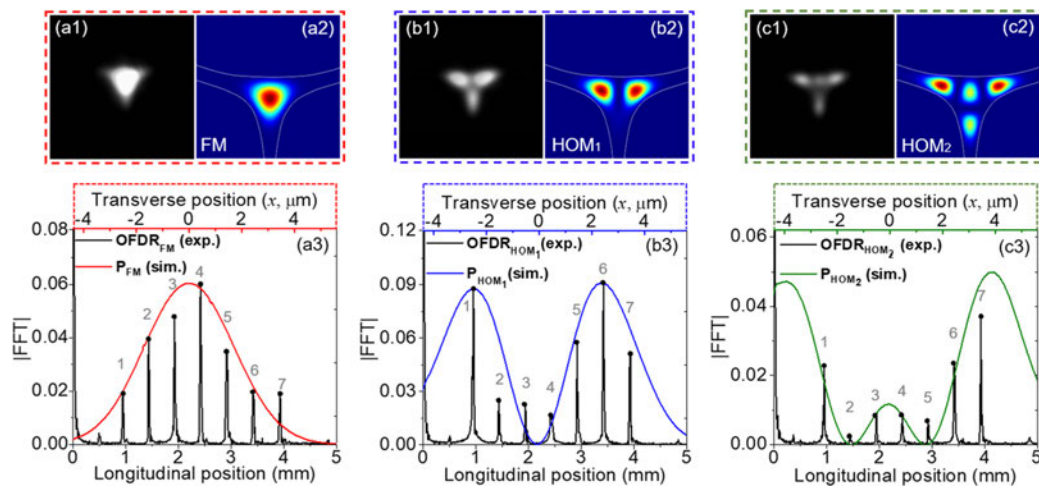


**FIG. 3.** Experimental measurements under different launch conditions to demonstrate the 2D sensing concept. Real-time near-field mode images are displayed in (a1)–(c1) with their corresponding simulated mode profiles, named as “FM,” “HOM<sub>1</sub>,” and “HOM<sub>2</sub>,” shown in (a2)–(c2), respectively. (a3)–(c3) The absolute FFT signals (black) are shown with labels “OFDR<sub>FM</sub> (exp.),” “OFDR<sub>HOM1</sub> (exp.),” and “OFDR<sub>HOM2</sub> (exp.),” the bottom axis displays the longitudinal/axial positions of the ablation points (peaks named with numbers “1–7”) on the ECF [see Fig. 2(a)]. The colored curves show the simulated Poynting vector distributions at the ECF surface [red, blue, and green in (a3)–(c3), respectively], which were scaled to best match the height of the FFT peaks (marked as black dots). The top colored axis (secondary  $x$ -axis) displays the transverse positions of the ablation points based on the matching process detailed in Sec. III B.



results in Fig. 3. This peak is potentially from the optical interference associated with the regularly longitudinal-spaced ablation points. However, this peak is relatively small compared to the dominant signals, which demonstrates that the scattered light recoupled to the fiber modes is relatively weak compared to the reference signal (from the fiber input end). This is as would be expected for evanescent field recoupling, such as <1% previously calculated for fluorescence-based recoupling.<sup>25,26</sup> Therefore, undesired multiple scattering from adjacent ablation points is negligible in our demonstration.

Next, we demonstrate visually the validity of our assumption that the returned OFDR signal correlates proportionately with the mode's evanescent field at the surface. We use our prior knowledge of the uniform spacing between the ablation points (1.0  $\mu\text{m}$  spacing) to correlate the OFDR signals with the transverse distance across the ECF surface. This allows us to add the upper  $x$ -axis scale in Figs. 3(a3)–3(c3), noting that this is only valid for the OFDR peaks relating to the ablation points as their positions are known and do not apply to, say, other unintended environmental particles (i.e., dust) along the optical fiber. We are then able to overlay the Poynting vector at the ECF surface as shown by the colored curves in Figs. 3(a3)–3(c3) for the three modes, respectively.

The transverse offset of the OFDR data relative to Poynting vector center  $x = 0$  (ECF core center) has been adjusted to account for systematic error associated with the positioning of the ablation points across the core, while the height of the simulated Poynting vector curves has been adjusted to best match the FFT peaks to account for errors in the coupling efficiency for the three modes. This was performed by minimizing the following expression:

$$\Delta P_m(x') = \frac{1}{7} \sum_{k=1}^7 |a_m P_{mk}(x) - I_{mk}(x - x')|, \quad (6)$$

where  $P_{mk}$  and  $I_{mk}$  are the simulated Poynting vector and measured OFDR peak for the  $m$ th mode and  $k$ th peak, respectively,  $x'$  is the transverse offset between the laser writing points and the simulated Poynting vector distributions across the ECF core,  $k$  is the scatterer number (1 to 7), and  $a_m$  is the vertical scaling of the simulation relative to the OFDR signal.

The transverse offset comes from positioning error in the fs-laser ablation process. While there is a high degree of precision in the relative transverse positions of the ablation points, we expect a systematic error common to all seven points due to the difficulty in visually locating the center of the optical fiber core. By applying Eq. (6) for an arbitrary offset  $x'$ , as shown in Fig. 4, we can find the minima position and correct the actual laser writing locations relative to the core center. Figure 4 shows that the simulation and experiment match most closely for a value of  $x' = 0.4 \mu\text{m}$ , which is within expectations, giving the optical resolution of the imaging system used for identifying the core center during the fs laser writing.

To match the vertical scaling of the Poynting vector simulations for each mode,  $a_m$ , with the OFDR peaks, Eq. (6) was again minimized. We first applied the previously determined offset value of  $x' = 0.4 \mu\text{m}$  and then evaluated the deviation of each simulated mode with the measured results as a function of  $a_m$  (see Fig. S1 in the supplementary material). The minima locations were then determined for each mode, yielding the simulation curves shown in Fig. 3.

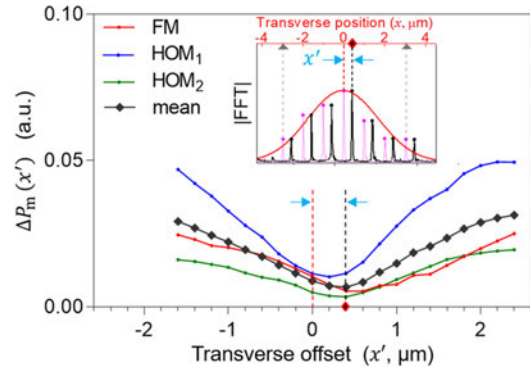


FIG. 4. Determining the transverse offset between the simulated Poynting vector distribution and the OFDR signal averaged for the seven fs-laser ablation points for the three individually launched modes as described by Eq. (6). The mean across the three modes is shown by the black curve, which yields an offset of  $x' = 0.4 \mu\text{m}$  as shown by the dashed lines. Inset shows the corresponding shift in the OFDR trace for the fundamental mode.

Note that, in the future, the vertical scaling could equally be achieved through intentional reference points along the ECF, similar to what has been done here, or by accounting for the total coupled power for each mode such as by measuring the ECF output with an optical power meter.

We can see from Fig. 3 that the distribution of the OFDR peaks matches closely with the Poynting vector distributions on the surface, indicating that the linear matrix approach outlined in Sec. II can, indeed, be applied to determine the transverse information about the surface scatterers.

### C. Determining scatterer location

We now apply the matrix method in Eq. (5) to determine the transverse location of the scatterers without using the prior knowledge of their location from the laser writing process. Due to the symmetric shape of the Poynting vector distributions shown in Fig. 1(g), we split the transverse regions of the ECF exposed surface by three absolute distances from the center of the core. That is, the integration regions in Eq. (4) are grouped into (i)  $0 \mu\text{m} - 1 \mu\text{m}$ , (ii)  $1 \mu\text{m} - 2 \mu\text{m}$ , and (iii)  $>2 \mu\text{m}$  from the core center. Integrating the three simulated modes with corrected vertically scaling as discussed in Sec. III B over the three regions yields the following  $3 \times 3$  (3 modes  $\times$  3 regions) transfer matrix:

$$M = \begin{bmatrix} 0.112 & 0.079 & 0.039 \\ 0.026 & 0.120 & 0.161 \\ 0.016 & 0.003 & 0.038 \end{bmatrix}. \quad (7)$$

Solving Eq. (5) using the matrix in Eq. (7) and the OFDR data ( $I$ ) yields the results shown in Fig. 5.

The red pixels in Fig. 5(a) show the known locations of the seven fs laser inscribed scatterers according to the positions chosen during the fs laser inscription process, which correspond to the locations presented in Figs. 3(a3)–3(c3). The calculated results in Fig. 5(b) show a strong correlation with the known locations, where

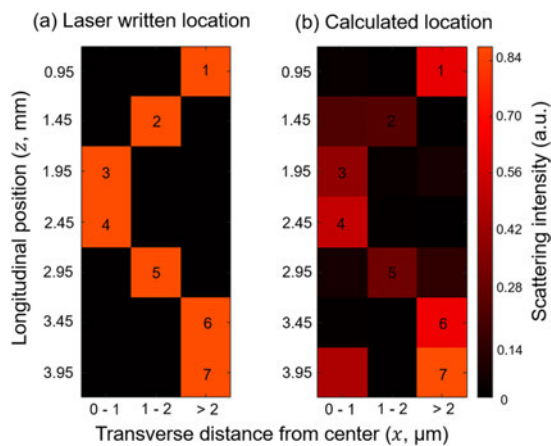


**FIG. 5.** (a) Fs-laser writing locations grouped into three transverse regions from the center of the ECF core. The numbers 1 to 7 indicate the laser ablation points corresponding to their intended location, factoring the  $x' = 0.4 \mu\text{m}$  offset as determined through the results in Fig. 4(b). Measured location of the scatterers using the proposed matrix approach. The y-axis shows the longitudinal position of the scatterers as determined from the OFDR trace.

the pixel with the lightest color in each row represents the most probable area associated with a specific scatterer.

The results in Fig. 5(b) show a strong correlation with Fig. 5(a) but with some variation in intensity and some signal in locations that should show no scattering. We believe the major causes of these discrepancies are as follows. First, the exposed surface is not as flat as other regular quadrate structures, leading to minor inconsistencies in the focus depth for each ablation point when they were written at different locations across the core. This fabrication error may cause differences both in ablation depth and size. A deeper focus, in principle, leads to stronger interaction with the optical field and thus causes greater scatter relative to other surface-only defects. It is also likely that the modes were not launched with 100% efficiency, that is, a small fraction of other modes may have been coupled, which would impact the results particularly where the expected field energy is low. For example, the excitation of the mode  $\text{HOM}_1$  in Fig. 3(b1) shows a faint third lobe when only two are expected from the numerical simulation. This could be solved in the future by using advanced coupling techniques such as the use of a spatial light modulator for mode launching,<sup>27,28</sup> femtosecond-laser-written mode couplers,<sup>29</sup> and photonic lanterns.<sup>30</sup>

#### D. Discussion

We have demonstrated 2D mapping of single point-like scatterers in the form of surface ablation points. In this work, the fs-laser ablation points are strong scatterers due to the glass-air interface and their position embedded into the core surface and thus would be more strongly scattering than particles located on the core surface. For comparison, we have previously shown that the same configuration can detect much larger scatterers through the evanescent

field, where we detected  $10 \mu\text{m}$  polystyrene beads on the fiber surface.<sup>21</sup> The simulated optical field (see Fig. S2 in the [supplementary material](#)) indicates that the Poynting vector distribution of the fundamental mode (FM) on the exposed surface is 20% of that at a depth beneath the surface of 300 nm (300 nm is an estimation of the average ablation depth beneath the surface<sup>24</sup>). Therefore, we expect this same technique would be also applicable to surface scatterers through an evanescent field interaction with a trade-off in sensitivity. This could be improved by using an optical detection system of greater dynamic range compared to the 40 dB used in our demonstration. On the other hand, large particles would backscatter with stronger signals and interact more strongly with modes of greater transverse spatial extent. Large particles would thus show signals for more pixels after the matrix method is applied, in addition to a greater extent in the axial OFDR trace.

For this to be effective, the transverse spatial resolution should be improved beyond the currently demonstrated three regions. To improve the transverse resolution, more modes must be launched, which again could be solved using a spatial light modulator, and it would further improve the accuracy of the transfer matrix with more subdivided integration regions with less variation of energy across each region. It is important to note, though, that it is essential that the mode launching is performed, with only individual modes excited, to avoid deleterious inter-modal interference effects. It is also important to avoid mode coupling along the optical fiber length. The ECF used in our work is a high numerical aperture and birefringent fiber (see Table S1 in the [supplementary material](#)), which allows the selected launched modes, including the polarization, to be maintained even under moderate bending (see bending results in Figs. S3 and S4 in the [supplementary material](#)). Mode coupling is dependent on the specific fiber properties and thus needs to be considered before applying our proposed technique.

Another important factor that should be considered is that the three modes launched in this work display highly symmetric properties across the ECF core surface. This is to be expected for an optical fiber with a reflection plane of symmetry, where the Poynting vector distribution follows this symmetry. To obtain information on transverse scatterers where more than one region is involved and obtain an unambiguous result (discriminate positive/negative transverse location), it would be necessary to utilize modes with asymmetric Poynting vector distributions. Due to slight imperfections in the fiber fabrication, the ECF used in our work shows a subtle asymmetry, which leads to asymmetric higher-order modes (see Fig. S5 in the [supplementary material](#)) that could be exploited for this purpose. This would, again, require the use of more complex mode launching techniques or by fabricating an intentionally asymmetric fiber structure to break the symmetry of the supported modes.

#### IV. CONCLUSION

We have demonstrated a technique for detecting the longitudinal and transverse location of micron-scaled scatterers along an optical fiber using a combination of optical frequency domain reflectometry and selective excitation of transverse guided modes. We have demonstrated this technique using femtosecond laser inscribed ablation points as model scatterers and then comparing the optical response to numerically simulated optical mode profiles. A matrix

approach has been proposed to determine the locations of the surface scatterers, which matches well with the known locations of the laser written ablation points. Although only demonstrated here for mapping the transverse location of single ablation points, our technique can be expanded in the future for the detection of particle size. All the measurements are based on a single fiber path without relying on an external complex side-imaging instrument. We believe the proposed technique has potential for the detection and sizing of biological particles of interest for *in vivo* biomedical applications such as cancer or bacteria detection or the tracking of drug delivery particles. Our proposed scheme is not limited to the use of exposed-core fibers or even evanescent field devices, but can be used to detect the location of any scatterer within a waveguide if the waveguide's modes can be individually launched and simulated numerically. The technique could therefore also be applied to the characterization of defects in waveguides or even for the study of the fundamental physics of micro-/nano-particles and their interactions with surfaces or other particles.

#### SUPPLEMENTARY MATERIAL

See the [supplementary material](#) for additional information mentioned in the main text.

#### ACKNOWLEDGMENTS

This work was supported by the Ramsay Fellowship provided by the University of Adelaide. The authors would like to thank OptoFab Node of the Australian National Fabrication Facility utilizing Commonwealth and South Australian State Government Funding, China Scholarship Council (Grant No. 201706750012), the Australian Research Council Centre for Nanoscale BioPhotonics (Grant No. CE14010003), the National Heart Foundation (Fellowship Grant No. 102093) and Australian Research Council (ARC) Future Fellowship (FT200100154). The authors acknowledge Evan Johnson and Alastair Dowler for their contribution to fiber fabrication.

#### DATA AVAILABILITY

The data that support the findings of this study are available from the corresponding author upon reasonable request.

#### REFERENCES

- A. Ashkin, *Proc. Natl. Acad. Sci. U. S. A.* **94**(10), 4853–4860 (1997).
- A. S. Urban, A. A. Lutich, F. D. Stefani, and J. Feldmann, *Nano Lett.* **10**(12), 4794–4798 (2010).
- J. Li, E. H. Hill, L. Lin, and Y. Zheng, *ACS Nano* **13**(4), 3783–3795 (2019).
- H. Shen, L. J. Tazuin, R. Baiyasi, W. Wang, N. Moringo, B. Shuang, and C. F. Landes, *Chem. Rev.* **117**(11), 7331–7376 (2017).
- M. Liebel, J. T. Hugall, and N. F. van Hulst, *Nano Lett.* **17**(2), 1277–1281 (2017).
- Y. Li, H. Xin, X. Liu, Y. Zhang, H. Lei, and B. Li, *ACS Nano* **10**(6), 5800–5808 (2016).
- I. T. Leite, S. Turtaev, X. Jiang, M. Šiler, A. Cuschieri, P. S. J. Russell, and T. Čížmar, *Nat. Photonics* **12**(1), 33–39 (2018).
- D. S. Bykov, O. A. Schmidt, T. G. Euser, and P. S. J. Russell, *Nat. Photonics* **9**(7), 461–465 (2015).
- D. S. Bykov, S. Xie, R. Zeltner, A. Machnev, G. K. Wong, T. G. Euser, and P. S. J. Russell, *Light: Sci. Appl.* **7**(1), 22 (2018).
- I.-B. Lee, H.-M. Moon, J.-H. Joo, K.-H. Kim, S.-C. Hong, and M. Cho, *ACS Photonics* **5**(3), 797–804 (2017).
- X.-C. Yu, B.-B. Li, P. Wang, L. Tong, X.-F. Jiang, Y. Li, Q. Gong, and Y.-F. Xiao, *Adv. Mater.* **26**(44), 7462–7467 (2014).
- N. P. Mauranyapin, L. S. Madsen, L. Booth, L. Peng, S. C. Warren-Smith, E. P. Schartner, H. Ebendorff-Heidepriem, and W. P. Bowen, *Opt. Express* **27**(13), 18601–18611 (2019).
- J. Zhao, D. Jin, E. P. Schartner, Y. Lu, Y. Liu, A. V. Zvyagin, L. Zhang, J. M. Dawes, P. Xi, J. A. Piper, E. M. Goldys, and T. M. Monro, *Nat. Nanotechnol.* **8**(10), 729–734 (2013).
- S. Faez, Y. Lahini, S. Weidlich, R. F. Garmann, K. Wondraczek, M. Zeisberger, M. A. Schmidt, M. Orrit, and V. N. Manoharan, *ACS Nano* **9**(12), 12349–12357 (2015).
- S. Jiang, J. Zhao, R. Förster, S. Weidlich, M. Plidschun, J. Kobelke, R. Fatobene Ando, and M. A. Schmidt, *Nanoscale* **12**(5), 3146–3156 (2020).
- R. Förster, S. Weidlich, M. Nissen, T. Wieduwilt, J. Kobelke, A. M. Goldfain, T. K. Chiang, R. F. Garmann, V. N. Manoharan, and Y. Lahini, *ACS Sens.* **5**(3), 879–886 (2020).
- J. Li, E. Schartner, S. Musolino, B. C. Quirk, R. W. Kirk, H. Ebendorff-Heidepriem, and R. A. McLaughlin, *Opt. Lett.* **43**(8), 1682–1685 (2018).
- E. P. Schartner, M. R. Henderson, M. Purdey, D. Dhattrak, T. M. Monro, P. G. Gill, and D. F. Callen, *Cancer Res.* **76**(23), 6795–6801 (2016).
- A. Khalid, L. Peng, A. Arman, S. C. Warren-Smith, E. P. Schartner, G. M. Sylvia, M. R. Hutchinson, H. Ebendorff-Heidepriem, R. A. McLaughlin, B. C. Gibson, and J. Li, *Sens. Actuators, B* **311**, 127864 (2020).
- W. Eickhoff and R. Ulrich, *Appl. Phys. Lett.* **39**(9), 693–695 (1981).
- L. Peng, J. Li, R. A. McLaughlin, H. Ebendorff-Heidepriem, and S. C. Warren-Smith, *Sens. Actuators, A* **303**, 111762 (2020).
- S. C. Warren-Smith and T. M. Monro, *Opt. Express* **22**(2), 1480–1489 (2014).
- A. W. Snyder and J. Love, *Optical Waveguide Theory* (Springer Science & Business Media, 2012).
- S. C. Warren-Smith, R. Kostecki, L. V. Nguyen, and T. M. Monro, *Opt. Express* **22**(24), 29493–29504 (2014).
- V. S. Afshar, Y. Ruan, S. C. Warren-Smith, and T. M. Monro, *Opt. Lett.* **33**(13), 1473–1475 (2008).
- V. S. Afshar, S. C. Warren-Smith, and T. M. Monro, *Opt. Express* **15**(26), 17891–17901 (2007).
- T. G. Euser, G. Whyte, M. Scharer, J. S. Y. Chen, A. Abdolvand, J. Nold, C. F. Kaminski, and P. S. J. Russell, *Opt. Express* **16**(22), 17972–17981 (2008).
- A. Ruskuc, P. Koehler, M. A. Weber, A. Andres-Arroyo, M. H. Froz, P. S. J. Russell, and T. G. Euser, *Opt. Express* **26**(23), 30245–30254 (2018).
- S. Gross, N. Riesen, J. D. Love, and M. J. Withford, *Laser Photonics Rev.* **8**(5), L81–L85 (2014).
- D. Yu, S. Fu, Z. Cao, M. Tang, L. Deng, D. Liu, I. Giles, T. Koonen, and C. Okonkwo, *Opt. Express* **24**(11), 12192–12201 (2016).

## Supplementary material for “Two-dimensional mapping of surface scatterers on an optical fiber core using selective mode launching”

Lu Peng,<sup>1,2,3,a)</sup> Linh Viet Nguyen,<sup>1,2,4</sup> Jiawen Li,<sup>2,3,5</sup> Nicolas Riesen,<sup>1,2,4</sup> Dale Otten,<sup>4</sup> David G. Lancaster,<sup>4</sup> Heike Ebdorff-Heidepriem,<sup>1,2,3</sup> and Stephen C. Warren-Smith,<sup>1,2,3</sup>

### AFFILIATIONS

<sup>1</sup>School of Physical Sciences, The University of Adelaide, Adelaide, SA 5005, Australia.

<sup>2</sup>Institute for Photonics and Advanced Sensing, The University of Adelaide, Adelaide, SA 5005, Australia.

<sup>3</sup>Australian Research Council Centre of Excellence for Nanoscale Biophotonics, Adelaide, SA 5005, Australia.

<sup>4</sup>Future Industries Institute, University of South Australia, Mawson Lakes, SA 5095, Australia.

<sup>5</sup>Adelaide Medical School, The University of Adelaide, Adelaide, SA 5005, Australia.

<sup>a)</sup> Author to whom correspondence should be addressed: [lu.peng@adelaide.edu.au](mailto:lu.peng@adelaide.edu.au)

### 1. Vertical scaling

The method used to vertically scale the simulated Poynting vector distributions at the core surface to match with the experimental results is shown in Fig. S1, which shows the difference for each mode as a function of the scaling coefficient  $a_m$  as defined in Eq. 6. The transverse offset parameter was set at  $x' = 0.4 \mu\text{m}$ , as previously determined through the results in Fig. 4.

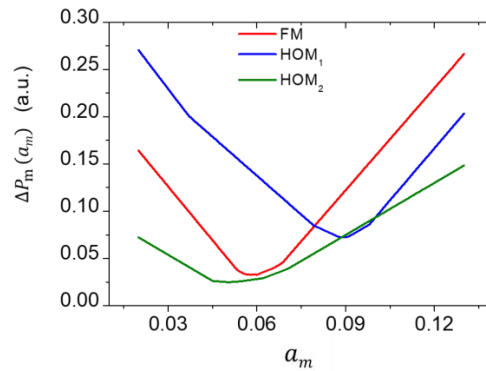


Fig. S1. Difference between the simulated Poynting vector distributions at the ECF core surface and the experimental OFDR signals. The locations where  $\Delta P_m$  is minimized represent the best fit for each mode, which occurs at  $a_1 = 0.060$  (FM),  $a_2 = 0.091$  (HOM<sub>1</sub>), and  $a_3 = 0.050$  (HOM<sub>2</sub>).

### 2. Surface versus in-core scattering

Fig. S2 shows the Poynting vector distribution of the fundamental mode (FM) at the exposed surface as a function of depth into the fibercore. The results show that the signal reduces to approximately 20% at the surface compared to a depth beneath the surface of 300 nm, which is an estimation of the average depth of the ablation points used in this work.

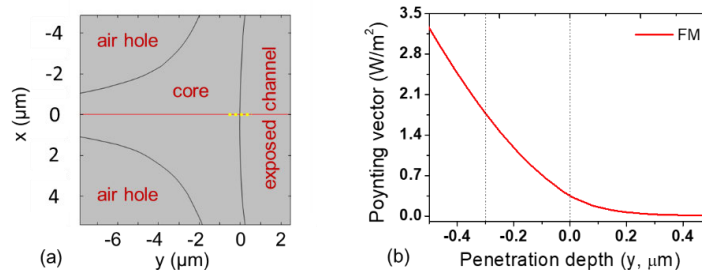


Fig. S2. (a) Geometry of the ECF used for the simulation. (b) Poynting vector distribution of the fundamental mode as a function of depth into the core of the ECF, corresponding to the yellow dashed region shown in (a).

### 3. Mode effective index and birefringence

**Table S1:** The effective refractive index for both polarizations and the corresponding birefringence and beat length of the simulation results for the three considered modes at a wavelength of 1550 nm.

	Horizontal polarization	Vertical polarization	Birefringence	Beat length
FM	1.43362	1.43351	0.00011	14.09 mm
HOM <sub>1</sub>	1.42269	1.42157	0.00112	1.38 mm
HOM <sub>2</sub>	1.41280	1.41156	0.00124	1.25 mm

### 4. Mode stability under bending

In this work we have used a high numerical aperture and high birefringence microstructured optical fiber, where the difference of effective refractive index ( $n_{eff}$ ) between different order modes is relatively large as shown in Table 1 and Fig. S3. We therefore expect that the propagation of each individual mode is resistant to intermodal coupling under standard handling conditions including fiber bending. We have performed a series of bending tests to demonstrate that the modes used in this work are stable under significant bending, with the transmitted near field mode images under varying degrees of bending shown in Fig. S3. The optical fiber was approximately 1 m long and the bending radius refers to the bend of a single loop.

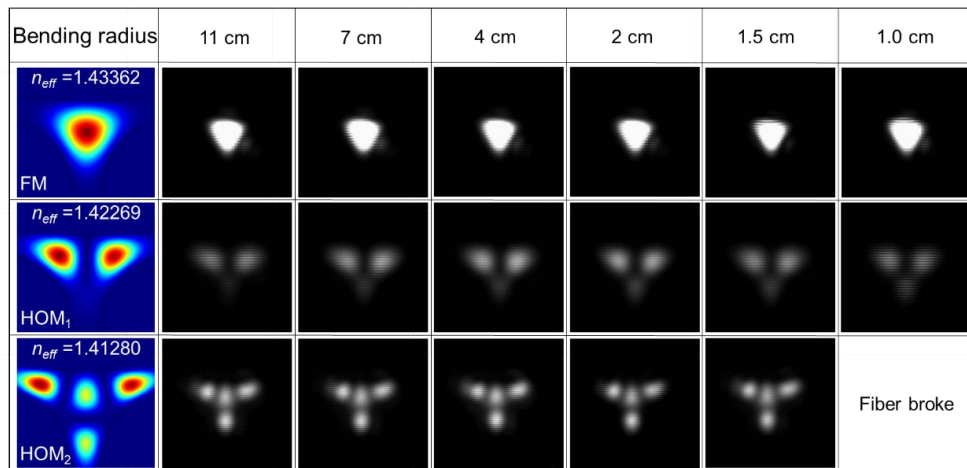


Fig. S3. Bending results under different bending radii for three different modes, respectively.

In addition, the ECF is a high birefringence fiber with non-degenerate modes and thus we also expect the fiber to display polarization maintaining behavior. We have demonstrated this by using an input polarizer to launch the vertically polarized fundamental mode (i.e., polarized perpendicular to the exposed surface) and monitoring the output power transmitted through either a parallel ( $0^\circ$ ) or orthogonally ( $90^\circ$ ) orientated polarizer while the fiber was coiled to varying degrees of bending. No significant intensity fluctuations were detected during the bending test as shown in Fig. S4.

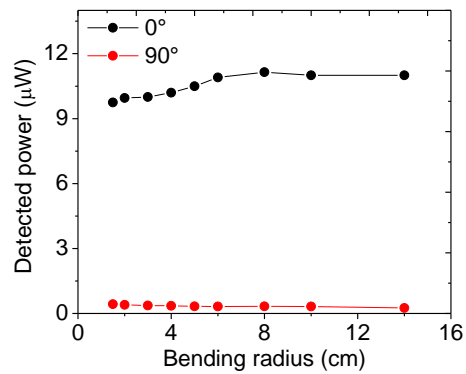


Fig. S4. Detected power of the vertically polarized fundamental mode transmitted through an output polarizer with either parallel ( $0^\circ$ ) or orthogonal ( $90^\circ$ ) orientation under varying degrees of fiber bending.

### 5. Asymmetry in higher-order modes

The fabricated ECF used in our work does not exhibit perfect reflection symmetry, particularly seen by slightly different strut thicknesses on the two sides of the core. This leads to asymmetries in the Poynting vector distribution, particularly at the core surface, which increases for higher order modes as shown in the Fig. S5. The excitation of such modes, using more complex mode launching techniques, could be exploited for resolving features on the two sides of the core.

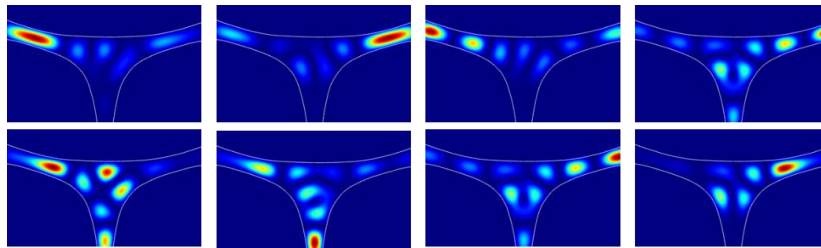


Fig. S5. Numerically simulated Poynting vector distributions at a wavelength of 1550 nm of selected higher-order modes for the fiber used in our work showing asymmetry across the core surface.

## **CHAPTER 5**

### **Particle detection and whispering gallery modes**

This chapter introduces particle size characterisation based on both the OFDR technique and the multimode property of the ECFs. Whispering gallery modes (WGMs) were observed during this process, which enabled the ECFs to act as a novel WGM coupler.

## **5.1 Particle size characterisation**

Particle size characterisation of microscale particles is investigated in this section. In Chapter 4.2, it was shown that higher-order mode excitation could be used to resolve transverse locations of scatterers on the ECF surface. This required individual mode launching to avoid multimode interference (MMI). In this section, it is shown that this condition can be related when applying machine learning algorithms to account for the inherent complexity of the MMI. It is applied towards determining the particle size, in this case to classify between two different polystyrene microsphere sizes.

### **5.1.1 Manuscript overview**

The work [M1] described in this section proposes a new particle size characterisation method using a multimode ECF based on OFDR technique. Particles on the multimode ECF have very complex scattering processes, both the evanescent-field excited scattering and the recoupling into the multiple guided modes. Embedded in this scattering OFDR data is information on the particle size and shape, as indicated by the easier to understand spherical particles. Machine learning is proposed to understand the complex scattering as a general tool for detection of particles and the classification of particle size is demonstrated here.

### **5.1.2 Statement of contribution**



## Statement of Authorship

Title of Paper	Particle size characterization using a multimode exposed-core fiber
Publication Status	<input type="checkbox"/> Published <input type="checkbox"/> Accepted for Publication <input type="checkbox"/> Submitted for Publication <input checked="" type="checkbox"/> Unpublished and Unsubmitted work written in manuscript style
Publication Details	Lu Peng, Linh Viet Nguyen, Jiawen Li, Nicolas Riesen, Mengke Han, Heike Ebendorff-Heidepriem and Stephen C. Warren-Smith. Particle size characterization using a multimode exposed-core fiber based on distributed sensing. Manuscript will be submitted to Photonics Research.

### Principal Author

Name of Principal Author (Candidate)	Lu Peng
Contribution to the Paper	The idea was mainly conceptualised by Lu Peng. All the experiments, analysis, and paper writing were majorly done by Lu Peng.
Overall percentage (%)	70%
Certification:	This paper reports on original research Lu Peng conducted during the period of her Higher Degree by Research candidature and is not subject to any obligations or contractual agreements with a third party that would constrain its inclusion in this thesis. Lu Peng is the primary author of this paper.
Signature	_____ Date <b>24-08-2021</b>

### Co-Author Contributions

By signing the Statement of Authorship, each author certifies that:

- i. the candidate's stated contribution to the publication is accurate (as detailed above);
- ii. permission is granted for the candidate to include the publication in the thesis; and
- iii. the sum of all co-author contributions is equal to 100% less the candidate's stated contribution.

Name of Co-Author	Linh Viet Nguyen
Contribution to the Paper	Linh Viet Nguyen helped with the machine learning algorithms and revised the manuscript.
Signature	_____ Date <b>24-08-2021</b>

Name of Co-Author	Jiawen Li
Contribution to the Paper	Jiawen Li contributed to general discussions for drafting the manuscript and revising the manuscript.
Signature	_____ Date <b>24-08-2021</b>

Name of Co-Author	Nicolas Riesen		
Contribution to the Paper	Nicolas Riesen contributed to technical discussions and revised the manuscript.		
Signature		Date	24-08-2021

Name of Co-Author	Mengke Han		
Contribution to the Paper	Mengke Han provided tapered tubes to support the experiments and revised the manuscript.		
Signature		Date	24-08-2021

Name of Co-Author	Heike Ebendorff-Heidepriem		
Contribution to the Paper	Heike Ebendorff-Heidepriem contributed to general discussions and revised the manuscript.		
Signature		Date	25-08-2021

Name of Co-Author	Stephen C. Warren-Smith		
Contribution to the Paper	Stephen C. Warren-Smith helped conceptualise the idea and checked the theory. He contributed to structure and edit the manuscript.		
Signature		Date	24-08-2021

# Particle size characterization using a multimode exposed-core fiber

LU PENG<sup>1,2,3,\*</sup>, LINH VIET NGUYEN<sup>1,2</sup>, JIAWEN LI<sup>2,3,4</sup>, NICOLAS RIESEN<sup>2,5</sup>, MENGKE HAN<sup>1,2,3</sup>, HEIKE EBENDORFF-HEIDEPRIEM<sup>1,2,3</sup>, AND STEPHEN C. WARREN-SMITH<sup>1,2,3,5</sup>

<sup>1</sup>School of Physical Sciences, The University of Adelaide, Adelaide, SA 5005, Australia

<sup>2</sup>Institute for Photonics and Advanced Sensing, The University of Adelaide, Adelaide, SA 5005, Australia

<sup>3</sup>Australian Research Council Centre of Excellence for Nanoscale Biophotonics, The University of Adelaide, Adelaide, SA 5005, Australia

<sup>4</sup>School of Electrical and Electronic Engineering, The University of Adelaide, Adelaide, SA 5005, Australia

<sup>5</sup>Future Industries Institute, University of South Australia, Mawson Lakes, SA 5095, Australia

\*Corresponding author: lu.peng@adelaide.edu.au

Compiled September 7, 2021

Individual particle tracking and analysis are important for cellular studies relating to disease diagnostics and drug research. Optical fiber-based devices have previously been developed towards portable particle characterization platforms. Existing methods, however, require external optics along the side of the optical fiber to image particles, which is not suitable for out-of-lab and in-vivo use. To address this significant limitation, we exploit the multimoded nature of an exposed core fiber to allow for the measurement of both particle size and spatial distribution using optical frequency domain reflectometry. By using machine learning algorithms, the complex optical scattering signal of small particles in the evanescent field of the multimode waveguide was successfully correlated with particle size, achieving an accuracy of more than 90%. ©

2021 Optical Society of America

<http://dx.doi.org/10.1364/ao.XX.XXXXXX>

## 1. INTRODUCTION

The sensing of small particles has attracted significant interest, as the understanding of their dynamics and interactions is key for cell biology research and drug development [1–4]. Flow cytometry, has for example, brought great advances in clinical diagnostics [5, 6], where particle sorting and counting are well established. Despite this, the detailed analysis of individual particles in portable devices for out-of-lab usage is yet to be extensively explored [4].

Many optical fiber-based platforms have been reported in the literature for sensing particles due to the inherent advantages of optical fibers being small and lightweight and thus having great potential for in-vivo applications. Fiber-tip based approaches for sensing particles have been proposed such as schemes for particle size detection by monitoring the phase shift induced by a particle [5, 7], as well as designs with multiple microlenses integrated on the end-face to trap and kill targeted cells

[8]. Microfluidic chips integrated with optical fibers have also been demonstrated as biosensing platforms, including particle counters for the analysis of micron-scale particles [6, 9–11].

In addition to the measurement of the size or presence of particles, the capability to show spatial information of the particles could be used to investigate their dynamics. Fiber-based schemes have been reported in the literature based on waveguides with nanoscale channels or hollow core fibers including single virus detection by using a nanofluidic fiber [12], nano-object detection by using a similar nanofluidic fiber sensor [13], or the monitoring of Brownian motion among nano-objects inside a hollow core fiber [14]. Although these methods could provide both the spatial information and the size of particles even down to the nanoscale level, they required external microscope objectives to collect the scattered light from particles to the image particle motion, behavior or shape. This limits their application, making them less suited to portable and in-vivo devices [2, 15]. Another common particle sensing approach is based on using the evanescent fields along a tapered nanowire, including tapered nanofiber pairs [16] and single tapered nanofibers [17]. Although this approach can be achieved without the use of an external microscope, the fragility of the tapered fibers severely limits practical applications.

Alternatively, microstructured optical fibers can be tailored to probe their surrounding environment using the evanescent field. The exposed-core fiber (ECF) design takes this one step further to allow detection along the entire optical fiber length. The use of ECF is seen as particularly promising because of its ability to reveal spatial information of micro/nano-objects based on e.g., optical frequency domain reflectometry (OFDR) [18]. This is because of the longitudinally exposed side of the ECF which provides a channel for hosting particles [19]. Our previous studies reported the detection of micron-scale particles based on a dark-field heterodyne measurement technique [20], and the detection of axial distributions of the particles along the longitudinal length of the fiber based on an OFDR technique [21]. This sensing capability was further advanced to map surface scatterers in two dimensions by using the few-mode property of the ECF [22].

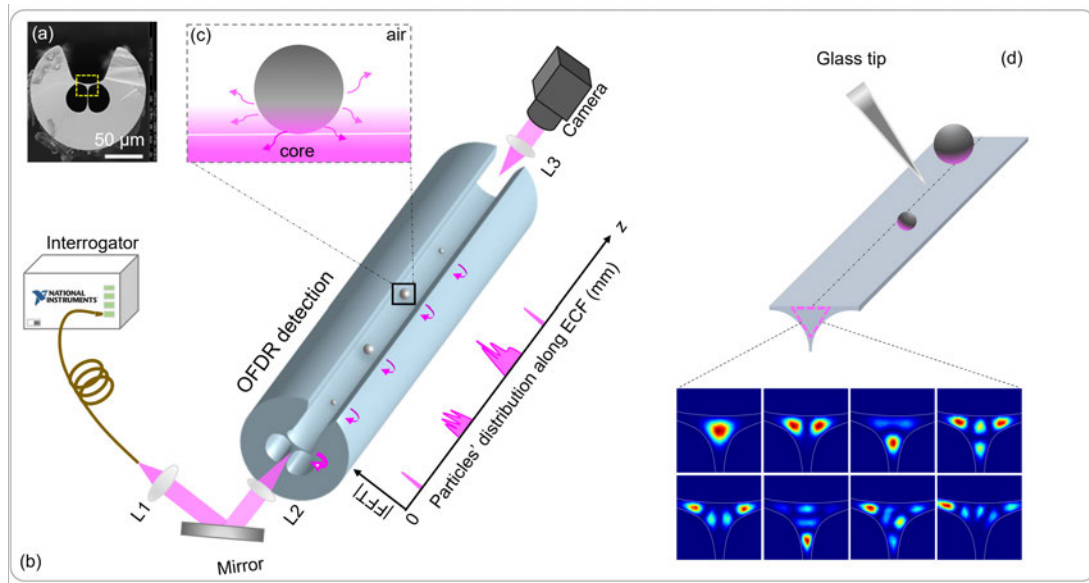


**Fig. 1.** (a) A scanning electron microscope (SEM) image of the cross-section of the ECF used. (b) Experimental set-up with a corresponding OFDR signal map of micron-scale particles (polystyrene spheres with different sizes) based on the OFDR detection. The output near-field mode profile is monitored by an InGaAs camera. (c) An example of complex scattering coupling back into the ECF's guided modes and contributing to the OFDR signal. (d) A micron-scale tapered glass capillary is used to position particles, controlled by both a three-axis optical stage and the translation stage of the optical microscope. The black dashed line in the middle of waveguide indicates the center of the ECF core. Poynting vector mode distributions are shown as examples of modes launched into the fiber that can interact with the particles through the evanescent field.

In this work, we seek to analyze the morphology of microscale particles distributed along the ECF that interact with the evanescent field. In addition to the detection of the spatial distributions of the particles, achieved using OFDR, we demonstrate the use of the multimoded nature of the fiber to obtain the second dimension, i.e., particle size. In this case we naturally introduce an additional element of complexity, which is the scattering properties of the particles in the evanescent field and the recapture of this scattered light into the guided modes of the optical fiber. We hypothesize that by using basic machine learning algorithms we can decode the complex multimode scattering of these particles to classify their sizes. Although spherical particles are specifically measured in this paper, a diverse range of measurands could be considered in the future using the same technique.

## 2. EXPERIMENTAL CONFIGURATION AND PRINCIPLE

The experimental configuration is shown in Fig. 1, with the cross-section of the ECF shown in Fig. 1(a). The fiber core is surrounded by two large air holes and an exposed channel. The exposed channel enables light-matter interactions between the waveguide's evanescent-field and the surrounding environment. Micron-scale particles (Thermo fisher: duke series, polystyrene beads with refractive index of 1.59 at 590 nm) were deposited on the exposed channel of the ECF along the longitudinal direction as shown in Fig. 1(b). Specifically, a 1  $\mu\text{L}$  particle solution (polystyrene spheres diluted in milli-Q water: 0.04  $\text{mg}/\text{cm}^3$ ) was pipetted on the fiber with particles remaining after the water evaporated. As illustrated in Fig. 1(d), a tapered micron-scale glass capillary which was made in-house [23], was then used to

position particles and remove redundant particles such as dust. The remaining particles were bound to the silica surface through physisorption [24].

Several Poynting vector mode distributions are shown at the bottom of Fig. 1(d) (simulated by COMSOL 5.3,  $\lambda = 1550$  nm), which can be launched into the fiber. An optical sensor interrogator (National Instruments, PXIe-4844, 1510-1590 nm, 4 pm resolution, sampling rate 10 Hz) was used, having both input source and photodetector integrated into one system. This allowed for the measurement of a portion of scattering from the particles (illustrated by magenta arrows in Fig. 1(c)) according to Eq. (1) [20]:

$$P_m(x, r) = \frac{1}{2} S_n(x, r) \iint_A (\hat{e}_m \times \hat{h}_m) d\vec{A} \quad (1)$$

where  $m$  represents a specific mode, while  $n$  represents a specific sphere.  $S_n$  is the scattering coefficient resulting from the specific particle, and which is dependent on its located transverse position  $x$  (i.e.,  $x$  represents the distance along the ECF exposed boundary with  $x = 0$  being the center of the core) and  $r$  is the radius of the sphere.  $A$  is the overlapping area between the sphere and the evanescent field,  $e_m$  and  $h_m$  are the orthonormal electric and magnetic fields for the launched mode respectively.

A fraction of the scattered light couples into backward-propagating ECF modes that generate interference with the ECF input-end (shown as the bold magenta arrow in Fig. 1(b)), similar to Fabry-Perot interferences. Based on the OFDR [21], mixed interferences from multiple Fabry-Perot cavities (ECF input to particles) are demultiplexed after taking the fast Fourier transform (FFT), to yield longitudinally-related signals. Due

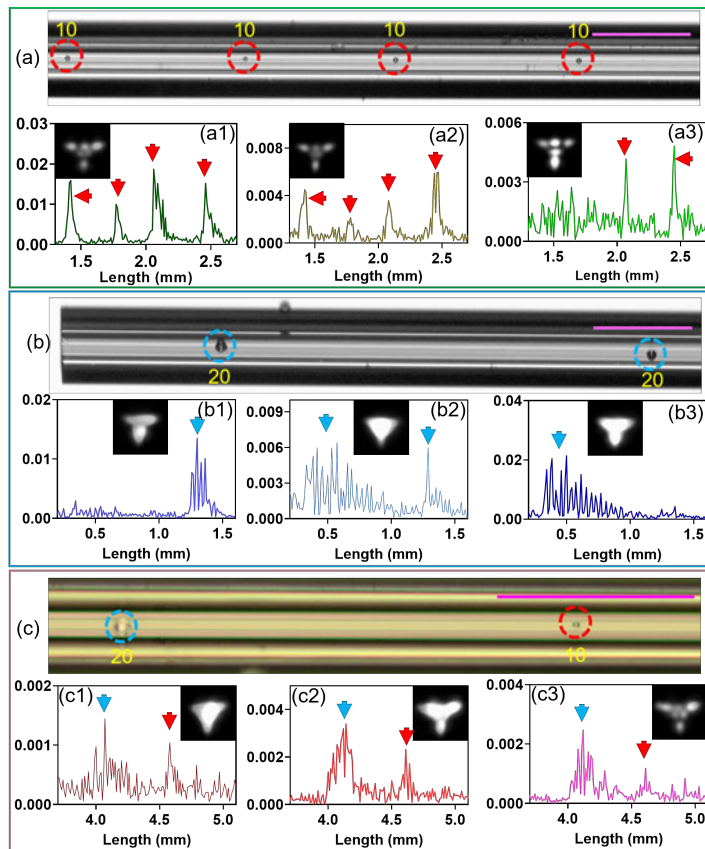


**Fig. 2.** FFT results for polystyrene beads along the ECF. Each panel (a), (b) and (c) is composed of three different FFT signals with correlated output mode profiles shown in the insets. The dashed circles indicate the polystyrene spheres which are either  $10\ \mu\text{m}$  (red marker) or  $20\ \mu\text{m}$  (blue marker) located on the exposed channel of the ECFs, and the magenta scale bar is  $200\ \mu\text{m}$ .

116 to the difference in size and transverse positions of the positioned particles on the exposed channel of the ECF, the scattering from different particles interfering with the ECF input differ even with the same mode launching condition. By varying the launched mode, signals from different particles change uniquely because of the difference in overlap between the evanescent fields and the located particles. In addition to the differences arising from different transverse locations, large particles are expected to show different signals due to their larger scattering cross-section which potentially enables them to interact more strongly with higher-order guided modes compared to smaller particles, thereby potentially enabling one to distinguish their size.

### 3. RESULTS AND ANALYSIS

#### A. Measured results

131 To investigate the possibility of detecting different sized microscale particles, the following experiments were carried out where polystyrene beads with different sizes were distributed along the ECFs, and the FFT results are shown in Fig. 2. Particles of average size  $10\ \mu\text{m}$  (marked as red),  $20\ \mu\text{m}$  (marked as blue) and both  $10\ \mu\text{m}$  and  $20\ \mu\text{m}$ , are displayed in Fig. 2(a), 2(b) and 2(c), respectively (with  $\pm 2\ \mu\text{m}$  size variations). Their relevant

138 OFDR signals are presented individually in each inset (a1-a3, b1-b3, c1-c3) with a real-time near-field image indicating the mode launching conditions. The positioned polystyrene beads that contribute to the signal are marked with dashed red or blue circles, as captured with an optical microscope.

139 We included only several particles in each fiber sample to enable them to be easily seen in the microscope images. The longitudinal position of particles located on the ECF could be directly detected based on our OFDR set-up where the marked FFT peak (red or blue arrows) results from a particle interfering with the ECF input and this was in good agreement with the microscope images. The strength of the FFT peaks from different particles differ depending on their sizes, transverse locations and the launching conditions. As the scale of the x-axis is consistent amongst each figure, the difference in OFDR signals from different particles can clearly be seen. In this case the OFDR signals from the  $10\ \mu\text{m}$  particles are far narrower with clear single peaks compared with the broad and complex peaks observed for the  $20\ \mu\text{m}$  particles.

#### B. Analysis

157 Here we discuss some phenomena observed in Figs. 2(b2) and (b3), where multiple oscillatory FFT peaks from the large polystyrene sphere occur due to the excitation of whispering

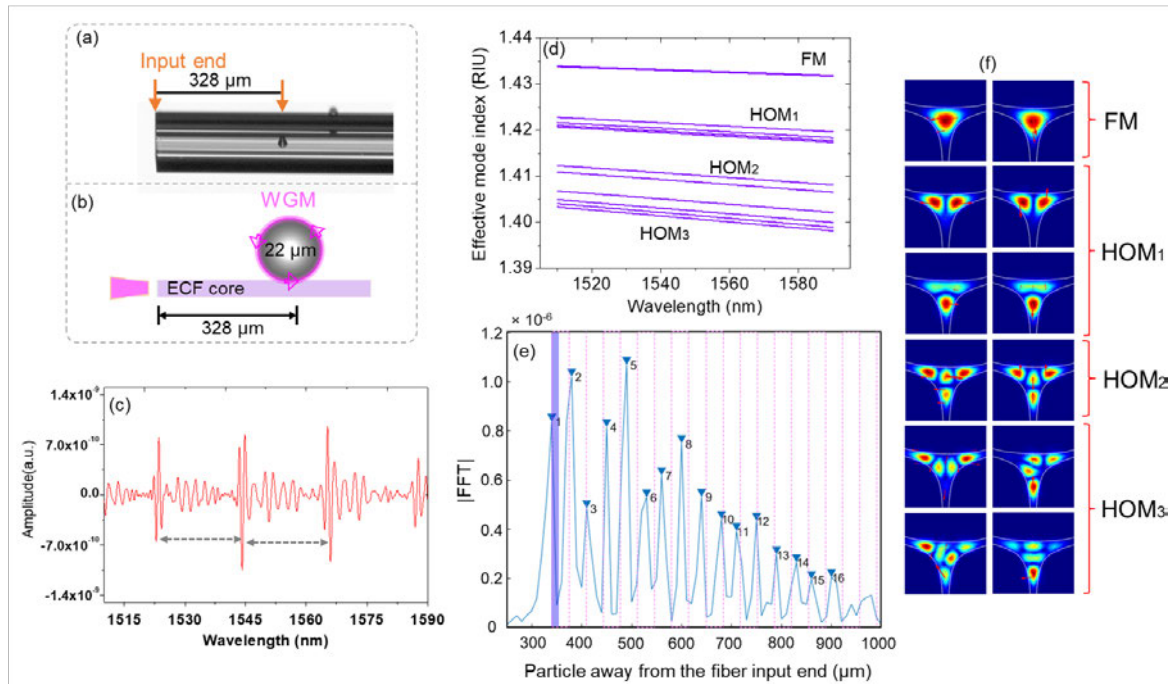


**Fig. 3.** Effects of multiple mode interference and multiple WGM modes interfering with the fiber input. (a) The polystyrene sphere is positioned on the ECF, while the illustration of WGM excitation based on the evanescent field using our ECF is shown in (b). (c) An extracted spectrum from the 22  $\mu\text{m}$  polystyrene sphere with the fiber sample used shown in (a). (d) The effective refractive index of several modes of the used ECF as a function of wavelength. (e) The correlated FFT signal from the spectrum of (c). While the purple shaded region indicates that the interferences resulting from multiple modes interfering with the fiber input, The magenta lines in (e) are an illustration of consecutive reflections of a particular WGM mode interfering with the fiber input leading to an oscillation period of 34  $\mu\text{m}$  in the FFT map. (f) The mode profiles with both polarizations (red arrows) are presented at right with relevant labels and they were simulated using COMSOL at a wavelength of 1550 nm.

gallery modes (WGMs) [24]. The particle (the same with the first particle shown in Fig. 2(b)), is displayed again in Fig. 3(a) for clarity, which shows a measured diameter of  $22 \pm 0.5 \mu\text{m}$  under an optical microscope. An illustration of WGMs excited from this particle is shown in Fig. 3(b). The inverse FFT that can be obtained from the FFT in Fig. 2(b2) from this single particle is displayed in Fig. 3(c). In Fig. 3(c), the period between these resonant peaks is around 22 nm marked with grey dashed arrow lines. This resonant period value is close to the calculated resonant period of 23 nm from a standard 22  $\mu\text{m}$  polystyrene sphere according to the free spectral range (FSR) [25]:

$$FSR = \frac{c}{\pi n_{eff} D} \quad (2)$$

where  $D$  is the diameter of the sphere, and  $n_{eff}$  is the effective index of the specific WGM. The value is within the error of the size distribution of the polystyrene spheres, with it being difficult to define the precise diameter owing to the ambiguous edge under the optical microscope. This particle is 328  $\mu\text{m}$  away from the fiber input as measured with the optical microscope and this is consistent with the longitudinal signal tracking from the FFT signals in Fig. 3(e). In this case more than 16 significant individual peaks are observed decaying towards the longer axial direction in Fig. 3(e).

To account for the multiple FFT peaks, mode dispersion is considered in Fig. 3(d) by using COMSOL 5.3 simulations to

show multimode disturbance. The relevant mode profiles (polarizations are indicated by the red arrows) are shown at right with relevant labels at a wavelength of 1550 nm, where the effective refractive index of several modes including: fundamental mode 'FM', and higher-order modes are given as 'HOM<sub>1</sub>', 'HOM<sub>2</sub>', 'HOM<sub>3</sub>', and 'HOM<sub>4</sub>' in Fig. 3(f). Therefore, multiple modes interfering with the reference light (from ECF input-end) are presented in the shaded purple region in Fig. 3(e) for comparison. It is no surprise to find this narrow purple region occurs within a single peak area due to the micron-scale optical path difference (OPD), and this indicates the dispersion from multiple modes is very small and almost negligible compared to consecutive peaks observed. Therefore, it suggests that these evenly spaced FFT peaks are not from multimode interference. The possible multiple revolutions from WGMs interfering with the ECF input continuously are indicated by the magenta dashed lines in the Fig. 3(e). After compensating for the refractive index of the silica fiber and the circular physical path from the polystyrene sphere, this oscillation period is calculated as 34  $\mu\text{m}$  in the FFT map according to an estimated diameter of a 22  $\mu\text{m}$  for the polystyrene sphere. The theoretical limitation of the interrogator used in this work is 10  $\mu\text{m}$  resolution, although in practice the resolution is closer to 20  $\mu\text{m}$  after considering the full width at half maximum (FWHM) of a single peak [21]. This leads to some minor errors when generalizing individual peaks after FFT especially when

the peak width is close to the spatial resolution. Although these peaks do not perfectly match with the hypothetical WGM circulating lines, the difference between them is within the tolerance associated with the limited spatial resolution of our interrogator. This is also explained by the FFT peaks from the third 10  $\mu\text{m}$  polystyrene sphere shown in Fig. 2(a1), while the resolution of the interrogator prevents the WGM resonances from being observed clearly. Therefore, the entire FFT peak width from this small particle is observed to be narrow even under the excitation of WGMs, allowing the possibility to show size difference based on the FFT features.

### C. Size characterization

Although the FFT peak features from different size polystyrene spheres shown in Fig. 2 are different, there is no consistent conclusion that can be drawn based on a few spectra to determine the particle size. As displayed in Fig. 2(b2), both peaks correspond to 20  $\mu\text{m}$  particles, but the peak from the second particle displays characteristics similar to 10  $\mu\text{m}$  particles. The generalized FFT peaks from 20  $\mu\text{m}$  particles are significantly different from one sample to another depending on launching conditions, transverse positions and particle characteristics (e.g., sphericity), which results in difficulties when using simple mathematical algorithms such as the FFT width or peak height to distinguish the particles.

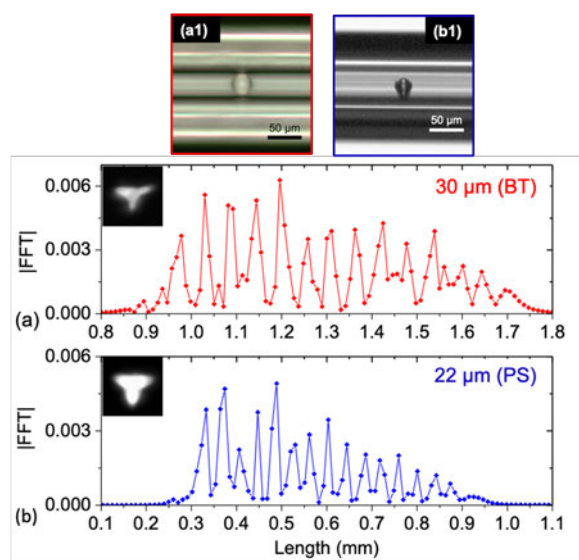


**Fig. 4.** Particle detection. (a) The OFDR result from a BT microsphere with a diameter of 30  $\mu\text{m}$  displayed in (a1). (b) The OFDR result from a PS microsphere with a diameter of 22  $\mu\text{m}$  displayed in (b1). The x-axis is the axial position of the particle away from the ECF input end based on the OFDR technique. The longitudinal length between two adjacent data points represents the theoretical limitation of the spatial resolution of the interrogator.

Ideally, the occurrence of WGMs would be sufficient to show the difference between spheres with different sizes on the ECF. As shown in Fig. 4, two different sized microspheres were further used to demonstrate how particle size might be determined

by the FFT peaks under a WGM excitation. The microsphere in Fig. 4(a1) consists of barium titanate (BT, Cospheric, refractive index around 1.9 at 590 nm), while the microsphere in Fig. 4(b1) consists of polystyrene (PS), which is the same particle as shown in Fig. 3(a). Regarding to the spacing of FFT peaks (around 50  $\mu\text{m}$ ) shown Fig. 4(a), the estimated size of this BT sphere is approximately 31.8  $\mu\text{m}$  ( $\text{OPD} = \pi n_{\text{eff}} D$ ), which is in good agreement with the observation from the optical microscope ( $30 \pm 0.5 \mu\text{m}$ ). Except the minor difference in the effective index from excited WGMs, this result demonstrates that the size of microspheres can indeed be determined based on both WGMs and OFDR.

However, the specific phase-matching requirements for exciting WGMs between waveguides and morphology-dependent micro-resonators (sphericity at the excitation plane) is challenging and thus limits the ability to use WGMs in complex situations. In other words, these evenly spaced FFT peaks are not observed for all the large spheres ( $> 20 \mu\text{m}$ ) but only from a few particles during the experiments. Moreover, typically only particles with near-perfect sphericity will exhibit WGMs, whereas real biological particles may have sphericity but will not typically support WGMs. Therefore, a reliable approach to analyze these measured results to distinguish particle sizes is necessary.

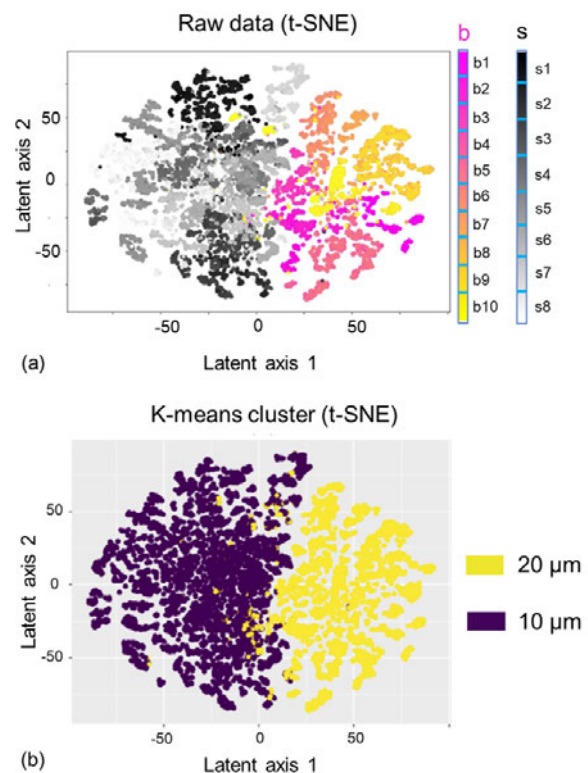


**Fig. 5.** (a) t-SNE algorithm for mapping the labeled data (FFT signals) where the big particles (20  $\mu\text{m}$ ) are displayed with colorful and small particles (10  $\mu\text{m}$ ) are displayed in greyscale color. (b) K-means clusters are shown based on an unsupervised algorithm for unlabeled data, which correlates well with the labeled results in (a).

The approach presented here to overcome these challenges is inspired by the rapid development of machine learning algorithm, which has revolutionized many fields including physics and is fast becoming an indispensable analytical tool towards reliable instrumental developments. Since our FFT signals are collected by changing the launching conditions, it has already displayed indications of different sized spheres. By taking advantage of statistical algorithms, the potential exists to reduce the possible errors in particle characterization with more input data (FFT signals) to show a more reliable analysis of particle size. Therefore, hundreds of FFT signals were collected from individual fiber samples by simply changing the launching conditions (i.e., adjusting the axes of the optical stage).

FFT peaks were then extracted with continuous as 51 data point windows, where two adjacent data points represent  $10\ \mu\text{m}$  in longitudinal length along the fiber. The 51 data points with covering  $500\ \mu\text{m}$  in physical length were extracted for a particle as each segment. This segment contains most of the peak features from a given particle, for each particle as a database for the preparation of the following statistical analysis. The total sampling number of the whole dataset consists of 22297 FFT traces from 18 particles, with 8448 FFT traces from 10 big particles ( $20\ \mu\text{m}$ ) positioned on 4 fiber samples and 13849 from 8 small particles ( $10\ \mu\text{m}$ ) positioned on 3 fiber samples. Among them, half of each size particles are mixture positioned on 2 fiber samples, while the remaining of them only positioned individually either only  $10\ \mu\text{m}$  or only  $20\ \mu\text{m}$  on other individual fibers. All data from particles was normalized.

Firstly, we used t-distributed stochastic neighbor embedding (t-SNE), which is a machine learning algorithm for visualizing complex data by reducing high dimensional data into two dimensions while preserving the local data structure [27]. By using t-SNE, results from two types of spheres ( $10/20\ \mu\text{m}$ ) with correct (size) labels are shown in Fig. 5(a), where the label which begins with 'b' means big particles ( $20\ \mu\text{m}$ ) and 's' means small particles ( $10\ \mu\text{m}$ ). While the same cluster color means different signals from the same particle but with different launching condition, different cluster colors result from different particles.

To demonstrate the possibility of distinguishing between these two types of polystyrene spheres, a non-supervised clustering algorithm 'K-means' (an algorithm without knowing the labels but with a given number of clusters/types), was then applied to group the same data (displayed in Fig. 5(a)) as two clusters. We could see the clear separation of two groups in Fig. 5(b) based on the 'K-means' algorithm, and this result is in good agreement with the labeled results in Fig. 5(a), where the dark cluster matches with the mapping of  $10\ \mu\text{m}$  particles and the yellow cluster matches with the mapping of  $20\ \mu\text{m}$  particles. The ability of the K-means clustering to accurately cluster the  $10\ \mu\text{m}$  and  $20\ \mu\text{m}$  particles demonstrates that there is sufficient information contained with the OFDR signals to differentiate these two particles, even if not apparent upon first inspection.

To quantitatively classify the particle size, we used a simple supervised machine learning algorithm, k-nearest neighbors (KNN). By using the same dataset (extracted FFT peaks which is the same as Fig. 5), some particles are used to generate the training dataset and remaining particles are used to generate/create testing datasets, as illustrated in Fig. 6(a). The size of training dataset is around four times larger than the testing dataset, while the distributions of chosen tested particles are random. The untrained particles could be well predicted with 91% accuracy for  $10\ \mu\text{m}$  particles and 93% accuracy for  $20\ \mu\text{m}$  particles as shown in the confusion matrix in Fig. 6(b). Therefore, our sensing scheme

in the present work can predict information from micron-scale particles.

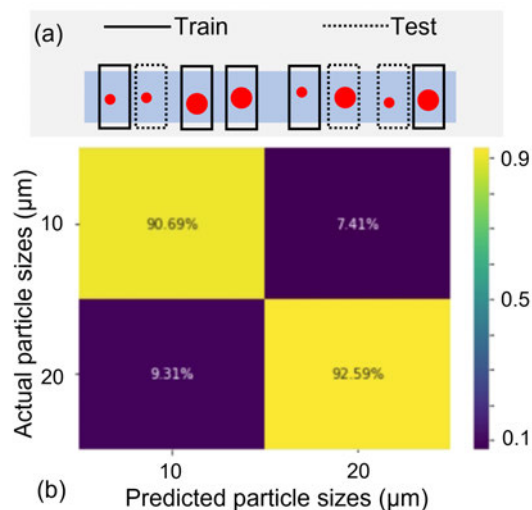


**Fig. 6.** (a) Illustration of the training and testing samples. Each data window is actually associated with the spatial length of  $500\ \mu\text{m}$  in the fiber. (b) KNN prediction of the new particles.

#### 4. CONCLUSION

In summary, the proof-of-concept of spherical particle size characterization is demonstrated by incorporating the OFDR technique and WGM resonance. For complex cases when particles are not perfectly spherical as typically required to allow WGMs excitation, we have further demonstrated that by incorporating with basic machine learning algorithms, it is possible for distinguishing particle size based on the multimoded nature of the ECF. Although we have only shown the proof-of-concept of distinguishing two particle sizes so far, further complexity (e.g., shape) could be added.

The sensing technique presented in this article is neither limited to the usage of the specific microstructured fiber nor is it limited to evanescent field devices. It could be used for standard waveguided fibers such as hollow core fibers. If we were to replace the current fiber with hollow core fibers in the future, the strong light-matter interaction with flow-cell contact could play a key role in enabling the detection of more features of particles with diverse applications in biochemical sensing. Our sensing scheme could make significant inroads for cellular research to identify diseases base on the size with only the requirement of very small sample volumes and our simple experimental set-up, holding great potential for use as in-vivo devices.

**Funding.** Australian Research Council (ARC) Future Fellowship (FT200100154). Optofab node of the Australian National Fabrication Facility (ANFF) utilizing Commonwealth and South Australian State Government Funding. China Scholarship Council (201706750012). ARC Centre for Nanoscale BioPhotonics (CE14010003). National Heart Foundation (Fellowship 102093). ARC Integrated Devices for End-user Analysis at Low Levels (IDEAL) Research Hub.

**Acknowledgments.** The authors acknowledge Evan Johnson and Alastair Dowler for their contribution to the fiber fabrication.



357 **Disclosures.** The authors declare no conflicts of interest.

## 358 REFERENCES

- 359 1. H. Shen, L. J. Tauzin, R. Baiyasi, W. Wang, N. Moringo, B. Shuang,  
360 and C. F. Landes, "Single particle tracking: from theory to biophysical  
361 applications," *Chem. Rev.* **117**, 7331–7376 (2017).
- 362 2. F. Xing and L. Yang, "Robust nucleus/cell detection and segmentation  
363 in digital pathology and microscopy images: a comprehensive review,"  
364 *IEEE Rev. Biomed. Eng.* **9**, 234–263 (2016).
- 365 3. P. Sajeesh and A. K. Sen, "Particle separation and sorting in microflu-  
366 idic devices: a review," *Microfluid. Nanofluidics* **17**, 1–52 (2014).
- 367 4. N.-T. Huang, H.-I. Zhang, M.-T. Chung, J. H. Seo, and K. J. L. o. a. C.  
368 Kurabayashi, "Recent advancements in optofluidics-based single-cell  
369 analysis: optical on-chip cellular manipulation, treatment, and property  
370 detection," *Lab Chip* **14**, 1230–1245 (2014).
- 371 5. B. Jiang, H. Dai, Y. Zou, and X. J. O. e. Chen, "Continuous detection of  
372 micro-particles by fiber bragg grating fabry-pérot flow cytometer," *Opt.*  
373 *Express* **26**, 12579–12584 (2018).
- 374 6. L.-M. Fu, R.-J. Yang, C.-H. Lin, Y.-J. Pan, and G.-B. Lee, "Electrokineti-  
375 cally driven micro flow cytometers with integrated fiber optics for on-line  
376 cell/particle detection," *Anal. Chimica Acta* **507**, 163–169 (2004).
- 377 7. Q. Li, H. Huang, F. Lin, and X. J. O. e. Wu, "Optical micro-particle size  
378 detection by phase-generated carrier demodulation," *Opt. Express* **24**,  
379 11458–11465 (2016).
- 380 8. Y. Li, H. Xin, X. Liu, Y. Zhang, H. Lei, and B. Li, "Trapping and detection  
381 of nanoparticles and cells using a parallel photonic nanojet array," *ACS*  
382 *Nano* **10**, 5800–5808 (2016).
- 383 9. W. Huang, T. Wu, A. Shalan, R. Kostecki, C. K. Rayner, C. Priest,  
384 H. Ebendorff-Heidepriem, and J. J. A. s. Zhao, "A multiplexed microflu-  
385 idic platform toward interrogating endocrine function: Simultaneous  
386 sensing of extracellular ca<sup>2+</sup> and hormone," *ACS Sens.* **5**, 490–499  
387 (2020).
- 388 10. S. Hampson, W. Rowe, S. D. Christie, and M. Platt, "3d printed mi-  
389 crofluidic device with integrated optical sensing for particle analysis,"  
390 *Sens. Actuator B Chem.* **256**, 1030–1037 (2018).
- 391 11. X. Chen, Y. Gu, J. Chen, C.-H. Lee, I. Gagne, R. Tang, L. Waller,  
392 Z. Zhang, A. C. Zhang, and Y. Han, "Image-guided cell sorting using  
393 fast scanning lasers," *APL Photon.* **5**, 040801 (2020).
- 394 12. S. Faez, Y. Lahini, S. Weidlich, R. F. Garmann, K. Wondraczek, M. Zeis-  
395 berger, M. A. Schmidt, M. Orrit, and V. N. Manoharan, "Fast, label-free  
396 tracking of single viruses and weakly scattering nanoparticles in a  
397 nanofluidic optical fiber," *ACS Nano* **9**, 12349–12357 (2015).
- 398 13. S. Jiang, J. Zhao, R. Förster, S. Weidlich, M. Plidschun, J. Kobelke,  
399 R. F. Ando, and M. A. Schmidt, "Three dimensional spatiotemporal  
400 nano-scale position retrieval of the confined diffusion of nano-objects  
401 inside optofluidic microstructured fibers," *Nanoscale* **12**, 3146–3156  
402 (2020).
- 403 14. R. Forster, S. Weidlich, M. Nissen, T. Wieduwilt, J. Kobelke, A. M.  
404 Goldfain, T. K. Chiang, R. F. Garmann, V. N. Manoharan, and Y. Lahini,  
405 "Tracking and analyzing the brownian motion of nano-objects inside  
406 hollow core fibers," *ACS Sens.* **5**, 879–886 (2020).
- 407 15. F. Ekiz-Kanik, D. D. Sevenler, N. L. Ünlü, M. Chiari, and M. S. Ünlü,  
408 "Surface chemistry and morphology in single particle optical imaging,"  
409 *Nanophotonics* **6**, 713–730 (2017).
- 410 16. X. Yu, B. Li, P. Wang, L. Tong, X. Jiang, Y. Li, Q. Gong, and Y. Xiao,  
411 "Single nanoparticle detection and sizing using a nanofiber pair in an  
412 aqueous environment," *Adv. Mater.* **26**, 7462–7467 (2014).
- 413 17. N. Mauranyapin, L. Madsen, M. Taylor, M. Waleed, and W. Bowen,  
414 "Evanescence single-molecule biosensing with quantum-limited preci-  
415 sion," *Nat. Photon.* **11**, 477–481 (2017).
- 416 18. W. Eickhoff and R. Ulrich, "Optical frequency domain reflectometry in  
417 single-mode fiber," *Appl. Phys. Lett.* **39**, 693–695 (1981).
- 418 19. S. C. Warren-Smith and T. M. Monro, "Exposed core microstructured  
419 optical fiber bragg gratings: refractive index sensing," *Opt. Express* **22**,  
420 1480–1489 (2014).
- 421 20. N. P. Mauranyapin, L. S. Madsen, L. Booth, L. Peng, S. C. Warren-  
422 Smith, E. P. Schartner, H. Ebendorff-Heidepriem, and W. P. Bowen,  
"Quantum noise limited nanoparticle detection with exposed-core fiber,"  
*Opt. Express* **27**, 18601–18611 (2019).
21. L. Peng, J. Li, R. A. McLaughlin, H. Ebendorff-Heidepriem, and S. C.  
Warren-Smith, "Distributed optical fiber sensing of micron-scale parti-  
cles," *Sens. Actuator A Phys.* **303**, 111762 (2020).
22. L. Peng, L. V. Nguyen, J. Li, N. Riesen, D. Otten, D. G. Lancaster,  
H. Ebendorff-Heidepriem, and S. C. Warren-Smith, "Two-dimensional  
mapping of surface scatterers on an optical fiber core using selective  
mode launching," *APL Photon.* **6**, 026105 (2021).
23. M. Han, J. Zhao, J. M. Fabian, S. Evans, S. Mustafa, Y. Ruan, S. Wieder-  
man, and H. Ebendorff-Heidepriem, "Cytoplasmic delivery of quantum  
dots via microelectrophoresis technique," *Electrophoresis* **42**, 1247–  
1254 (2021).
24. L. Peng, N. Riesen, J. Li, M. Han, L. V. Nguyen, H. Ebendorff-  
Heidepriem, and S. C. Warren-Smith, "Whispering gallery mode excita-  
tion using exposed-core fiber," *Opt. Express* **29**, 23549–23557 (2021).
25. M. R. Foreman, J. D. Swaim, and F. Vollmer, "Whispering gallery mode  
sensors," *Adv. Opt. Photon.* **7**, 168–240 (2015).

## 5.2 Whispering gallery mode excitation using ECFs

In addition to using the evanescent field of the ECF for particle detection, this section shows that the evanescent field of the ECF can couple into the deposited microspheres. This demonstrates that the ECF can also act as a coupling platform to excite WGMs. Fano resonance observed from the ECF excited micro-sphere configuration is also discussed in this section.

Fano resonance [213] has been found when the WGM resonance is disturbed by an external cavity (e.g., FP interferometers). This behaviour is particularly favourable for building photonic switches, modulators, filters and sensors due to the sharp tuning and narrow linewidth. When interference occurs between a quasi-continuous state (waveguides) and discrete states (resonators), it leads to a Fano resonance where the constructive and destructive interference is manifested as sharp tuning of the spectrum between total transmission and reflection [214, 215]. Since S. Fan *et al.* reported theoretical work where WGM resonance was disturbed by an external FP interference based on a simulated photonic configuration in 2002 [216], many literature have been published showing Fano resonance based on similar schemes [91, 153, 217].

### 5.2.1 Publication overview

This work [P3] proposes a new WGMs excitation scheme, using the ECF as a WGM coupler. It overcomes the fragility of using ultra-thin fibre tapers and is able to integrate multiple resonators on a single fibre. Furthermore, the outer jacket of the ECF provides a physical protection of located micro-resonators from disturbances of the outside environment. Through a Fano resonance effect, greater flexibility in tuning the spectrum between reflection and transmission has been presented, which brings insights for building photonic devices. The excitation of WGMs from two in-line polystyrene spheres were realised both separately and simultaneously, which brings future research interest in multi-point sensing/lasing, and study of evanescent field coupling from closely spaced spheres.

### 5.2.2 Statement of contribution

## Statement of Authorship

Title of Paper	Whispering gallery mode excitation using exposed-core fiber
Publication Status	<input checked="" type="checkbox"/> Published <input type="checkbox"/> Accepted for Publication <input type="checkbox"/> Submitted for Publication <input type="checkbox"/> Unpublished and Unsubmitted work written in manuscript style
Publication Details	Lu Peng, Nicolas Riesen, Jiawen Li, Mengke Han, Linh Viet Nguyen, Heike Ebendorff-Heidepriem and Stephen C. Warren-Smith. Whispering gallery mode excitation using exposed-core fiber. Optics Express, 2021.

### Principal Author

Name of Principal Author (Candidate)	Lu Peng
Contribution to the Paper	The idea was mainly conceptualised by Lu Peng. All the experiments, analysis, and paper writing were majorly done by Lu Peng.
Overall percentage (%)	70%
Certification:	This paper reports on original research Lu Peng conducted during the period of her Higher Degree by Research candidature and is not subject to any obligations or contractual agreements with a third party that would constrain its inclusion in this thesis. Lu Peng is the primary author of this paper.
Signature	<div style="display: flex; justify-content: space-between;"> <div style="border-bottom: 1px solid black; width: 80%;"></div> <div style="border-bottom: 1px solid black; width: 15%;"></div> <div style="border-bottom: 1px solid black; width: 5%; text-align: center;">Date</div> <div style="border-bottom: 1px solid black; width: 10%; text-align: center;">08-08-2021</div> </div>

### Co-Author Contributions

By signing the Statement of Authorship, each author certifies that:

- i. the candidate's stated contribution to the publication is accurate (as detailed above);
- ii. permission is granted for the candidate to include the publication in the thesis; and
- iii. the sum of all co-author contributions is equal to 100% less the candidate's stated contribution.

Name of Co-Author	Nicolas Riesen
Contribution to the Paper	Nicolas Riesen provided substantial support for building the theoretical part of this paper and revised the manuscript.
Signature	<div style="display: flex; justify-content: space-between;"> <div style="border-bottom: 1px solid black; width: 80%;"></div> <div style="border-bottom: 1px solid black; width: 15%;"></div> <div style="border-bottom: 1px solid black; width: 5%; text-align: center;">Date</div> <div style="border-bottom: 1px solid black; width: 10%; text-align: center;">09-08-2021</div> </div>

Name of Co-Author	Jiawen Li
Contribution to the Paper	Jiawen Li contributed to general discussions for drafting the manuscript and revising the manuscript.
Signature	<div style="display: flex; justify-content: space-between;"> <div style="border-bottom: 1px solid black; width: 80%;"></div> <div style="border-bottom: 1px solid black; width: 15%;"></div> <div style="border-bottom: 1px solid black; width: 5%; text-align: center;">Date</div> <div style="border-bottom: 1px solid black; width: 10%; text-align: center;">9/8/2021</div> </div>

Name of Co-Author	Mengke Han
Contribution to the Paper	Mengke Han provided tapered tubes to support the experiments and revised the manuscript.
Signature	<hr style="display: inline-block; width: 150px; vertical-align: middle;"/> <span style="margin-left: 100px;"><hr style="display: inline-block; width: 150px; vertical-align: middle;"/></span> Date <b>9/8/2021</b>




Name of Co-Author	Linh Viet Nguyen
Contribution to the Paper	Linh Viet Nguyen contributed to general discussions and revised the manuscript.
Signature	<hr style="display: inline-block; width: 150px; vertical-align: middle;"/> <span style="margin-left: 100px;"><hr style="display: inline-block; width: 150px; vertical-align: middle;"/></span> Date <b>09-08-2021</b>

Name of Co-Author	Heike Ebendorff-Heidepriem
Contribution to the Paper	Heike Ebendorff-Heidepriem contributed to general discussions and revised the manuscript.
Signature	<hr style="display: inline-block; width: 150px; vertical-align: middle;"/> <span style="margin-left: 100px;"><hr style="display: inline-block; width: 150px; vertical-align: middle;"/></span> Date <b>9 Aug 2021</b>

Name of Co-Author	Stephen C. Warren-Smith
Contribution to the Paper	Stephen C. Warren-Smith helped conceptualise the idea and checked the theory. He contributed to structure and edit the manuscript.
Signature	<hr style="display: inline-block; width: 150px; vertical-align: middle;"/> <span style="margin-left: 100px;"><hr style="display: inline-block; width: 150px; vertical-align: middle;"/></span> Date <b>09-08-2021</b>



# Whispering gallery mode excitation using exposed-core fiber

LU PENG,<sup>1,2,3,\*</sup> NICOLAS RIESEN,<sup>2,4</sup>  JIAWEN LI,<sup>2,3,5</sup>  MENGKE HAN,<sup>1,2,3</sup> LINH VIET NGUYEN,<sup>1,2</sup> HEIKE EBENDORFF-HEIDPRIEM,<sup>1,2,3</sup>  AND STEPHEN C. WARREN-SMITH<sup>1,2,3,4</sup> 

<sup>1</sup>School of Physical Sciences, The University of Adelaide, Adelaide, SA 5005, Australia

<sup>2</sup>Institute for Photonics and Advanced Sensing, The University of Adelaide, Adelaide, SA 5005, Australia

<sup>3</sup>Australian Research Council Centre of Excellence for Nanoscale Biophotonics, The University of Adelaide, Adelaide, SA 5005, Australia

<sup>4</sup>Future Industries Institute, University of South Australia, Mawson Lakes, SA 5095, Australia

<sup>5</sup>Adelaide Medical School, The University of Adelaide, Adelaide, SA 5005, Australia

\*lu.peng@adelaide.edu.au

**Abstract:** Whispering gallery modes (WGMs) in micro-resonators are of interest due to their high Q-factors. Ultra-thin fiber tapers are widely deployed to couple light into micro-resonators but achieving stable and practical coupling for out-of-lab use remains challenging. Here, a new WGM coupling scheme using an exposed-core silica fiber (ECF) is proposed, which overcomes the challenge of using fragile fiber tapers. Microspheres are deposited onto the exposed channel for excitation via the evanescent field of the fiber's guided modes. The outer jacket of the ECF partially encapsulates the microspheres, protecting them from external physical disturbance. By varying the mode launching conditions in this few-mode ECF, in combination with a Fano resonance effect, we demonstrate a high degree of tunability in the reflection spectrum. Furthermore, we show multi-particle WGM excitation, which could be controlled to occur either simultaneously or separately through controlling the ECF mode launching conditions. This work can bring value towards applications such as optical switches and modulators, multiplexed/distributed biosensing, and multi-point lasing, integrated in a single optical fiber device that avoids fiber post-processing.

© 2021 Optical Society of America under the terms of the [OSA Open Access Publishing Agreement](#)

## 1. Introduction

Electromagnetic waves can circulate within micro-cavities based on total internal reflection, a phenomenon known as whispering gallery mode (WGM) resonance. This leads to strong resonances useful for many applications including biochemical sensing, lasing, and nonlinear/quantum optical devices [1–3]. Earlier reports have utilized prism or fiber taper coupling for the excitation of WGMs with more recent demonstrations using microstructured optical fibers [4–12]. While fiber tapers have been used widely to excite micro-resonators with high Q-factors up to  $10^8$  [2,3], handling the fragile micro-scaled tapered region and the requirement of a supporting platform to position the fiber and resonator remains challenging (e.g., for in-vivo applications). Integrated fiber couplers have been reported by melting a sphere at the tip of the optical fiber [13,14] or etching/melting the optical fiber to expose the core while retaining the outer fiber structure to hold the resonator [15–18]. Although they are portable and potentially suitable for out-of-lab use, the melting/etching procedures are time-consuming, produce fragile structures, and lack high repeatability.

An alternative approach is the use of suspended core microstructured fibers (SCFs), which have the advantage of using the built-in air channels to immobilize resonators [4,6,8]. In these studies, either capillary action was used to encapsulate the particle inside one of the SCF air channels, or the particles were positioned at the SCF end-face. In either case there is limited

ability to manipulate the position of the particles and distributed multi-resonator placement is difficult. Similar to SCFs, exposed core microstructured optical fibers (ECFs) provide an accessible evanescent field along the entire fiber length but with an exposed channel to allow direct access to the core from the surrounding environment at any location along the fiber [19]. This is similar to a D-shaped optical fiber, but for comparable core diameters the evanescent field of the ECF is several times higher (depending on the specific mode) [20]. The ECF also avoids the preform or fiber polishing/micromachining required to fabricate D-shaped fibers [21–23], which can be difficult to avoid cracking the optical core of the preform or to control the precise depth in the case of polishing the fiber. Our work has recently demonstrated that the ECF is a good candidate to be deployed for distributed sensing, including the detection of micro-scaled particles [24,25].

In this paper, we present a new scheme for exciting micro-resonator WGMs. Having standard fiber dimensions (160  $\mu\text{m}$ ) and the ability to be drawn with kilometer lengths, the ECF overcomes the fragility of using ultra-thin fiber tapers and avoids fiber post-processing (i.e., tapering, etching, melting, and polishing). Furthermore, the microspheres could be positioned on the exposed surface in a controllable way due to the direct access provided by the open side channel, allowing the WGMs to be excited via the evanescent field of the guided modes of the ECF. We show that by controlling the mode launching into the few-mode ECF, the spectrum can be switched between transmission and reflection of the resonant wavelengths through a Fano resonance interaction. Furthermore, the scheme is naturally amenable to multi-resonator coupling, which we demonstrate by exciting WGMs in two microspheres with different sizes on the exposed channel either separately or simultaneously. Our scheme holds potential as a tunable reflector or filter for integrated photonic processing or as a platform for multi-point sensing/lasing and slow light [26].

## 2. Experimental setup

The WGM fiber coupler is shown in Fig. 1(a), where light from a swept source interrogator (National Instruments, PXIe-4844, 1510 - 1590 nm, 4 pm resolution, sampling rate 10 Hz) is injected into the ECF core. The ECF cross-section is shown in Fig. 1(b), with a core diameter of 5.4  $\mu\text{m}$ , which was fabricated in-house as previously reported in [27]. Several simulated (COMSOL 5.3) ECF modes are presented in the bottom of Fig. 1(a), where the fundamental mode is labeled as 'FM' and other higher-order modes are shown as 'HOM' followed by sequential integers (1-7), with corresponding effective mode index listed below each image at a wavelength of 1550 nm. The WGM excitation of a polystyrene microsphere via the ECF evanescent field is illustrated in Fig. 1(c). The reflected light [indicated by the red arrow in Fig. 1(c)] from the microspheres is then recoupled into the ECF's guided modes and detected by the interrogator. Meanwhile, the near-field ECF output from the far end of the fiber is monitored using an InGaAs camera. Note that the reflection configuration used here is to reduce the background signal from the light source to allow WGM signals to be observed, as the coupling efficiency in this relatively large core ECF is low due to the limited evanescent field.

An image of the ECF with microsphere placed onto the core is presented in Fig. 1(d), where a 20  $\mu\text{m}$  polystyrene sphere (Thermo Fisher: Duke Standards 2020A, refractive index: 1.59 at 589 nm) was located 29  $\mu\text{m}$  away from the ECF input, and the magnified image is shown in Fig. 1(e). To deposit the particles, a droplet (1  $\mu\text{L}$ ) of polystyrene sphere solution (diluted in milli-Q water: 0.04  $\text{g}/\text{cm}^3$ ) was placed inside the exposed channel and the microspheres were deposited inside the channel while the water was evaporated after tens of seconds. Then, microspheres were positioned inside the exposed channel using a tapered micro-scaled glass tube, which was controlled by a three-axis translation stage under an optical microscope. The polystyrene spheres adhere to the ECF (silica) surface through physisorption unless there is a

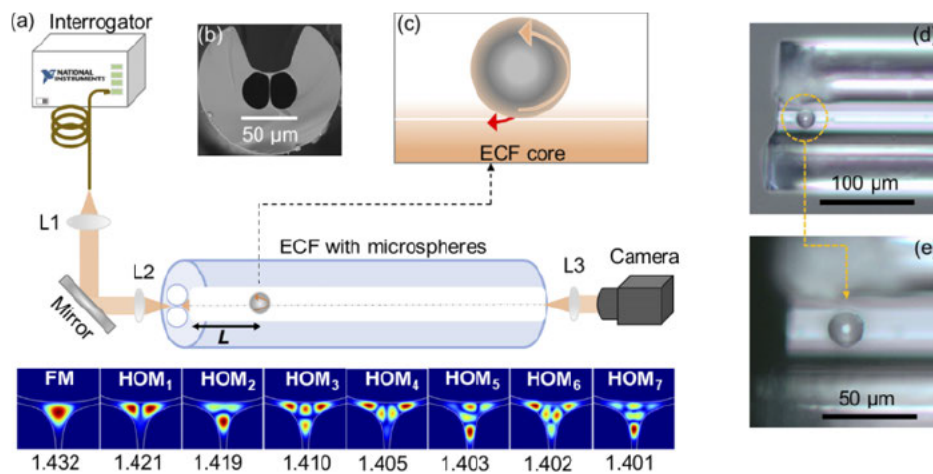


**Fig. 1.** Experimental set-up and the fiber sample (length: 220 mm) used for the experiments. (a) Schematic diagram based on reflection detection, while simulated modes are shown in the bottom. (b) Scanning electron microscope image of the ECF cross-section. (c) Illustration of WGM excitation based on the evanescent field. (d) Microscope image: a polystyrene sphere located on the input side of the ECF exposed channel, while the magnified image is in (e).

destructive mechanical force from the outside environment. The ECF input end was angle-cleaved ( $6.2^\circ$ ) to avoid strong reflections.

### 3. Results

#### 3.1. Fabry-Perot interference

An example reflection spectrum is shown in Fig. 2(a), which results from the mode launching shown by the output near-field image in the inset. The spectrum exhibits weak Fabry-Perot (FP) interference with a free spectral range (FSR) of 35 nm. This corresponds to the physical distance between the ECF input and the located sphere and is apparent in the fast Fourier transform (FFT) in Fig. 2(b).

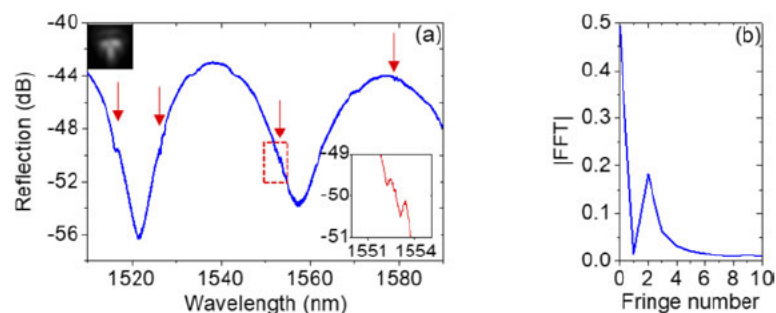


**Fig. 2.** (a) Large interference fringes from the FP cavity formed between the ECF input and the microsphere). Red arrows indicate the occurrence of WGMs. Inset shows a magnified view of the spectrum in the red dashed box. The near-field output image is at top left. (b) The absolute FFT calculated from the spectrum of (a).

The FSR in the wavelength domain is determined by the expression:

$$FSR_{\Delta\lambda} = \lambda^2 / 2n_g L. \quad (1)$$

where  $L$  is the physical length of the FP cavity [marked in Fig. 1(a)],  $n_g$  is the group index of the propagating optical fiber mode within the cavity, and  $\lambda$  is the center wavelength (1550 nm) of the light source.

The calculated FSR of the FP (input-sphere) cavity is 29 nm using a calculated group index of 1.44 [HOM<sub>2</sub> shown in the bottom of Fig. 1(a)], which is in reasonable agreement with the measured result. The error is primarily due to both the angle of the cleave (it is not easy to define the exact edge of the ECF core position under the optical microscope to determine the exact distance), error in the group index calculated in the numerical model, and modal dispersion due to a superposition of the excited modes. Several small features are observed in the reflection spectrum in Fig. 2(a) shown by the arrows (the red dashed box region is magnified in the inset), which are indicative of the WGM resonances and we now investigate in detail. In particular, we now see how the presence of the background FP interference and the WGM excitation leads to the potential of Fano resonance interactions resulting from the interference between a continuum and a discrete state [28,29].

### 3.2. Fano resonance

Fano resonances can occur through interaction between micro-resonators and external cavities such as FP interferometers, which not only allows for higher sensitivity due to the narrower linewidth but can also be used for photonic switches due to sharp tuning between reflection and transmission features [28,30–32]. In our work, the launching conditions were manually adjusted by changing the transverse dimensions (i.e., x and y axes) of a three-axis optical stage used to free-space launch the laser beam into the ECF. The degree of the reflection from the angle-cleaved ECF returned to the interrogator was then used to tune the Fano resonance, while the WGM excitation was simultaneously adjusted due to the variation of the launched modes. This is demonstrated in Figs. 3(a-c), where three different reflection spectra are shown using the same sample under different launching conditions. In this case the launching was adjusted to yield strong WGM resonance features. The mode images (insets in Fig. 3) show that the launched modes were not primarily the fundamental (Gaussian) mode, but rather that higher-order modes of the ECF were phase-matched to the 20 μm polystyrene sphere's WGMs. Extracted signal features from 1575 to 1585 nm are presented in Fig. 3(a1, b1, c1) to show the peaks more clearly, while the corresponding FFTs are presented in Fig. 3(a2, b2, c2). The resonance condition for the transverse electric (TE) and transverse magnetic (TM) WGMs are given by [33]:

$$n_p^p \frac{\psi_l'(n_p k_0 \rho)}{\psi_l(n_p k_0 \rho)} = n_s \frac{\chi_l'(n_s k_0 \rho)}{\chi_l(n_s k_0 \rho)}. \quad (2)$$

where  $n_p$  is the index of the microsphere,  $n_s$  is the surrounding index,  $l$  is the azimuthal mode number,  $p$  is the polarization coefficient,  $k_0$  is the resonance wavenumber, and  $\psi_l$  and  $\chi_l$  are associated with spherical Ricatti-Bessel and Ricatti-Neumann functions. A summary of the theoretical TE and TM resonant wavelengths based on Eq. (2) are shown in Table 1 as a function of azimuthal mode number (radial mode number:  $q = 1$ ), based on a polystyrene sphere (diameter of 20 μm, refractive index of 1.55) in the wavelength range of interest. The resonant peaks and troughs of the experimentally measured spectra ('A' and 'B' in Fig. 3) are also listed in the table for comparison. The azimuthal mode order alignment of 'A' and 'B' is based on the difference of resonant wavelength compared to the theoretical values under the same azimuthal mode order. In Table 1, the difference between each pair of experimentally measured adjacent peaks or troughs in series A (or B) is 25 to 27 nm, which matches well with the theoretical difference between



each adjacent TE (or TM) resonant wavelength. Therefore, the observed peaks and troughs in the reflection spectra from Fig. 3 are concluded to have occurred from WGM resonances.

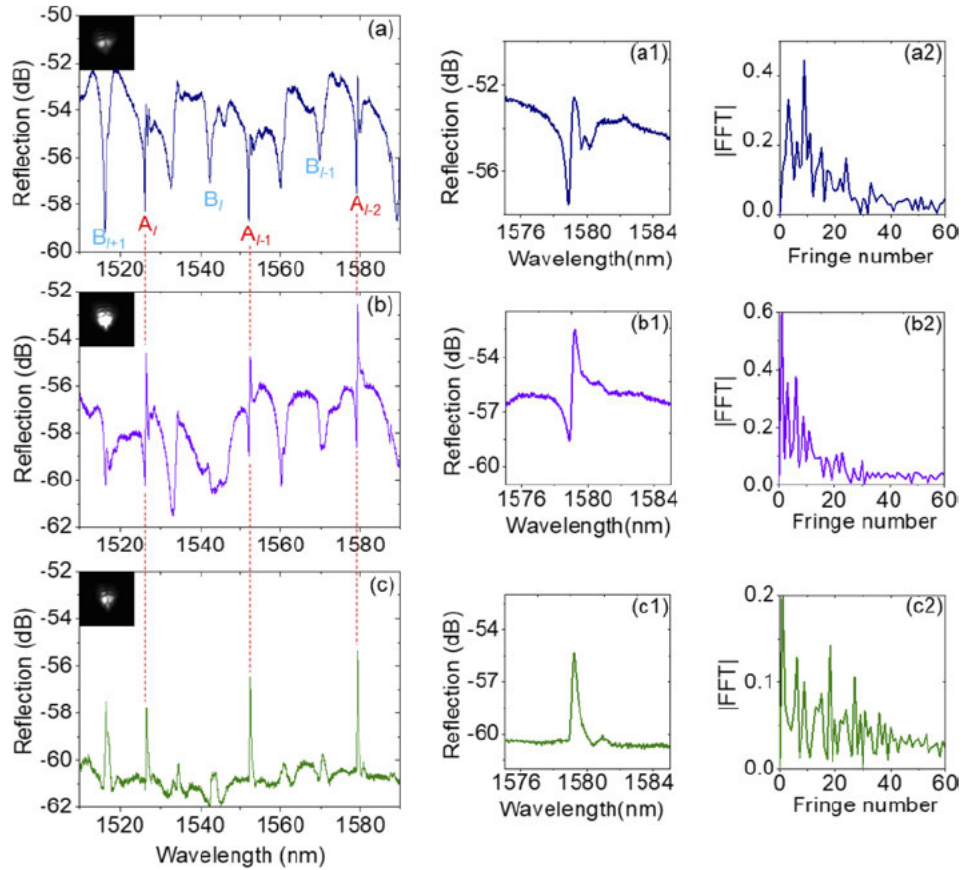


**Fig. 3.** Reflection spectra of observed WGMs under different launching conditions in (a), (b), and (c) with relevant near-field images captured from the far end of the ECF shown in the insets. Magnified reflection spectra are shown in (a1), (b1) and (c1). The corresponding FFTs are displayed in (a2), (b2) and (c2) with the same color, respectively.

**Table 1.** Simulated resonant wavelength of ( $20\ \mu\text{m}$  sphere) WGMs.

Mode	$l+1$	$l$	$l-1$	$l-2$
TE	1515 nm	1539 nm	1563 nm	1589 nm
TM	N.A.	1522 nm	1546 nm	1571 nm
A	N.A.	1526 nm	1552 nm	1579 nm
B	1516 nm	1542 nm	1569 nm	N.A.

In theory, TE modes have longer resonant wavelengths compared to TM modes under the same azimuthal order according to Table 1. Therefore, the observed dips at positions ‘A’ in Fig. 3(a) are fundamental TM resonant modes ( $q=1$ ), while ‘B’ series are fundamental TE resonant modes, and the remaining peaks and troughs are higher order radial modes ( $q>1$ ) [7,15,17]. We have not

listed the exact value of  $l$ , which is estimated to be  $57 \pm 2$ , as it is difficult to precisely assign due to errors in the size and refractive index of the polystyrene spheres in the simulation.

In addition, the FP cavity plays a significant role during the tuning of the spectrum under various launching conditions. This can be seen by the change in resonant peak properties under different mode launching conditions at positions 'A' indicated by the red dashed lines in Figs. 3(a-c). When the maximum of the FP interference varies around the sphere resonance wavelengths, it leads to Fano asymmetric features as shown in Fig. 3(a1) and (b1). Unlike Fig. 3(a1) and (b1), the reflection peaks in Fig. 3(c1) are purely from WGM resonances. This can be explained by the lower background ( $< -60$  dB) as the reflection from the fiber input is not collected by the interrogator due to the cleaved angle under the specific launch conditions of the incident light. On the other hand, the spacing of the sharp peaks is 25 to 27 nm in Fig. 3(c), which is impossible to match with the three maxima of FP fringes (FSR=35 nm) to contribute three total reflections (with symmetric Lorentzian shapes) [32]. That is, at least one of the three resonant wavelengths [ $A_{l-2}/A_{l-1}/A_l$  in Fig. 3(c)] would show an obvious Fano asymmetry if the FP interference was involved.

### 3.3. Coupling to multiple particles

To demonstrate multi-particle WGM excitation, a new fiber sample was prepared, initially by having a single 12  $\mu\text{m}$  polystyrene sphere as shown in Fig. 4(a). Two reflection spectra were obtained as shown in Fig. 4(a1) with related (color matched) mode images at top. Two obvious peaks at 1515 and 1561 nm are from the fundamental TE mode with a wavelength spacing of 46 nm, which is well matched with theory, while small peaks at 1531 and 1577 nm are from the fundamental TM mode. We measured a Q-factor of  $2.2 \times 10^4$  as shown in the magnified inset of Fig. 4(a1), which is comparable to other reported Q-factors using polystyrene spheres [5,6,8].

A second sphere with a diameter of 26  $\mu\text{m}$  was then added to the same fiber as in-line as possible with the 1<sup>st</sup> sphere, with a center-to-center separation of 28  $\mu\text{m}$  between the two spheres. The measured reflection spectra from the sample with two spheres are shown in Fig. 4(b1, b2). The two peaks shown at 1516 and 1562 nm in Fig. 4(b1) match with the spectra from the smaller original sphere in Fig. 4(a1), while the broader peak at 1522 nm is from the larger added sphere. In comparison, the peaks shown in the black spectrum in Fig. 4(b2) are dominantly from the 2<sup>nd</sup> larger sphere while those in the orange spectrum are dominantly from the 1<sup>st</sup> smaller sphere due to a slight difference in the ECF launching conditions. The WGM resonance from the second, larger, microsphere was relatively weaker compared to the first, smaller, microsphere, which is counter-intuitive given smaller microspheres generally have greater geometric loss leading to lower Q-factor. We attribute this to the fabrication variability of the microspheres (i.e., sphericity) for the particular excitation plane used in our experiments. Regardless, our results in Fig. 4 demonstrate that ECF mode launching can be controlled to excite WGMs in the two microspheres either separately or simultaneously.

Coupling between the two spheres is unlikely to have occurred in our case due to their large separation, but it could be considered in future work to investigate the evanescent coupling between several closely placed spheres/resonators (e.g., slow light) [26,34]. In future, it would also be possible to redesign the ECF geometry in order to hold and excite particles with a larger size (e.g., 50–200  $\mu\text{m}$  silica spheres) to achieve even higher Q-factors [11]. Note that there is a trade-off between better Q-factor and higher sensitivity (wavelength shift) for sensing applications, where large spheres would contribute a higher Q-factor but relatively smaller wavelength shift during biosensing measurements [1]. Our current scenario with using small resonators would be particularly favorable for biosensing applications. Therefore, there is a range of flexibility for using the ECFs to couple into different spheres (size and material), to adjust either better Q-factor or sensitivity for serving specific purposes.

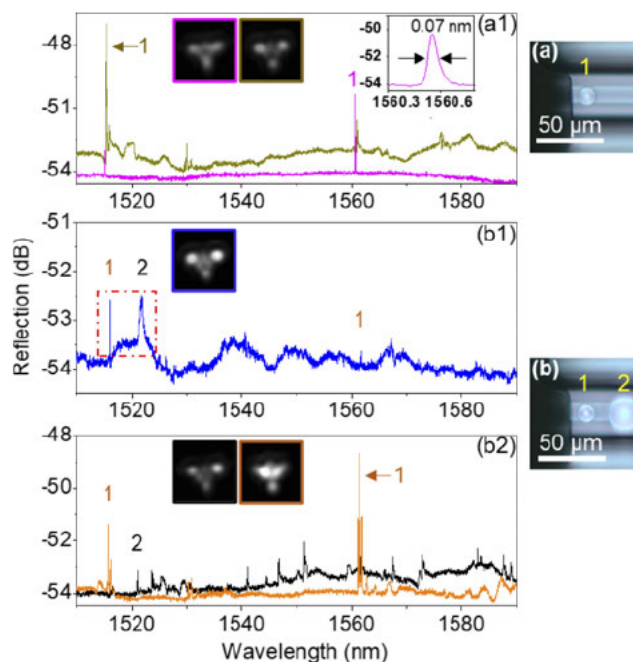


**Fig. 4.** Multi-particle WGM excitation. (a) ECF sample (length: 210 mm) with a single small polystyrene sphere. (a1) Two measured reflection spectra from the sample with a single sphere under different mode launching conditions (insets show corresponding near-field output). Inset: a magnified peak at 1561 nm to show the achievable high Q-factor using a small microsphere. (b) A large sphere is added on the ECF without changing the 1st small sphere. (b1) Reflection spectrum from the sample with two microspheres, showing the simultaneous excitation of WGMs from both microspheres. (b2) Reflection spectrum from the sample with two microspheres, showing either predominantly exciting WGMs in the small microsphere (orange) or the larger microsphere (black).

#### 4. Conclusions and outlook

We have proposed and demonstrated an evanescent field WGM excitation scheme using an ECF. In addition to being a robust platform for WGM excitation, we show that by controlling the mode launching conditions of this few-moded fiber, combined with a Fano resonance effect, we have a high degree of flexibility in tuning the resulting reflection spectrum. In particular, multi-particle WGM excitation has been achieved in a single fiber either simultaneously or separately via adjustment of the mode launching conditions. We now outline several practical and optical refinements to our approach that could be addressed in the future.

One consideration is the trade-off between the tunability gained by the free-space launching used in this work versus an all-fiber integrated configuration by splicing. In previous work we have shown that the ECF can be spliced with standard single mode fibers [25,27,35], and an all-fiber WGM device could be considered in future. Although the spectrum tunability would thus be restricted, a spliced scheme would be practical for real-world sensing applications especially in a reflection configuration with distal end measurements.

Another practical issue is fixing the microsphere resonators onto the ECF. In this work the resonators were held simply by physisorption. To increase the mechanical robustness, other techniques to fix the resonator to the ECF surface could be considered, such as chemical bonding or embedding it into a low refractive index glue as has been reported for lasing or thermal

sensing devices [36,37], noting that the latter would not be suitable for interaction between the micro-coupler and an analyte in liquid or a biological environment.

The efficiency of the coupling to the micro-resonators and the corresponding trade-off with the number of resonators along the fiber should also be considered. That is, subsequent downstream microspheres will have reduced signal intensity due to the induced scattering loss resulting from the upstream microspheres. The evanescent field of the ECF used in this work is relatively small, which is suitable for multi-resonator coupling along a single fiber. On the other hand, a smaller core ECF (e.g.,  $< 2 \mu\text{m}$  [38]) with a stronger evanescent field could be considered to improve the fiber-resonator coupling efficiency, potentially allowing for use in intensity-dependent lasing or non-linear light generation applications.

The above considerations show the scope of potential advancements beyond our proof-of-concept demonstration, which could be tailored according to the desired application such as nonlinear and quantum optics devices and multi-point sensors and lasers.

**Funding.** Australian Research Council (ARC) (Future Fellowship (FT200100154)); Optofab node of the Australian National Fabrication Facility utilizing Commonwealth and South Australian State Government Funding; China Scholarship Council (201706750012); ARC Centre for Nanoscale BioPhotonics (CE14010003); National Heart Foundation of Australia (Fellowship 102093); ARC Integrated Devices for End-user Analysis at Low Levels (IDEAL) Research Hub.

**Acknowledgments.** The authors acknowledge Evan Johnson and Alastair Dowler for their contribution to the fiber fabrication.

**Disclosures.** The authors declare no conflicts of interest.

**Data availability.** Data underlying the results presented in this paper are not publicly available at this time but may be obtained from the authors upon reasonable request.

## References

1. M. R. Foreman, J. D. Swaim, and F. Vollmer, "Whispering gallery mode sensors," *Adv. Opt. Photonics* 7(2), 168–240 (2015).
2. L. He, ŞK Özdemir, and L. Yang, "Whispering gallery microcavity lasers," *Laser & Photon. Rev.* 7(1), 60–82 (2013).
3. F. Vollmer and S. Arnold, "Whispering-gallery-mode biosensing: label-free detection down to single molecules," *Nat. Methods* 5(7), 591–596 (2008).
4. T. Reynolds, A. François, N. Riesen, M. E. Turvey, S. J. Nicholls, P. Hoffmann, and T. M. J. A. c. Monroe, "Dynamic self-referencing approach to whispering gallery mode biosensing and its application to measurement within undiluted serum," *Anal. Chem.* 88(7), 4036–4040 (2016).
5. A. François, N. Riesen, H. Ji, S. Afshar V, and T. M. Monroe, "Polymer based whispering gallery mode laser for biosensing applications," *Appl. Phys. Lett.* 106(3), 031104 (2015).
6. K. Kosma, G. Zito, K. Schuster, and S. Pissadakis, "Whispering gallery mode microsphere resonator integrated inside a microstructured optical fiber," *Opt. Lett.* 38(8), 1301–1303 (2013).
7. O. Svitelskiy, Y. Li, A. Darafsheh, M. Sumetsky, D. Carnegie, E. Rafailov, and V. N. Astratov, "Fiber coupling to BaTiO<sub>3</sub> glass microspheres in an aqueous environment," *Opt. Lett.* 36(15), 2862–2864 (2011).
8. A. François, K. J. Rowland, and T. M. Monroe, "Highly efficient excitation and detection of whispering gallery modes in a dye-doped microsphere using a microstructured optical fiber," *Appl. Phys. Lett.* 99(14), 141111 (2011).
9. J. Lutti, W. Langbein, and P. Borri, "A monolithic optical sensor based on whispering-gallery modes in polystyrene microspheres," *Appl. Phys. Lett.* 93(15), 151103 (2008).
10. N. M. Hanumegowda, C. J. Stica, B. C. Patel, I. White, and X. Fan, "Refractometric sensors based on microsphere resonators," *Appl. Phys. Lett.* 87(20), 201107 (2005).
11. J. C. Knight, G. Cheung, F. Jacques, and T. J. O. Birk, "Phase-matched excitation of whispering-gallery-mode resonances by a fiber taper," *Opt. Lett.* 22(15), 1129–1131 (1997).
12. F. Lei, R. M. Murphy, J. M. Ward, Y. Yang, and S. N. J. P. R. Chormaic, "Bandpass transmission spectra of a whispering-gallery microcavity coupled to an ultrathin fiber," *Photonics Res.* 5(4), 362–366 (2017).
13. Y. Ruan, K. Boyd, H. Ji, A. Francois, H. Ebendorff-Heidepriem, J. Munch, and T. M. Monroe, "Tellurite microspheres for nanoparticle sensing and novel light sources," *Opt. Express* 22(10), 11995–12006 (2014).
14. P. Wang, G. S. Murugan, T. Lee, X. Feng, Y. Semenova, Q. Wu, W. Loh, G. Brambilla, J. S. Wilkinson, and G. Farrell, "Lead silicate glass microsphere resonators with absorption-limited Q," *Appl. Phys. Lett.* 98(18), 181105 (2011).
15. X. Liu, X. Cui, and D. Wang, "Integrated in-fiber coupler for a whispering-gallery mode microsphere resonator," *Opt. Lett.* 45(6), 1467–1470 (2020).
16. X. Bai and D. Wang, "Whispering-gallery-mode excitation in a microsphere by use of an etched cavity on a multimode fiber end," *Opt. Lett.* 43(22), 5512–5515 (2018).
17. R. Wang, M. Fraser, J. Li, X. Qiao, and A. Wang, "Integrated in-fiber coupler for microsphere whispering-gallery modes resonator excitation," *Opt. Lett.* 40(3), 308–311 (2015).

18. J. Wang, X. Zhang, M. Yan, L. Yang, F. Hou, W. Sun, X. Zhang, L. Yuan, H. Xiao, and T. J. P. R. Wang, "Embedded whispering-gallery mode microsphere resonator in a tapered hollow annular core fiber," *Photonics Res.* **6**(12), 1124–1129 (2018).
19. S. C. Warren-Smith, H. Ebendorff-Heidepriem, T. C. Foo, R. Moore, C. Davis, and T. M. Monro, "Exposed-core microstructured optical fibers for real-time fluorescence sensing," *Opt. Express* **17**(21), 18533–18542 (2009).
20. V. S. Afshar, S. C. Warren-Smith, and T. M. Monro, "Enhancement of fluorescence-based sensing using microstructured optical fibres," *Opt. Express* **15**(26), 17891–17901 (2007).
21. Z. Cai, F. Liu, T. Guo, B.-O. Guan, G.-D. Peng, and J. Albert, "Evanescence coupled optical fiber refractometer based a tilted fiber Bragg grating and a D-shaped fiber," *Opt. Express* **23**(16), 20971–20976 (2015).
22. L. Shi, T. Zhu, D. Huang, C. Liang, M. Liu, and S. J. O. Liang, "In-fiber Mach-Zehnder interferometer and sphere whispering gallery mode resonator coupling structure," *Opt. Lett.* **42**(1), 167–170 (2017).
23. L. Shi, T. Zhu, D. Huang, M. Liu, M. Deng, and W. J. O. Huang, "In-fiber whispering-gallery-mode resonator fabricated by femtosecond laser micromachining," *Opt. Lett.* **40**(16), 3770–3773 (2015).
24. L. Peng, L. V. Nguyen, J. Li, N. Riesen, D. Otten, D. G. Lancaster, H. Ebendorff-Heidepriem, and S. C. Warren-Smith, "Two-dimensional mapping of surface scatterers on an optical fiber core using selective mode launching," *APL Photonics* **6**(2), 026105 (2021).
25. L. Peng, J. Li, R. A. McLaughlin, H. Ebendorff-Heidepriem, and S. C. Warren-Smith, "Distributed optical fiber sensing of micron-scale particles," *Sens. Actuator A Phys.* **303**, 111762 (2020).
26. F. Morichetti, C. Ferrari, A. Canciamilla, A. J. L. Melloni, and P. Reviews, "The first decade of coupled resonator optical waveguides: bringing slow light to applications," *Laser & Photon. Rev.* **6**(1), 74–96 (2012).
27. S. C. Warren-Smith, R. Kostecki, L. V. Nguyen, and T. M. Monro, "Fabrication, splicing, Bragg grating writing, and polyelectrolyte functionalization of exposed-core microstructured optical fibers," *Opt. Express* **22**(24), 29493–29504 (2014).
28. M. F. Limonov, M. V. Rybin, A. N. Poddubny, and Y. S. Kivshar, "Fano resonances in photonics," *Nat. Photonics* **11**(9), 543–554 (2017).
29. Y. Wang, H. Zhao, Y. Li, F. Shu, M. Chi, Y. Xu, and Y. J. P. R. Wu, "Mode splitting revealed by Fano interference," *Photonics Res.* **7**(6), 647–651 (2019).
30. Y. Xiao, V. Gaddam, and L. Yang, "Coupled optical microcavities: an enhanced refractometric sensing configuration," *Opt. Express* **16**(17), 12538–12543 (2008).
31. W. Liang, L. Yang, J. K. Poon, Y. Huang, K. J. Vahala, and A. Yariv, "Transmission characteristics of a Fabry-Perot etalon-microtoroid resonator coupled system," *Opt. Lett.* **31**(4), 510–512 (2006).
32. S. Fan, "Sharp asymmetric line shapes in side-coupled waveguide-cavity systems," *Appl. Phys. Lett.* **80**(6), 908–910 (2002).
33. I. Teraoka and S. Arnold, "Theory of resonance shifts in TE and TM whispering gallery modes by nonradial perturbations for sensing applications," *J. Opt. Soc. Am. B* **23**(7), 1381–1389 (2006).
34. L. Maleki, A. Matsuoka, A. Savchenkov, and V. Ilchenko, "Tunable delay line with interacting whispering-gallery-mode resonators," *Opt. Lett.* **29**(6), 626–628 (2004).
35. N. P. Mauranyapin, L. S. Madsen, L. Booth, L. Peng, S. C. Warren-Smith, E. P. Schartner, H. Ebendorff-Heidepriem, and W. P. Bowen, "Quantum noise limited nanoparticle detection with exposed-core fiber," *Opt. Express* **27**(13), 18601–18611 (2019).
36. G. Zhao, ŞK Özdemir, T. Wang, L. Xu, E. King, G.-L. Long, and L. J. S. B. Yang, "Raman lasing and Fano lineshapes in a packaged fiber-coupled whispering-gallery-mode microresonator," *Sci. Bull.* **62**(12), 875–878 (2017).
37. F. Monifi, S. K. Özdemir, J. Friedlein, and L. Yang, "Encapsulation of a fiber taper coupled microtoroid resonator in a polymer matrix," *IEEE Photonics Technol. Lett.* **25**(15), 1458–1461 (2013).
38. E. P. Schartner, A. Dowler, and H. J. O. M. E. Ebendorff-Heidepriem, "Fabrication of low-loss, small-core exposed core microstructured optical fibers," *Opt. Mater. Express* **7**(5), 1496–1502 (2017).

## **CHAPTER 6**

### **Conclusions and future work**

This thesis focuses on the development of a novel photonics platform, an exposed core microstructured optical fibre (ECF), as a versatile tool for micron-scaled distributed sensing. Distributed particle sensing and micro-resonator coupling, have been demonstrated towards this aim.

The studying of individual particles can help us understand their properties and dynamics (e.g., functional responses and intracellular interactions) for disease diagnostics and drug research. Many fibre sensing schemes for single particle detection have been reported but lack a capability to integrate both spatial information and particle characteristics (e.g., size and shape). There is a need to develop a practical, minimally-invasive, label-free and multiplexed fibre sensing scheme, which would bring insights to both fibre optics and biomedical communities.

To address this need, distributed sensing of microscale particles with microscale spatial resolution is first demonstrated, and the detection distance is up to tens of millimetres. In this device, micron-scale particles' scattered signals can be coupled back to the fibre's guided modes via an evanescent field interaction and their axial positions are determined using the optical frequency domain reflectometry (OFDR) technique.

Building upon from this first work, a demonstration of two-dimensional mapping of surface scatterers (femto-second written ablations) was then realised using a single ECF based on both the OFDR technique and the few-mode property of the ECF. Three individual modes were launched into the fibre, separately, and the signals from surface scatterers varied with the overlapping evanescent field of the launched mode. The transverse distributions of the surface scatterers were mapped using a mode-multiplexed matrix approach while the axial distributions of the scatterers were detected based on the OFDR technique.

To acquire the particle characteristics, such as size, machine learning algorithms were used to analyse the particles' size information. Due to the multimoded nature of the ECF, OFDR data from particles were obtained with different modal superpositions, which shows a pathway to uncover the property of the particles under evanescent field excitation. This is a study of particle size characterisation using a single ECF, with the spatial axial information obtained simultaneously using OFDR.

The above studies looked at sensing the position and characteristics of particles,

however, the ECF platform can also be used as a tool for coupling the light to the whispering gallery modes (WGMs) of spherical particles (micro-resonators), which can in-turn be used for sensing. Furthermore, it was shown that the resulting WGM spectrum can be further tailored through a Fano resonance and mode launching conditions. WGM excitation from two in-line polystyrene spheres with different sizes has been realised simultaneously or separately by controlling the mode launching conditions. This is amenable to building multi-point sensors/lasers with multiple resonators distributed along the ECF.

Based on the work investigated in this thesis, potential future works are listed as follows:

- Particles in microfluids could be tracked based on the proposed sensing scheme. Hollow core fibres providing greater light-matter interaction could be considered.
- Particles could be biological samples such as cells, so their spatial distributions and morphology are as targets towards disease diagnosis and precise treatment. Machine learning would be possible to learn the complex behaviour resulting from the micron-scale particles' scattering under evanescent field excitation towards instrumental applications.
- WGM multipoint lasing and sensing could be investigated based on the ECF coupling platform with the consideration of coupling efficiency by replacing with a smaller core ECF, and single mode selection resulting from several closely coupling resonators is another potential direction based on evanescent field interaction.



# Appendices

## A In vivo pH fibre probe using ECFs

### Publication overview

This section is composed of a publication [P4], whereby the ECF is shown as a suitable platform for *in vivo* biosensing based on the evanescent field. Although the previous chapters are all based on label-free configurations, luminescent materials are still commonly used for current *in vivo* sensing or imaging measurements. As introduced in the literature review, sol-gel and polymer are general materials to encapsulate the fluorophores for fabricating fibre sensing probes. Here, a natural silk is used as a base material with the major consideration of biocompatibility. At the same time, the fabrication of PMMA ECFs was explored due to the potential advantage—greater flexibility towards *in vivo* applications, with the fabrication results displayed in the following subsection.

### Statement of contribution

This publication was the outcome of a collaboration with Dr. Asma Khalid and Prof. Brant C. Gibson at RMIT through the Centre of Excellence for Nanoscale Biophotonics. The feasibility of fibre probes integrated with ECFs for *in vivo* pH sensing measurement in a mouse is demonstrated, for the first time. While pH is an important parameter in a biological body to evaluate the health status, other available fluorophores could be easily deployed to measure other parameters of interest (e.g., oxygen and calcium ions). In this work, I fabricated and characterised all pH fibre probes by splicing commercial double-clad fibres with ECFs; I built the optical set-up for pH measurements in buffer and mice; I did preliminary numerical modelling. This work was also published as a conference paper with me as the first author in [C2]. Silk solution, experimental data analysis and other characterisation were done by collaborators.

## Statement of Authorship

Title of Paper	Silk: A bio-derived coating for optical fiber sensing applications
Publication Status	<input checked="" type="checkbox"/> Published <input type="checkbox"/> Accepted for Publication <input type="checkbox"/> Submitted for Publication <input type="checkbox"/> Unpublished and Unsubmitted work written in manuscript style
Publication Details	Asma Khalid, Lu Peng, Azim Arman, Stephen C. Warren-Smith, Erik P. Schartner, Georgina M. Sylvia, Mark R. Hutchinson, Heike Ebendorff-Heidepriem, Robert A. McLaughlin, Brant C. Gibson and Jiawen Li. "Silk: A bio-derived coating for optical fiber sensing applications". Sensors and Actuators B: Chemical, 311: 127864 (2020).

### Principal Author

Name of Principal Author	Asma Khalid			
Contribution to the Paper	The silk used in the experiments was prepared by Asma Khalid. She participated all the experiments, analysed most of the experimental results and wrote the manuscript.			
Overall percentage	55%			
Certification:	Asma Khalid is the primary author of this paper.			
Signature	<table border="1" style="width: 100%;"> <tr> <td style="width: 80%;"></td> <td style="width: 20%;">Date</td> <td>08-09-2021</td> </tr> </table>		Date	08-09-2021
	Date	08-09-2021		

### Co-Author Contributions

By signing the Statement of Authorship, each author certifies that:

- i. the candidate's stated contribution to the publication is accurate;
- ii. permission is granted for the candidate to include the publication in the thesis; and
- iii. the sum of all co-author contributions is equal to 100% less the primary author's contribution.

Name of Co-Author (candidate)	Lu Peng			
Contribution to the Paper	Lu Peng made all the fibre probes, prepared the optical set-up, and conducted the optical experiments. She also contributed to the theoretical analysis of the fibre sensor with a coating layer and revised the manuscript.			
Overall percentage	22%			
Signature	<table border="1" style="width: 100%;"> <tr> <td style="width: 80%;"></td> <td style="width: 20%;">Date</td> <td>09-08-2021</td> </tr> </table>		Date	09-08-2021
	Date	09-08-2021		

Name of Co-Author	Azim Arman			
Contribution to the Paper	Azim Arman prepared the mice and conducted the in-vivo experiments. He contributed to revise the manuscript.			
Signature	<table border="1" style="width: 100%;"> <tr> <td style="width: 80%;"></td> <td style="width: 20%;">Date</td> <td>10-08-2021</td> </tr> </table>		Date	10-08-2021
	Date	10-08-2021		

Name of Co-Author	Stephen C. Warren-Smith			
Contribution to the Paper	Stephen C. Warren-Smith helped conceptualise the idea. He contributed to the theoretical analysis about the exposed-core fibre, and revised the manuscript.			
Signature	<table border="1" style="width: 100%;"> <tr> <td style="width: 80%;"></td> <td style="width: 20%;">Date</td> <td>09-08-2021</td> </tr> </table>		Date	09-08-2021
	Date	09-08-2021		

Name of Co-Author	Erik P. Schartner		
Contribution to the Paper	Erik P. Schartner contributed to the optical set-up and revised the manuscript.		
Signature	_____	Date	08-09-2021

Name of Co-Author	Georgina M. Sylvia		
Contribution to the Paper	Georgina M. Sylvia made all pH buffers, provided fluorophores and revised the manuscript.		
Signature	_____	Date	09-08-2021

Name of Co-Author	Mark R. Hutchinson		
Contribution to the Paper	Mark R. Hutchinson contributed to the organisation of the collaboration and revised the manuscript.		
Signature	_____	Date	10-08-2021

Name of Co-Author	Heike Ebendorff-Heidepriem		
Contribution to the Paper	Heike Ebendorff-Heidepriem contributed to the organisation of the collaboration and revised the manuscript.		
Signature	_____	Date	09-08-2021

Name of Co-Author	Robert A. McLaughlin		
Contribution to the Paper	Robert A. McLaughlin contributed to the organization of the collaboration, discussion of experimental results and edited the manuscript.		
Signature	_____	Date	09-08-2021

Name of Co-Author	Brant C. Gibson		
Contribution to the Paper	Brant C. Gibson contributed to the organization of the collaboration, discussion of experimental results and edited the manuscript.		
Signature	_____	Date	09-08-2021

Name of Co-Author	Jiawen Li		
Contribution to the Paper	Jiawen Li organised the project, conducted experiments and edited the manuscript.		
Signature	_____	Date	09-08-2021



Contents lists available at ScienceDirect

## Sensors and Actuators B: Chemical

journal homepage: [www.elsevier.com/locate/snb](http://www.elsevier.com/locate/snb)

## Silk: A bio-derived coating for optical fiber sensing applications

Asma Khalid<sup>a,\*</sup>, Lu Peng<sup>b,c</sup>, Azim Arman<sup>d</sup>, Stephen C. Warren Smith<sup>b,c</sup>, Erik P. Schartner<sup>b,c</sup>, Georgina M. Sylvia<sup>b,c</sup>, Mark R. Hutchinson<sup>c,d</sup>, Heike Eberndorff Heidepriem<sup>b,c</sup>, Robert A. McLaughlin<sup>c,d</sup>, Brant C. Gibson<sup>a</sup>, Jiawen Li<sup>c,d</sup>



<sup>a</sup> Australian Research Council Centre of Excellence for Nanoscale BioPhotonics & School of Science, RMIT University, Melbourne, VIC, 3001 Australia

<sup>b</sup> Australian Research Council Centre of Excellence for Nanoscale BioPhotonics, School of Physical Sciences, The University of Adelaide, Adelaide, SA, 5005, Australia

<sup>c</sup> Institute for Photonics and Advanced Sensing, The University of Adelaide, Adelaide, SA, 5005, Australia

<sup>d</sup> Australian Research Council Centre of Excellence for Nanoscale BioPhotonics, Adelaide Medical School, Faculty of Health and Medical Sciences, The University of Adelaide, Adelaide, SA 5005, Australia

## ARTICLE INFO

**Keywords:**  
Silk fibroin  
Optical sensing  
Exposed core fibers  
Biocompatible coatings  
*In vivo* sensing  
pH  
Fiber sensing

## ABSTRACT

Optical fiber chemical sensing is generally achieved through attachment of sensor molecules to the fiber, a process that involves chemicals that are not biologically compatible or are limited to thin monolayer coatings. To address these limitations and enable *in vivo* biosensing, we report here, for the first time, silk fibroin coating of optical fibers for encapsulating fluorescent sensor molecules. Silica exposed core fiber (ECF) samples were coated with a thin layer of silk – a naturally derived biopolymer composed entirely of proteins and amino acids. The silk was doped with the fluorophore 5,6-carboxynaphthofluorescein (CNF), which allows optical measurement of pH by a robust ratiometric fluorescence method. The fluorescent signal from the doped silk layer is coupled into the core of the ECF, enabling remote measurement of pH along the length of the fiber. We have demonstrated real time *in vivo* pH sensing measurements in a mouse model of hypoxia. Our results showed a continuous drop in the subcutaneous pH in the mouse lumbar area as hypoxia developed. The work explores, for the first time, the potential of a natural silk protein coating to perform fiber sensing inside the body.

## 1. Introduction

Biosensing is globally employed in health sciences and biomedical research for disease detection and monitoring of physiological changes [1]. Fluorescence-based biosensing can offer sensitive measurement of physiological parameters such as temperature [2], pH [3], pressure [4], levels of insulin and glucose [5], oxygen and concentration of ions in biological specimens [6]. Through measurement of the fluorescence intensity or wavelength, a biosensor can track changes in the biological system under examination, some of which may reach levels considered abnormal or pathological. The biosensors are usually tested in cells and tissues *ex vivo*, or in collected biological fluids such as blood or urine [7]. *In vivo* sensing is required for applications such as early diagnosis of cancers without surgical procedures, [7,8] and real-time health monitoring such as glucose tracking in diabetes [5] and pH sensing in the case of pulmonary exacerbation [8].

However, application of the biosensors in *in vivo* conditions remains a significant challenge due to limitations in detection techniques that are unable to precisely measure at the targeted area of interest deep

inside the body [8]. To address this, optical fiber based sensors [5,9,10], which are thin and flexible enough to reach previously difficult-to-access regions, have found extensive use in the areas of early disease sensing and health monitoring [1,11]. These optical fiber technologies in combination with fluorescence biosensors enable tracking of physiological parameters at positions remote from the excitation source and detection equipment [1,6,12]. The optical fiber technology has thus emerged as a powerful and reliable tool, allowing the development of new techniques for biological sensing and detection [10].

For optical fiber-based biosensing, it is necessary that the sensor molecules are immobilised onto the glass surface of the fiber. Two classes of immobilisation are typically employed, (a) attachment *via* surface functionalisation or (b) physical encapsulation. The surface functionalisation method involves binding chemicals to the glass surface to provide appropriate functional groups for attachment of the sensor molecules. For example, silanes are covalently attached to the silica glass surface, which can subsequently be attached to biochemicals such as antibodies [13,14]. Alternatively, polyelectrolytes can be

\* Corresponding author.

E-mail address: [asma.khalid@rmit.edu.au](mailto:asma.khalid@rmit.edu.au) (A. Khalid).

<https://doi.org/10.1016/j.snb.2020.127864>

Received 12 October 2019; Received in revised form 13 January 2020; Accepted 12 February 2020

Available online 12 February 2020

0925-4005/ © 2020 Elsevier B.V. All rights reserved.

attached to the silica glass surface through electrostatic interaction with the electronegative glass surface to provide appropriate functional groups for subsequent binding [15,16]. Both processes produce a thin typically less than 10 nm coating, which is more appropriate for binding and sensing larger biomolecules and also provides no physical robustness for the bare optical fiber. For smaller chemicals of physiological interest, such as pH, oxygen, and metal ions, it is more appropriate to encapsulate the sensor molecule within a thicker, semi-permeable coating. For example, pH indicators can be embedded within acrylamide polymer coated onto the tip of an optical fiber, which has been applied to cancer margin detection [3]. However, for long duration *in vivo* measurements there is an ongoing need to develop biocompatible, optical grade coatings for encapsulating fluorescent chemical sensors, which can be coated at ambient temperature and pressure conditions, and homogeneously cover the optical fiber surface.

A biocompatible, optical grade coating is hence needed that encapsulates the fluorescent biosensors, can be coated at ambient temperature and pressure conditions, and homogeneously covers the optical fiber surface for *in situ* or *in vivo* fluorescence-based optical fiber sensing. Silk obtained from caterpillars is an attractive biopolymer for biophotonic applications [17,18]. Silk fiber has been used in medicine for centuries as a suture. However, the unprocessed fiber is opaque and cannot be used in optical applications. Recently, a regenerated form of silk has been obtained through degumming the cocoons, dissolving the fibers and dialyzing in deionized water at room temperature to yield a transparent solution of pure silk fibroin in water [19]. The resulting liquid silk protein self assembles into various structures through application of physical stimuli [19]. The resulting structures exhibit biocompatibility, tunable biodegradability, disintegration into simple proteins, and *in-vivo* non-immunogenicity [17] and have been used as a biomaterial for enhancing optical emission of nanoparticles [17], tissue engineering, drug release [20], and other biomedical imaging and sensing applications [18]. Moreover, the elastic modulus of silk structures matches that of biological tissues, which reduces the likelihood of trauma to surrounding soft tissue due to either fiber motion or natural body motions [21,22]. Finally silk can be doped with a wide range of chemical indicators, fluorescent agents [23] and molecules [20] making it an excellent underlying substance for fabricating biomedical materials and biosensing devices.

Traditional solid optical fibers can only provide a single sensing point at the tip of the fiber [3,24]. To demonstrate the capability of utilizing silk coating to enable a sensing platform along the length of a fiber, we employed exposed core fiber (ECF) in this project. ECF is a class of specialty optical fiber where a micron-scale suspended core is partially exposed to the external environment, allowing the analyte to directly access the core [16]. Through interactions with the evanescent field, ECFs provide a platform for biochemical sensing integrated along the fiber length with the potential for high-sensitivity real-time measurements [25,26].

To demonstrate *in vivo* sensing with silk coated ECF probes, we have used real time pH sensing as an example. Sensing the pH *in vivo* enables the monitoring of the acidification levels in the body associated with pathological conditions [27]. The extracellular pH in normal tissue is known to be relatively basic [28]. Slight variations of pH provide an exploitable avenue for tracking of abnormalities, monitoring of physiological function and the treatment of disease. Perturbations in the levels of oxygen ( $O_2$ ) and carbon dioxide ( $CO_2$ ) may cause changes in the subcutaneous tissue pH. Increase in the levels of  $CO_2$  can increase acidity, which decreases the tissue pH.

This work reports a unique hybrid silk-coated fiber that combines the biocompatibility and optical transparency of silk with the real time remote sensing capability of microstructured ECF. Silk was functionalized with 5,6-carboxynaphthofluorescein (CNF) – a ratiometric fluorescent pH sensor, where the dual emission profile is a result of the acid and base forms of CNF having two different fluorescence emission maxima. The first emission maximum is centred around 560 nm and the

other one around 680 nm. The ratio of these two emission maxima change with pH and determines the acidity or basicity of the local environment efficiently within a biologically-relevant pH window of 6.5–8.0 [34]. The first emission peak mainly increases with the increase in acidity, while the 2nd emission peak rises when the environment is predominantly basic.

A change in pH leads to changes in dual emission peaks of the ratiometric fluorophore CNF. Ratiometric approach removes the intensity dependence which typically restricts the precision of intensity-based fluorophore measurements [3]. CNF silk solution was used to functionalize coating along the length of the ECF via a simple and quick dip-coating procedure. The thin-coated film (~200 nm) of silk-CNF created a sensor capable of detecting events of interest along the ECF. The fabrication and characterization of a silk-CNF coated ECF was performed and successfully employed for real time *in-vivo* pH sensing.

Section 3.1 illustrates the synthesis and optical characterization of silk and CNF via *in-solution* spectroscopy. Section 3.2 performs a numerical simulation to investigate the optimum silk coating thickness required for effective light guidance through the ECF. Section 3.3 explores the fabrication of the silk-CNF coated ECF probes and thickness monitoring through scanning electron microscopy (SEM). The silk-CNF coated ECF probes are calibrated in a set of known pH media as presented in Section 3.4. Finally, in Section 3.5 we demonstrate real time, pH sensing measurements in a mouse model, which shows the potential of the silk coated ECF probes for remote biosensing applications.

## 2. Materials and methods

### 2.1. Silk fibroin extraction

The silk fibroin solution was obtained by boiling and de-gumming *Bombyx mori* cocoons in an alkaline solution of 0.02 M sodium carbonate for 30 min. The silk fibroin hence obtained was then rinsed thoroughly with water and dissolved in 9.3 M LiBr aqueous solution. The solution was then dialyzed in water using a dialysis cassette with a molecular cut off weight of 3500 Da for 48 h. After dialysis, the fibroin solution was transferred into a centrifuge tube. Finally, the dialyzed solution was centrifuged for 2 h at 9000 rpm and the purified supernatant silk solution was stored at a temperature of 4 °C [17].

### 2.2. Structural characterization and thickness of silk coating

The surface morphology and thickness of the silk coating around the ECF was examined with a high-resolution FEI Nova Scanning electron microscope. The SEM was operated in the low vacuum mode at an electron accelerating voltage of 15 kV to avoid charging and melting of silk fibroin coating respectively. The samples were coated with a thin 5 nm layer of platinum (Pt) prior to imaging. The images were collected at high magnifications of 500–4000 $\times$ . The coating thickness was determined through image processing in MATLAB. The scale bars in the corresponding SEM images were first calibrated to the number of pixels. This provided the pixel to  $\mu\text{m}$  conversion factor  $L_m$  for each SEM image. The length tool in the MATLAB image processing window was then used to mark the silk coating at several points along the fiber cross section, as shown with small black lines in results section. These lines in pixels were finally converted to  $\mu\text{m}$  or nm by using the conversion factors  $L_m$ .

### 2.3. In-solution spectroscopy

A pulsed white light laser (WhiteLase WL-SC400, Fianium, NKT Photonics USA) was used to excite the aqueous solutions of silk, CNF, and silk-CNF mixture at a pump wavelength of  $480 \pm 10$  nm. The solutions were transferred to cuvettes and placed in the path of the excitation beam. The fluorescence was collected after passing through a long pass 500 nm filter, which was used to remove the pump light from

the fluorescence signal. The filtered signal was finally detected by the spectrometer (SpectraPro, Princeton Instruments, USA).

#### 2.4. Fiber assembly and system design

Prior to coating, the ECF was fusion spliced to a double clad fiber in order to efficiently couple the fluorescence signal from the ECF to the detection electronics. To excite the CNF fluorophore in the silk-CNF coating, the 473-nm laser was coupled into the distal end of the double clad fiber. The coupled laser light then excited the silk-CNF coated ECF, and a portion of this fluorescent light was then captured into the back-propagating modes of the fiber. The fluorescent signal then passed through a 473-nm long-pass filter (Semrock EdgeBasic) to remove excess excitation light, before being coupled into a spectrometer (Ocean Optics QE Pro) via a 200- $\mu$ m optical fiber patch cable as described in literature [3].

#### 2.5. Subjects

Adult male Balb/c mice were supplied from the Animal Resources Centre (Murdoch, WA, Australia) housed in 18 °C  $\pm$  6 with 12:12 hours light: dark and with food and water provided *ad libitum*. All procedures were conducted under the University of Adelaide Animal Ethics approval number M-2018-024 in compliance with the Australian code for the care and use of animals for scientific purposes.

#### 2.6. Surgical procedure

Under deep anaesthesia with 2% inhalation isoflurane and animal in ventral recumbency, the lower lumbar area was prepared aseptically for the surgical procedure. A subcutaneous pocket was created via an 18-gauge needle insertion in the lower lumbar area. The CNF-silk coated fiber sensor was implanted in the subcutaneous space for the duration of the experiment. To induce hypoxia, inhalation isoflurane increased to 5% and oxygen level reduced to the minimal level, pH sensing continued for the remainder of the experiment until the time of death.

### 3. Results and discussion

#### 3.1. Characterisation of silk CNF mixture

CNF is a sensitive dual-emission ratiometric dye, which fluoresces in the visible to near infrared range when excited in the blue spectral region (450–480 nm). As reported, the emission spectrum of the dye consists of two peaks, the first at approximately 560 nm and a second at 680 nm, with an intensity ratio dependent on the pH of the environment surrounding the fluorophore [3]. As reported in the literature, the CNF is able to detect pH values in the biologically relevant window of 6.5–8.0 [29]. Prior to performing optical sensing with silk-CNF coated ECF probes, it was important to explore if silk effects the chemical or optical characteristics of the CNF dye, or introduces a background fluorescence noise that suppresses the optical emission of the dye. Hence, we first tested the colloidal stability as well as the fluorescence of CNF in silk as a function of pH via in-solution spectroscopy.

##### 3.1.1. Colloidal stability of CNF in silk

CNF (0.5 mg) was first mixed in 100  $\mu$ L of phosphate buffer solution (PBS), and then combined with 900  $\mu$ L of silk (7 mg/mL) solution in one vial and with 900  $\mu$ L milli Q water in a separate vial. The CNF was only partially miscible in water and large agglomerates were formed as is visible in the vial (inset) of Fig. 1(a).

In contrast, the dye was homogeneously suspended in silk aqueous solution as shown in the vial (inset) of Fig. 1(b). Dynamic light scattering (DLS) was used to determine the size of dye agglomerates in the two solutions. The DLS graph of Fig. 1(a) shows a wide distribution of size, which indicates high degree of agglomeration in the micrometer

range for CNF-water mixture. In comparison, the DLS graph of Fig. 1(b) demonstrates a narrow distribution centered around 5 nm, indicating that the CNF molecules agglomerate to a much lesser extent in silk. This suggests that the silk proteins stabilize the dye molecules, leading to a homogenous silk-CNF aqueous solution.

Silk possesses a unique block copolymer structure, consisting of large hydrophobic domains and small hydrophilic spacers. These promote self-assembly into organized nanoscale crystalline domains ( $\beta$ -sheets) separated by more flexible hydrophilic spacers [30]. Silk fibroin is hence known to offer a highly stabilizing environment [31] for incorporated molecules [30].

##### 3.1.2. Fluorescence properties of CNF in solution

The optical emission properties of the silk-CNF were investigated via an in-solution spectroscopy setup, with the results shown in Fig. 2. The samples were held in a cuvette and exposed to 480  $\pm$  10 nm excitation wavelength light. The fluorescence was filtered with a 500 nm long pass filter and collected through a spectrometer (SpectraPro fitted with a PIXIS CCD camera, Princeton Instruments, USA). The fluorescence spectra of the CNF dye in water and silk aqueous solution at an excitation wavelength of 480 nm are shown with black and blue plots of Fig. 2(a), respectively. The concentrations of silk, CNF and silk-CNF in aqueous solutions are shown inside the legend. CNF in water shows bright fluorescence, with the short wavelength peak at 560 nm and a second longer wavelength peak at 680 nm, at a neutral pH of 7.0. Since the silk proteins consist mainly of amino acids, combining CNF and silk reduces the overall pH of the mixture, which was measured to be 6.5 with a standard electrode pH meter probe. The fluorescence spectrum of the silk-CNF mixture does not show the second peak, indicative of slightly acidic pH. However, for both cases, the fluorescence spectra of CNF in water and silk are bright and well distinguished.

##### 3.1.3. Silk autofluorescence

The silk only solution at a concentration of 5 mg/mL shows a broad fluorescence band with low intensity at 500–700 nm, centered at 538 nm. The concentration of silk is 100 $\times$  larger than CNF, yet the autofluorescence background is substantially lower than the fluorescence intensity of the dye. This means that autofluorescence of silk does not interfere with CNF sensor's performance.

##### 3.1.4. pH response of silk-CNF mixture

As mentioned earlier, CNF is usually employed as a dual-emission dye where the intensity ratio of the two emission peaks, centered around 560 nm and at 680 nm, depends on the external pH. To obtain the response of the dye in the silk solution, the fluorescence spectra were obtained for the silk-CNF mixture in a range of known pH media. The pH of the mixture was increased in steps of 0.2 from 6.8 to 8.0, by adding 10  $\mu$ L drops of 1 mM NaOH. Fig. 2(b) shows the corresponding fluorescence spectra of the silk-CNF mixture. As reported in literature [3], the intensity of the 2nd peak gradually increased as the overall pH of the mixture increased beyond the neutral pH of 7.0. Accordingly, we can determine pH variations by monitoring the fluorescence spectra of the silk-CNF solution.

via in-solution spectroscopy, it was validated that no quenching was introduced by silk. Hence the biopolymer does not influence the chemical or optical characteristics of CNF dye.

#### 3.2. Optical properties of silk coated fiber

The silk coating has a refractive index larger than that of silica glass (approximately 1.54 [17] compared to 1.4639). Therefore, if the silk coating is excessively thick compared to the wavelength of light it will support guided modes and result in the excitation and fluorescence light to leak from the optical fiber core into the coating. To determine the coating thickness that allows detection without the leakage of light, a simulation was performed based on the finite element method by

A. Khalid, et al.

Sensors & Actuators: B. Chemical 311 (2020) 127864

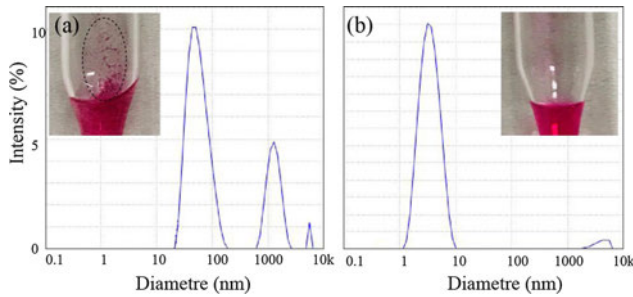


Fig. 1. (a) Comparison of the colloidal stability of CNF dye in water and (b) silk aqueous solution. The insets show images of the respective mixtures in glass vials. Large agglomerates are visible in water as indicated with a dotted oval in the inset of (a). The graphs show the DLS particle size distribution for (a) CNF in water and (b) CNF in silk solutions performed via zeta sizer. (For colored image, the reader is referred to the web version of this article.)

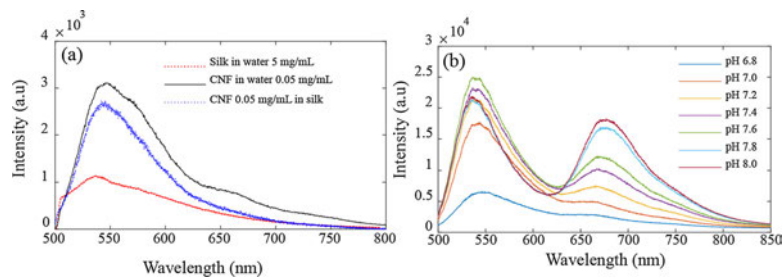


Fig. 2. (a) In solution fluorescence spectra for silk (red), CNF (black) and silk CNF aqueous solutions (blue). (b) The spectral variation of the silk CNF mixture with change in pH. (For interpretation of the references to colour in this figure legend, the reader is referred to the web version of this article.)

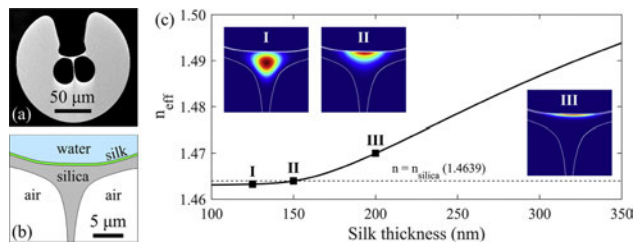


Fig. 3. (a) SEM image of the ECF, with a core diameter of approximately 7.5  $\mu\text{m}$  and outer diameter of 160  $\mu\text{m}$ . (b) The simulation model consisting of the exposed fiber section coated with silk (green) and immersed in water (blue). (c) Effective refractive index of the fundamental mode, showing the Poynting vector mode distribution at thicknesses of 125 nm (I, core guided), 150 nm (II, hybrid guided) and 200 nm (III, coating guided). Only the fundamental mode polarized parallel to the exposed core surface is shown, noting that the behavior of higher order modes and the fundamental mode polarized perpendicular to the exposed core surface display the same basic properties and transition behavior between core/hybrid/coating guided modes. (For interpretation of the references to colour in this figure legend, the reader is referred to the web version of this article.)

importing an SEM image of the ECF shown in Fig. 3(a) into COMSOL 5.2 (Comsol Inc., MA, USA). The model used is shown in Fig. 3(b), indicating the silica glass core (grey,  $n = 1.4639$ ), which is surrounded by two air holes (white,  $n = 1.0$ ) and the exposed side coated with thin silk film (green,  $n = 1.54$ ) and exposed to water (blue,  $n = 1.33$ ).

Fig. 3(c) shows the effective index of the fundamental mode of the structure at the excitation wavelength  $\lambda_{\text{exc}} = 472 \text{ nm}$  for CNF, that is, the guided mode with the highest effective index. It can be seen that for a sufficiently subwavelength coating thickness (e.g. mode image I in Fig. 3(c) with thickness 125 nm) the fundamental mode is predominantly bound to the core of the fiber. Here the silk coating does not support guided modes and thus cannot leak light out of the ECF. As the coating thickness is increased (e.g. mode image II in Fig. 3(c) with thickness 150 nm) the mode becomes a hybrid of core-guided and coating-guided with an effective index that surpasses the glass refractive index. Beyond 150 nm thickness (e.g. mode image III in Fig. 3(c) with thickness 200 nm) the silk coating supports a coating-guided mode. Note that the ECF-coating structure also supports other higher order (lower effective index) modes, which all share the same

basic behavior for the above described core/hybrid/coating-guided regions. Beyond approximately 200 nm the silk coating acts as a waveguide that can effectively leak light out of the optical fiber core into the coating, which is ultimately lost. Hence increasing silk content on ECF may compromise the sensing performance of the fiber if the silk content is excessively increased and the thickness of the coating becomes above 200 nm. To maintain the sensing performance and efficiency of the ECF, the silk content should be kept below 200 nm.

### 3.3. Structural characterization of silk coated exposed core fibers

The ECF probes were coated with two different concentrations of silk and imaged with scanning electron microscopy (SEM). Silk fibroin obtained from Bombyx mori silk cocoons was purified and dialysed in water that yielded an as-prepared silk fibroin solution with a concentration of 70 mg/mL. A  $10\times$  diluted silk solution at 7 mg/mL was also prepared by adding milliQ water to the as-prepared silk solution. CNF dye (0.5 mg) was combined with 1 mL of the as-prepared and diluted silk solutions in two separate vials. The ECF probes were first



A. Khalid, et al.

Sensors &amp; Actuators: B. Chemical 311 (2020) 127864

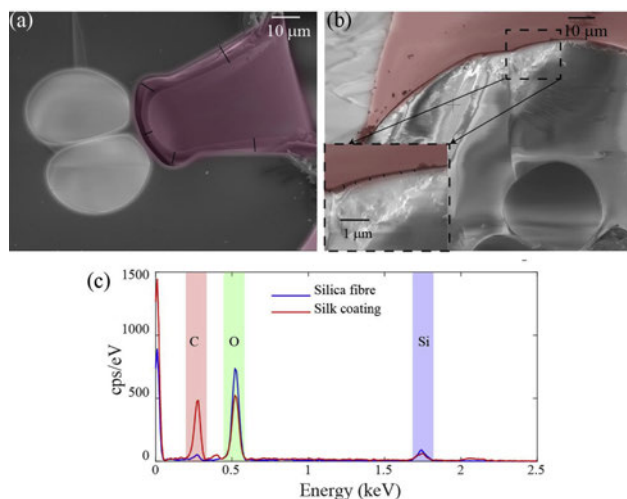


Fig. 4. (a) SEM image of an ECF probe coated using silk solution with 70 mg/mL concentration. Silk layer coated uniformly on the outside of the ECF as indicated with shaded pink region. (b) The SEM image of an ECF coated using silk solution with 7 mg/mL concentration showing relatively thinner silk coating (pink) on the fiber. The grey region represents the non coated fiber cross section. The inset inside the dotted rectangle shows a magnified area of the fiber used to measure the coating thickness. (c) EDS spectra of the silk coated region (red curve) and non coated exposed silica fiber (blue curve). (For interpretation of the references to colour in this figure legend, the reader is referred to the web version of this article.)

sealed by melting each end using an arc splicer (FSM-100 P, Fujikura, Japan) to ensure that the silk solution does not enter the air holes of the structured fibers. The fibers were then coated with the two mixtures by dipping these in the silk solution for 30 s using an automated dip coater (RDC 21-K, Bungard, Germany). The fibers were then lifted and dried in air for 60 s, followed by dipping in 90 % ethanol for 30 s. After ethanol treatment, the silk-coated ECF probes were allowed to dry for 30–60 s. The treatment was performed to induce crystallinity to the amorphous silk fibroin, leading to higher stiffness and mechanical strength of the coating [32]. The edges of the fibers were then cleaved to remove the seal and expose the core and silk coating for further characterization.

The dimensions and cross-sectional structure of the silk coated fiber samples were imaged using SEM. Fig. 4(a) and (b) show SEM images of the ECF coated with the as-prepared (70 mg/mL) and diluted (7 mg/mL) silk concentrations, respectively.

The thickness of silk coating was determined through image processing in MATLAB. A thickness of  $x_p = 3.0 \pm 1.4 \mu\text{m}$  was achieved for the as-prepared silk concentration of Fig. 4(a), which is larger than the optimum coating ( $\leq 200 \text{ nm}$ ) calculated numerically in the previous section. To reduce the coating thickness a  $10\times$  dilution of the silk was prepared, and dip coated on the ECF. Image 4(b) shows a coating much thinner compared to the diameter of the fiber. The area inside the dotted rectangle was zoomed several times as shown in the inset of Fig. 4(b). Image processing revealed a thickness between 120–250 nm, averaging at a value of  $x_d = 220 \pm 50 \text{ nm}$  around the ECF. This is roughly  $10\times$  smaller compared to  $x_p$  for the as-prepared silk solution.

The energy dispersive X-ray spectroscopy (EDS) mode was selected in SEM to perform an elemental analysis of the uncoated and silk coated regions of the ECF probe. The EDS spectra of Fig. 4(c) were collected from the cross section of the silica fiber (grey) and silk coating (pink) from SEM image of Fig. 4(b). The red data in (c) collected from silk protein coating, made of hydrocarbon chains, shows a distinct carbon (C) peak as opposed to the blue data from non-coated fiber cross-section. In contrast, the blue data shows silicon and oxygen peaks as expected from glass ( $\text{SiO}_2$ ) structure.

In summary, the SEM analysis revealed that the thickness of the silk coating on the ECFs is dependent on the concentration of silk. A concentration of 7 mg/mL yielded a coating thickness of  $\sim 200 \text{ nm}$ , which according to the numerical simulation of Section 3.2 falls within the optimum coating range that can efficiently propagate the fluorescence

through the core of the ECF. Hence the 7 mg/mL concentration was used for pH sensing.

#### 3.4. Calibration of silk-CNF coated fiber probes

To employ the hybrid silk-CNF as a pH sensor, it is important to quantify the fluorescence of the hybrid material to external pH changes. A calibration was performed for the ECF probe with  $\sim 200 \text{ nm}$  silk-CNF coating by determining the ratio of the CNF fluorescence peaks as a function of pH.

##### 3.4.1. pH response of silk-CNF fiber coating

Fluorescence spectra were obtained for the silk-CNF coated ECF probes. The ECF probes, like the one shown in Fig. 4(b), were tested for pH sensing in a series of phosphate buffers with known pH values from 6.8–8.0. Fig. 5(a) demonstrates the fluorescence spectra obtained from one of the silk-CNF coated ECF probes. Similar to the result of silk-CNF solution (Fig. 2(b)), the intensity of the 2nd peak gradually increases with increase in pH for the coated ECF probe.

##### 3.4.2. Peak ratios versus pH

For the ratiometric analysis, the area under the curve (AUC) for the 1st peak (510–625 nm) was divided by that for the 2nd peak (626–850 nm). MATLAB was used to determine the area under the two peaks. The ratio of the AUCs of the two emission peaks was plotted as a function of pH, as shown with blue circles in the plot of Fig. 5(b). To evaluate the repeatability of the silk-CNF coated ECF probe, the data for three different runs of the probe was taken and error bars (blue) were plotted around the average data. The average data was fitted with a linear curve (black) with a negative slope,  $-0.91 \times \text{pH} + 8.25$ , demonstrating that the ratio increases linearly in intensity as the local pH of the environment increases. The figure also demonstrates the AUC ratios for the silk-CNF mixture (red stars). The data clearly indicates that irrespective of silk-CNF in solution or as coating, the peak ratios match and coincide with each other at most pH values. To evaluate the reproductivity of the probe, four additional fiber probes were fabricated and characterised. The results are shown in supplementary information Figure S5.

The result above demonstrates that silk-CNF ECF can be used as a reliable fluorescence-based ratiometric sensor for monitoring pH and

A. Khalid, et al.

Sensors &amp; Actuators: B. Chemical 311 (2020) 127864

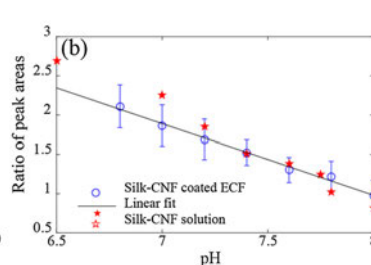
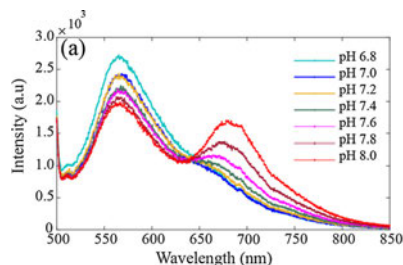


Fig. 5. (a): Fluorescence spectra of silk CNF coated ECF probe at different pH values from 6.8 to 8.0 (b) Calibration curve for the silk coated ECF as a function of pH. Blue data represents the average ratiometric data (circles) for silk CNF coated fiber (3 repeated measurements) as well as error bars indicate measurement variations. The linear fit to these averaged values is represented by the black linear equation  $R = 0.91 \times pH + 8.25$ , where R is the ratio of the 1st peak with respect to the 2nd peak. The red stars are ratios

obtained for silk CNF mixture through in solution spectroscopy from Fig. 2(b). (For interpretation of the references to colour in this figure legend, the reader is referred to the web version of this article.)

establishes a calibration curve that can be used for subsequent measurements.

### 3.5. Real time pH sensing *in vivo*

After calibration of the silk-CNF coated fiber probe in phosphate buffer solutions of known pH and confirming the linear response of the silk-CNF coating with changes in the local pH, the fiber probe was tested *in vivo* for biosensing in a mouse model. The fiber probe was introduced subcutaneously through a hypodermic needle incision, as shown in Fig. 6. The fluorescence spectra and subcutaneous pH measurements were recorded in a live animal for the first 4 min of data recording. The oxygen supply was then cut off slowly, and the spectral changes and pH were recorded for an additional 15 min. The changing fluorescence spectra, and corresponding pH values as a function of time are shown in Fig. 7(a) and (b) respectively.

The pH sensing was performed *in vivo*, and the optical fiber enabled sensing remotely from the excitation source and detection electronics. The spectral changes were monitored as the subcutaneous pH changed during the reduction of oxygen supply in the animal captured during an unrelated surgical procedure (University of Adelaide Animal Ethics approval M-2018-024). The fluorescence variation of silk-CNF coating was obtained successfully through the core of the ECF. The top three spectra correspond to the measurements while the mouse was maintained with a supply of oxygen for the first five minutes of sensing.

The peak ratios were transformed to pH using the calibration equation  $Peak\ ratio = -0.91 \times pH + 8.25$  from Section 3.4. The measured pH values over time in Fig. 7(b), are separated with a dotted black line taken while the animal was normoxic (left) and hypoxic (right) before and after cutting off the oxygen supply respectively.

For the normoxic (isoflurane anesthetised) animal, the pH values were slightly alkaline in the first 3–4 min, characteristic of a healthy functioning body [33], and varied within a range of 7.8 to 8.0. The oxygen supply to the animal was slowly ceased whilst isoflurane anesthesia was maintained.

Within 2 min of data collection after ceasing inhaled oxygen supply ( $t_1 + 2$  min), the pH dropped to  $7.0 \pm 0.2$ , shown by the blue plot in Fig. 7(a). Because of the reduction in oxygen supply under isoflurane anaesthesia hypoventilation is induced leading to  $CO_2$ -induced acidification of the body. After 9 min of ceasing inhaled oxygen ( $t_1 + 10$

min), the pH further declined to  $6.6 \pm 0.1$ . This is demonstrated by the brown curve in Fig. 7(a). The 2nd peak completely disappeared on  $t_1 + 15$  min, resulting in an even higher acidic pH of  $5.5 \pm 0.3$ , shown by the black curve in the figure, indicating that the animal became hypoxic.

## 4. Conclusions

This work demonstrates the development of a bio-derived silk coating for fiber sensing applications. The performance of the fiber probe was investigated in an *in vivo* mouse model for real time pH sensing. A ratiometric fluorescent dye CNF was encapsulated in liquid silk and then coated on ECF probes. Numerical modeling indicated that a silk-CNF coating of thickness less or equal to 200 nm successfully guides the dye's fluorescence through the ECF core. The structural and surface analysis of the silk coated fibers indicated that a desired coating thickness can be achieved by controlling silk concentration. The ratios obtained for silk-CNF mixture through in-solution spectroscopy and those measured for silk-CNF coating through fiber sensing were found to be consistent. A linear trend in the fluorescence ratio was observed as a function of pH. The silk-CNF coated fiber probe after calibration was employed for real time pH sensing subcutaneously inside a mouse. The sensing data showed that the subcutaneous pH in a live animal is slightly alkaline, consistent with literature. A continuous drop in the pH was observed when the oxygen supply to the lungs was reduced. This is due to the hypoxia development, which introduces acidity in the body. The work explores, for the first time, the potential of a natural silk protein coating to perform real time tracking and sensing inside the body. We demonstrated that silk coating can be easily produced and functionalized *via* all aqueous processing. We believe such a bio-derived transparent functional coating could enable a wide range of *in vivo* biosensing applications.

## Declaration of Competing Interest

The authors declare that they have no known competing financial interests or personal relationships that could have appeared to influence the work reported in this paper.

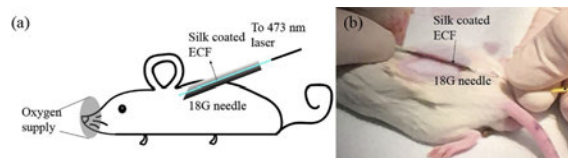
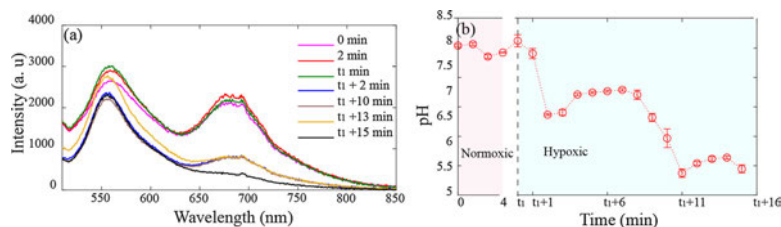


Fig. 6. Silk CNF coated ECF probe used for real time pH sensing. (a) Schematic and (b) animal image showing subcutaneous puncture *via* an 18 gauge needle at the back of the mouse for the insertion of the hybrid silk CNF ECF sensing probe. (For coloured image, the reader is referred to the web version of this article.)

A. Khalid, et al.



**Fig. 7.** (a) Real time pH sensing *in vivo* to indirectly monitor oxygen levels subcutaneously. Oxygen was cut off after 4 min. (b) Measured pH inside the animal as a function of time. The black dotted line indicates the point where the supply of oxygen to the animal ceased ( $t_1$ ). The circles indicate the averaged measurement repeated every 1 min (10/20 times) for each time point. Standard deviation in the mean values are plotted as error bars for each data point. The time interval  $\Delta t = 1$  min between each measurement before and after ceasing oxygen.

### Acknowledgements

The authors acknowledge support from the ARC Centre of Excellence for Nanoscale Biophotonics (CE14010003) and a Premier's Research and Industry Fund grant provided by the South Australian Government Department for Industry and Skills. The authors like to acknowledge the RMIT Microscopic and Microanalysis Facility (RMMF) for SEM analysis and the RMIT node of the Australian Research Council Centre of Excellence for Nanoscale BioPhotonics (CNBP) for in solution spectroscopy data. The authors also acknowledge Mr Ashleigh Hofferma and Dr Edwin Mayes for assisting with SEM microscopy data. A. Khalid is supported by RMIT University's vice chancellor postdoctoral fellowship. S. C. Warren-Smith is supported by a Ramsay Fellowship from the University of Adelaide. Lu Peng is supported by the China Scholarship Council. Jiawen Li is funded by grants from the National Heart Foundation of Australia (Postdoctoral Fellowship 102093) and the University of Adelaide. This work was performed, in part, at the Optofab node of the Australian National Fabrication Facility utilizing Commonwealth and SA State Government funding.

### Appendix A. Supplementary data

Supplementary material related to this article can be found, in the online version, at doi:<https://doi.org/10.1016/j.snb.2020.127864>.

### References

- J. Li, H. Ebendorff Heidepriem, B.C. Gibson, A.D. Greentree, M.R. Hutchinson, P. Jia, R. Kostecki, G. Liu, A. Orth, M. Ploschner, E.P. Scharfner, S.C. Warren Smith, K. Zhang, G. Tsiminis, E.M. Goldys, Perspective: biomedical sensing and imaging with optical fibers: innovation through convergence of science disciplines, *APL Photonics* 3 (10) (2018) 100902.
- W.W. Hsiao, Y.Y. Hui, P. C. Tsai, H. C. Chang, Fluorescent nanodiamond: a versatile tool for long term cell tracking, super resolution imaging, and nanoscale temperature sensing, *Acc. Chem. Res.* 49 (3) (2016) 400–407.
- E.P. Scharfner, M.R. Henderson, M. Purdey, D. Dhattrak, T.M. Monro, P.G. Gill, D.F. Callen, Cancer detection in human tissue samples using a fiber tip pH probe, *Cancer Res.* 76 (23) (2016) 6795–6801.
- A. Germond, H. Fujita, T. Ichimura, T.M. Watanabe, Design and development of genetically encoded fluorescent sensors to monitor intracellular chemical and physical parameters, *Biophys. Rev.* 8 (2) (2016) 121–138.
- K. C. Liao, T. Hogen Esch, F.J. Richmond, L. Marcu, W. Clifton, G.E. Loeb, Percutaneous fiber optic sensor for chronic glucose monitoring *in vivo*, *Biosens. Bioelectron.* 23 (10) (2008) 1458–1465.
- X. Wang, O.S. Wolfbeis, Fiber optic chemical sensors and biosensors (2013–2015), *Anal. Chem.* 88 (1) (2016) 203–227.
- S. Mishra, D. Saadat, O. Kwon, Y. Lee, W. S. Choi, J. H. Kim, W. H. Yeo, Recent advances in salivary cancer diagnostics enabled by biosensors and bioelectronics, *Biosens. Bioelectron.* 81 (2016) 181–197.
- A. Sun, T. Phelps, C. Yao, A.G. Venkatesh, D. Conrad, D.A. Hall, Smartphone based pH sensor for home monitoring of pulmonary exacerbations in cystic fibrosis, *Sensors (Basel)* 17 (6) (2017) 1245.
- C. Ribaut, M. Loyez, J. C. Larrieu, S. Chevigneau, P. Lambert, M. Rimmelink, R. Wattiez, C. Caucheteur, Cancer biomarker sensing using packaged plasmonic optical fiber gratings: towards *in vivo* diagnosis, *Biosens. Bioelectron.* 92 (2017) 449–456.
- G. Wandermur, D. Rodrigues, R. Allil, V. Queiroz, R. Peixoto, M. Werneck, M. Miguel, Plastic optical fiber based biosensor platform for rapid cell detection, *Biosens. Bioelectron.* 54 (2014) 661–666.
- S.T. Musolino, E.P. Scharfner, M.R. Hutchinson, A. Salem, Improved method for optical fiber temperature probe implantation in brains of free moving rats, *J. Neurosci. Methods* 313 (2019) 24–28.
- R. Correia, S. James, S.W. Lee, S.P. Morgan, S. Korposh, Biomedical application of optical fiber sensors, *J. Opt.* 20 (7) (2018) 073003.
- S.A. Pidenko, N.A. Burmistrova, A.A. Shuvalov, A.A. Chibrova, Y.S. Skibina, I.Y. Goryacheva, Microstructured optical fiber based luminescent biosensing: is there any light at the end of the tunnel? A review, *Anal. Chim. Acta* 1019 (2018) 14–24.
- Y. Ruan, T.C. Foo, S. Warren Smith, P. Hoffmann, R.C. Moore, H. Ebendorff Heidepriem, T.M. Monro, Antibody immobilization within glass microstructured fibers: a route to sensitive and selective biosensors, *Opt. Express* 16 (22) (2008) 18514–18523.
- L.V. Nguyen, K. Hill, S. Warren Smith, T. Monro, Interferometric type optical bio sensor based on exposed core microstructured optical fiber, *Sens. Actuators B Chem.* 221 (2015) 320–327.
- S.C. Warren Smith, R. Kostecki, L.V. Nguyen, T.M. Monro, Fabrication, splicing, Bragg grating writing, and polyelectrolyte functionalization of exposed core microstructured optical fibers, *Opt. Express* 22 (24) (2014) 29493–29504.
- A. Khalid, R. Lodin, P. Domachuk, H. Tao, J.E. Moreau, D.L. Kaplan, F.G. Omenetto, B.C. Gibson, S. Tomljenovic Hanic, Synthesis and characterization of biocompatible nanodiamond silk hybrid material, *Biomed. Opt. Express* 5 (2) (2014) 596–608.
- F. Omenetto, *Silk based Optics and Photonics*, Frontiers in Optics 2012/Laser Science XXVIII, Optical Society of America, Rochester, New York, 2012 p. FM3E.3.
- D.N. Rockwood, R.C. Preda, T. Yücel, X. Wang, M.L. Lovett, D.L. Kaplan, Materials fabrication from *Bombyx mori* silk fibroin, *Nat. Protoc.* 6 (10) (2011), <https://doi.org/10.1038/nprot.2011.1379>.
- A. Khalid, A.N. Mitropoulos, B. Marelli, S. Tomljenovic Hanic, F.G. Omenetto, Doxorubicin loaded nanodiamond silk spheres for fluorescence tracking and controlled drug release, *Biomed. Opt. Express* 7 (1) (2016) 132–147.
- M.B. Applegate, G. Perotto, D.L. Kaplan, F.G. Omenetto, Biocompatible silk step index optical waveguides, *Biomed. Opt. Express* 6 (11) (2015) 4221–4227.
- L.W. Tien, F. Wu, M.D. Tang Schomer, E. Yoon, F.G. Omenetto, D.L. Kaplan, Silk as a multifunctional biomaterial substrate for reduced glial scarring around brain penetrating electrodes, *Adv. Funct. Mater.* 23 (25) (2013) 3185–3193.
- A. Khalid, A.N. Mitropoulos, B. Marelli, D.A. Simpson, P.A. Tran, F.G. Omenetto, S. Tomljenovic Hanic, Fluorescent nanodiamond silk fibroin spheres: advanced nanoscale bioimaging tool, *ACS Biomater. Sci. Eng.* 1 (11) (2015) 1104–1113.
- J. Li, E. Scharfner, S. Musolino, B.C. Quirk, R.W. Kirk, H. Ebendorff Heidepriem, R.A. McLaughlin, Miniaturized single fiber based needle probe for combined imaging and sensing in deep tissue, *Opt. Lett.* 43 (8) (2018) 1682–1685.
- E.P. Scharfner, G. Tsiminis, M.R. Henderson, S.C. Warren Smith, T.M. Monro, Quantification of the fluorescence sensing performance of microstructured optical fibers compared to multi mode fiber tips, *Opt. Express* 24 (16) (2016) 18541–18550.
- S.C. Warren Smith, H. Ebendorff Heidepriem, T.C. Foo, R. Moore, C. Davis, T.M. Monro, Exposed core microstructured optical fibers for real time fluorescence sensing, *Opt. Express* 17 (21) (2009) 18533–18542.
- S. Chen, Y. Hong, Y. Liu, J. Liu, C.W. Leung, M. Li, R.T. Kwok, E. Zhao, J.W. Lam, Y. Yu, B.Z. Tang, Full range intracellular pH sensing by an aggregation induced emission active two channel ratiometric fluorogen, *J. Am. Chem. Soc.* 135 (13) (2013) 4926–4929.
- L.E. Gerweck, K. Seetharaman, Cellular pH gradient in tumor versus normal tissue: potential exploitation for the treatment of cancer, *Cancer Res.* 56 (6) (1996) 1194–1198.
- T. Scientific, *Molecular Probes™ Handbook A Guide to Fluorescent Probes and Labeling Technologies*, (2010).
- E.M. Pritchard, P.B. Dennis, F. Omenetto, R.R. Naik, D.L. Kaplan, Review physical and chemical aspects of stabilization of compounds in silk, *Biopolymers* 97 (6) (2012) 479–498.
- Q. Lu, X. Wang, X. Hu, P. Cebe, F. Omenetto, D.L. Kaplan, Stabilization and release of enzymes from silk films, *Macromol. Biosci.* 10 (4) (2010) 359–368.
- Y. Qi, H. Wang, K. Wei, Y. Yang, R. Y. Zheng, I.S. Kim, K. Q. Zhang, A review of structure construction of silk fibroin biomaterials from single structures to multi level structures, *Int. J. Mol. Sci.* 18 (3) (2017) 237.

A. Khalid, et al.

Sensors & Actuators: B. Chemical 311 (2020) 127864

- [33] M.G. Dickson, D.T. Sharpe, Continuous subcutaneous tissue pH measurement as a monitor of blood flow in skin flaps: an experimental study, *Br. J. Plast. Surg.* 38 (1) (1985) 39–42.
- [34] O. Wolfbeis, N. Rodriguez, T. Werner, LED compatible fluorosensor for measurement of near neutral pH values, *Microchimica Acta* 108 (3) (1992) 133–141.

**Dr Asma Khalid** is a Vice Chancellor Postdoctoral Fellow at RMIT University. She received her PhD from the University of Melbourne in 2016 and worked as an exchange researcher at the Silk Lab, Tufts University in 2014. Her work focuses on exploring silk for designing and characterising hybrid optical structures that are implantable or injectable in the body. These optically transparent, biocompatible, tunably degradable silk based materials have wide applications in biosensing, bioimaging and drug release.

**Lu Peng** achieved her M.S. from South China Normal University, China, in 2017. She is awarded an Adelaide University China Fee Scholarships (AUCFS) and is studying as a PhD student in the University of Adelaide since 2017. Her research interests are fiber interferometry sensors and plasmonic sensors for biochemical applications.

**Azim Arman** is a PhD candidate in the Faculty of Health and Medical Sciences, University of Adelaide, Australia. His research interests focus on preclinical assessment of hyponociception.

**Dr Stephen C. Warren Smith** completed his PhD in 2011 at the University of Adelaide, Australia, on the topic of microstructured optical fiber chemical sensing. He was then employed from 2011 to 2014 as an Australian Research Council (ARC) Super Science Fellow at the Institute for Photonics and Advanced Sensing and the School of Chemistry and Physics at the University of Adelaide, working on optical fiber biosensing for women's health applications. In 2015 and 2016 he worked as a European Union Marie Curie International Incoming Fellow at the Leibniz Institute of Photonic Technology, Jena, Germany, on a project investigating the micro/nano structuring of optical fibers for sensing. Since October 2016 he is with the University of Adelaide as a Ramsay Fellow, developing microstructured optical fibers for sensing and imaging applications.

**Dr Erik Schartner** is a postdoctoral researcher at the Institute for Photonics and Advanced Sensing and the ARC Centre of Excellence for Nanoscale Biophotonics at the University of Adelaide. His research focuses on optical fibre fabrication, primarily looking at sensing using these fibres within biological or industrial applications.

**Dr Georgina M. Sylvia** is a postdoctoral researcher in the School of Physical Sciences,

University of Adelaide. Her research focuses on the development and optimisation of biophotonic devices for medical and industrial applications.

**Prof Mark R Hutchinson** BSc(Hons), PhD(Med) is the Director of the Australian Research Council Centre of Excellence for Nanoscale BioPhotonics, and ARC Future Fellow and a Professor in the Adelaide Medical School at the University of Adelaide. His research focus is on understanding the neuroimmune synapse through imaging and sensing it in a dynamic behaving environment and how this functional multicellular unit is involved in controlling brain behaviour.

**Prof Heike Ebendorff Heidepriem** is Research Professor in Photonics Materials and fibres at the University of Adelaide. She is Senior Investigator of the ARC Centre of Excellence for Nanoscale BioPhotonics (CNBP) and Deputy Director of the Institute for Photonics and Advanced Sensing of the University of Adelaide. Her research focuses on the development of novel optical glasses, specialty optical fibres, surface functionalization and sensing approaches.

**Prof Robert A. McLaughlin** is the Chair of Biophotonics and a Professor at Adelaide Medical School, University of Adelaide. He is also co-founder of the company Miniprobes Pty Ltd. His research focuses on the design of optical fibre probes for biomedical applications and the development of intelligent algorithms for automated quantification.

**Prof Gibson** was awarded his PhD from La Trobe University in 2004. From 2005–09, he was a Photonics Development Engineer at Quantum Communications Victoria (QCV) where he and colleagues designed and developed Australia's first commercial quantum security product (QCV SPS 1.01). In 2011 he was awarded an Australian Research Council (ARC) Future Fellowship on Hybrid Diamond Materials for Next Generation Sensing, Biodiagnostic and Quantum Devices. Currently, Prof Gibson is a Deputy Director and RMIT Node Leader of the ARC Centre of Excellence for Nanoscale BioPhotonics. And he has wide ranging research interests in the areas of fluorescent nanoprobe, biophotonics, hybrid integration and confocal microscopy.

**Dr Jiawen Li** received her PhD degree in Biomedical Engineering from University of California Irvine in 2015. Her PhD work focused on developing optical coherence tomography (OCT) probes and multimodal optical ultrasonic imaging catheters for *in vivo* applications. She joined the University of Adelaide as a Lecturer in 2016. She is currently supported by National Heart Foundation of Australia to develop *in vivo* intravascular fluorescence + OCT imaging catheters. Her research interests include OCT, fibre sensing, multimodal imaging, and ultra thin endoscopes.

## A.1 PMMA ECF fabrication

In [P4], a fibre pH probe was fabricated by coating a silk layer on the silica ECF. For *in vivo* testing, a millimetre-sized needle was necessary to protect the silica fibre probe for insertion into the biological sample. In order to improve the handling and deployment capability, the fabrication of a polymer ECF is considered here. Although the final structure achieved is not ideal, the fabrication results shown in the following are a guide for future investigation.

In the first trial, a preform was made by drilling with a long open slot. Cracks resulted from the drilling process, which was not well controlled due to the first attempt to drill this PMMA rod. Despite the cracks, the preform was drawn, where the hole with an exposed side was sealed by the pink glue as shown in Fig. A.1 to allow pressurisation of the two internal holes. Significant bubbles were formed during drawing, leading to a dehydration process being applied in subsequent draws.

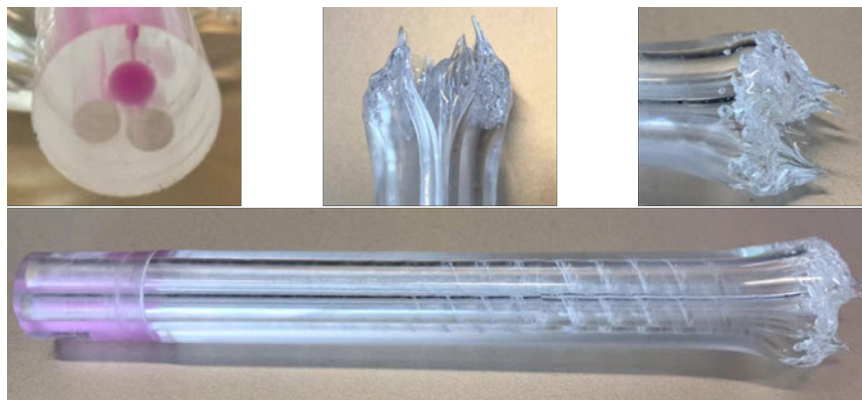


**Fig. A.1** The first PMMA ECF preform (three air holes with diameter of 3.7 mm, a slot with diameter of 1.3 mm and total preform length is 16 mm) and other images were to show the air bubbles occurring during the heating process due to water inside the PMMA material.

A dehydration process was recorded as shown in the Fig. A.2, where the PMMA rods were maintained inside an oven at a temperature from 70 to 75 °C. It shows that the weight of the PMMA rods were almost stabilised after 10 days. PMMA rods without having inner structure were drawn at this stage, to investigate the property of the PMMA and quantify the drawing parameters (i.e., temperature, draw speed, feed speed and outer diameter control). The drawn PMMA bare fibre is shown in the Fig. A.3, which displays a reasonable roundness. The outer diameter was well controlled around 160

$\mu\text{m}$  in this draw.

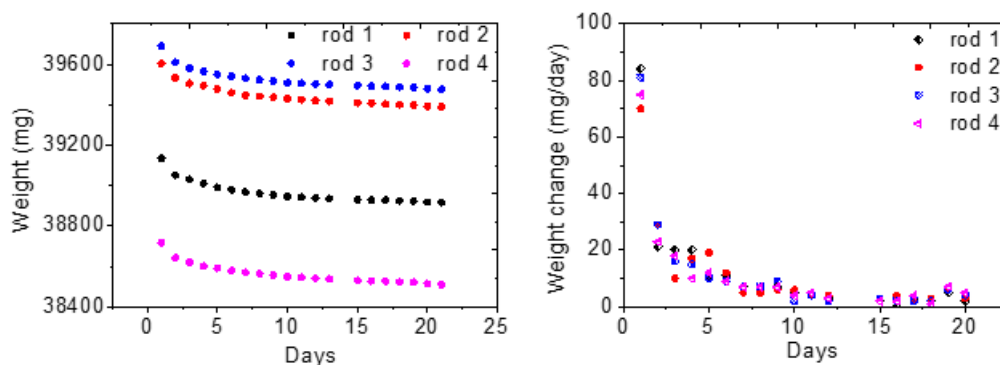


**Fig. A.2** Dehydration process: four PMMA rods were placed inside an oven and their weights were recorded daily to quantify the dehydration process. The temperature was 70-75 °C.

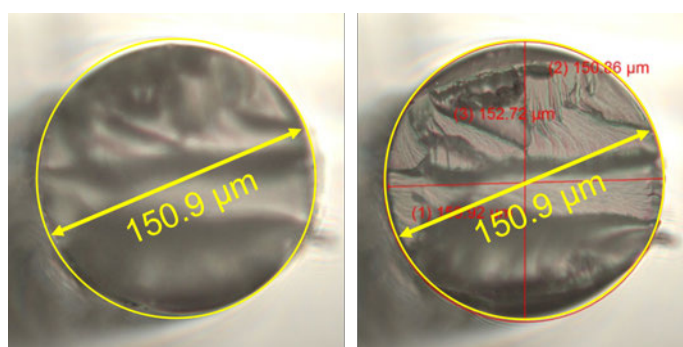


**Fig. A.3** Cross section images of the successful drawing of dehydrated PMMA non-structured fibres.

New PMMA ECF draws were implemented after the dehydration process. The open slot opened up in the middle of the preform during the drawing process, which was attributed to nonuniform heating in the furnace. To investigate the property of PMMA ECF fibre drawing, a small open slot (20 mm) for the next preparation of PMMA ECF preforms as shown in the Fig. A.4 was attempted [59]. This allowed the ECF structure to be maintained as shown in Fig. A.5. However, the adjustment time meant the draw was limited to a few minutes due to such a short slot, so the fabrication for an ideal structure was hard to achieve during this fibre drawing. The smallest outer diameter achieved was 256  $\mu\text{m}$ , compared to 160  $\mu\text{m}$  for the silica-based ECFs. The nitrogen flow into the internal holes also needs to increase to expand the air holes in order to narrow the struts to allow for core guidance.

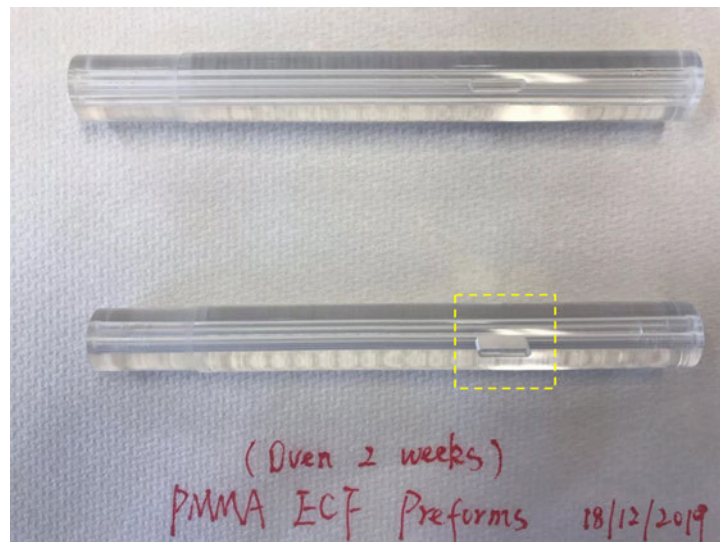


**Fig. A.4** PMMA ECF preforms after 2 weeks dehydration before fibre drawing, where the yellow dashed box was to indicate the short slot (20 mm).

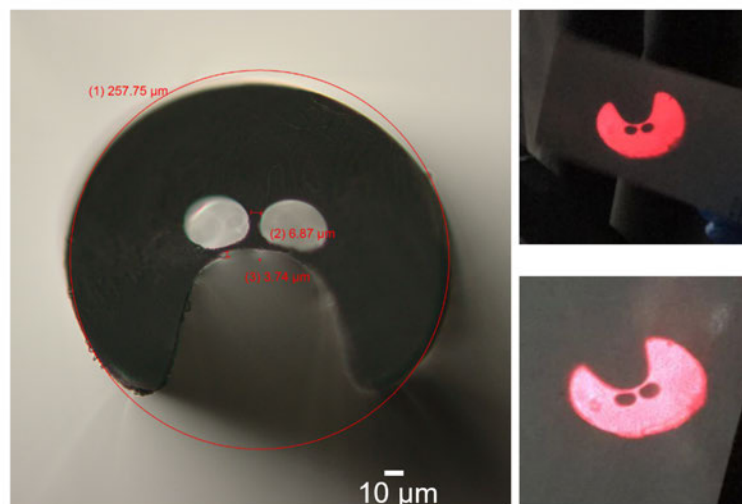


**Fig. A.5** The ECF structure was maintained during the drawing process using the above short slot PMMA preforms. The light guidance property of the fibre is shown on the right-hand side, indicating a lot of core guidance.

Nonetheless, this preliminary work has shown promising results towards making the polymer ECFs for potential biomedical applications in the future.

## **B Nanoscale particle detection using ECFs**

### **Publication overview**

This work [P5] aims to detect small particles (suspended in liquid environment) down to nanoscale size using a label-free and robust fibre-integrated scheme based on the evanescent field sensing. The use of smaller core ECFs firstly spliced with commercialised single mode fibres are detailed introduced in the following subsection. A heterodyne detection scheme further enhanced the particle signal abstraction significantly.

### **Statement of contribution**

This publication was the outcome of a collaboration with Dr. Nicolas P. Mauranyapin, Dr. Lars S. Madsen, Larnii Booth, and Prof. Warwick P. Bowen at the University of Queensland. The novel detection scheme previously used by The University of Queensland for tapered fibres [218] was implemented for the ECF. This work [P5] demonstrates the feasibility of detecting nanoscale sized particles. In this work I developed a technique for splicing small core ECFs (less than  $2 \mu\text{m}$ ) to conventional single mode fibre (see Appendix B.1) for a robust biosensing platform and prepared all fibre-integrated sensors that were shipped to The University of Queensland. The experimental demonstrations and numerical investigations were done by the collaborators.



## Statement of Authorship

Title of Paper	Quantum noise limited nanoparticle detection with exposed-core fiber
Publication Status	<input checked="" type="checkbox"/> Published <input type="checkbox"/> Accepted for Publication <input type="checkbox"/> Submitted for Publication <input type="checkbox"/> Unpublished and Unsubmitted work written in manuscript style
Publication Details	Nicolas P. Mauranyapin, Lars S. Madsen, Larnii Booth, Lu Peng, Stephen C. Warren-Smith, Erik P. Schartner, Heike Ebendorff-Heidepriem, and Warwick P. Bowen. "Quantum noise limited nanoparticle detection with exposed-core fiber". Optics Express, 27(13), 18601-18611 (2019).

### Principal Author

Name of Principal Author	Nicolas P. Mauranyapin
Contribution to the Paper	The experimental measurements, analysis and paper writing were majorly done by Nicolas P. Mauranyapin.
Overall percentage (%)	70%
Certification:	Nicolas P. Mauranyapin is the primary author of this paper.
Signature	<div style="display: flex; justify-content: space-between;"> <div style="border-bottom: 1px solid black; width: 80%;"></div> <div style="border-bottom: 1px solid black; width: 15%;"></div> </div> Date <b>09-08-2021</b>

### Co-Author Contributions

By signing the Statement of Authorship, each author certifies that:

- i. the candidate's stated contribution to the publication is accurate;
- ii. permission is granted for the candidate to include the publication in the thesis; and
- iii. the sum of all co-author contributions is equal to 100% less the primary author's stated contribution.

Name of Co-Author	Lars S. Madsen
Contribution to the Paper	Lars S. Madsen contributed to the experimental measurements and revised the manuscript.
Signature	<div style="display: flex; justify-content: space-between;"> <div style="border-bottom: 1px solid black; width: 80%;"></div> <div style="border-bottom: 1px solid black; width: 15%;"></div> </div> Date <b>17-08-2021</b>

Name of Co-Author	Larnii Booth
Contribution to the Paper	Larnii Booth contributed to the experimental measurements and revised the manuscript.
Signature	<div style="display: flex; justify-content: space-between;"> <div style="border-bottom: 1px solid black; width: 80%;"></div> <div style="border-bottom: 1px solid black; width: 15%;"></div> </div> Date <b>17-08-2021</b>

Name of Co-Author (candidate)	Lu Peng
Contribution to the Paper	Lu Peng fabricated all the fibre sensors and characterised their performance to support the practical experiments. She also contributed to revise the manuscript.
Overall percentage (%)	8%
Signature	<div style="display: flex; justify-content: space-between;"> <div style="border-bottom: 1px solid black; width: 80%;"></div> <div style="border-bottom: 1px solid black; width: 15%;"></div> </div> Date <b>09-08-2021</b>

Name of Co-Author	Stephen C. Warren-Smith		
Contribution to the Paper	Stephen C. Warren-Smith contributed to technical discussions and revised the manuscript.		
Signature	_____	Date	09-08-2021

Name of Co-Author	Erik P. Schartner		
Contribution to the Paper	Erik P. Schartner contributed to the exposed-core fibre's fabrication and revised the manuscript.		
Signature	_____	Date	09-08-2021

Name of Co-Author	Heike Ebendorff-Heidepriem		
Contribution to the Paper	Heike Ebendorff-Heidepriem contributed to the exposed-core fibre's fabrication and revised the manuscript.		
Signature	_____	Date	09-08-2021

Name of Co-Author	Warwick P. Bowen		
Contribution to the Paper	Warwick P. Bowen contributed to the general discussion and revised the manuscript.		
Signature	_____	Date	09-08-2021

# Quantum noise limited nanoparticle detection with exposed-core fiber

NICOLAS P. MAURANYAPIN,<sup>1,\*</sup> LARS S. MADSEN,<sup>1</sup> LARNII BOOTH,<sup>1</sup> LU PENG,<sup>2,3</sup> STEPHEN C. WARREN-SMITH,<sup>2,3</sup> ERIK P. SCHATNER,<sup>2,3</sup> HEIKE EBENDORFF-HEIDEPRIEM,<sup>2,3</sup> AND WARWICK P. BOWEN<sup>1</sup>

<sup>1</sup>ARC Centre for Engineered Quantum Systems (EQUS), School of Mathematics and Physics, The University of Queensland, Australia

<sup>2</sup>Institute for Photonics and Advanced Sensing (IPAS), School of Physical Sciences, The University of Adelaide, Adelaide, South Australia 5005, Australia

<sup>3</sup>ARC Centre for Nanoscale Biophotonics (CNBP), The University of Adelaide, Adelaide, South Australia 5005, Australia

\*n.mauranyapin@uq.edu.au

**Abstract:** Label-free biosensors are important tools for clinical diagnostics and for studying biology at the single molecule level. The development of optical label-free sensors has allowed extreme sensitivity but can expose the biological sample to photodamage. Moreover, the fragility and complexity of these sensors can be prohibitive to applications. To overcome these problems, we develop a quantum noise limited exposed-core fiber sensor providing robust platform for label-free biosensing with a natural path toward microfluidic integration. We demonstrate the detection of single nanoparticles down to 25 nm in radius with optical intensities beneath known biophysical damage thresholds.

© 2019 Optical Society of America under the terms of the [OSA Open Access Publishing Agreement](#)

## 1. Introduction

The past few decades have seen rapid improvements in the sensitivity of label-free optical biosensors. Single proteins of a few nanometres in size and below can now be routinely detected in solution [1–4]. Recently, these biosensors have been used to shed light on fundamental biophysics phenomena [1, 5] and have been shown to have potential applications ranging from medical diagnostics [2] to high-resolution imaging [6] and environmental monitoring [1]. Among the currently developed sensors are whispering gallery mode (WGM) resonators [7, 8] and plasmonic sensors [3, 9]. Combining both approaches allows resolution of the motion of single enzymes [5] and detection of single ions in solution [1]. However, these sensors generally operate with optical intensities far above known thresholds for photochemical intrusion and photodamage [10–12]. To overcome this problem, quantum-noise limited measurement techniques have been developed using a nanofiber combined with dark field heterodyne measurement [2]. Sensors based on these techniques are capable of detecting single BSA molecules (3.5 nm) with four orders of magnitude reduced optical intensity. However, the relative fragility of these sensors and the lack of integrated microfluidic channels has, so far, prevented their integrated use. Nanofluidic optical fibers can overcome some of these issues and have been used to detect and differentiate label-free single viruses via their optical scattering when illuminated by the guided mode of the fiber [4, 13]. Here we introduce a biosensor combining the advantages of these techniques using exposed-core fiber and quantum noise limited dark field heterodyne measurement. Exposed-core fibers can be integrated with microfluidics channels [14] and are more robust than nanofibers due to their hundred microns diameter. We demonstrate detection of single label-free nanoparticles in solution at the quantum noise limit and compare our results with theory and simulations.

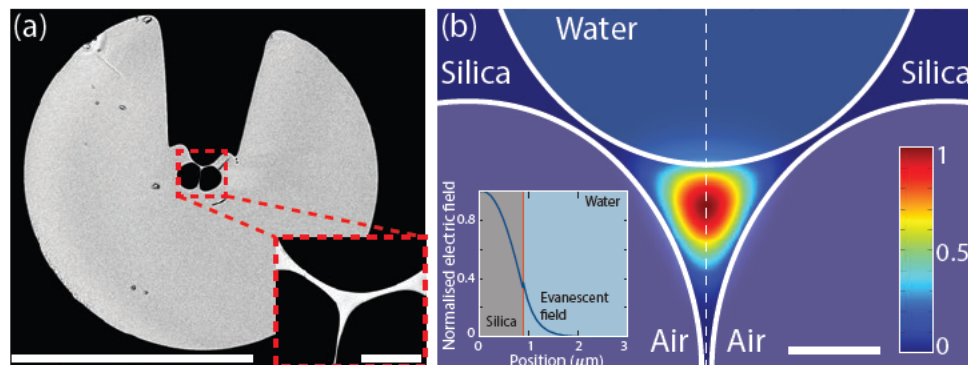


Fig. 1. (a) SEM image of the cross-section of an exposed-core fiber (scale bar =  $100\ \mu\text{m}$ ). Inset: SEM picture of the core of the exposed-core fiber (scale bar =  $5\ \mu\text{m}$ ). (b) Finite element simulation of the first fundamental propagating mode of a  $2\ \mu\text{m}$  diameter silica exposed-core fiber (scale bar =  $2\ \mu\text{m}$ ). The bottom (internal) holes are filled with air and the top (open) hole is filled with water. Inset: normalized electric field as function of the distance from the center of the exposed core fiber. The inset is computed by taking a cut of (b) along the dashed line.

## 2. Approach

### 2.1. Exposed-core fibers

The exposed-core fibers used here are microstructured optical fibers that confine light through three longitudinal air holes [15–17], as seen in the scanning electron microscopy (SEM) image in Fig. 1(a). The air holes introduce a large refractive index mismatch so that the light can be guided in a micrometre sized core of the same material as the cladding (see Fig. 1(b)). In exposed-core fibers, one of the air holes is engineered to be open to the surrounding medium allowing direct interaction between the guided light and the environment. This is shown in Fig. 1(b) where we have simulated the fundamental mode shape of a  $2\ \mu\text{m}$  diameter exposed-core fiber with the top hole opened to a solution of water, which could contain the particles of interest. One can see that most of the light is guided in the core of the fiber but a fraction propagates in the surrounding medium as an evanescent field (see Fig. 1(b) inset). Similar to other evanescent field techniques such as WGM or nanofiber sensors, any perturbation in refractive index within the evanescent field will perturb the propagating field and can potentially be detected. The region where the evanescent field propagates determines the interaction volume between the light and the surrounding medium. This accessible interaction volume allowed a wide variety of applications including sensors for biology [18, 19]. For example, exposed-core fibers have been used for the detection of fluorescence signals [20, 21] and for detection of label-free molecule ensembles in an interferometric configuration [18, 19].

Compared with optical nanofibers, the advantages of exposed-core fibers are that they are made from a single material and can be consistently drawn for hundreds of meters, allowing large-scale production [16]. By comparison, nanofibers must be pulled individually and their typical sensing region is only a few mm long [22]. Even though the core of the exposed-core fiber is small ( $\sim 2\ \mu\text{m}$ ), when including the cladding they are about  $120\ \mu\text{m}$  in diameter (see Fig. 1(a)) making them much less fragile than nanofibers ( $\sim 500\ \text{nm}$ ). Moreover, they have already been demonstrated to be compatible with microfluidics channels [14].

## 2.2. Evanescent sensing mechanism

As displayed in Fig. 2, to detect nanoparticles with exposed-core fiber, we focus a probe beam (yellow) on the exposed-core fiber immersed in a solution containing nanoparticles. When a particle enters the region close to the fiber where the probe light is focussed, it will scatter the probe light and a portion of the scattered light will be collected by the guided mode of the exposed-core fiber. This forms a dark field configuration since the probe field is orthogonal to the direction of propagation in the fiber and when no particle is present, a very small amount of probe light will be collected (additional details in appendix).

When a detection event occurs, for a focussed Gaussian probe beam, the scattered power  $P_{scatt}$  by the nanoparticle is given by [23]:

$$P_{scatt} = \frac{\sigma}{4\pi w^2} P_{in}, \quad (1)$$

where  $P_{in}$  is the input power,  $w$  is the probe beam waist,  $\sigma$  is the scattering cross-section of the nanoparticle and we have neglected modifications of the optical density of states due to the presence of the fiber, which we expect to be small. The standard model used to determine  $\sigma$  for particles smaller than the wavelength of the light is the dipole scattering model [24]:

$$\sigma = \frac{8\pi k^4 a^6}{3} \left( \frac{m^2 - 1}{m^2 + 2} \right)^2, \quad (2)$$

where  $a$  is the radius of the particle,  $k = 2\pi/\lambda$  is the wave vector of the light,  $\lambda$  is the wavelength of the light and  $m = n_p/n_m$  is the refractive index ratio of the nanoparticle material  $n_p$  and the surrounding medium  $n_m$ . The power of the detected signal at one end of the exposed-core fiber,  $P_{sig}$ , will depend on how much of  $P_{scatt}$  is collected by the exposed-core fiber. Thus, we have  $P_{sig} = \eta P_{scat}$ , with  $\eta$  being the collection efficiency of the exposed-core fiber. Overall, the detection of single nanoparticles is challenging because the fraction of collected photons and the number of scattered photons can be very small. Indeed, as seen in Eqs. (1) and (2) the signal power scales with the particle volume squared and is greatly reduced when the radius reaches nanometres in size.

The parameter  $\eta$  is equal to the overlap integral between the scattered field and the guided modes of the exposed-core fiber, which is hard to determine analytically. This problem has been solved in the case of a scattering loss measurement where the change in transmitted power through an optical nanofiber is monitored [25]. For our darkfield configuration, we used finite element simulation to determine the collection efficiency (see appendix). In the case of a 2  $\mu\text{m}$  exposed-core fiber, we estimate the collection efficiency to be around 1 to 8 percent.

## 2.3. Apparatus

Experimentally, to setup a dark field heterodyne measurement, we split a 780 nm laser beam into a local oscillator (LO) and an illumination field (probe), as seen in Fig. 3(a). The illumination field, is shifted up in frequency by an acousto-optic modulator (AOM), expanded and focused using a water immersion microscope objective (60x, 0.9 NA) on a 5 to 10 cm long exposed-core fiber. To guide the collected signal toward detection, one of the ends of the exposed-core fiber is spliced to an ultra high NA fiber (UHNA4). This also prevent the solution from entering into the two air holes and the detection system. The collected signal is then interfered with the local oscillator on a 50-50 fiber beam splitter single mode at 780 nm. The interference is detected on a balanced detector which creates a photocurrent with a beat note at the AOM frequency. The amplitude of this beat note is proportional to the nanoparticle scattered field amplitude and is amplified by the LO. After detection, the heterodyne beat note is mixed down with a home-built dual-phase lock-in amplifier (not shown on the figure) creating two orthogonal quadratures ( $X$

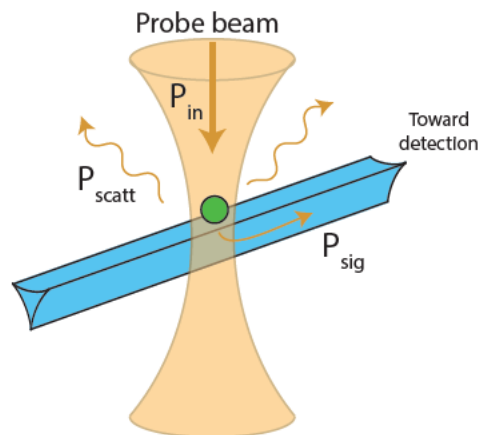


Fig. 2. Scheme of the exposed-core sensor in dark field configuration. The incident light is sent to the nanoparticle (green sphere) on the exposed-core fiber from the top as a probe beam (yellow beam) and guided toward detection by the exposed-core fiber (in blue).

and  $Y$ ), which are digitalized on an oscilloscope. These two quadratures are used to extract a value  $A$  proportional to the amplitude of the collected signal in post-processing as  $A = \sqrt{X^2 + Y^2}$ .

Two optical isolators are used to suppress any back reflected probe light to avoid contaminating the LO beam and thereby creating extra noise. A polarization controller is used in the probe arm to maximize the probe power transmitted through a PBS situated just before the microscope objective. This sets the polarization of the focused probe beam and also the nanoparticle induced dipole orientation perpendicular to the direction of propagation in the fiber and thereby maximizes the collection efficiency. A half wave plate is used before splitting the laser to control how much power goes in each beam. Typically, 2 mW of probe power is sent to the objective and 1 mW of LO is sent to each photodiode of the balanced detector. Note that compared to our previous approach used in [2], the LO is not sent through the sensing fiber but interfered after on the beam splitter. This improves the signal to noise ratio by a factor of two since the signal is detected by both photo-diodes of the detector, and reduces the intensity of the light which the sample is exposed to.

To test the noise performance of the sensor we measured the power spectral density (PSD) of the apparatus in different configurations, see Fig. 3(b). In this figure, the black curve represents the electronic noise, with no light on the detector, the red curve the LO noise, when only the LO is detected. The blue curve represents the noise power spectral density when both probe and LO noise are sent to the detector with no particles present in the solution and the probe beam focussed on a static scatterer on the fiber. One can see that for frequencies smaller than  $\sim 4$  Hz the measurement is limited by electronic pick up and classical noise from the laser light. This can prevent observation of signal scattered by nanoparticles. However, above 4 Hz, the system is not limited by the electronic noise and only the laser noise dominates. One signature of the quantum laser noise is that its power spectral density is linearly proportional to the optical power due to the addition of vacuum noise [2]. We test this dependence in Fig. 3(c), which shows the average power spectral density of the laser noise over a bandwidth of 10 kHz against the optical power on the photodiodes of the balanced detector. The observed linear relationship shows that the laser noise is only composed of quantum noise. This demonstrates that by using heterodyne detection, we can achieve quantum noise limited detection for most frequencies of interest, improving the signal to noise ratio and allowing better sensitivity than conventional direct detection methods.

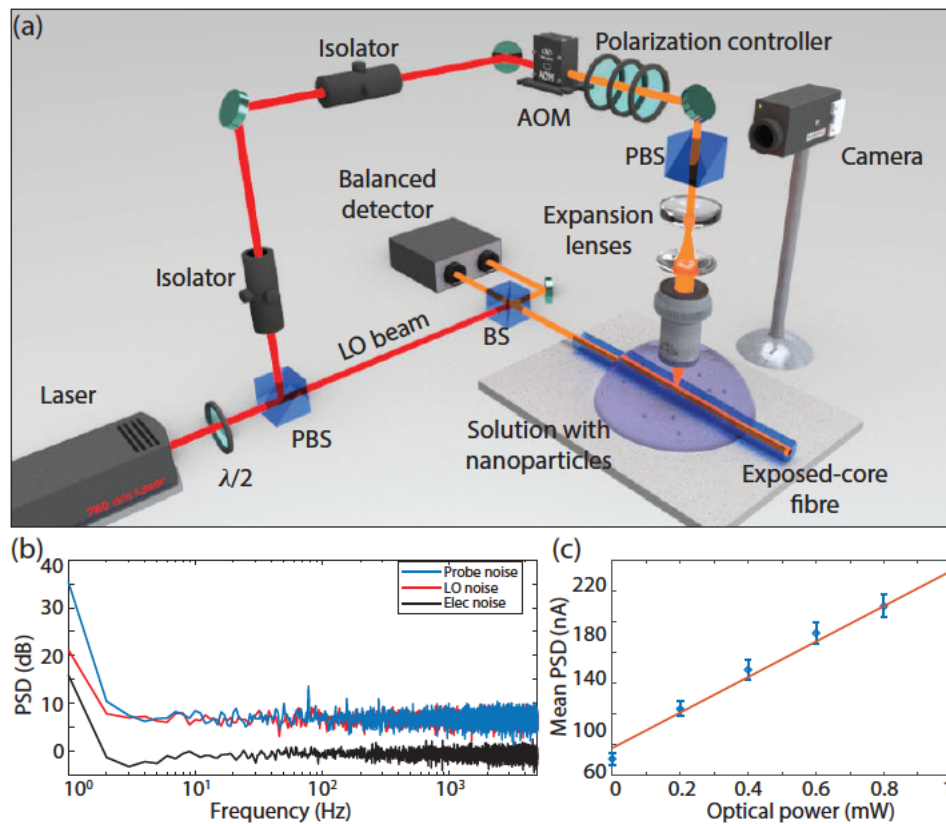


Fig. 3. (a) Experimental setup where (P)BS stands for (polarized) beam splitter, LO for local oscillator,  $\lambda/2$  for half wave plate and AOM for acousto-optic modulator. The camera is used to align the objective on the fiber visualized through the polarized beam splitter situated above the microscope objective. Note that the beam splitter before detection and the polarization controller (3-paddles) are in fiber but was represented in free space here for clarity. (b) PSD of the different noises in the apparatus. The black, red and blue curves represent the electronic noise, LO noise and probe noise respectively. (c) Mean power spectral density between -5 kHz and 5 kHz of the laser noise as function of optical power sent to the detector. The blue dots represent the experimental data with error bars as the standard error of the power spectral density over 10 measurements. The red curve represents a linear fit to the experimental data.

### 3. Results

#### 3.1. Nanoparticles detection

We have tested the sensor with solutions containing either silica nanoparticles of 25 nm or 50 nm in radius or polystyrene nanoparticles of 100 nm in radius. The solvent used here is dulbecco's phosphate buffered saline (DPBS). DPBS was used instead of deionized water because it contains many ions that can screen the surface charges present on the exposed-core fiber and the nanoparticles. These surface charges could prevent the nanoparticles from entering the fiber groove and diffusing close to the core of the fiber due to electrostatic repulsion.

Experiments were performed following four steps. First, the exposed-core fiber was immersed in a  $\sim 0.6$  mL droplet of pure DPBS and the probe field was focussed on the fiber using the

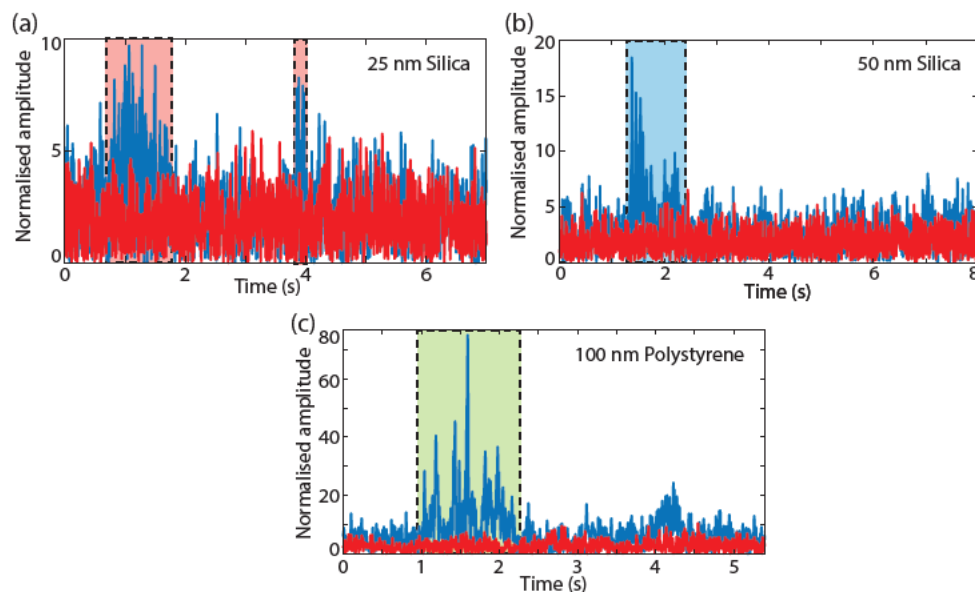


Fig. 4. (a), (b), (c) Time trace in blue containing detection events of single 25 nm, 50 nm silica particles and 100 nm polystyrene particles highlighted in red, blue and green respectively. The red curve in each graph represents a quantum noise trace taken before particles were added to the solution. For clarity, the traces are band pass filtered at 4 Hz to 100 Hz (quantum noise limited frequencies) and the signal amplitude is normalized by the standard deviation of the quantum noise. Before each experiment, the nanoparticle solution was tested in a Zetasizer to verify that there was no contamination or aggregations.

microscope objective. Second, a set of noise measurements were taken to record the electronic noise and the laser noise of the apparatus. Third,  $40 \mu\text{L}$  of nanoparticle solution, at concentration of  $6.7 \times 10^9$ ,  $2.4 \times 10^9$  and  $7.6 \times 10^9$  particles per mL for the 25 nm, 50 nm and 100 nm particles respectively, was added to the droplet. These concentrations have been chosen sufficiently low that the chance of multi-particles events are negligibly small since there are around  $1.4 \times 10^{-3}$ ,  $5 \times 10^{-4}$  and  $1.6 \times 10^{-3}$  particles per detection volume respectively. Finally, the signal was monitored and recorded on an oscilloscope.

Typical experimental time traces are shown in Figs. 4(a)-4(c) where the detection events are highlighted in red, blue and green for the 25 nm, 50 nm and 100 nm particles respectively. As expected (see the previous section 2.2), larger particles have higher scattering cross-section. Consistent with this, we observe that the signal-to-noise ratio increases when increasing the nanoparticle size.

The capacity to detect 25 nm particles shows the effectiveness of heterodyne detection and compares favourably to other direct detection experiments with nanofibers which have reported detection of particles with sizes of 100 nm [26] and 130 nm [27] in radius. Our sensor is competitive with nanofluidic optical fibers sensors which have been demonstrated to detect single 19 nm polystyrene particles [4]. However, the accessible core, in our case, offers greater flexibility for applications, while the use of dark field heterodyne allows megahertz detection bandwidth, compared to the camera-limited of few kilohertz in [4].



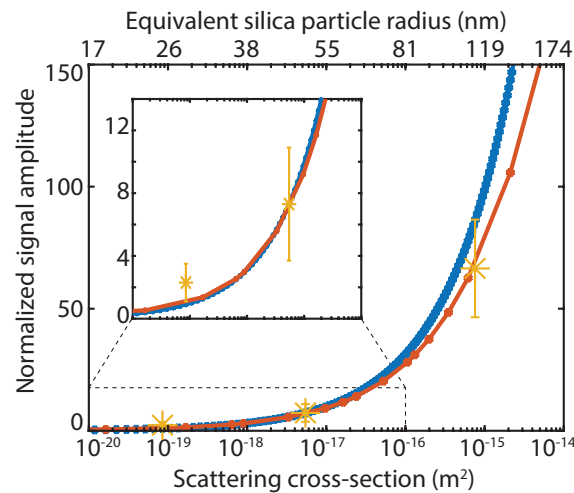


Fig. 5. Mean normalized signal amplitude against particle scattering cross-section from experiment (yellow stars, error bars given by the standard deviation). This is compared to finite element simulations (red curve) and dipole scattering theory (blue curve) of the collected power. The scattering cross-section can be converted to an equivalent silica particle radius (top x-axis) using Eq. (2). The scattering from the 100 nm PS particle is equivalent to the scattering of a  $\sim 114$  nm silica particle.

### 3.2. Particle radius scaling

In Fig. 5 we investigate how the experimental mean maximum signal amplitude (yellow dots) scales with particle scattering cross-section. We compare the experimental data with finite element simulation of exposed-core fiber (red curve, see appendix for details) and with the theoretical dipole scattering of section 2.2 (blue curve). The scattering cross-section x-axis can be converted to an equivalent silica particle (top x-axis) using Eq. (2) providing a more intuitive representation of the size of the particles. Because some experimental parameters such as the conversion of light signal power into voltage by the detector are unknown, to compare theory and simulation to the experimental data, we normalize the theoretical and simulated data to the 50 nm particle signal (see Fig. 5 inset). The experimental mean maximum amplitude of the detection events used to characterize the nanoparticle signal is corrected by removing the contribution of the quantum noise. This was determined by calculating the average of the noise maximum value over typical event duration. One can see that the experimental data and the finite element simulation are in good agreement with the theoretical dipole scattering model and the amplitude signal scales with radius of the particle cube as expected.

## 4. Discussion

We have demonstrated that exposed-core fibers combined with dark field heterodyne detection can be used to detect single label-free nanoparticles as small as 25 nm silica particles at the quantum noise limit in a biologically compatible solution. The light intensity used was only  $\sim 7 \times 10^7$  W/m<sup>2</sup> (probe beam) which is an order of magnitude smaller than intensities used for nanofibers ( $7 \times 10^8$  W/m<sup>2</sup> in [2]) and five orders of magnitude lower than intensities used in WGM resonator sensors. It is two orders of magnitude lower than known photodamage threshold [10] showing that the exposed-core fiber sensor should be compatible with observation of biophysics phenomena for an extended period of time. Increasing the intensity of the probe beam by an order of magnitude would still result in intensities below photodamage thresholds and, according

to Eq. (1), could allow detection of single nanoparticles with a scattering cross-section ten times smaller than 25 nm silica particles with the same signal to noise ratio. From Figs. 2 and 3, one can see that half of the signal is guided toward the other end of the exposed-core fiber and is not used. This signal could be also detected by using a fiber coupled mirror, for example, and could increase the signal to noise ratio of our sensor by a factor of  $\sqrt{2}$ .

To further enhance the sensitivity of the sensor, the exposed-core fiber could be designed with smaller core. Our simulation in Fig. 1(b) shows that the electric field amplitude at the surface of a 2  $\mu\text{m}$  exposed-core fiber is around 34% of the maximum field amplitude. Performing a simulation with a 500 nm core exposed-core fiber shows that the field can be enhanced to 74% of the maximum. This means that the signal amplitude could be enhanced by a factor of more than two as well as the sensitivity of the sensor assuming that the sensor remains quantum limited. In addition, the portion of the evanescent field outside the fiber will be larger, which will increase the detection volume.

In general, our results show that the exposed-core fiber sensor is sufficiently sensitive to compete with other label-free sensors. Because exposed-core fibers are less fragile and can be produced at large scale, they can be used in robust detection devices or in lab-on-chip configuration and integrated to microfluidic channels. For example, they could be used in medical diagnostic devices to detect disease markers. With such sensitivity, very few markers need to be detected and very low sample volume will be needed.

### Appendix: Exposed-core fiber simulation

To simulate the exposed-core fiber sensor, we used the finite element simulation software COMSOL multiphysics. For simplicity, only the core of the exposed-core fiber made of silica was simulated in a  $4\mu\text{m} \times 4\mu\text{m} \times 10\mu\text{m}$  volume, as seen in Fig. 6(a). The simulated volume was surrounded by a perfect matching layer (PML, not shown in the figure) to avoid contamination by back reflections. Because the PML material should be continuous with the simulation volume and made of a single material, we have immersed the core of the fiber in water and the air holes are also filled with water. A 780 nm Gaussian beam of 1 mW was focused on a nanoparticle on the fiber from the top and the electromagnetic field distribution was solved for the scattered field in the entire simulation volume. Two parameters were extracted from this simulation for a range of nanoparticle radii. The first one is the collected signal power  $P_{sig}$ , calculated using:

$$P_{sig} = \iint_S \vec{n} \cdot \vec{\Pi}(x, y) dx dy, \quad (3)$$

where  $S$  is the surface at one end of the exposed-core fiber (see green surface in Fig. 6(a)),  $\vec{\Pi}(x, y)$  is the Poynting vector at the cartesian coordinates  $x, y$  and  $\vec{n}$  is a unitary vector perpendicular to the surface  $S$ . In Fig. 5(a) we have compared the normalized amplitude from the experiment with the amplitude of the collected signal power  $A_{sig} = C\sqrt{P_{sig}}$  with  $C$  a constant as explained in section 3.2. The second parameter extracted from the simulation is the scattered power  $P_{scatt}$  from the nanoparticle which is obtained similarly by integrating the Poynting vector around the nanoparticle surface (red surface in Fig. 6(a)).

In Fig. 6(b), the solution of the electric field norm is shown for a 100 nm silica particle. One can see that part of the incident field is reflected back to the top by the fiber and creates some interferences but most of the field is transmitted and exits the simulation volume from the bottom. The solution of the collected signal field is displayed by the cut at the left end of the fiber. One can see that the collected light is not only guided in the fundamental mode of the exposed-core fiber displayed in Fig. 1(b). We believe the nanoparticle excites several modes supported by the exposed core fiber and the cut of collected signal results from the interference between these modes. The first few modes are displayed in Fig. 6(c) and one can see that the collected signal could be mostly supported by the second and fourth mode.

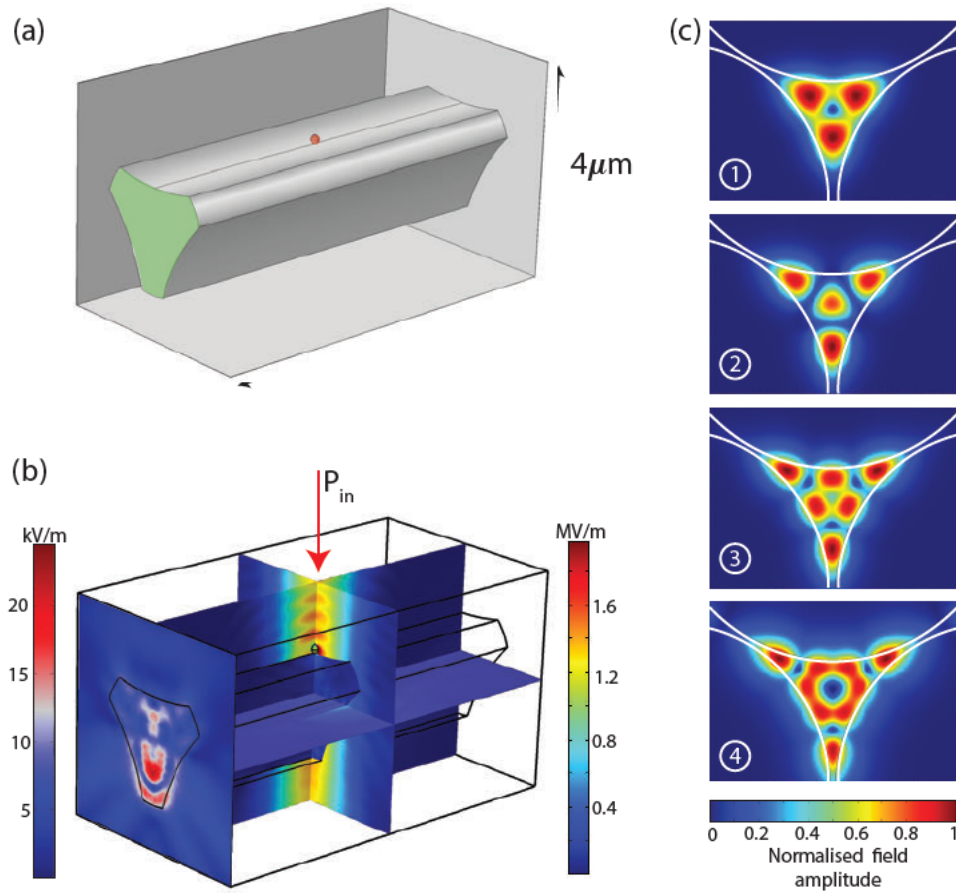


Fig. 6. (a) Simulation geometry showing the silica core of an exposed-core fiber in water. The green surface represents the surface used to calculate the signal power and the red sphere represents a 100 nm nanoparticle. (b) Solution of the norm of the electric field. Left colorbar corresponds to the value of the field only at left end of the fiber and the right colorbar to the rest of the simulation volume. (c) First four higher order modes supported by the exposed-core fiber at a wavelength of 780 nm. For this mode analysis, all holes are filled with water to be compared to b). Modes are sorted with decreasing effective refractive index: 1.431, 1.409, 1.389, 1.379 and 1.357 for the fundamental mode (0, similar to Fig. 1(b)), modes 1, 2, 3 and 4 respectively.

Using Eq. (3), the collected signal power calculated for a 100 nm silica particle is  $5.3 \times 10^{-4}$  mW and the scattered power is around  $7.4 \times 10^{-3}$  mW. From these two parameters, the collection efficiency can be calculated using  $\eta = P_{sig}/P_{scatt}$  which gives 7.2 percent for the 100 nm particle. For particles of other sizes, ranging from 10 nm to 200 nm, the calculated collection efficiency is between 1.7 and 8.1 percent. Note that the collection efficiency is actually twice this value as there are collected photons that propagate in the other direction, but are not detected.

Finally, to verify that our simulation is valid, a control simulation was performed with no particle and showed that the collected power at the end of the fiber was at least 6 orders of magnitude lower than when a 100 nm particle is present.

## Funding

Air Force Office of Scientific Research (FA9550-17-10397); ARC Centre of Excellence for Engineered Quantum Systems (CE110001013); ARC Centre of Excellence for Nanoscale Biophotonics (CE14010003); Australian Research Council (Future Fellowship FT140100650); University of Adelaide (Ramsay Fellowship); China Scholarship Council.

## Acknowledgments

The authors thank Alastair Dowler and Evan Johnson from the University of Adelaide for the exposed-core fiber fabrication. The authors would like to acknowledge the OptoFab node of the Australian National Fabrication Facility supported by the Commonwealth and South Australian State Government.

## References

1. M. D. Baaske, M. R. Foreman, and F. Vollmer, "Single-molecule nucleic acid interactions monitored on a label-free microcavity biosensor platform," *Nat. Nanotechnol.* **9**, 933 (2014).
2. N. Mauranyapin, L. Madsen, M. Taylor, M. Waleed, and W. Bowen, "Evanescent single-molecule biosensing with quantum-limited precision," *Nat. Photonics* **11**, 477 (2017).
3. Y. Pang and R. Gordon, "Optical trapping of a single protein," *Nano Lett.* **12**, 402–406 (2011).
4. S. Faez, Y. Lahini, S. Weidlich, R. F. Garmann, K. Wondraczek, M. Zeisberger, M. A. Schmidt, M. Orrit, and V. N. Manoharan, "Fast, label-free tracking of single viruses and weakly scattering nanoparticles in a nanofluidic optical fiber," *ACS Nano* **9**, 12349–12357 (2015).
5. E. Kim, M. D. Baaske, I. Schuldes, P. S. Wilsch, and F. Vollmer, "Label-free optical detection of single enzyme-reactant reactions and associated conformational changes," *Sci. Adv.* **3**, e1603044 (2017).
6. M. D. Baaske and F. Vollmer, "Optical observation of single atomic ions interacting with plasmonic nanorods in aqueous solution," *Nat. Photonics* **10**, 733 (2016).
7. J. D. Swaim, J. Knittel, and W. P. Bowen, "Detection of nanoparticles with a frequency locked whispering gallery mode microresonator," *Appl. Phys. Lett.* **102**, 183106 (2013).
8. S. Arnold, D. Keng, S. Shopova, S. Holler, W. Zurawsky, and F. Vollmer, "Whispering gallery mode carousel—a photonic mechanism for enhanced nanoparticle detection in biosensing," *Opt. Express* **17**, 6230–6238 (2009).
9. C. Chen, M. L. Juan, Y. Li, G. Maes, G. Borghs, P. Van Dorpe, and R. Quidant, "Enhanced optical trapping and arrangement of nano-objects in a plasmonic nanocavity," *Nano Lett.* **12**, 125–132 (2011).
10. U. Mirsaidov, W. Timp, K. Timp, M. Mir, P. Matsudaira, and G. Timp, "Optimal optical trap for bacterial viability," *Phys. Rev. E* **78**, 021910 (2008).
11. M. P. Landry, P. M. McCall, Z. Qi, and Y. R. Chemla, "Characterization of photoactivated singlet oxygen damage in single-molecule optical trap experiments," *Biophys. J.* **97**, 2128–2136 (2009).
12. S. Wäldchen, J. Lehmann, T. Klein, S. Van De Linde, and M. Sauer, "Light-induced cell damage in live-cell super-resolution microscopy," *Sci. Rep.* **5**, 15348 (2015).
13. L. Ma, S. Zhu, Y. Tian, W. Zhang, S. Wang, C. Chen, L. Wu, and X. Yan, "Label-free analysis of single viruses with a resolution comparable to that of electron microscopy and the throughput of flow cytometry," *Angewandte Chemie Int. Ed.* **55**, 10239–10243 (2016).
14. N. Luan and J. Yao, "Surface plasmon resonance sensor based on exposed-core microstructured optical fiber placed with a silver wire," *IEEE Photonics J.* **8**, 1–8 (2016).
15. E. P. Schartner, A. Dowler, and H. Ebendorff-Heidepriem, "Fabrication of low-loss, small-core exposed core microstructured optical fibers," *Opt. Mater. Express* **7**, 1496–1502 (2017).
16. R. Kostecki, H. Ebendorff-Heidepriem, C. Davis, G. McAdam, S. C. Warren-Smith, and T. M. Monro, "Silica exposed-core microstructured optical fibers," *Opt. Mater. Express* **2**, 1538–1547 (2012).
17. R. Kostecki, H. Ebendorff-Heidepriem, S. C. Warren-Smith, and T. M. Monro, "Predicting the drawing conditions for microstructured optical fiber fabrication," *Opt. Mater. Express* **4**, 29–40 (2014).
18. X. Li, L. V. Nguyen, Y. Zhao, H. Ebendorff-Heidepriem, and S. C. Warren-Smith, "High-sensitivity sagnac-interferometer biosensor based on exposed core microstructured optical fiber," *Sensors Actuators B: Chem.* **269**, 103–109 (2018).
19. L. V. Nguyen, K. Hill, S. Warren-Smith, and T. Monro, "Interferometric-type optical biosensor based on exposed core microstructured optical fiber," *Sensors Actuators B: Chem.* **221**, 320–327 (2015).
20. S. C. Warren-Smith, E. Sinchenko, P. R. Stoddart, and T. M. Monro, "Distributed fluorescence sensing using exposed core microstructured optical fiber," *IEEE Photonics Technol. Lett.* **22**, 1385–1387 (2010).
21. R. Kostecki, H. Ebendorff-Heidepriem, S. Afshar V., G. McAdam, C. Davis, and T. M. Monro, "Novel polymer functionalization method for exposed-core optical fiber," *Opt. Mater. Express* **4**, 1515–1525 (2014).
22. L. S. Madsen, C. Baker, H. Rubinsztein-Dunlop, and W. P. Bowen, "Nondestructive profilometry of optical nanofibers," *Nano Lett.* **16**, 7333–7337 (2016).

23. J. D. Jackson, *Classical electrodynamics* (Wiley, 1999).
24. M. A. Taylor and W. P. Bowen, "Quantum metrology and its application in biology," *Phys. Reports* **615**, 1–59 (2016).
25. M. Chemnitz, M. Zeisberger, and M. A. Schmidt, "Performance limits of single nano-object detection with optical fiber tapers," *J. Opt. Soc. Am. B* **34**, 1833–1841 (2017).
26. X.-C. Yu, B.-B. Li, P. Wang, L. Tong, X.-F. Jiang, Y. Li, Q. Gong, and Y.-F. Xiao, "Single nanoparticle detection and sizing using a nanofiber pair in an aqueous environment," *Adv. Mater.* **26**, 7462–7467 (2014).
27. J. D. Swaim, J. Knittel, and W. P. Bowen, "Tapered nanofiber trapping of high-refractive-index nanoparticles," *Appl. Phys. Lett.* **103**, 203111 (2013).

### B.1 Small core ECFs spliced to small core SMFs

The results in Table B.1 show the coupling efficiency of sandwiching the small core ECF (Fig. 3.5(d)) between two commercial single mode fibres (UHNA4) as illustrated in Fig. B.1. This is a supportive information for publication [P5] for nanoscale particle detection based on a heterodyne measurement.



**Fig. B.1** An illustration of the splicing configuration, where S1 is the ECF input splice location while S2 is the ECF output splice location.

In Table B.1, samples were prepared in two separate times, so the input power from A was different. For samples (1-4), the power from input A is 240  $\mu\text{W}$ . For samples (5-9), the power from input A is 356  $\mu\text{W}$ . The measured power after the first splice (S1) was recorded as shown in the second column ‘B’; the measured power after the second splice (S2) was recorded as shown in the third column ‘C’. The final coupling efficiency is calculated by  $C/A$  with results in the final column of Table B.1.

9 spliced fibre devices				
Fibre samples	A ( $\mu\text{W}$ )	B ( $\mu\text{W}$ )	C ( $\mu\text{W}$ )	C/A
sample 1 (ECF 80 mm)	240	89	19.6	8%
sample 2 (ECF 99 mm)	240	56	52	22%
sample 3 (ECF 90 mm)	240	58	43	18%
sample 4 (ECF 95 mm)	240	81	44	18%
sample 5 (ECF 60 mm)	356	83	56	15%
sample 6 (ECF 55 mm)	356	50	30	8%
sample 7 (ECF 50 mm)	356	156	69	19%
sample 8 (ECF 50 mm)	356	128	84	24%
sample 9 (ECF 35 mm)	356	117	58	16%

**Table B.1** Coupling efficiency results for several integrated fibre samples are given by sandwiching small core ECF between two commercial UHNA4 fibres. These fibre samples were used in [P5] for measuring nanoscale particles based on evanescent field interaction.

## C Particle flow measurements

In order to track biological cells in the future, polystyrene beads were used in preliminary experiments to test the feasibility. Results of tracking polystyrene beads (diameter of  $5\ \mu\text{m}$  suspended in milli-Q water with a concentration of  $0.01\ \text{g}/\text{cm}^3$ ) are shown here. A simple flow chamber was made by stacking several capillaries as shown in Fig. C.1, where a single fibre (SMF-28) was used for probing and signal collection based on the OFDR technique. The light from the far-end of the SMF interferes with the scattered light from the individual particles over the detectable range (limited by diffraction and the coherence length of the light source) to generate optical interference. The measured signal is shown in the Fig. C.2.

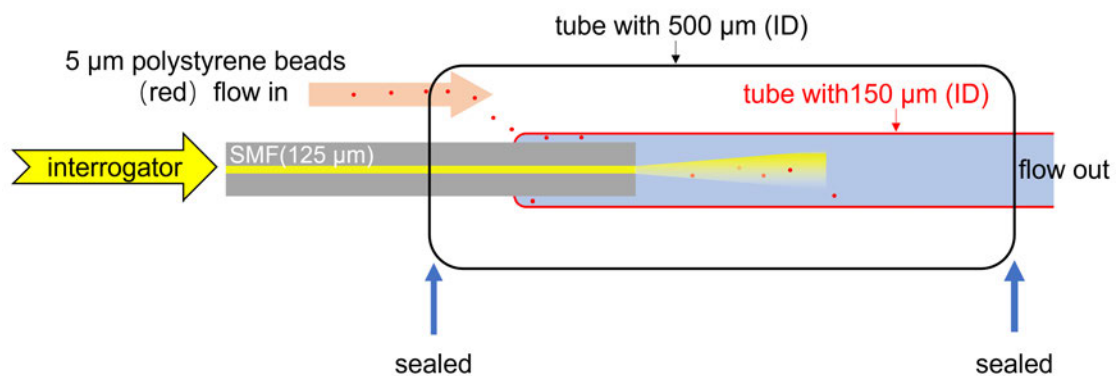


**Fig. C.1** Polystyrene spheres (red dots) from the left side were pumped into the capillary, which has an inner diameter of  $150\ \mu\text{m}$  to stack with the SMF ( $125\ \mu\text{m}$ ). Particles were then able to be detected by the fibre probe based on the OFDR system.

Single particles were able to be tracked as the function of time, shown as separate colours as a sequence with time spacing of  $1\ \text{s}$  in Fig. C.2. In this case, two particles were shown in the detection range as two groups of peaks seen to drop off with time. The probing light is diverging as illustrated by the yellow beam diffusion in Fig. C.1 due to the bare SMF output without further collimation, so particles with the same size at further distances show lower signals. The variation in the peak strength is associated with the transverse location of the particle, which is affected by both the flow speed and the hydrodynamic properties of the particle. This was a preliminary experiment aiming towards the tracking of real biological cells.

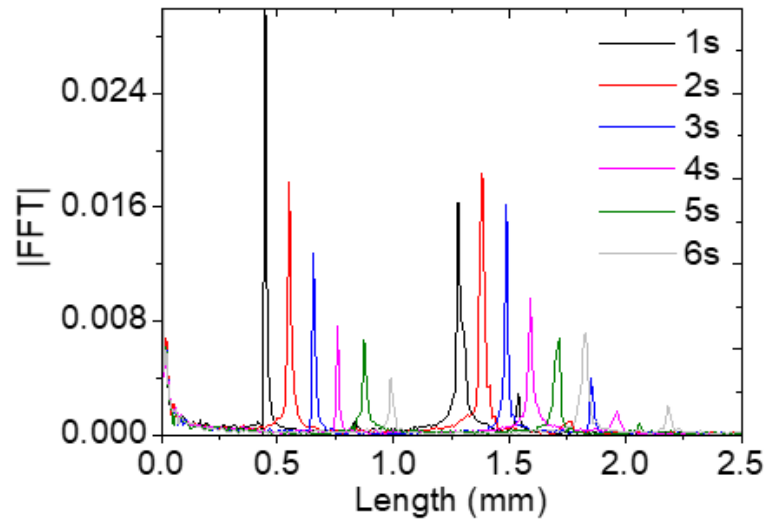


**Fig. C.2** Polystyrene spheres were suspended in milli-Q water to demonstrate particle tracking in fluids, using the configuration illustrated in Fig. C.1. The corresponding OFDR signals were recorded to show the movement of the individual particles as a function of the time.

Human embryonic kidney cells were then measured directly [211] as shown in Fig. C.3. Due to the lower contrast of the refractive index from the biological cell and the surrounding buffer, the signal from the cells were barely detected above the noise compared with the optical measurements using polystyrene spheres in Fig. C.2. While the detection distance is within 0.3 mm to allow a very weak signal to be collected, it is thus difficult to integrate the current OFDR system (with limited dynamic range of 40 dB) to do biological cell tracking experiments using either ECFs or SMFs. A possible approach would be the use of hollow core fibres, due to the direct hollow core waveguide providing a greater light-matter interaction. This could be future work, contributing to real-time tracking of biological cells and related cellular studies, while the tracking speed needs further improvements. As the sampling frequency of the interrogator used is limited to 10 Hz, it is potentially too slow to track particle's dynamics compared with reported speeds of 1 kHz in other reports [10].



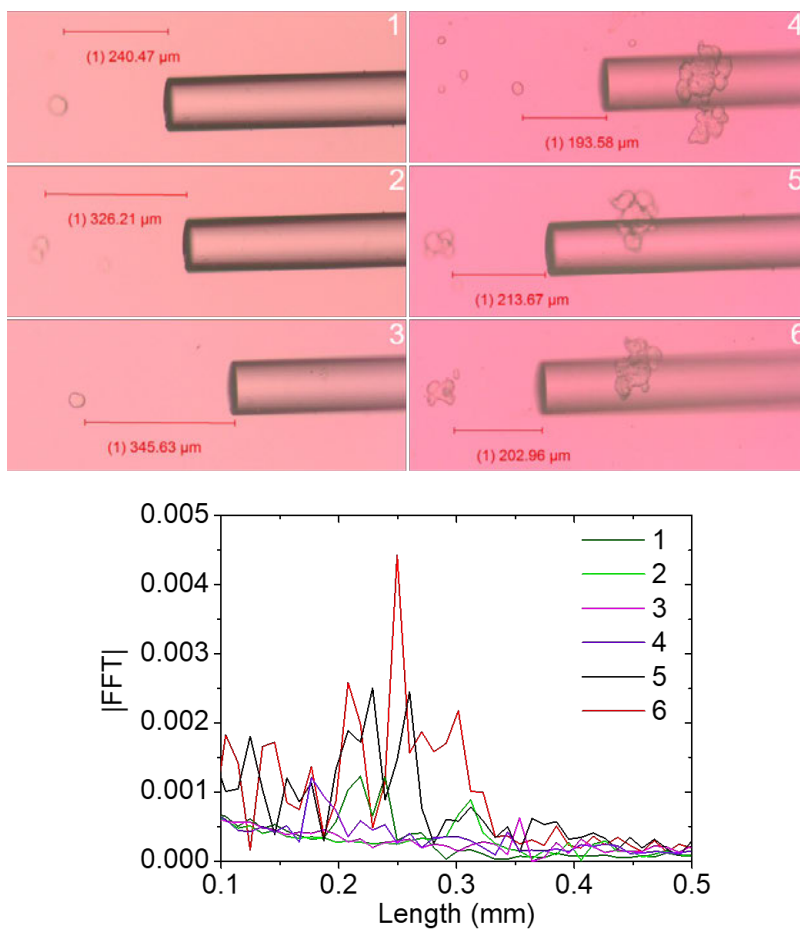


**Fig. C.3** A single SMF positioned near different biological cells, where the numbered FFT curve is matched with the numbered cell image at the top.

## D Mode launching using a spatial light modulator

Single mode excitation in the few-moded ECF via free space launching was used to achieve two-dimensional mapping of surface scatterers in Chapter 4.2 [P2]. This was limited to the excitation of lower-order modes. As for launching clean high-order modes (HOMs), the spatial light modulator (SLM) can be used to achieve such a purpose for high resolution mapping of surface scatterers.

Here, the details of how to use the SLM to modulate the input light beam is introduced. The principle of liquid crystal SLM is that a change in the voltage (greyscale levels of the loaded holograms) regulates the polarisability of the liquid crystal molecules. The wavefront modulation can be expressed as [219]:

$$E_{out}(x, y)e^{kr_{des}} = E_{in}(x, y)e^{ikr_{in}} \times e^{iH(x, y)} \quad (\text{D.1})$$

where  $E_{in}(x, y)e^{ikr_{in}}$  and  $E_{out}(x, y)e^{kr_{des}}$  represent the input and output wave field, and  $H(x, y)$  is the additional phase induced by the SLM. For modulation of a specific microstructured optical fibre mode, the phase information could be extracted from numerical simulations.

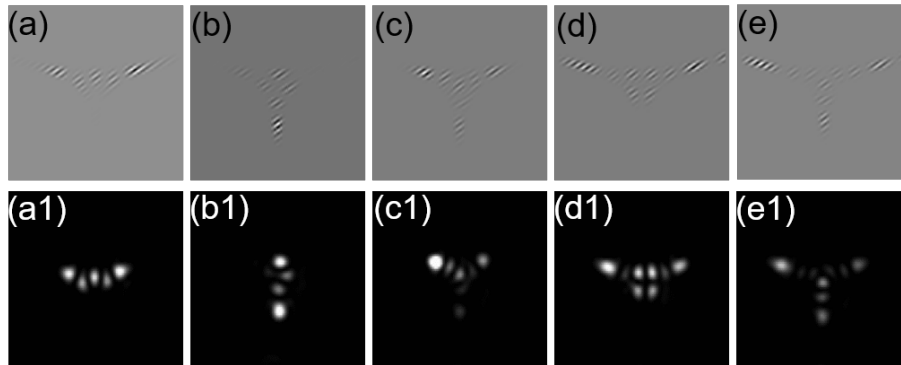


**Fig. D.1** (a-e) Holographic masks of ECF's HOMs generated using Matlab code. Experimentally measured beam using these holographic masks (in free space without coupling into the fibre) are in (a1-e1).

By programming in MATLAB [220], holographic masks based on the imported specific phase information (if the SLM is a phase-only modulated device) can be generated to modulate the desired beam. For example, the phase term of a specific fibre mode could be extracted from COMSOL 5.3, which can then be applied on SLM

to obtain the desired fibre mode profile. As shown in Figs. D.1(a1)-(e1), they were captured from the output after reflecting from the SLM with selectively loaded hologram masks (phase information of fibre modes with superimposed gratings) shown on the top in Figs. D.1(a)-(e). The SLM is modulated in phase, but a grating superimposed on the mode images (from COMSOL) is used to diffract and separate the modulated desired beam.

Calibration is needed for different light sources when using SLMs (Santec: SLM-100, in this work). Here a portable laser source 1550 nm (with power up to 1.6 mW) was used for this test. By changing one of the binary grating with different greyscale value (0-255) shown in Fig. D.2(a) [220], modulated light under different power was measured as shown in Fig. D.2(b). The greyscale could be regulated from 0 to 75 as an entire period in this system.

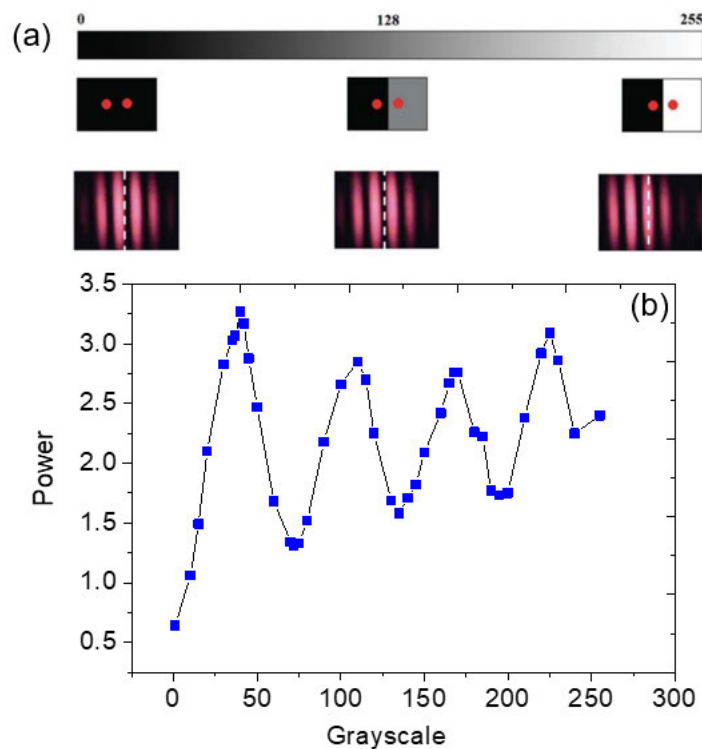


**Fig. D.2** (a) An illustration of calibration for the SLM according to the specific light source, from Ref. [220]. (b) The calibrated result using the 1550 nm laser in this experimental system according to the approach in (a).

A visible 532 nm laser was then used to modulate the incident beam to launch into the ECF, and the following results in Fig. D.3 show the output ECF mode profiles

captured from a visible camera. These results were preliminary examples to show the feasibility of using the SLM to launch the ECF modes.

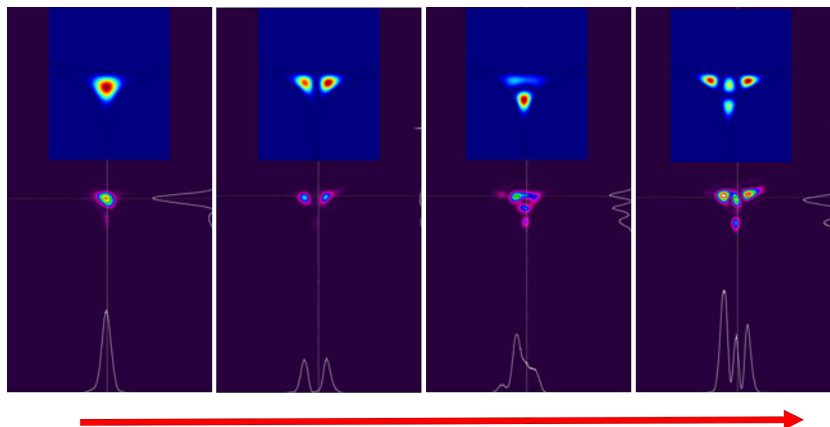


**Fig. D.3** ECF output mode profiles captured by a visible camera using the digital masks.

The interrogator used in this thesis has a fixed power of  $66 \mu\text{W}$  and a limited dynamic range of 40 dB. It is difficult to use the SLM for the proposed OFDR experiments as the modulation for high purity modes has only 11% diffraction efficiency [219].

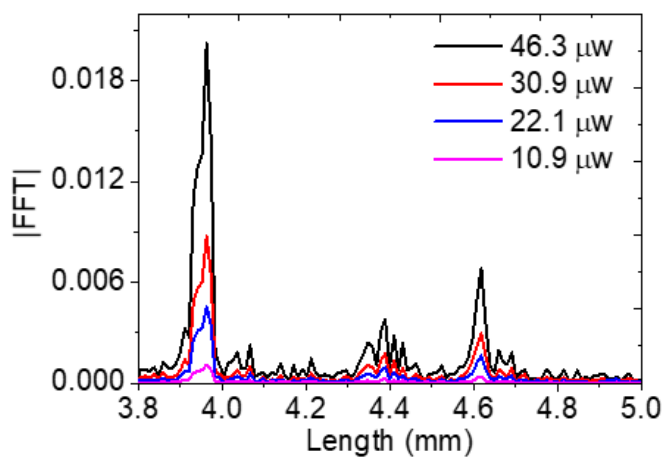


**Fig. D.4** Signal from polystyrene microspheres as a function of the input power.

Fig. D.4 shows the impact of reduced signal for the signal from polystyrene spheres. This was obtained without the SLM but neutral density filters were used to mimic the impact of reduced power. It is seen that the current measurement system is too close to the noise floor for implementing the SLM. However, there are

commercially available instruments with greater dynamic range such as those used for optical coherence tomography (OCT) systems, that could be used in the future.

## Bibliography

- [1] Thomas G Giallorenzi, Joseph A Bucaro, Anthony Dandridge, George H Sigel, James H Cole, Scott C Rashleigh, and Richard G Priest. Optical fiber sensor technology. *IEEE Trans. Microw. Theory Tech.*, 30(4):472–511, 1982.
- [2] Byoung-ho Lee. Review of the present status of optical fiber sensors. *Opt. Fiber Technol.*, 9(2):57–79, 2003.
- [3] Brian Culshaw. Optical fiber sensor technologies: opportunities and-pitfalls. *J. Light. Technol.*, 22(1):39, 2004.
- [4] Hao Guo, Qiang Zhu, Jun Tang, Fushun Nian, Wenyao Liu, Rui Zhao, Fangfang Du, Baoguo Yang, and Jun Liu. A temperature and humidity synchronization detection method based on microwave coupled-resonator. *Sens. Actuator B-Chem.*, 261:434–440, 2018.
- [5] Qing Bai, Qinglin Wang, Dong Wang, Yu Wang, Yan Gao, Hongjuan Zhang, Mingjiang Zhang, and Baoquan Jin. Recent advances in Brillouin optical time domain reflectometry. *Sens.*, 19(8):1862, 2019.
- [6] Frank Vollmer and Stephen Arnold. Whispering-gallery-mode biosensing: label-free detection down to single molecules. *Nat. Methods*, 5(7):591, 2008.
- [7] Xiao Chong Yu, Bei Bei Li, Pan Wang, Limin Tong, Xue Feng Jiang, Yan Li, Qihuang Gong, and Yun Feng Xiao. Single nanoparticle detection and sizing using a nanofiber pair in an aqueous environment. *Adv. Mater.*, 26(44):7462–7467, 2014.
- [8] Sanli Faez, Yoav Lahini, Stefan Weidlich, Rees F Garmann, Katrin Wondraczek, Matthias Zeisberger, Markus A Schmidt, Michel Orrit, and Vinodhan N Manoharan. Fast, label-free tracking of single viruses and weakly scattering

- nanoparticles in a nanofluidic optical fiber. *ACS Nano*, 9(12):12349–12357, 2015.
- [9] Shiqi Jiang, Jiangbo Zhao, Ronny Förster, Stefan Weidlich, Malte Plidschun, Jens Kobelke, Ron Fatobene Ando, and Markus A Schmidt. Three dimensional spatiotemporal nano-scale position retrieval of the confined diffusion of nano-objects inside optofluidic microstructured fibers. *Nanoscale*, 12(5):3146–3156, 2020.
- [10] Ronny Förster, Stefan Weidlich, Mona Nissen, Torsten Wieduwilt, Jens Kobelke, Aaron M Goldfain, Timothy K Chiang, Rees F Garmann, Vinothan N Manoharan, Yoav Lahini, and Markus A Schmidt. Tracking and analyzing the brownian motion of nano-objects inside hollow core fibers. *ACS Sens.*, 5(3):879–886, 2020.
- [11] Stephen C Warren-Smith, Heike Ebendorff-Heidepriem, Tze Cheung Foo, Roger Moore, Claire Davis, and Tanya M Monro. Exposed-core microstructured optical fibers for real-time fluorescence sensing. *Opt. Express*, 17(21):18533–18542, 2009.
- [12] Tanya M Monro, Stephen Warren-Smith, Erik P Schartner, Alexandre François, Sabrina Heng, Heike Ebendorff-Heidepriem, and Shakraam Afshar. Sensing with suspended-core optical fibers. *Opt. Fiber Tech.*, 16(6):343–356, 2010.
- [13] Stephen C Warren-Smith, Elena Sinchenko, Paul R Stoddart, and Tanya M Monro. Distributed fluorescence sensing using exposed core microstructured optical fiber. *IEEE Photon. Tech. Lett.*, 22(18):1385–1387, 2010.
- [14] <https://fisens.com/fbg-sensors/>. 2022.
- [15] <https://www.ia.omron.com/products/category/sensors/fiber-sensors/index.html>. 2022.
- [16] <https://www.keyence.com/products/sensor/fiber-optic/>. 2022.
- [17] <https://www.cn.neubrex.com/index.html>. 2022.

- [18] <https://lunainc.com/product-category/sensing-and-non-destructive-test-products?family=18category-13>. 2022.
- [19] Tobias Müller, Christian Schumann, and Annette Kraegeloh. STED microscopy and its applications: new insights into cellular processes on the nanoscale. *Chem. Phys. Chem.*, 13(8):1986–2000, 2012.
- [20] Stewart Miller. *Optical fiber telecommunications*. Elsevier, 2012.
- [21] Philip St J Russell. Photonic crystal fibers. *Science*, 299(5605):358–362, 2003.
- [22] Philip St J Russell. Photonic-crystal fibers. *J. Lightwave Tech.*, 24(12):4729–4749, 2006.
- [23] Tanya M Monro and Heike Ebendorff-Heidepriem. Progress in microstructured optical fibers. *Annu. Rev. Mater. Res.*, 36:467–495, 2006.
- [24] Detlef Gloge. Weakly guiding fibers. *Appl. Opt.*, 10(10):2252–2258, 1971.
- [25] Katsunari Okamoto. *Fundamentals of optical waveguides*. Academic press, 2006.
- [26] Govind P Agrawal. *Fiber-optic communication systems*, volume 222. John Wiley and Sons, 2012.
- [27] Xingde Li, Christian Chudoba, Tony Ko, Costas Pitris, and James G Fujimoto. Imaging needle for optical coherence tomography. *Opt. Lett.*, 25(20):1520–1522, 2000.
- [28] Youxin Mao, Shoude Chang, Sherif Sherif, and Costel Flueraru. Graded-index fiber lens proposed for ultrasmall probes used in biomedical imaging. *Appl. Opt.*, 46(23):5887–5894, 2007.
- [29] Chen Wang and Na Ji. Characterization and improvement of three-dimensional imaging performance of GRIN-lens-based two-photon fluorescence endomicroscopes with adaptive optics. *Opt. Express*, 21(22):27142–27154, 2013.



- [30] David J Richardson, John M Fini, and Lynn E Nelson. Space-division multiplexing in optical fibres. *Nat. Photon.*, 7(5):354–362, 2013.
- [31] Roy G H Van Uden, R Amezcua Correa, E Antonio Lopez, F M Huijskens, Cen Xia, G Li, A Schülzgen, H De Waardt, A M J Koonen, and Chigo M Okonkwo. Ultra-high-density spatial division multiplexing with a few-mode multicore fibre. *Nat. Photon.*, 8(11):865–870, 2014.
- [32] Jonathan C Knight, Tim A Birks, Philip St J Russell, and Dave M Atkin. All-silica single-mode optical fiber with photonic crystal cladding. *Opt. Lett.*, 21(19):1547–1549, 1996.
- [33] Jonathan C Knight, Jes Broeng, Tim A Birks, and Philip St J Russell. Photonic band gap guidance in optical fibers. *Science*, 282(5393):1476–1478, 1998.
- [34] Tim A Birks, Jonathan C Knight, and Philip St J Russell. Endlessly single-mode photonic crystal fiber. *Opt. Lett.*, 22(13):961–963, 1997.
- [35] Ana M Cubillas, Sarah Unterkofler, Tijmen G Euser, Bastian J M Etzold, Anita C Jones, Peter J Sadler, Peter Wasserscheid, and Philip St J Russell. Photonic crystal fibres for chemical sensing and photochemistry. *Chem. Society Rev.*, 42(22):8629–8648, 2013.
- [36] Andrey D Pryamikov, Alexander S Biriukov, Alexey F Kosolapov, Victor G Plotnichenko, Sergei L Semjonov, and Evgeny M Dianov. Demonstration of a waveguide regime for a silica hollow-core microstructured optical fiber with a negative curvature of the core boundary in the spectral region  $> 3.5 \mu\text{m}$ . *Opt. Express*, 19(2):1441–1448, 2011.
- [37] Philip St J Russell, Jonathan C Knight, Tim A Birks, B J Mangan, and W J Wadsworth. Recent progress in photonic crystal fibres. In *Optical Fiber Communication Conference*, page ThG1. Optical Society of America, 2000.
- [38] N M Litchinitser, A K Abeeluck, C Headley, and B J Eggleton. Antiresonant reflecting photonic crystal optical waveguides. *Opt. Lett.*, 27(18):1592–1594, 2002.

- [39] Francesco Poletti. Nested antiresonant nodeless hollow core fiber. *Opt. Express*, 22(20):23807–23828, 2014.
- [40] R F Cregan, B J Mangan, Jonathan C Knight, Tim A Birks, Philip St J Russell, P J Roberts, and D C Allan. Single-mode photonic band gap guidance of light in air. *Science*, 285(5433):1537–1539, 1999.
- [41] Fetah Benabid, Jonathan C Knight, G Antonopoulos, and P St J Russell. Stimulated Raman scattering in hydrogen-filled hollow-core photonic crystal fiber. *Science*, 298(5592):399–402, 2002.
- [42] F Couny, Fetah Benabid, P J Roberts, P S Light, and M G Raymer. Generation and photonic guidance of multi-octave optical-frequency combs. *Science*, 318(5853):1118–1121, 2007.
- [43] Francois Couny, Fetah Benabid, and P S Light. Subwatt threshold CW Raman fiber-gas laser based on  $H_2$ -filled hollow-core photonic crystal fiber. *Phys. Rev. Lett.*, 99(14):143903, 2007.
- [44] Rudrakant Sollapur, Daniil Kartashov, Michael Zürich, Andreas Hoffmann, Teodora Grigorova, Gregor Sauer, Alexander Hartung, Anka Schwuchow, Joerg Bierlich, Jens Kobelke, et al. Resonance-enhanced multi-octave supercontinuum generation in antiresonant hollow-core fibers. *Light Sci. Appl.*, 6(12):e17124–e17124, 2017.
- [45] Shoichi Okaba, Deshui Yu, Luca Vincetti, Fetah Benabid, and Hidetoshi Katori. Superradiance from lattice-confined atoms inside hollow core fibre. *Comm. Phys.*, 2(1):1–10, 2019.
- [46] Xinyue Zhu, Dakun Wu, Yazhou Wang, Fei Yu, Qiurui Li, Yunfeng Qi, Jonathan Knight, Shufen Chen, and Lili Hu. Delivery of CW laser power up to 300 watts at 1080 nm by an uncooled low-loss anti-resonant hollow-core fiber. *Opt. Express*, 29(2):1492–1501, 2021.
- [47] Shou-fei Gao, Ying-ying Wang, Wei Ding, Dong-liang Jiang, Shuai Gu, Xin Zhang, and Pu Wang. Hollow-core conjoined-tube negative-curvature fibre with ultralow loss. *Nat. Commun.*, 9(1):1–6, 2018.

- [48] Matthew A Terrel, Michel J F Digonnet, and Shanhui Fan. Resonant fiber optic gyroscope using an air-core fiber. *J. Lightwave Tech.*, 30(7):931–937, 2011.
- [49] P J Roberts, F Couny, H Sabert, B J Mangan, D P Williams, L Farr, M W Mason, A Tomlinson, Tim A Birks, Jonathan C Knight, and Philip St J Russell. Ultimate low loss of hollow-core photonic crystal fibres. *Opt. Express*, 13(1):236–244, 2005.
- [50] Antonino Nespola, Stefano Straullu, Thomas D Bradley, Kerriane Harrington, Hesham Sakr, Gregory T Jasion, Eric Numkam Fokoua, Yongmin Jung, Yong Chen, John R Hayes, et al. Transmission of 61 C-band channels with L-band interferers over record 618 km of hollow-core-fiber. In *Optical Fiber Communication Conference*, pages Th4B–5. Optical Society of America, 2020.
- [51] Tanya M Monro, D J Richardson, and PJ Bennett. Developing holey fibres for evanescent field devices. *Electron. Lett.*, 35(14):1188–1189, 1999.
- [52] Yinian Zhu, Henry Du, and Ryan Bise. Design of solid-core microstructured optical fiber with steering-wheel air cladding for optimal evanescent-field sensing. *Opt. Express*, 14(8):3541–3546, 2006.
- [53] T G Euser, J S Y Chen, M Scharrer, P St J Russell, N J Farrer, and P J Sadler. Quantitative broadband chemical sensing in air-suspended solid-core fibers. *J. Appl. Phys.*, 103(10):103108, 2008.
- [54] Shahraam V Afshar, Stephen C Warren-Smith, and Tanya M Monro. Enhancement of fluorescence-based sensing using microstructured optical fibres. *Opt. Express*, 15(26):17891–17901, 2007.
- [55] Andrew S Webb, Francesco Poletti, David J Richardson, and Jayanta Kumar Sahu. Suspended-core holey fiber for evanescent-field sensing. *Opt. Eng.*, 46(1):010503, 2007.
- [56] YL Hoo, Wei Jin, Hoi Lut Ho, Dongning Wang, and Robert S Windeler. Evanescent-wave gas sensing using microstructure fiber. *Opt. Eng.*, 41(1):8–9, 2002.

- [57] Xianfeng Chen, Kaiming Zhou, Lin Zhang, and Ian Bennion. Simultaneous measurement of temperature and external refractive index by use of a hybrid grating in D fiber with enhanced sensitivity by HF etching. *Appl. Opt.*, 44(2):178–182, 2005.
- [58] Ming-Hung Chiu, Shinn-Fwu Wang, and Rong-Seng Chang. D-type fiber biosensor based on surface-plasmon resonance technology and heterodyne interferometry. *Opt. Lett.*, 30(3):233–235, 2005.
- [59] Felicity M Cox, Richard Lwin, Maryanne C J Large, and Cristiano M B Cordeiro. Opening up optical fibres. *Opt. Express*, 15(19):11843–11848, 2007.
- [60] Heike Ebendorff-Heidepriem and Tanya M Monro. Extrusion of complex preforms for microstructured optical fibers. *Opt. Express*, 15(23):15086–15092, 2007.
- [61] Stephen C Warren-Smith, Roman Kostecki, Linh V Nguyen, and Tanya M Monro. Fabrication, splicing, Bragg grating writing, and polyelectrolyte functionalization of exposed-core microstructured optical fibers. *Opt. Express*, 22(24):29493–29504, 2014.
- [62] Erik P Schartner, Alastair Dowler, and Heike Ebendorff-Heidepriem. Fabrication of low-loss, small-core exposed core microstructured optical fibers. *Opt. Mat. Express*, 7(5):1496–1502, 2017.
- [63] Radislav A Potyrailo, Steven E Hobbs, and Gary M Hieftje. Optical waveguide sensors in analytical chemistry: today's instrumentation, applications and trends for future development. *Fresenius' journal of analytical chemistry*, 362(4):349–373, 1998.
- [64] Christiane Munkholm, David R Walt, and Fred P Milanovich. A fiber-optic sensor for CO<sub>2</sub> measurement. *Talanta*, 35(2):109–112, 1988.
- [65] Otto S Wolfbeis. Fiber-optic chemical sensors and biosensors. *Anal. Chem.*, 80(12):4269–4283, 2008.
- [66] Mark A Arnold. Fiber-optic chemical sensors. *Anal. Chem.*, 64(21):1015A–1025A, 1992.

- [67] Jiří Homola and Marek Piliarik. *Surface plasmon resonance (SPR) sensors*, pages 45–67. Springer, 2006.
- [68] Christophe Caucheteur, Tuan Guo, and Jacques Albert. Review of plasmonic fiber optic biochemical sensors: improving the limit of detection. *Anal. Bioanal. Chem.*, 407(14):3883–3897, 2015.
- [69] Shaopeng Wang, Xinping Huang, Xiaonan Shan, Kyle J Foley, and Nongjian Tao. Electrochemical surface plasmon resonance: basic formalism and experimental validation. *Anal. Chem.*, 82(3):935–941, 2010.
- [70] David L Stokes and Tuan Vo-Dinh. Development of an integrated single-fiber SERS sensor. *Sens. Actuator B: Chem.*, 69(1-2):28–36, 2000.
- [71] Xianliang Zheng, Dangwei Guo, Yunliang Shao, Shaojie Jia, Shuping Xu, Bing Zhao, Weiqing Xu, Charlie Corredor, and John R Lombardi. Photochemical modification of an optical fiber tip with a silver nanoparticle film: a SERS chemical sensor. *Langmuir*, 24(8):4394–4398, 2008.
- [72] Luis M Liz-Marzán. Tailoring surface plasmons through the morphology and assembly of metal nanoparticles. *Langmuir*, 22(1):32–41, 2006.
- [73] Borja Sepúlveda, Paula C Angelomé, Laura M Lechuga, and Luis M Liz-Marzán. LSPR-based nanobiosensors. *Nano Today*, 4(3):244–251, 2009.
- [74] Yong Zhao, Rui-jie Tong, Feng Xia, and Yun Peng. Current status of optical fiber biosensor based on surface plasmon resonance. *Biosens. Bioelectron.*, 142:111505, 2019.
- [75] Elizaveta Klantsataya, Alexandre François, Heike Ebendorff-Heidepriem, Peter Hoffmann, and Tanya M Monro. Surface plasmon scattering in exposed core optical fiber for enhanced resolution refractive index sensing. *Sensors*, 15(10):25090–25102, 2015.
- [76] Brenda Doherty, Andrea Csáki, Matthias Thiele, Matthias Zeisberger, Anka Schwuchow, Jens Kobelke, Wolfgang Fritzsche, and Markus A Schmidt. Nanoparticle functionalised small-core suspended-core fibre—a novel platform for efficient sensing. *Biomed. Opt. Express*, 8(2):790–799, 2017.

- [77] Matthew R Foreman, Jon D Swaim, and Frank Vollmer. Whispering gallery mode sensors. *Adv. Opt. Photon.*, 7(2):168–240, 2015.
- [78] Lina He, Şahin Kaya Özdemir, and Lan Yang. Whispering gallery microcavity lasers. *Laser Photon. Rev.*, 7(1):60–82, 2013.
- [79] Eugene Kim, Martin D Baaske, and Frank Vollmer. Towards next-generation label-free biosensors: recent advances in whispering gallery mode sensors. *Lab Chip*, 17(7):1190–1205, 2017.
- [80] Guoping Lin, Aurélien Coillet, and Yanne K Chembo. Nonlinear photonics with high-Q whispering-gallery-mode resonators. *Adv. Opt. Photon.*, 9(4):828–890, 2017.
- [81] Ya-nan Zhang, Tianmin Zhou, Bo Han, Aozhuo Zhang, and Yong Zhao. Optical bio-chemical sensors based on whispering gallery mode resonators. *Nanoscale*, 10(29):13832–13856, 2018.
- [82] Martin D Baaske and Frank Vollmer. Optical observation of single atomic ions interacting with plasmonic nanorods in aqueous solution. *Nat. Photon.*, 10(11):733–739, 2016.
- [83] Guo-Qing Wei, Xue-Dong Wang, and Liang-Sheng Liao. Recent advances in organic whispering-gallery mode lasers. *Laser Photon. Rev.*, 14(11):2000257, 2020.
- [84] A Weller, FC Liu, R Dahint, and M Himmelhaus. Whispering gallery mode biosensors in the low-Q limit. *Appl. Phys. B*, 90(3):561–567, 2008.
- [85] Andrea M Armani, Rajan P Kulkarni, Scott E Fraser, Richard C Flagan, and Kerry J Vahala. Label-free, single-molecule detection with optical microcavities. *Science*, 317(5839):783–787, 2007.
- [86] J Cheung Knight, G Cheung, F Jacques, and TA Birks. Phase-matched excitation of whispering-gallery-mode resonances by a fiber taper. *Opt. Lett.*, 22(15):1129–1131, 1997.

- [87] Oleksiy Svitelskiy, Yangcheng Li, Arash Darafsheh, Misha Sumetsky, David Carnegie, Edik Rafailov, and Vasily N Astratov. Fiber coupling to BaTiO<sub>3</sub> glass microspheres in an aqueous environment. *Opt. Lett.*, 36(15):2862–2864, 2011.
- [88] Alexandre François, Kristopher J Rowland, and Tanya M Monro. Highly efficient excitation and detection of whispering gallery modes in a dye-doped microsphere using a microstructured optical fiber. *Appl. Phy. Lett.*, 99(14):141111, 2011.
- [89] Kyriaki Kosma, Gianluigi Zito, Kay Schuster, and Stavros Pissadakis. Whispering gallery mode microsphere resonator integrated inside a microstructured optical fiber. *Opt. Lett.*, 38(8):1301–1303, 2013.
- [90] Alexandre François, Nicolas Riesen, Hong Ji, Shahraam Afshar V, and Tanya M Monro. Polymer based whispering gallery mode laser for biosensing applications. *Appl. Phy. Lett.*, 106(3):031104, 2015.
- [91] Ruohui Wang, Michael Fraser, Jiacheng Li, Xueguang Qiao, and Anbo Wang. Integrated in-fiber coupler for microsphere whispering-gallery modes resonator excitation. *Opt. Lett.*, 40(3):308–311, 2015.
- [92] Ming Cai, Oskar Painter, and Kerry J Vahala. Observation of critical coupling in a fiber taper to a silica-microsphere whispering-gallery mode system. *Phys. Rev. Lett.*, 85(1):74, 2000.
- [93] X Q Bai and D N Wang. Whispering-gallery-mode excitation in a microsphere by use of an etched cavity on a multimode fiber end. *Opt. Lett.*, 43(22):5512–5515, 2018.
- [94] Xin Liu, XL Cui, and DN Wang. Integrated in-fiber coupler for a whispering-gallery mode microsphere resonator. *Opt. Lett.*, 45(6):1467–1470, 2020.
- [95] Shahraam V Afshar, Yinlan Ruan, Stephen C Warren-Smith, and Tanya M Monro. Enhanced fluorescence sensing using microstructured optical fibers: a comparison of forward and backward collection modes. *Opt. Lett.*, 33(13):1473–1475, 2008.

- [96] Jiangang Zhu, Sahin Kaya Ozdemir, Yun-Feng Xiao, Lin Li, Lina He, Da-Ren Chen, and Lan Yang. On-chip single nanoparticle detection and sizing by mode splitting in an ultrahigh-Q microresonator. *Nat. Photon.*, 4(1):46, 2010.
- [97] Lina He, Şahin Kaya Özdemir, Jiangang Zhu, Woosung Kim, and Lan Yang. Detecting single viruses and nanoparticles using whispering gallery microlasers. *Nat. Nanotech.*, 6(7):428–432, 2011.
- [98] Marcel Schubert, Anja Steude, Philipp Liehm, Nils M Kronenberg, Markus Karl, Elaine C Campbell, Simon J Powis, and Malte C Gather. Lasing within live cells containing intracellular optical microresonators for barcode-type cell tagging and tracking. *Nano Lett.*, 15(8):5647–5652, 2015.
- [99] Nikita Toropov, Gema Cabello, Mariana P Serrano, Rithvik R Gutha, Matías Rafti, and Frank Vollmer. Review of biosensing with whispering-gallery mode lasers. *Light Sci. Appl.*, 10(1):1–19, 2021.
- [100] Yun Jiang Rao. In-fibre Bragg grating sensors. *Meas. Sci. Technol*, 8(4):355, 1997.
- [101] Kenneth O Hill and Gerald Meltz. Fiber Bragg grating technology fundamentals and overview. *J. Light. Technol.*, 15(8):1263–1276, 1997.
- [102] Alan D Kersey, Michael A Davis, Heather J Patrick, Michel LeBlanc, KP Koo, CG Askins, MA Putnam, and E Joseph Friebele. Fiber grating sensors. *J. Light. Technol.*, 15(8):1442–1463, 1997.
- [103] Yunmiao Wang, Jianmin Gong, Dorothy Y Wang, Bo Dong, Weihong Bi, and Anbo Wang. A quasi-distributed sensing network with time-division-multiplexed fiber Bragg gratings. *IEEE Photon. Technol. Lett.*, 23(2):70–72, 2010.
- [104] George T Kanellos, George Papaioannou, Dimitris Tsiokos, Christos Mitrogiannis, George Nianios, and Nikos Pleros. Two dimensional polymer-embedded quasi-distributed FBG pressure sensor for biomedical applications. *Opt. Express*, 18(1):179–186, 2010.



- [105] Yue-Jing He, Yu-Lung Lo, and Jen-Fa Huang. Optical-fiber surface-plasmon-resonance sensor employing long-period fiber gratings in multiplexing. *JOSA B*, 23(5):801–811, 2006.
- [106] Galina Nemova and Raman Kashyap. Fiber-Bragg-grating-assisted surface plasmon-polariton sensor. *Opt. Lett.*, 31(14):2118–2120, 2006.
- [107] Yiping Wang. Review of long period fiber gratings written by CO<sub>2</sub> laser. *J. Appl. Phys.*, 108(8):11, 2010.
- [108] Tuan Guo, Fu Liu, Bai-Ou Guan, and Jacques Albert. Tilted fiber grating mechanical and biochemical sensors. *Opt. Laser Technol.*, 78:19–33, 2016.
- [109] Jiajie Lao, Peng Sun, Fu Liu, Xuejun Zhang, Chuanxi Zhao, Wenjie Mai, Tuan Guo, Gaozhi Xiao, and Jacques Albert. In situ plasmonic optical fiber detection of the state of charge of supercapacitors for renewable energy storage. *Light Sci. Appl.*, 7(1):1–11, 2018.
- [110] Joseph Schmitt. Optical coherence tomography (OCT): a review. *IEEE J. Sel. Top. Quant. Electron.*, 5(4):1205–1215, 1999.
- [111] D Malacara. Twyman–Green interferometer. *Opt. Shop Testing*, 2:46–96, 1992.
- [112] Teng Zhang, Stefan L Danilishin, Sebastian Steinlechner, Bryan W Barr, Angus S Bell, Peter Dupej, Christian Gräf, Jan-Simon Hennig, Alasdair E Houston, Sabina H Huttner, Sean S. Leavey, Daniela Pascucci, Borja Sorazu, Andrew Spencer, Jennifer Wright, Kenneth A Strain, and Stefan Hild. Effects of static and dynamic higher-order optical modes in balanced homodyne readout for future gravitational waves detectors. *Phys. Rev. D*, 95(6):062001, 2017.
- [113] Xuegang Li, Stephen C Warren-Smith, Heike Ebendorff-Heidepriem, Ya-nan Zhang, and Linh V Nguyen. Optical fiber refractive index sensor with low detection limit and large dynamic range using a hybrid fiber interferometer. *J. Light. Technol.*, 37(13):2954–2962, 2019.
- [114] Linh V Nguyen, Dusun Hwang, Sucbei Moon, Dae Seung Moon, and Youngjoo Chung. High temperature fiber sensor with high sensitivity based on core diameter mismatch. *Opt. Express*, 16(15):11369–11375, 2008.

- [115] Hae Young Choi, Kwan Seob Park, Seong Jun Park, Un-Chul Paek, Byeong Ha Lee, and Eun Seo Choi. Miniature fiber-optic high temperature sensor based on a hybrid structured Fabry-Pérot interferometer. *Opt. Lett.*, 33(21):2455–2457, 2008.
- [116] Xingwei Wang, Juncheng Xu, Yizheng Zhu, Kristie L Cooper, and Anbo Wang. All-fused-silica miniature optical fiber tip pressure sensor. *Opt. Lett.*, 31(7):885–887, 2006.
- [117] Chuang Wu, HY Fu, Khurram Karim Qureshi, Bai-Ou Guan, and Hwa Yaw Tam. High-pressure and high-temperature characteristics of a Fabry-Pérot interferometer based on photonic crystal fiber. *Opt. Lett.*, 36(3):412–414, 2011.
- [118] Chuang Wu, Zhengyong Liu, A Ping Zhang, Bai-Ou Guan, and Hwa-Yaw Tam. In-line open-cavity Fabry-Pérot interferometer formed by C-shaped fiber for temperature-insensitive refractive index sensing. *Opt. Express*, 22(18):21757–21766, 2014.
- [119] Stephen C Warren-Smith, Ricardo M André, Jan Dellith, Tina Eschrich, Martin Becker, and Hartmut Bartelt. Sensing with ultra-short Fabry-Pérot cavities written into optical micro-fibers. *Sens. Actuator B-Chem.*, 244:1016–1021, 2017.
- [120] Victor Vali and RW Shorthill. Fiber ring interferometer. *Appl. Opt.*, 15(5):1099–1100, 1976.
- [121] Peng Zu, Chi Chiu Chan, Lew Wen Siang, Yongxing Jin, Yifan Zhang, Liew Hwi Fen, Lihan Chen, and Xinyong Dong. Magneto-optic fiber Sagnac modulator based on magnetic fluids. *Opt. Lett.*, 36(8):1425–1427, 2011.
- [122] Peng Zu, Chi Chiu Chan, Guo Wei Koh, Wen Siang Lew, Yongxing Jin, Hwi Fen Liew, Wei Chang Wong, and Xinyong Dong. Enhancement of the sensitivity of magneto-optical fiber sensor by magnifying the birefringence of magnetic fluid film with Loya-Sagnac interferometer. *Sens. Actuator B-Chem.*, 191:19–23, 2014.
- [123] Ben Xu, CL Zhao, Fan Yang, Huaping Gong, DN Wang, Jixiang Dai, and

- Minghong Yang. Sagnac interferometer hydrogen sensor based on panda fiber with Pt-loaded  $\text{WO}_3/\text{SiO}_2$  coating. *Opt. Lett.*, 41(7):1594–1597, 2016.
- [124] Xuegang Li, Linh V Nguyen, Yong Zhao, Heike Ebendorff-Heidepriem, and Stephen C Warren-Smith. High-sensitivity Sagnac-interferometer biosensor based on exposed core microstructured optical fiber. *Sens. Actuator B-Chem.*, 269:103–109, 2018.
- [125] MK Barnoski and SM Jensen. Fiber waveguides: a novel technique for investigating attenuation characteristics. *Applied optics*, 15(9):2112–2115, 1976.
- [126] Alfredo Güemes, Antonio Fernández-López, and Brian Soller. Optical fiber distributed sensing—physical principles and applications. *Struct. Health Monit.*, 9(3):233–245, 2010.
- [127] Xiaoyi Bao and Liang Chen. Recent progress in distributed fiber optic sensors. *Sens.*, 12(7):8601–8639, 2012.
- [128] David A Krohn, Trevor MacDougall, and Alexis Mendez. *Fiber optic sensors: fundamentals and applications*. Spie Press Bellingham, WA, 2014.
- [129] J P Dakin, D J Pratt, G W Bibby, and J N Ross. Distributed optical fibre Raman temperature sensor using a semiconductor light source and detector. *Electron. Lett.*, 21(13):569–570, 1985.
- [130] Mostafa Ahangrani Farahani and Torsten Gogolla. Spontaneous Raman scattering in optical fibers with modulated probe light for distributed temperature Raman remote sensing. *J. Light. Technol.*, 17(8):1379, 1999.
- [131] Meng Wang, Hao Wu, Ming Tang, Zhiyong Zhao, Yunli Dang, Can Zhao, Ruolin Liao, Wen Chen, Songnian Fu, Chen Yang, et al. Few-mode fiber based Raman distributed temperature sensing. *Opt. Express*, 25(5):4907–4916, 2017.
- [132] Tsuneo Horiguchi and Mitsuhiro Tateda. Optical-fiber-attenuation investigation using stimulated Brillouin scattering between a pulse and a continuous wave. *Opt. Lett.*, 14(8):408–410, 1989.

- [133] W f Eickhoff and R f Ulrich. Optical frequency domain reflectometry in single-mode fiber. *Appl. Phys. Lett.*, 39(9):693–695, 1981.
- [134] Tsuneo Horiguchi, Kaoru Shimizu, Toshio Kurashima, Mitsuhiro Tateda, and Yahei Koyamada. Development of a distributed sensing technique using Brillouin scattering. *J. Light. Technol.*, 13(7):1296–1302, 1995.
- [135] Xiaoyi Bao and Liang Chen. Recent progress in Brillouin scattering based fiber sensors. *Sens.*, 11(4):4152–4187, 2011.
- [136] Qi Liu, Jing Chai, Shaojie Chen, Dingding Zhang, Qiang Yuan, and Shuai Wang. Monitoring and correction of the stress in an anchor bolt based on pulse pre-pumped Brillouin optical time domain analysis. *Energy Sci. Eng.*, 8(6):2011–2023, 2020.
- [137] Zhenyang Ding, Chenhuan Wang, Kun Liu, Junfeng Jiang, Di Yang, Guanyi Pan, Zelin Pu, and Tiegeng Liu. Distributed optical fiber sensors based on optical frequency domain reflectometry: A review. *Sens.*, 18(4):1072, 2018.
- [138] Shiyuan Zhao, Jiwen Cui, Zhanjun Wu, and Jiubin Tan. Accuracy improvement in OFDR-based distributed sensing system by image processing. *Opt. Laser Eng.*, 124:105824, 2020.
- [139] Claudia Preininger, Ingo Klimant, and Otto S Wolfbeis. Optical fiber sensor for biological oxygen demand. *Anal. Chem.*, 66(11):1841–1846, 1994.
- [140] Limin Tong, Rafael R Gattass, Jonathan B Ashcom, Sailing He, Jingyi Lou, Mengyan Shen, Iva Maxwell, and Eric Mazur. Subwavelength-diameter silica wires for low-loss optical wave guiding. *Nature*, 426(6968):816–819, 2003.
- [141] Leilei Shi, Tao Zhu, Dongmei Huang, Min Liu, Ming Deng, and Wei Huang. In-fiber whispering-gallery-mode resonator fabricated by femtosecond laser micromachining. *Opt. Lett.*, 40(16):3770–3773, 2015.
- [142] Leilei Shi, Tao Zhu, Dongmei Huang, Chuancan Liang, Min Liu, and Shibin Liang. In-fiber Mach–Zehnder interferometer and sphere whispering gallery mode resonator coupling structure. *Opt. Lett.*, 42(1):167–170, 2017.

- [143] Boris Polyak, Efim Bassis, Alex Novodvoretz, Shimshon Belkin, and Robert S Marks. Bioluminescent whole cell optical fiber sensor to genotoxicants: system optimization. *Sens. Actuator B-Chem.*, 74(1-3):18–26, 2001.
- [144] Sunil K Khijwania, Kirthi L Srinivasan, and Jagdish P Singh. An evanescent-wave optical fiber relative humidity sensor with enhanced sensitivity. *Sens. Actuator B-Chem.*, 104(2):217–222, 2005.
- [145] S K Khijwania and B D Gupta. Fiber optic evanescent field absorption sensor: effect of fiber parameters and geometry of the probe. *Opt. Quant. Electron.*, 31(8):625–636, 1999.
- [146] B D Gupta and Navneet K Sharma. Fabrication and characterization of u-shaped fiber-optic ph probes. *Sens. Actuator B: Chem.*, 82(1):89–93, 2002.
- [147] Jian Yao Zheng, Yongli Yan, Xiaopeng Wang, Wen Shi, Huimin Ma, Yong Sheng Zhao, and Jiannian Yao. Hydrogen peroxide vapor sensing with organic core/sheath nanowire optical waveguides. *Adv. Mat.*, 24(35):OP194–OP199, 2012.
- [148] Limin Tong, Jingyi Lou, and Eric Mazur. Single-mode guiding properties of subwavelength-diameter silica and silicon wire waveguides. *Opt. Express*, 12(6):1025–1035, 2004.
- [149] Stephen C Warren-Smith, Mario Chemnitz, Henrik Schneidewind, Roman Kostecky, Heike Ebendorff-Heidepriem, Tanya M Monro, and Markus A Schmidt. Nanofilm-induced spectral tuning of third harmonic generation. *Opt. Lett.*, 42(9):1812–1815, 2017.
- [150] Erik J Sánchez, Lukas Novotny, and X Sunney Xie. Near-field fluorescence microscopy based on two-photon excitation with metal tips. *Phys. Rev. Lett.*, 82(20):4014, 1999.
- [151] Yuri Nakayama, Peter J Pauzauskie, Aleksandra Radenovic, Robert M Onorato, Richard J Saykally, Jan Liphardt, and Peidong Yang. Tunable nanowire nonlinear optical probe. *Nature*, 447(7148):1098–1101, 2007.

- [152] Jiangbo Zhao, Dayong Jin, Erik P Schartner, Yiqing Lu, Yujia Liu, Andrei V Zvyagin, Lixin Zhang, Judith M Dawes, Peng Xi, James A Piper, Ewa M. Goldys, and Tanya M. Monro. Single-nanocrystal sensitivity achieved by enhanced upconversion luminescence. *Nat. Nanotechnol.*, 8(10):729–734, 2013.
- [153] Yujia Liu, Yiqing Lu, Xusan Yang, Xianlin Zheng, Shihui Wen, Fan Wang, Xavier Vidal, Jiangbo Zhao, Deming Liu, and Zhiguang Zhou. Amplified stimulated emission in upconversion nanoparticles for super-resolution nanoscopy. *Nature*, 543(7644):229–233, 2017.
- [154] Renee Drougard. Optical transfer properties of fiber bundles. *JOSA*, 54(7):907–914, 1964.
- [155] Karen S Bronk, Karri L Michael, Paul Pantano, and David R Walt. Combined imaging and chemical sensing using a single optical imaging fiber. *Anal. Chem.*, 67(17):2750–2757, 1995.
- [156] Xianpei Chen, Kristen Lantz Reichenbach, and Chris Xu. Experimental and theoretical analysis of core-to-core coupling on fiber bundle imaging. *Opt. Express*, 16(26):21598–21607, 2008.
- [157] J M Stone, H A C Wood, K Harrington, and T A Birks. Low index contrast imaging fibers. *Opt. Lett.*, 42(8):1484–1487, 2017.
- [158] H A C Wood, Kerriane Harrington, T A Birks, J C Knight, and J M Stone. High-resolution air-clad imaging fibers. *Opt. Lett.*, 43(21):5311–5314, 2018.
- [159] Stephen C Warren-Smith, Alastair Dowler, and Heike Ebendorff-Heidepriem. Soft-glass imaging microstructured optical fibers. *Opt. Express*, 26(26):33604–33612, 2018.
- [160] David Huang, Eric A Swanson, Charles P Lin, Joel S Schuman, William G Stinson, Warren Chang, Michael R Hee, Thomas Flotte, Kenton Gregory, Carmen A Puliafito, and James G Fujimoto. Optical coherence tomography. *Science*, 254(5035):1178–1181, 1991.
- [161] Adolf Friedrich Fercher. Optical coherence tomography. *J. Biomed. Opt.*, 1(2):157–173, 1996.

- [162] Michael R Hee, Joseph A Izatt, Eric A Swanson, David Huang, Joel S Schuman, Charles P Lin, Carmen A Puliafito, and James G Fujimoto. Optical coherence tomography of the human retina. *Archives of Ophthalmology*, 113(3):325–332, 1995.
- [163] Mehreen Adhi and Jay S Duker. Optical coherence tomography—current and future applications. *Current Opinion in Ophthalmology*, 24(3):213, 2013.
- [164] Talisa E De Carlo, Andre Romano, Nadia K Waheed, and Jay S Duker. A review of optical coherence tomography angiography (OCTA). *International J. Retina and Vitreous*, 1(1):5, 2015.
- [165] A Gh Podoleanu. Optical coherence tomography. *The British J Radiology*, 78(935):976–988, 2005.
- [166] Richard F Spaide, James G Fujimoto, Nadia K Waheed, Srinivas R Sadda, and Giovanni Staurenghi. Optical coherence tomography angiography. *Progress in Retinal and Eye Res.*, 64:1–55, 2018.
- [167] Adolf F Fercher, Wolfgang Drexler, Christoph K Hitzenberger, and Theo Lasser. Optical coherence tomography—principles and applications. *Rep. Prog. Phys.*, 66(2):239, 2003.
- [168] Michalina J Gora, Melissa J Suter, Guillermo J Tearney, and Xingde Li. Endoscopic optical coherence tomography: technologies and clinical applications. *Biomed. Opt. Express*, 8(5):2405–2444, 2017.
- [169] Hamid Pahlevaninezhad, Mohammadreza Khorasaninejad, Yao-Wei Huang, Zhujun Shi, Lida P Hariri, David C Adams, Vivien Ding, Alexander Zhu, Cheng-Wei Qiu, Federico Capasso, and Melissa J Suter. Nano-optic endoscope for high-resolution optical coherence tomography in vivo. *Nat. Photon.*, 12(9):540–547, 2018.
- [170] Reza Nasiri Mahalati, Ruo Yu Gu, and Joseph M Kahn. Resolution limits for imaging through multi-mode fiber. *Opt. Express*, 21(2):1656–1668, 2013.

- [171] Gregoire PJ Laporte, Nicolino Stasio, Christophe Moser, and Demetri Psaltis. Enhanced resolution in a multimode fiber imaging system. *Opt. Express*, 23(21):27484–27493, 2015.
- [172] Antonio M Caravaca-Aguirre and Rafael Piestun. Single multimode fiber endoscope. *Opt. Express*, 25(3):1656–1665, 2017.
- [173] Amnon Yariv. Phase conjugate optics and real-time holography. *IEEE J. Quantum Electron.*, 14(9):650–660, 1978.
- [174] Ioannis N Papadopoulos, Salma Farahi, Christophe Moser, and Demetri Psaltis. Focusing and scanning light through a multimode optical fiber using digital phase conjugation. *Opt. Express*, 20(10):10583–10590, 2012.
- [175] Tomáš Čižmár and Kishan Dholakia. Shaping the light transmission through a multimode optical fibre: complex transformation analysis and applications in biophotonics. *Opt. Express*, 19(20):18871–18884, 2011.
- [176] Youngwoon Choi, Changhyeong Yoon, Moonseok Kim, Taeseok Daniel Yang, Christopher Fang-Yen, Ramachandra R Dasari, Kyoung Jin Lee, and Wonshik Choi. Scanner-free and wide-field endoscopic imaging by using a single multimode optical fiber. *Phys. Rev. Lett.*, 109(20):203901, 2012.
- [177] Antonio M Caravaca-Aguirre, Eyal Niv, Donald B Conkey, and Rafael Piestun. Real-time resilient focusing through a bending multimode fiber. *Opt. Express*, 21(10):12881–12887, 2013.
- [178] Moussa NGom, Theodore B Norris, Eric Michielssen, and Raj Rao Nadakuditi. Mode control in a multimode fiber through acquiring its transmission matrix from a reference-less optical system. *Opt. Lett.*, 43(3):419–422, 2018.
- [179] Sébastien Popoff, Geoffroy Lerosey, Mathias Fink, Albert Claude Boccara, and Sylvain Gigan. Image transmission through an opaque material. *Nat. Commun.*, 1(1):1–5, 2010.
- [180] Nadav Shabairou, Eyal Cohen, Omer Wagner, Dror Malka, and Zeev Zalevsky. Color image identification and reconstruction using artificial neural networks on



- multimode fiber images: Towards an all-optical design. *Opt. Lett.*, 43(22):5603–5606, 2018.
- [181] Navid Borhani, Eirini Kakkava, Christophe Moser, and Demetri Psaltis. Learning to see through multimode fibers. *Optica*, 5(8):960–966, 2018.
- [182] Pengfei Fan, Tianrui Zhao, and Lei Su. Deep learning the high variability and randomness inside multimode fibers. *Opt. Express*, 27(15):20241–20258, 2019.
- [183] Wen Xiong, Brandon Redding, Shai Gertler, Yaron Bromberg, Hemant D Tagare, and Hui Cao. Deep learning of ultrafast pulses with a multimode fiber. *APL Photon.*, 5(9):096106, 2020.
- [184] Yan Liu, Guangde Li, Qi Qin, Zhongwei Tan, Muguang Wang, and Fengping Yan. Bending recognition based on the analysis of fiber specklegrams using deep learning. *Opt. Laser Tech.*, 131:106424, 2020.
- [185] Thiago D Cabral, Eric Fujiwara, Stephen C Warren-Smith, Heike Ebendorff-Heidepriem, and Cristiano M B Cordeiro. Multimode exposed core fiber specklegram sensor. *Opt. Lett.*, 45(12):3212–3215, 2020.
- [186] Linh V Nguyen, Cuong C Nguyen, Gustavo Carneiro, Heike Ebendorff-Heidepriem, and Stephen C Warren-Smith. Sensing in the presence of strong noise by deep learning of dynamic multimode fiber interference. *Photon. Res.*, 9(4):B109–B118, 2021.
- [187] Emiel W A Visser, Junhong Yan, Leo J van IJzendoorn, and Menno W J Prins. Continuous biomarker monitoring by particle mobility sensing with single molecule resolution. *Nat. Commun.*, 9(1):1–10, 2018.
- [188] Wei Gao, Sam Emaminejad, Hnin Yin Yin Nyein, Samyuktha Challa, Kevin Chen, Austin Peck, Hossain M Fahad, Hiroki Ota, Hiroshi Shiraki, Daisuke Kiriya, Der-Hsien Lien, George A Brooks, Davis W Ronald, and Ali Javey. Fully integrated wearable sensor arrays for multiplexed in situ perspiration analysis. *Nature*, 529(7587):509–514, 2016.
- [189] Hyunjae Lee, Changyeong Song, Yong Seok Hong, Min Sung Kim, Hye Rim Cho, Taegyu Kang, Kwangsoo Shin, Seung Hong Choi, Taeghwan Hyeon, and

- Dae-Hyeong Kim. Wearable/disposable sweat-based glucose monitoring device with multistage transdermal drug delivery module. *Science Adv.*, 3(3):e1601314, 2017.
- [190] Saraswathi Padmanabhan, Vengalathunadakal K Shinoj, Murukeshan Vadakke Matham, and Parasuraman Padmanabhan. Highly sensitive optical detection of specific protein in breast cancer cells using microstructured fiber in extremely low sample volume. *J. Biomed. Opt.*, 15(1):017005, 2010.
- [191] Zhongxu Cao, Baicheng Yao, Chenye Qin, Run Yang, Yanhong Guo, Yufeng Zhang, Yu Wu, Lei Bi, Yuanfu Chen, Zhenda Xie, Guanding Peng, Shu-Wei Huang, Chee Wei Wong, and Yunjiang Rao. Biochemical sensing in graphene-enhanced microfiber resonators with individual molecule sensitivity and selectivity. *Light Sci. Appl.*, 8(1):1–10, 2019.
- [192] Qing Li, He Huang, Feng Lin, and Xingkun. Wu. Optical micro-particle size detection by phase-generated carrier demodulation. *Opt. Express*, 24(11):11458–11465, 2016.
- [193] Virginia Pretini, Mischa H Koenen, Lars Kaestner, Marcel HAM Fens, Raymond M Schiffelers, Marije Bartels, and Richard Van Wijk. Red blood cells: chasing interactions. *Frontiers in Physiology*, 10:945, 2019.
- [194] Rustem I Litvinov and John W Weisel. Role of red blood cells in haemostasis and thrombosis. *ISBT science series*, 12(1):176–183, 2017.
- [195] Subra Suresh, J Spatz, John P Mills, Alexandre Micoulet, Ming Dao, C T Lim, M Beil, and Thomas Seufferlein. Connections between single-cell biomechanics and human disease states: gastrointestinal cancer and malaria. *Acta Biomaterialia*, 1(1):15–30, 2005.
- [196] P Sajeesh and Ashis Kumar Sen. Particle separation and sorting in microfluidic devices: a review. *Microfluid. Nanofluidics*, 17(1):1–52, 2014.
- [197] Xinyu Chen, Yi Gu, Jiajie Chen, Chang-Hung Lee, Ivan Gagne, Rui Tang, Lauren Waller, Zunming Zhang, Alex Ce Zhang, and Yuanyuan Han. Image-guided cell sorting using fast scanning lasers. *APL Photon.*, 5(4):040801, 2020.

- [198] Eduard J Van Beers, Leigh Samsel, Laurel Mendelsohn, Rehan Saiyed, Kleber Y Fertrin, Christine A Brantner, Mathew P Daniels, James Nichols, J Philip McCoy, and Gregory J Kato. Imaging flow cytometry for automated detection of hypoxia-induced erythrocyte shape change in sickle cell disease. *American J. Hematology*, 89(6):598–603, 2014.
- [199] Francesco Merola, Pasquale Memmolo, Lisa Miccio, Roberto Savoia, Martina Mugnano, Angelo Fontana, Giuliana D’ippolito, Angela Sardo, Achille Iolascon, Antonella Gambale, and Pietro Ferraro. Tomographic flow cytometry by digital holography. *Light Sci. Appl.*, 6(4):e16241–e16241, 2017.
- [200] Bei Jiang, Hailang Dai, Yun Zou, and Xianfeng Chen. Continuous detection of micro-particles by fiber Bragg grating Fabry-Pérot flow cytometer. *Opt. Express*, 26(10):12579–12584, 2018.
- [201] Nien-Tsu Huang, Hua-li Zhang, Meng-Ting Chung, Jung Hwan Seo, and Katsuo Kurabayashi. Recent advancements in optofluidics-based single-cell analysis: optical on-chip cellular manipulation, treatment, and property detection. *Lab Chip*, 14(7):1230–1245, 2014.
- [202] SM Hampson, William Rowe, Steven DR Christie, and Mark Platt. 3D printed microfluidic device with integrated optical sensing for particle analysis. *Sens. Actuator B-Chem.*, 256:1030–1037, 2018.
- [203] Weikun Huang, Tongzhi Wu, Aliaa Shallan, Roman Kostecki, Christopher K Rayner, Craig Priest, Heike Ebendorff-Heidepriem, and Jiangbo Zhao. A multiplexed microfluidic platform toward interrogating endocrine function: Simultaneous sensing of extracellular  $Ca^{2+}$  and hormone. *ACS Sens.*, 5(2):490–499, 2020.
- [204] Dawei Yu, Songnian Fu, Zizheng Cao, Ming Tang, Lei Deng, Deming Liu, Ian Giles, Ton Koonen, and Chigo Okonkwo. Characterization of Rayleigh backscattering arising in various two-mode fibers. *Opt. Express*, 24(11):12192–12201, 2016.
- [205] Arthur Ashkin. Optical trapping and manipulation of neutral particles using

- lasers. *Proceedings of the National Academy of Sciences*, 94(10):4853–4860, 1997.
- [206] Ivo T Leite, Sergey Turtaev, Xin Jiang, Martin Šiler, Alfred Cuschieri, Philip St J Russell, and Tomáš Čižmár. Three-dimensional holographic optical manipulation through a high-numerical-aperture soft-glass multimode fibre. *Nat. Photon.*, 12(1):33–39, 2018.
- [207] D S Bykov, O A Schmidt, T G Euser, and Philip St J Russell. Flying particle sensors in hollow-core photonic crystal fibre. *Nat. Photon.*, 9(7):461–465, 2015.
- [208] Dmitry S Bykov, Shangran Xie, Richard Zeltner, Andrey Machnev, Gordon KL Wong, Tijmen G Euser, and Philip St J Russell. Long-range optical trapping and binding of microparticles in hollow-core photonic crystal fibre. *Light Sci. Appl.*, 7(1):1–7, 2018.
- [209] Erik P Schartner, Matthew R Henderson, Malcolm Purdey, Deepak Dhatrak, Tanya M Monro, P Grantley Gill, and David F Callen. Cancer detection in human tissue samples using a fiber-tip pH probe. *Cancer Res.*, 76(23):6795–6801, 2016.
- [210] Stephen C Warren-Smith and Tanya M Monro. Exposed core microstructured optical fiber Bragg gratings: refractive index sensing. *Opt. Express*, 22(2):1480–1489, 2014.
- [211] Mengke Han, Jiangbo Zhao, Joseph Mahandas Fabian, Samuel Evans, Sanam Mustafa, Yinlan Ruan, Steven Wiederman, and Heike Ebendorff-Heidepriem. Cytoplasmic delivery of quantum dots via microelectrophoresis technique. *Electrophoresis*, 2021.
- [212] Yuxiang Du, Chang-Ling Zou, Chunhuan Zhang, Kang Wang, Chan Qiao, Jiannian Yao, and Yong Sheng Zhao. Tuneable red, green, and blue single-mode lasing in heterogeneously coupled organic spherical microcavities. *Light: Sci. Appl.*, 9(1):1–9, 2020.
- [213] Ugo Fano. Effects of configuration interaction on intensities and phase shifts. *Phys. Rev.*, 124(6):1866, 1961.

- [214] Mikhail F Limonov, Mikhail V Rybin, Alexander N Poddubny, and Yuri S Kivshar. Fano resonances in photonics. *Nat. Photon.*, 11(9):543, 2017.
- [215] Linpeng Gu, Liang Fang, Hanlin Fang, Juntao Li, Jianbang Zheng, Jianlin Zhao, Qiang Zhao, and Xuetao Gan. Fano resonance lineshapes in a waveguide-microring structure enabled by an air-hole. *APL Photon.*, 5(1):016108, 2020.
- [216] Shanhui Fan. Sharp asymmetric line shapes in side-coupled waveguide-cavity systems. *Appl. Phys. Lett.*, 80(6):908–910, 2002.
- [217] Wei Liang, Lan Yang, Joyce K Poon, Yanyi Huang, Kerry J Vahala, and Amnon Yariv. Transmission characteristics of a Fabry-Pérot etalon-microtoroid resonator coupled system. *Opt. Lett.*, 31(4):510–512, 2006.
- [218] Nicolas P Mauranyapin, Lars Madsen, MA Taylor, M Waleed, and WP Bowen. Evanescent single-molecule biosensing with quantum-limited precision. *Nat. Photon.*, 11(8):477–481, 2017.
- [219] Thomas W Clark, Rachel F Offer, Sonja Franke-Arnold, Aidan S Arnold, and Neal Radwell. Comparison of beam generation techniques using a phase only spatial light modulator. *Opt. Express*, 24(6):6249–6264, 2016.
- [220] Carmelo Rosales-Guzmán and Andrew Forbes. *How to shape light with spatial light modulators*. SPIE Press, 2017.